

# **MEMS for Glaucoma**

Thesis by

**Jeffrey Chun-Hui Lin**

In Partial Fulfillment of the Requirements

for the degree of

Doctor of Philosophy



CALIFORNIA INSTITUTE OF TECHNOLOGY

Pasadena, California

2012

(Defended February 6, 2012)

© 2012

Jeffrey Chun-Hui Lin

All Rights Reserved

To my family



# ACKNOWLEDGEMENTS

First, I would faithfully express my gratitude to my advisor, Prof. Yu-Chong Tai, who admitted me in 2005 to this fantastic Micromachining group at Caltech. Since I was a new Ph.D. graduate student at Caltech, Prof. Tai was an extremely good advisor to me during my years in the group. Prof. Tai is so knowledgeable that he could always foresee what I could not see in terms of the research, and therefore guide me on the right path to success. Every time when I felt frustrated about the experiments, he opened my eyes to the issues when I spoke to him, and I could always overcome the problems by incorporating his excellent ideas or advice. I always feel his enthusiasm about the research, and his optimism and confidence encouraged me to complete every tough experiment repeatedly. Under Prof. Tai's strict and complete trainings about the research, I started to understand something about this amazing MEMS world and make some working devices.

Prof. Tai has never let the students worry about the availability of research resources in the group. Undoubtedly, his vast knowledge and astute creativity has led the entire research team, and even the entire MEMS field, into the cutting-edge technologies and discoveries. Because of this, he is always able to maintain the whole research operation without stopping, even in such competitive academia today. Therefore, Prof. Tai can manage our research team as one of the top-leading MEMS research groups worldwide. Prof. Tai's attentive guidance and generous tolerance to the students, his desire and pursuit of new knowledge, and even his personality, are the best example for young researchers.

As I was a new international student, Dr. Tai became one of my best friends during my years at Caltech. In addition to academic research, Dr. Tai taught me a lot of important attitudes and necessary characteristics for me to lead a successful life in this new environment. I believe all the philosophy I have learned from him is as precious as the research results in the lab. It will accompany me and be my Holy Grail guiding me to success in my future life.

I would show my greatest appreciation to all my defense committee members, Prof. Joel Burdick, Prof. Changhui Yang, Prof. Azita Emami, and Prof. Hyuck Choo, for their instructive advice during my defense. I would especially like to thank Prof. Mark Humayun at Doheny Eye Institute at USC for his leading this wonderful glaucoma-management project. I was always stunned by his amazing skill in implanting devices. His clinical experiences always inspired me to improve the device designs. As a member of both the National Academy of Engineering and the Institute of Medicine, Prof. Humayun is a prodigy of learning and is an inspiring example for young academic researchers. His profound knowledge can always arouse the invention of new medical devices and therefore it makes me aspire to achieve the same level of expertise all the time. I would also specially thank my collaborative workers at USC, Dr. Rohit Varma and Dr. Salomeh Saati, for their assistance in the devices' animal trials and useful suggestions in terms of the device design.

I would like to thank our lab manager, Trevor Roper, for his endless maintenance of all kinds of facilities in the group as well as suggestions in terms of the device testing. With his sophisticated skill in repairing the equipment in the cleanroom, we always felt relieved when we saw Trevor working in the lab because Trevor is the person who calms

the fears of those who think they have to cease research due to equipment troubles. I would like to give thanks to our group administer, Christine Garske, for her kindly many aspects of the group, particularly for her big help in in managing group's purchasing orders. Christine always keeps track of every purchase order, ensuring that they are on schedule so that students have never to worry about the delay of getting the materials. She is very thoughtful to every group member. As a result, everything is well-ordered and goes smoothly under her organization. Besides, I very much appreciate our previous group administrator, Agnes Tong, for her help during my first few years in the group.

I would also like to say thanks to my lab-mates who joined the group with me in the same year, Ray Huang, Luca Giacchino, and Monty Nandra, for their useful help and constructive suggestions of my device fabrication and test. Working in a group with joint efforts and mutual support all towards the same goal of a Ph.D will be an unforgettable memory in my lifetime. I give special thanks to Po-Jui Chen, who was my mentor when I just joined the team and my co-worker when we worked together on the glaucoma-management project. Additionally, thanks to all previous and current group members in Caltech Micromachining Group for their assistance, encouragement, and tolerance. Working with the world's best group of students makes me aware of my insufficiencies and lack of capabilities in certain areas. It constantly pushes me to progress and pursue excellence in in all aspects of life. I would also like to thank all my talented SURF students, Brian Yu, Gilbert Lam, Rujian Chen, and Chenxi Qui, for their remarkable contribution and excellent jobs in the my experiments. It was so memorable to work with talented young undergrads like them in the lab during the summer. In short, I am pleased

to have worked and learned in one of the best MEMS research group worldwide and am extremely proud to be one of the group members among them.

I would like to express my great appreciation to my guitar teacher, Dr. Matthew Elgart, for instructing me in playing the classical guitar over the past few years. In addition to being a great performer, Matthew is also a very good teacher who has taught me from the start until now, and I can already perform some ensemble pieces. Matthew has always showed a lot of patience in explaining the music to me and helping me to choose the proper way to interpret it. It takes a lot of effort and different thoughts to crack every music piece and therefore playing a musical instrument actually helps me cultivate my concentration on lab work and perseverance on doing the research. Playing classical guitar enriches my life as a graduate student at Caltech and it is really a good stress reliever for the busy research life. Most importantly, Matthew's instruction satisfies my desire for understanding the classical guitar and even classical music. Thank Matthew for taking me into such a beautiful and amazing classical guitar world. I believe the classical guitar will be one of my best companions in my life.

I would like to thank all my friends who I became acquainted with at Caltech. It was so interesting to take the classes, work in the lab, and go to the Gym together with all them. Making so many friends from different countries really broadens my mind and views. In addition, I would like to thank all the Caltech Taiwanese students for their continuous support and help. In addition to the common discussions and suggestions about the research, it was always exciting to go grocery shopping with Taiwanese students at every Fri. night. I give particular thanks to the ACT (Association of Caltech Taiwanese) for holding all kinds of events during our traditional Taiwanese holidays such

as Chinese New Year, Dragon Boat Festival, and Mid-Autumn Festival, etc. Those events always made me feel warm during these holidays and not alone outside Taiwan.

I am grateful to my parents for their constant support of my decisions, and always encouraging me to pursue the best during my student's life. Their educating me as a person of integrity by setting themselves as examples, financially supporting me through my studies, and helping me make decisions all determine who I am now. I also feel so blessed for my parents-in-law's kindness, particularly for their unreserved support for my marriage with their daughter. Finally, I owe my dear wife, Yi-Ying Tang, for her continuous support and encouragement to me through several years. Although separated by a long distance for many years, Yi-Ying's tolerance and understanding has always been my firmest backbone giving me faith to proceed on and eventually fulfill the Ph.D. degree.

Finally yet importantly, I would like to thank my sweet Little-Turkey princess, Sharon Lin, who was born during my final last months of thesis writing period. My daughter's coming to the world makes me feel the miracle of life. Sharon's smile always cheers me up when I feel frustrated, and boosts me to work on my thesis and defense full steam ahead again.

Thank you to everyone who has given me helps in this exciting doctoral journey. Without you, this thesis would have not been possible.



# ABSTRACT

## MEMS for Glaucoma

Thesis by

**Jeffrey Chun-Hui Lin**

Doctor of Philosophy in Electrical Engineering

California Institute of Technology

Glaucoma is an eye disease that gradually steals vision. Open angle glaucoma is one of the most common glaucoma forms, in which eye fluid (aqueous humor) produced by the ciliary body cannot be drained away normally by patients' eyes. The accumulated eye fluid inside the anterior chamber causes high intraocular pressure (IOP), which is transmitted onto the retina in the back of the eyeball (globe), continuously suppressing and damaging the patient's optic nerves; this may lead to total blindness if not treated properly.

The current most-popular IOP monitoring technique is to use applanation tonometry, which applies applanation force onto the cornea and measures the resulting deformation in order to calculate the IOP. Even though applanation tonometry can provide quite useful information about patients' IOP, continuous monitoring of IOP is required for ophthalmologists to understand the IOP fluctuation of the patients, something which still cannot be achieved *via* current applanation approach. In addition, applanation tonometry requires skillful operation performed by well-trained professionals, such as ophthalmologists, making continuous IOP monitoring impractical.

In this work, we have developed a telemetric IOP sensor that is capable of monitoring IOP wirelessly and continuously. As the quality factor drops when a telemetric IOP sensor is implanted in the anterior chamber, due to the high loss tangent of the saline-based aqueous humor ( $\sim 0.2$ ) compared to air (0.0), a modified IOP sensor is developed to monitor IOP with sensing coil that is left exposed after implantation in order to avoid interruption from the eye fluid. Another approach is also proposed and tested to demonstrate that the quality factor can also be recovered by covering the sensing coil with low loss tangent materials.

Currently glaucoma is treated mostly by taking oral medications or applying eye drops. However, some glaucoma patients do not respond to those medications. Therefore, another physical approach, using a glaucoma drainage device (GDD), is necessary in order to drain out excessive eye fluid and serve as a long-term way to manage the increased IOP. Current commercially available glaucoma drainage devices do not have reliable valve systems to stop the drainage when the IOP falls into the normal range. Therefore, we have developed a dual-valved GDD to fulfill the “band-pass” flow regulation which drains out eye fluid only when IOP is higher than 20 mmHg, and stops drainage (closes the valve) when IOP is lower than 20 mmHg to prevent hypotony. The key component of GDD is a normally closed (NC) check-valve, which only opens to drain away the excess fluid when the pressure is higher than 20 mmHg. The proposed paradigm of our NC check-valve is to have a couple of parylene-C pre-stressed slanted tethers to provide the desired cracking pressure. The slanted tethers are achieved in this thesis by: 1) slanted photoresist generated by gray-scale photolithography, 2) pop-up mechanism, and 3) self-stiction bonding mechanism. The built-in residual tensile stress

can be controlled by mechanical stretching or thermal annealing. The protecting mechanism preventing the unwanted drainage when the eyes experience sudden unpredicted high IOP is achieved by utilizing a normally open (NO) check-valve. A “minimally invasive implantation” procedure is proposed in the thesis to implant the GDD subconjunctivally. The small size of the device allows its insertion using a #19-gauge needle.

To accurately design the desired cracking pressure and also predict the lifetime of the NC check-valve, parylene-C’s mechanical, thermal, and polymer properties are investigated. The results show that the properties of parylene-C are highly process-temperature-dependent and therefore can be tailored by adjusting the thermal annealing process.



# TABLE OF CONTENTS

<b>ACKNOWLEDGEMENTS .....</b>	<b>v</b>
<b>ABSTRACT .....</b>	<b>xi</b>
<b>TABLE OF CONTENTS .....</b>	<b>xv</b>
<b>LIST OF FIGURES .....</b>	<b>xxiii</b>
<b>LIST OF TABLES .....</b>	<b>xxxix</b>
<b>CHAPTER 1 INTRODUCTION.....</b>	<b>1</b>
1.1 INTRODUCTION TO GLAUCOMA.....	1
1.2 CURRENT TREATMENT OF PRIMARY OPEN ANGLE GLAUCOMA.....	2
1.2.1 Medications for glaucoma.....	2
1.2.2 Glaucoma filtration surgery .....	4
1.3 GLAUCOMA DRAINAGE DEVICE.....	4
1.3.1 Active glaucoma drainage device .....	4
1.3.2 Passive glaucoma drainage device.....	5
1.3.2.1 History of the development of glaucoma drainage devices	6
1.3.2.2 Contemporary passive glaucoma drainage device .....	9
1.3.2.3 Glaucoma drainage devices with no resistance .....	10
1.3.2.4 Glaucoma drainage devices with resistance .....	12
1.3.2.5 Comparison of current “tube-and-plate”-type glaucoma drainage devices.....	13
1.3.2.6 Postoperative complications of current glaucoma drainage devices.....	16

1.3.2.7 Long-term failure of the GDD: Bleb fibrosis .....	17
1.3.3 Proposed glaucoma drainage device design .....	18
1.4 INTRAOCULAR PRESSURE MONITORING .....	20
1.4.1 Current clinical IOP monitoring approaches .....	20
1.4.2 Wireless telemetric sensing technology .....	21
1.5 BIOCOMPATIBLE MATERIAL, PARYLENE-C, USAGE .....	23
1.6 CHARACTERISTICS OF PARYLENE-C .....	24
1.7 SUMMARY .....	26
<b>CHAPTER 2 PASSIVE NORMALLY CLOSED MICRO CHECK-VALVES .....</b>	<b>29</b>
2.1 OVERVIEW .....	29
2.2 THEORETICAL ANALYSIS OF NC MICRO CHECK-VALVES .....	32
2.2.1 Thin-film-flow theory of the check-valve .....	32
2.2.2 Calculation of the necessary pre-stress force .....	35
2.3 PRE-STRESSED SLANTED TETHER MICRO CHECK-VALVES .....	36
2.3.1 Slanted tether NC check-valve configuration .....	36
2.3.2 Thermal annealing pre-stressed NC check-valves .....	37
2.3.3 Sloped photoresist .....	38
2.3.3.1 One-time-exposure gray-scale photo-mask .....	38
2.3.3.2 Linearization of the sloped sacrificial photoresist .....	39
2.3.4 Fabrication .....	41
2.3.5 Device testing and discussion .....	44
2.4 INTEGRATION OF SLANTED TETHER CHECK-VALVES FOR HIGH-PRESSURE APPLICATIONS .....	47

2.4.1 Electrical-equivalent diode model .....	48
2.4.2 Multiple check-valve integration .....	48
2.4.3 Characterization results and discussion .....	51
2.5 POP-UP MICRO CHECK-VALVE.....	52
2.5.1 Pop-up micro check-valve device design .....	53
2.5.2 Device fabrication .....	54
2.5.3 Device characterization setup .....	58
2.5.4 Device characterization results .....	60
2.6 SELF-STICTION-BONDING MICRO NC CHECK-VALVES .....	62
2.6.1 Design concept of the self-stiction-bonding NC check-valve .....	62
2.6.2 Fabrication of the self-stiction-bonding NC check-valve .....	64
2.6.3 Characterization of the self-stiction-bonding NC check-valve.....	66
2.7 BLISTER TEST OF STICTION OF PARYLENE-C FILM .....	68
2.7.1 Experimental approaches .....	69
2.7.2 Theory of blister test .....	71
2.7.3 Blister test experimental setup .....	72
2.7.4 Testing results and discussion.....	74
2.7.5 Summary .....	78
2.8 SUMMARY AND CONCLUSION .....	79
2.8.1 Comparison of different types of micro check-valves .....	79
2.8.2 Lifetime of the slanted tether NC check-valves.....	81

## CHAPTER 3 INTEGRATION AND APPLICATIONS OF MICRO CHECK-

<b>VALVES FOR GLAUCOMA TREATMENT .....</b>	<b>83</b>
3.1 CONFIGURATION OF THE “BAND PASS” FLOW-RATE PROFILE DUAL-VALVE	
GDD SYSTEM .....	85
3.1.1 Dual back-to-back valves design .....	86
3.1.2 Numerical simulation of the glaucoma drainage device.....	87
3.2 DESIGN, FABRICATION, AND TEST OF THE NORMALLY OPEN VALVE.....	88
3.2.1 Design of the NO valve.....	88
3.2.2 Fabrication of the NO valve.....	90
3.2.3 Characterization of NO valve .....	91
3.3 SUTURELESS, MINIMALLY INVASIVE IMPLANTATION OF THE DUAL-VALVED	
GDD .....	93
3.3.1 Dual-valved GDD out-shape.....	94
3.3.2 Dual back-to-back valve configuration.....	94
3.3.3 Parylene-C protective tube carrier .....	95
3.3.4 Design and fabrication of the rollable/foldable parylene-C fixation	
anchors .....	96
3.3.5 Dual-valved glaucoma drainage device packaging.....	98
3.4 VALVE-POSITION-ADJUSTABLE DUAL-VALVED GDD.....	99
3.4.1 Configuration of the valve-position-adjustable dual-valved GDD	101
3.4.2 Grooved check-valves.....	102
3.4.3 Grooved check-valve fabrication procedures .....	103
3.4.4 Grooved check-valve packaging procedures .....	105

3.5 BENCH-TOP GDD CHARACTERIZATION.....	106
3.5.1 Bench-Top GDD characterization setup.....	106
3.5.2 Bench-Top GDD characterization results.....	107
3.6 GDD <i>EX VIVO</i> TEST AND DISCUSSION.....	109
3.6.1 GDD <i>ex vivo</i> implantation.....	110
3.6.2 Tapered hollow parylene-C protective tube mockup <i>ex vivo</i> implantation.....	111
3.7 SUMMARY AND CONCLUSION.....	114
<b>CHAPTER 4 HIGH-QUALITY-FACTOR PARYLENE-C-BASED</b>	
<b>    INTRAOcular PRESSURE SENSOR.....</b>	
4.1 OVERVIEW.....	117
4.2 SENSING THEORY AND THE DEVICE DESIGN.....	125
4.2.1 Sensing scheme.....	125
4.2.2 Electrical and mechanical design of the device.....	126
4.3 DEVICE FABRICATION AND CHARACTERIZATION.....	128
4.3.1 Device fabrication.....	128
4.3.2 Device characterization.....	129
4.4 CHARACTERIZATION RESULTS AND DISCUSSIONS.....	131
4.5 QUALITY FACTOR RECOVERY STUDY.....	134
4.5.1 Overview.....	134
4.5.2 Q factor recovery by passivation layers of different materials.....	135
4.5.3 Q factor recovery by parylene-C passivation layers.....	138
4.5.4 Summary.....	141

4.6 SUMMARY AND CONCLUSION .....	142
<b>CHAPTER 5 CHARACTERISTICS OF PARYLENE-C FILM.....</b>	<b>145</b>
5.1 OVERVIEW .....	145
5.2 INTRODUCTION TO PARYLENE-C POLYMERIZATION .....	146
5.3 DENSIFICATION .....	147
5.3.1 Thickness-change measurement .....	149
5.3.2 In situ length-change measurement during thermal annealing .....	150
5.3.2.1 Length change under long-time thermal annealing process at 100°C .....	150
5.3.2.2 One cycle thermal annealing treatment.....	154
5.3.2.3 Cyclic thermal annealing treatment up to 120°C.....	155
5.3.3 Summary .....	158
5.4 OXIDATION .....	159
5.4.1 XPS .....	160
5.4.2 FTIR.....	163
5.4.3 Summary and discussion.....	167
5.5 CRYSTALLIZATION .....	169
5.5.1 X-ray diffraction method .....	171
5.5.1.1 In situ consecutive XRD scanning at 100°C.....	171
5.5.1.2 In situ temperature ramping annealing study.....	177
5.5.2 Time constant of parylene-C annealed at 100°C .....	180
5.5.3 Effect of deposition pressure difference .....	182
5.5.4 Summary and discussion.....	184

5.6 GLASS TRANSITION TEMPERATURE .....	186
5.6.1 Identification of glass transition temperature .....	188
5.6.1.1 Reported glass transition temperature of parylene-C.....	188
5.6.1.2 Ramping-temperature-dependent modulus experiment..	189
5.6.1.3 Dynamic mechanical analysis.....	193
5.6.2 Measuring results and discussion.....	197
5.6.3 Summary .....	207
5.7 UNIAXIAL TENSILE TEST.....	208
5.7.1 As-deposited parylene-C film .....	211
5.7.2 Deposition pressure influence.....	213
5.7.3 Oxidation effect .....	215
5.7.4 Annealing temperature and time influence .....	218
5.7.5 Effect of testing environmental temperature.....	221
5.7.6 Summary .....	225
5.8 RHEOLOGICAL PROPERTIES OF PARYLENE-C FILM .....	226
5.8.1 Creep of parylene-C.....	228
5.8.1.1 Creep overview .....	228
5.8.1.2 Introduction of the Burger's model.....	229
5.8.1.3 Primary and secondary creep of parylene-C.....	232
5.8.1.4 Summary .....	256
5.8.2 As-deposited parylene-C creep study under a step temperature profile.....	258
5.8.2.1 Experimental setup.....	258

5.8.2.2 Experimental results and discussions.....	260
5.8.3 Stress relaxation of parylene-C .....	265
5.8.3.1 Stress relaxation overview .....	265
5.8.3.2 Solution of the Burger’s model for stress relaxation .....	266
5.8.3.3 Stress relaxation experiment .....	267
5.8.3.4 Summary .....	271
5.8.4 Summary .....	272
5.9 VISCOPLASTICITY OF PARYLENE-C FILM AT HUMAN BODY TEMPERATURE ..	274
5.9.1 Overview of parylene-C viscoplasticity study.....	274
5.9.2 Sample preparation and viscoplastic experiments .....	275
5.9.2.1 Sample preparation and testing environment setup .....	275
5.9.2.2 Testing results .....	275
5.9.2.3 Discussion .....	276
5.9.3 Summary .....	282
5.10 SUMMARY AND CONCLUSION .....	282
<b>CHAPTER 6 GENERAL CONCLUSION .....</b>	<b>287</b>
<b>BIBLIOGRAPHY .....</b>	<b>293</b>

## LIST OF FIGURES

Figure 1-1: Molecular structure of parylene-C .....	23
Figure 2-1: Concept of the normally closed (NC) check-valve: (a) The check-valve is closed when the applied pressure $P$ is lower than the cracking pressure $P_c$ ; (b) the check-valve is open when the applied pressure $P$ is higher than the cracking pressure $P_c$ .....	30
Figure 2-2: Check-valve model for unsteady flow analysis: (a) side view, and (b) top view.....	32
Figure 2-3: Schematic of cracking-pressure-controlled parylene-C check-valve using the residual tensile stress in parylene-C after thermal annealing .....	36
Figure 2-4: A closer view of designed gray-scale photo-mask for the creation of sloped photoresist. The right pattern magnifies part of the pixel structure of the ring. ....	38
Figure 2-5: One-time-exposure gray-scale sacrificial photoresist profile: (a) before linearization, and (b) after linearization.....	41
Figure 2-6: Fabrication procedures. Slanted sacrificial photoresist is achieved using a one-time-exposure gray-scale photo-mask photolithography approach.....	42
Figure 2-7: SEM pictures of fabricated check-valves: (a) check-valves before photoresist removal, (b) a closer view of a tether and the sloped photoresist, (c) check-valves after photoresist removal, (d) a closer view of a tether after photoresist removal, (e) the cross-sectional view of the parylene-C anchor, and (d) micrograph of the top view of the check-valve .....	43

Figure 2-8: Testing setup for MEMS micro check-valves.....	44
Figure 2-9: Parylene-C tether width effect of the characterization results of thermally pre-stressed slanted tether micro check-valves: different tether widths but with the same annealing temperature at 100°C .....	45
Figure 2-10: Temperature effect of the characterization results of thermally pre-stressed slanted tether micro check-valves: different annealing temperatures but with the same tether widths of 50 $\mu\text{m}$ .....	46
Figure 2-11: Equivalent electrical circuit component model of check-valves: (a) one-diode model of one check-valve. $k$ and $dz$ are the spring constant of the tethers and the covering plate displacement, respectively. (b) In-series diodes model of in-series check-valves.....	49
Figure 2-12: Valve packaging: (a) A single valve packaged in capillary tubes and (b) four individual modules integrated using coupling tubes .....	50
Figure 2-13: (a) Modified device testing setup, (b) the characterization of single valve, and (c) the characterization of four check-valves in series.....	50
Figure 2-14: (a) Flow characteristics of a single valve, (b) micrograph of a check-valve in tube after testing, (c) flow characteristics of a four-check-valve assembly ..	52
Figure 2-15: The configuration of a pop-up check-valve. A close-up of the undercut parylene-C foot is shown in the circular area. ....	54
Figure 2-16: Fabrication procedures of (a) the pop-up micro check-valve, and (b) the testing chips .....	56

Figure 2-17: Micrograph of (a) 10 $\mu\text{m}$ undercut of the LOR30B, (b) top view of the NC check-valve, (c) top view of the outlet orifice, and (d) final device appearance .....	57
Figure 2-18: SEM pictures of (a) undercut parylene-C foot coating (back side view), (b) close view of undercut parylene-C foot coating, (d) normally closed check-valve, and (d) covering plate after pop-up .....	58
Figure 2-19: Cross section view of the testing chip with mounted in-channel check-valve .....	59
Figure 2-20: (a) Top view of the fabricated testing chip. (b) A close view of mounted device on top of the testing chip, sealed with dried photoresist .....	59
Figure 2-21: Captured pictures of normally closed pop-up check-valve during popping-up process (shown in arrow): (a) right before pop-up, (b) during pop-up, and (d) after pop-up. (Top parylene-C membrane is peeled off for clarity.) .....	61
Figure 2-22: Testing result of the pop-up check-valve .....	61
Figure 2-23: Schematics of the self-stiction-bonding NC check-valve .....	64
Figure 2-24: Fabrication procedures of the self-stiction-anchoring NC check-valve .....	65
Figure 2-25: Fabrication results of the self-stiction-anchoring NC check-valves: (a) SEM picture showing the regular NC check-valve, (b) SEM picture showing the NC check-valve with small holes for epoxy enhancement, (c) top view of the NC check-valve, and (d) NC check-valve with epoxy bonding enhancement .....	66
Figure 2-26: Pressure/flow-rate profile characterization results of the self-stiction-bonding NC check-valve .....	67

Figure 2-27: Top view of finished parylene-C check-valves fabricated for blister test ...	69
Figure 2-28: Fabrication procedures for circular parylene-C check-valve with different valve-seat surface treatments.....	70
Figure 2-29: Theoretical blister formation during experimentation: (a) The applied pressure is less than or equal to the critical debonding pressure, $P_c$ . (b) The applied pressure is higher than the critical debonding pressure, $P_c$ ; the parylene-C film starts to propagate.....	71
Figure 2-30: Experimental setup of the blister test: (a) the cross-section view of the test jig, and (b) schematic diagram of the testing setup .....	73
Figure 2-31: A typical curve of the blister test. The parylene-C film starts to debond when the applied pressure is higher than the critical debonding pressure.....	74
Figure 2-32: Stiction of parylene-C with different substrate surfaces after three kinds of releasing processes. Blue: acetone soak followed by IPA and water soak. Green: acetone soak followed by HF dip and water rinse. Red: soaking in mixture of acetone and silicone oil followed by direct air drying .....	75
Figure 2-33: Hydrogen bonding that occurs between water molecules and the passivated silicon surface. As the device dries, decreasing water content between the parylene-C film and the silicon pulls the two surfaces together through hydrogen bonding.....	76
Figure 2-34: Stiction between parylene-C and various surfaces after releasing in a mixture of acetone and silicone oil.....	77

Figure 2-35: Stiction between the parylene-C and the silicon surface is reduced due to the silicone oil layer, which reduces surface passivation and the proximity between surfaces.....	77
Figure 3-1: Concept of the “band pass” flow-rate profile of the proposed GDD system comprising (a) an NC check-valve, and (b) an NO valve to achieve (c) a band pass flow-rate profile .....	85
Figure 3-2: The cross section of a normally open check-valve .....	88
Figure 3-3: COMSOL Multiphysics™ simulation of the dual-valved GDD system: (a) deflection simulation of the NC check-valve, (b) flow-rate simulation results of the NC check-valve, (c) deflection simulation of the NO valve, (c) flow-rate simulation results of the NC check-valve, (e) flow-rate simulation of the dual-valved GDD system, (f) flow-rate simulation results of the dual-valved GDD system.....	89
Figure 3-4: Fabrication procedures of the NO valve .....	90
Figure 3-5: Fabrication results of the NO valve: (a) top view of the NO valve, and (b) SEM picture of the NO valve .....	91
Figure 3-6: Pressure/flow-rate profile characterization results of the NO valve .....	92
Figure 3-7: Concept of the minimally invasive implantation: (a) Subconjunctival implantation idea of the (GDD) implanted through the anterior chamber of the eye. (b) A complete GDD system consisting of a dual-valve micro-flow regulation system (one NC check-valve at one end of the tube and one NO valve on the other end of the tube), a parylene-C protective tube carrier, and a rollable/foldable anchor .....	93

- Figure 3-8: (a) Fabrication procedures of the parylene-C protective tube carrier, (b) coated 40  $\mu\text{m}$  parylene-C on the sacrificial capillary glass tubing, (c) slanted and completed parylene-C protective tube carrier..... 95
- Figure 3-9: Fabrication procedures of the parylene-C fixation anchors..... 98
- Figure 3-10: Packaging procedures of the dual-valved GDD system: (a) NC check-valve; (b) NO valve; (c) NC check-valve with stiction bonding enhanced by epoxy; (d) hollow parylene-C protective tube carrier; (e) one NC and one NO valve sealed in the parylene-C protective tube carrier (transparent glass tube used here for clarity); (f) anchors with trenches of 300  $\mu\text{m}$  in radius, different anchor shapes designed to facilitate the surgical convenience, and future GDD fixation (left: ragged anchor; middle: foldable anchor; right: rollable squeeze-tail anchor); (g) completed assembled GDD in top view; (h) anchors can be rolled/folded for testing and implantation convenience. Check-valves are first sealed in the carrier, which is then assembled onto anchors. .... 100
- Figure 3-11: Schematics of valve-in-tube system: (a) Combination of one NC valve and one NO valve with a coupling tube to form the micro-flow regulating assembly. (b) Final finished valve-in-tube system ..... 102
- Figure 3-12: Cross section of the grooved self-stiction-bonding NC check-valve design ..... 103
- Figure 3-13: Modification of step 4 of the fabrication procedures of (a) NC check-valve and (b) NO valve by DRIE to incorporate a circular groove using the same photoresist mask for parylene-C patterning (photoresist mask not shown) 103

- Figure 3-14: Micrographs of: (a) the fabrication result of an NC check-valve, (b) the top view of a NC check-valve packaged inside a coupling tube, (c) packaging results of the micro-flow regulating assembly, (d) the micro-flow regulating assembly packaged inside a tapered parylene-C protective tube carrier 610  $\mu\text{m}$  in diameter, suitable for a #19-gauge hypodermic needle ..... 104
- Figure 3-15: The packaging procedures: (a) one check-valve attached to one end of the coupling tube, (b) complete micro-flow regulating assembly, (c) final valve-in-tube system..... 105
- Figure 3-16: Testing setup of the GDD: Photoresist is painted in the gap between GDD and Teflon tubing for sealing..... 107
- Figure 3-17: Dual-valved GDD characterization results: The fluid starts to flow after 0.33 psi ( $\sim 17$  mmHg) and closes at 1.1 psi ( $\sim 57$  mmHg). Water was chosen as the working fluid..... 108
- Figure 3-18: Testing setup of GDD *ex vivo* implantation test ..... 110
- Figure 3-19: (a) The plunger in the needle introducer, (b) a GDD with folded zigzag type parylene-C fixation anchor inserted into a #19-gauge hypodermic needle, (c) a hollow parylene-C tube subconjunctivally implanted into an enucleated porcine eye, (d) testing dye shunted into the hollow tube. The drained-out testing dye is visible..... 111
- Figure 3-20: *Ex vivo* implantation results of: (a) GDD 1 and (b) GDD 2. The testing dye started to drain out after fluids were injected and stopped at 24 mmHg. (c) Residual dye kept flowing slightly at 4 mmHg. .... 113

- Figure 3-21: Inspection of the NC check-valve after *ex vivo* implantation: (a) right after the implantation, and (b) after one week of soaking in DI water ..... 114
- Figure 4-1: (a) Wireless sensing concept of implantable IOP sensor in the anterior chamber, (b) the glass reader paradigm, (c) a real IOP sensor *in vivo* tested in a rabbit eye..... 120
- Figure 4-2: The concept of the wireless inductive coupling link: The frequency shift is registered through an external oil reader. .... 121
- Figure 4-3: Resonant frequency shift corresponds to the applied pressure: (a) Frequency decreases as the capacitance increases; (b) No frequency shift is observed when no pressure difference exists; (c) Frequency increases as the capacitance decreases. .... 122
- Figure 4-4: The new IOP sensor design: (a) Top view of the sensing part, (b) AA' cross-section view of the IOP sensor ..... 122
- Figure 4-5: The newly designed IOP sensor is implanted at the pars plana with the implantation tube going through the choroid, while the sensing part still remains outside the choroid, but under the conjunctiva of the eye. .... 124
- Figure 4-6: Fabrication procedures of the sensing part of the IOP sensor..... 128
- Figure 4-7: IOP sensor fabrication and assembling results: (a) Completed sensing part, (b) implantation tube attached onto the backside of the sensing part concentric with the pressure access hole, (c) IOP sensor mounted to the testing tube by photoresist, (d) final IOP sensor..... 130

Figure 4-8: IOP sensor characterization setup: a 1.5-mm-diameter hand-wound coil served as the reader coil and a HP4195A network/spectrum analyzer was used to register the frequency shift of the phase dip. ....	131
Figure 4-9: Bench-top characterization results of the IOP sensor: the resonant frequency was 379 MHz when the applied pressure difference was 0 mmHg, and shifted to higher frequency when the pressure difference increased. ....	132
Figure 4-10: Sensitivity analysis of the IOP sensor. ....	133
Figure 4-11: The idea of covering the device with different passivation layers: glass cover slip, photoresist, or epoxy. The IOP sensor is shown in gray in the figure. ....	135
Figure 4-12: IOP sensors covered by two different materials with low loss tangent: (a) photoresist and (b) epoxy. ....	136
Figure 4-13: The idea of covering the device with several layers of parylene-C sheets. The IOP sensor is shown in gray in the figure. ....	139
Figure 4-14: Quality factor recovering results versus parylene-C thickness by covering the IOP sensor with several parylene-C layers. ....	140
Figure 4-15: Modified sensing coil fabrication procedures: After 30 $\mu\text{m}$ parylene-C layer is deposited on top of the capacitor metal plate, an extra oxygen plasma etching process is executed to thin down the central parylene-C to retain the capacitor sensitivity. ....	142
Figure 5-1: Measured thickness of 20 $\mu\text{m}$ parylene-C film annealed at 100°C in the convection oven. ....	149

Figure 5-2: (a) Obtained length change of the parylene-C film annealed at 100°C in air for 8 hours, and (b) a closer view of the length change during the first 2.5 minutes.....	152
Figure 5-3: Length change of the parylene-C film which was annealed at 100°C in air for 8 hours in the previous test. The sample was annealed again at 100°C for another 2 hours. ....	153
Figure 5-4: Length change of parylene-C film annealed under the temperature ramping rate at 3.33°C/min and its hypothesized phenomenon interpretation by dominant effect .....	155
Figure 5-5: Six cycles of thermal annealing of parylene-C film up to 120°C: The length of the film never goes back to its original length after the first-time thermal annealing.....	157
Figure 5-6: The parylene-C film behaves differently after the first-time thermal annealing.....	157
Figure 5-7: The oxidative species of parylene-C proposed by Nowlin [189].....	160
Figure 5-8: Typical XPS results of parylene-C samples. Top left: A closer view of the peak of 531.6 eV representing the content of oxygen .....	161
Figure 5-9: Comparison of two XPS results of parylene-C annealed at 200°C for two days in air and in vacuum .....	163
Figure 5-10: Typical FTIR results of parylene-C film. The black curve represents the as-deposited parylene-C film, while the others represent the results of annealing at 100°C. ....	165
Figure 5-11: FTIR results of parylene-C annealed at 200°C in air for different times...	166

Figure 5-12: Comparison of the FTIR results of parylene-C annealed at 200°C in air and vacuum, all for two days.....	167
Figure 5-13: Typical XRD scanning results showing curve from 10°–30°C .....	172
Figure 5-14: XRD results of in situ XRD measurement of parylene-C consecutively annealed at 100°C in helium.....	174
Figure 5-15: Crystallite size growing history of parylene-C annealed at 100°C in helium .....	176
Figure 5-16: XRD results of parylene-C annealed at 30°, 37°, 40°, and 50°C.....	178
Figure 5-17: XRD results of in situ XRD measurement of parylene-C consecutively annealed at different temperatures in helium. Temperature ramping rate = 3°C/min.....	179
Figure 5-18: Crystallite size growing history of parylene-C annealed at different temperatures in helium .....	180
Figure 5-19: The crystallite size versus the annealing time.....	181
Figure 5-20: Comparison of the results of XRD measurement of parylene-C deposited at 22 mT and 35 mT .....	184
Figure 5-21: Elastic modulus response versus temperature change .....	186
Figure 5-22: Concept of the ramping-temperature-dependent modulus experiment. Every peak represents one uniaxial tensile test.....	190
Figure 5-23: Elastic (Young's) modulus versus temperature curve. The transition region I represents the general glass transition region for as-deposited parylene-C, while transition region II represents the general glass transition region for parylene-C annealed at 100°C. ....	191

- Figure 5-24: The concept of dynamic analytical analysis. (a) A sinusoidal oscillatory stress is applied and the material's sinusoidal strain response with a phase delay (viscoelastic materials) is measured. (b) The relationship of complex modulus ( $E^*$ ), the storage modulus ( $E'$ ), and the loss modulus ( $E''$ ) ..... 194
- Figure 5-25: A typical DMA testing curve showing the results of storage modulus, loss modulus, and tan delta. Every curve has its corresponding definition to identify  $T_g$ . ..... 195
- Figure 5-26: A comparison of the results of the ramping-temperature-dependent modulus experiment and the DMA test. Parylene-C sample was annealed at 100°C for one day in vacuum.  $T_g$  is found at the inflection point of each glass transition region. .... 197
- Figure 5-27: Measured  $T_g$  of four parylene-C annealed in different conditions: 3 samples at 100°C, with as-deposited parylene-C as a comparison..... 201
- Figure 5-28: Measured  $T_g$  of parylene-C samples all annealed in 100°C but for different times: 30 sec, 1 min, 3 min, and 30 min ..... 202
- Figure 5-29: Measured  $T_g$  of four parylene-C samples annealed in different temperatures ..... 202
- Figure 5-30: Measured  $T_g$  of seven parylene-C samples annealed in different temperatures. Samples were annealed in the DMA Q800 chamber for 30 min prior to the  $T_g$  test. .... 203
- Figure 5-31: Typical as-deposited parylene-C film uniaxial tensile test results obtained by TA instrument DMA Q800 system. Toe region is compensated to give the

final correct calculated parameters. All terminologies follow the definition of the ASTM standard D882-09 and D638-08 [233, 234].	210
Figure 5-32: Comparison of parylene-C film deposited at different pressures. (a) Two stress-strain curves. (b) A closer view of elastic modulus and yield point.	215
Figure 5-33: Comparison of uniaxial tensile test results of parylene-C film with three different treatments: as-deposited, 1 day annealed at 100°C in air, and 1 day annealed in vacuum	216
Figure 5-34: Comparison of uniaxial tensile test results of parylene-C film with six different treatments	218
Figure 5-35: A closer view of Figure 5-34 (strain lower than 10%)	219
Figure 5-36: A series of uniaxial tensile tests of parylene-C performed at different environmental temperatures	223
Figure 5-37: A closer view of Figure 5-36 (strain lower than 5%)	223
Figure 5-38: A comparison of elastic modulus measured by DMA (as-deposited curve in Figure 5-27 in 5.6) and obtained from Table 5-13	224
Figure 5-39: Creep behavior of polymers: (a) constant applied stress during creep test at a constant temperature; (b) total strain versus time; (c) removal of the stress at the beginning of the creep recovery test; (d) recovery strain curve	229
Figure 5-40: Schematic diagram of the Burger's model	230
Figure 5-41 (a): Creep results of the as-deposited parylene-C deposited at 22 mTorr ( $T_g=53.4^\circ\text{C}$ ); (b): Stress relaxation results of the as-deposited parylene-C deposited at 22 mTorr ( $T_g=53.4^\circ\text{C}$ )	240

Figure 5-42 (a): Creep results of the as-deposited parylene-C deposited at 35 mTorr ( $T_g=55.1^\circ\text{C}$ ); (b): Stress relaxation results of the as-deposited parylene-C deposited at 35 mTorr ( $T_g=55.1^\circ\text{C}$ ) .....	242
Figure 5-43 (a): Creep results of the parylene-C annealed at $100^\circ\text{C}$ for 30 minutes in the convection oven ( $T_g=108.2^\circ\text{C}$ ); (b): Stress relaxation results of the parylene-C annealed at $100^\circ\text{C}$ for 30 minutes in the convection oven ( $T_g=108.2^\circ\text{C}$ )	244
Figure 5-44 (a): Creep results of the parylene-C annealed at $100^\circ\text{C}$ for 1 day in the convection oven ( $T_g=111.8^\circ\text{C}$ ); (b): Stress relaxation results of the parylene-C annealed at $100^\circ\text{C}$ for 1 day in the convection oven ( $T_g=111.8^\circ\text{C}$ ) .....	246
Figure 5-45 (a): Creep results of the parylene-C annealed at $100^\circ\text{C}$ for 1 day in the vacuum oven ( $T_g=113.1^\circ\text{C}$ ); (b): Stress relaxation results of the parylene-C annealed at $100^\circ\text{C}$ for 1 day in the vacuum oven ( $T_g=113.1^\circ\text{C}$ ).....	248
Figure 5-46 (a): Creep results of the parylene-C annealed at $100^\circ\text{C}$ for 2 days in the vacuum oven ( $T_g=115.2^\circ\text{C}$ ); (b): Stress relaxation results of the parylene-C annealed at $100^\circ\text{C}$ for 2 days in the vacuum oven ( $T_g=115.2^\circ\text{C}$ ) .....	250
Figure 5-47 (a): Creep results of the parylene-C annealed at $200^\circ\text{C}$ for 1 day in the vacuum oven ( $T_g>200^\circ\text{C}$ ); (b): Stress relaxation results of the parylene-C annealed at $200^\circ\text{C}$ for 1 day in the vacuum oven ( $T_g>200^\circ\text{C}$ ).....	252
Figure 5-48 (a): Creep results of the parylene-C annealed at $200^\circ\text{C}$ for 2 days in the vacuum oven ( $T_g>200^\circ\text{C}$ ); (b): Stress relaxation results of the parylene-C annealed at $200^\circ\text{C}$ for 2 days in the vacuum oven ( $T_g>200^\circ\text{C}$ ) .....	254

Figure 5-49: The testing setup of parylene-C creep with Heaviside temperature profile: (a) convection oven setup with a video recording apparatus, (b) parylene-C sample mounting configuration in the convection oven.....	258
Figure 5-50: Typical capture photos of the parylene-C creep test (as-deposited parylene-C tested at 120°C) after (a) 20 sec, (b) 60 sec, (c) 5 minutes, and (d) 60 minutes. (Numbers shown on the measuring ruler represent centimeters.) .....	259
Figure 5-51: Creep results of as-deposited parylene-C performed at 80°C, 100°C, 120°C, and 150°C with a Heaviside temperature profile.....	261
Figure 5-52: Creep results of parylene-C pre-annealed at 100°C in the air, performed at 80°C, 100°C, 120°C, and 150°C with a Heaviside temperature profile.....	263
Figure 5-53: Creep results of parylene-C pre-annealed at 100°C in the vacuum, performed at 80°C, 100°C, 120°C, and 150°C with a Heaviside temperature profile...	264
Figure 5-54: The stress relaxation test of polymers: (a) constant applied strain during the stress relaxation test at a constant temperature, (b) the corresponding stress output versus time.....	265
Figure 5-55: The results of constant strain-rate tests .....	277
Figure 5-56: The results of cyclic loading/unloading tests .....	278
Figure 5-57: The results from the abrupt strain-rate change tests .....	278
Figure 5-58: The results of creep tests of parylene-C film under different loading stresses: Theoretical Burger's model shows good fitting for the applied stress less than 30 MPa.....	279
Figure 5-59: The results of stress relaxation tests. Stress relaxation is observed for all the chosen strains. Higher strain gives faster stress relaxation.....	280



## LIST OF TABLES

Table 1-1: Some current typical glaucoma medications and their corresponding possible side effects .....	3
Table 1-2: History of glaucoma drainage device development [12].....	8
Table 1-3: Contemporary glaucoma drainage devices (GDDs) [12, 20] .....	9
Table 1-4: A comparison of some of current commercially available “tube-and-plate”-type glaucoma drainage devices (GDDs) [12, 20].....	14
Table 1-5: Literature review of glaucoma drainage devices (GDDs) (1969–2002) [19, 20, 73, 74] .....	16
Table 2-1: Measured cracking pressures of four single check-valves and the assemblies of multiple check-valves .....	51
Table 2-2: Cracking pressure of parylene check-valves under different releasing procedures: (1) acetone and IPA soak followed by air drying, (2) HF dip, water rinse, followed by air drying, (3) soak in a mixture of acetone and silicone oil before air drying. Zero stiction means that the stiction is too small to be measured effectively. ....	76
Table 2-3: Comparison of different slanted tether parylene-C NC check-valves introduced in this chapter. Water was used as the working fluid. ....	80
Table 3-1: Cracking pressures of two GDD systems obtained from <i>in vitro</i> and <i>ex vivo</i> tests .....	109
Table 4-1: Dimension of the new IOP sensor and its measured electrical parameters...	132
Table 4-2: Measured quality factors with different isolation layers covered on top .....	137

Table 5-1: Table of thermal coefficients of expansions obtained in different states of the parylene-C film. The literature values are also listed for comparison..... 153

Table 5-2: Derived TCEs from six cycles shown in Figure 5-5 and Figure 5-6..... 158

Table 5-3: Measured atom percentage of chlorine, carbon, and oxygen for different oxidative parylene-C films ..... 162

Table 5-4: Measured initial (after 1 hour oxidation) oxygen uptake rate for parylene-C by Nowlin [189]..... 168

Table 5-5: A list of calculated parameters using the in situ XRD measurement results of parylene-C consecutively annealed at 100°C in helium ..... 176

Table 5-6: A list of calculated parameters based on the in situ XRD measurement of parylene-C consecutively annealed at different temperatures in helium..... 179

Table 5-7: The lists of the parameters of the crystallization of parylene-C individually annealed at 100°C for different annealing times ..... 182

Table 5-8: XRD results of two as-deposited parylene-C films deposited at 22 mTorr and 35 mTorr, respectively..... 183

Table 5-9: Some of the previous published parylene-C  $T_g$  characterizing results..... 189

Table 5-10: Measured elastic modulus and temperature range of glassy, transition, and rubbery regions ..... 192

Table 5-11: Measured glass transition temperature *via* DMA approach ..... 204

Table 5-12: Measured mechanical properties of parylene-C film’s uniaxial tensile test 212

Table 5-13: Measured mechanical properties obtained at different testing temperatures ..... 222

Table 5-14: Burger's model curve fitting results of the creep and stress relaxation behaviors of as-deposited parylene-C deposited at 22 mTorr ( $T_g=53.4^\circ\text{C}$ )	241
Table 5-15: Burger's model curve fitting results of the creep and stress relaxation behaviors of as-deposited parylene-C deposited at 35 mTorr ( $T_g=55.1^\circ\text{C}$ )	243
Table 5-16: Burger's model curve fitting results of the creep and stress relaxation behaviors of parylene-C annealed at $100^\circ\text{C}$ for 30 minutes in the convection oven ( $T_g=108.2^\circ\text{C}$ )	245
Table 5-17: Burger's model curve fitting results of the creep and stress relaxation behaviors of the parylene-C annealed at $100^\circ\text{C}$ for 1 day in the convection oven ( $T_g=111.8^\circ\text{C}$ )	247
Table 5-18: Burger's model curve fitting results of the creep and stress relaxation behaviors of the parylene-C annealed at $100^\circ\text{C}$ for 1 day in the vacuum oven ( $T_g=113.1^\circ\text{C}$ )	249
Table 5-19: Burger's model curve fitting results of the creep and stress relaxation behaviors of the parylene-C annealed at $100^\circ\text{C}$ for 2 days in the vacuum oven ( $T_g=115.2^\circ\text{C}$ )	251
Table 5-20: Burger's model curve fitting results of the creep and stress relaxation behaviors of the parylene-C annealed at $200^\circ\text{C}$ for 1 day in the vacuum oven ( $T_g>200^\circ\text{C}$ )	253
Table 5-21: Burger's model curve fitting results of the creep and stress relaxation behaviors of the parylene-C annealed at $200^\circ\text{C}$ for 2 days in the vacuum oven ( $T_g>200^\circ\text{C}$ )	255

Table 5-22: Time constant of as-deposited parylene-C samples tested at different temperatures.....	262
Table 5-23: Parameters of Burger’s model for creep. At 40 MPa, the sample breaks and no creep could be recorded. ....	281
Table 5-24: Parameters of Burger’s model for creep recovery.....	281
Table 5-25: Parameters of Burger’s model for stress relaxation .....	281

---

# CHAPTER 1

---

## INTRODUCTION

### 1.1 Introduction to Glaucoma

Aqueous humor is the fluid that is generated by eye's ciliary body. The production rate of the aqueous humor is about 2–3  $\mu\text{L}/\text{min}$  and has a turnover time of 1.5–2 hours [1]. The aqueous humor consists of 99.1% water [2]. The generated aqueous humor flows from the posterior chamber, through the pupil, and then goes into the anterior chamber. It is believed that the function of the aqueous humor is to nourish the eye tissues around the anterior chamber. The aqueous humor is drained out from the trabecular meshwork into the channel of Schlemm, and eventually leads the fluid through the sclera into the venous system. As the aqueous humor stays in the anterior chamber for 1.5–2 hours, it manifests the normal average intraocular pressure (IOP) as 16 mmHg above the atmosphere pressure with standard deviation of 2.5 mmHg [1].

Primary open angle glaucoma is an eye disease where aqueous humor produced by the ciliary body cannot be drained out normally by patients' eyes' trabecular meshwork. 21 mmHg is deemed as the "upper limit of normal" IOP. Without successful aqueous humor drainage, the aqueous humor will accumulate in the anterior chamber of the eye and result in abnormally high intraocular pressure [3]. The elevated pressure will then be transmitted onto the retina in the back of the eye and continuously suppress and

damage the patient's optic nerves—causing visual field loss and eventual blindness if not treated sufficiently.

It is estimated that 60.5 million people worldwide have glaucoma in 2010, most of which is associated with abnormally high intraocular pressure [4], and the number may increase to almost 80 million by 2020 [5]. Statistics show that glaucoma is the second leading cause of blindness in the world (World Health Organization [6]). In the United States, it is also estimated that 2.2 million Americans have glaucoma but only half of them are aware of it, because glaucoma has virtually no symptoms. Glaucoma causes blindness in approximately 120,000 Americans, accounting for 9%–12% of all blindness in the United States. Glaucoma is five times more common in people of African-American descent than in Caucasians, and is the leading cause of blindness among African Americans. Unfortunately, 10% of glaucoma patients who receive proper treatment still experience loss of vision [6].

## **1.2 Current Treatment of Primary Open Angle Glaucoma**

Current major clinical treatment of glaucoma includes traditional medication and glaucoma filtration surgery (GFS).

### **1.2.1 Medications for glaucoma**

The typical medication for primary open angle glaucoma includes eye drops or oral medication, which function either to reduce the eye fluid production rate or help the drainage rate, depending on the form of the patient's glaucoma. However, eye drops and oral medications may have several side effects, such as blurred vision, low blood pressure, and fluctuation in heart rhythm [6]. Table 1-1 summarizes some current typical glaucoma medications and their corresponding possible side effects. The medication

treatment may also come with compliance issues: this type of medication requires patients to take eye drops regularly (every morning and evening), making it inconvenient and easily forgotten over continuous treatment. In addition, the medication may gradually lose its effect over a period of time, and hence some glaucoma patients may become resistant to all medications, called “refractory glaucoma” [7]. Refractory glaucoma is more stubborn and difficult to treat, and therefore some alternate approaches which physically drain away the aqueous humor are considered to treat these patients. Apart from the reasons mentioned above causing refractory glaucoma, problems with inefficient dosage style or glaucoma patients’ allergic response to the drug composition also stimulate more research on alternative glaucoma treatments.

Table 1-1: Some current typical glaucoma medications and their corresponding possible side effects

<b>Medication name</b>	<b>Working mechanism</b>	<b>Possible side effects</b>
Timolol	Reduces aqueous humor production rate	Cardiac arrhythmias; Bronchospasm[8]
Travoprost (Travatan Z)	A prostaglandin that increases aqueous humor outflow rate	Blurred vision; Eyelid redness[9]
Latanoprost (Xalatan)	A prostaglandin that increases aqueous humor outflow rate	Blurred vision; Eyelid redness[10]
Pilocarpine	Increases aqueous humor outflow rate	Excessive sweating; Excessive salivation; Bronchospasm; Hypertension[11]

### **1.2.2 Glaucoma filtration surgery**

Glaucoma filtration surgery (GFS) is an alternative glaucoma treatment which has been shown more effective at preventing glaucoma progression than other primary treatments in open-angle glaucoma [12]. Trabeculectomy, one of the most commonly used GFS, removes part of a patient's trabecular meshwork around the iris to create a pathway to improve the extraocular drainage of aqueous humor [2]. However, the biggest drawback of the surgery is that the incisions might heal after a period of time, and therefore repeated surgery is likely required. In addition, removing the trabecular meshwork leaves the IOP uncontrollable. The aqueous humor can flow away easily without any flow resistance and hence lead to hypotony—when IOP is lower than 5 mmHg. Ocular hypotony can lead to corneal decompensation or a flat anterior chamber with subsequent choroidal detachment or cataract formation [13].

## **1.3 Glaucoma Drainage Device**

In order to have a reliable alternative in addressing those issues, a glaucoma drainage device (GDD)—with the intent of physically draining the excessive aqueous humor through the artificial drainage path so as to reduce the associated IOP—has been a persistent research goal. The drained-out excessive aqueous humor is redirected into a subconjunctival chamber, called a bleb [14]. The drained-out aqueous humor will be eventually absorbed by the human circulation system.

### **1.3.1 Active glaucoma drainage device**

The development of GDD can be categorized into active and passive devices. For example, Neagu developed glaucoma drainage devices using the electrochemical actuating mechanism in 1998 [2]. The flow-rate is regulated by deformation of a

membrane micro valve actuated by electrolyzing the electrolyte underneath the micro valve. Besides the actuating system, the whole active eye-fluid regulating system also includes the pressure sensor, feedback control system, and an inductive coupling coil behaving as the power transmission system. In 2001, Bae also proposed another type of active glaucoma drainage device using a membrane micro valve similar to Neagu's [15–18]. Rather than being driven by electrochemical actuator, Bae's membrane micro valve is driven by an electromagnetical actuator. Bae's *in vitro/vivo* experiments demonstrated the device's capability to regulate fluid pressure to the desired pressure settings with the help of a proper feedback control system.

The advantage of the active GDD system is that it can control the flow-rate and the IOP according to the requirements of different patients. However, there are many disadvantages to this device. For example, power transmission is always one of the main concerns of the active devices. In addition, the necessity and the combination of actuating system, feedback control system, and the power transmission system makes the active GDD system much more complicated than passive GDD to fabricate, integrate, and implant. The conducting metal and the actuator used in the GDD usually come with a biocompatibility issue. Therefore, a passivation layer is normally needed to cover active devices, and the influence of those embedded electronic circuits on the human body is still unknown.

### **1.3.2 Passive glaucoma drainage device**

Due to the complicated design and fabrication of the active GDD system, the GDD under development in this thesis focuses mainly on the passively driven approach. The GDD should have a micro check-valve that consumes no power, and can still

regulate the IOP within a normal pressure range (1020 mmHg), responding to different IOP situations. The material used must be biocompatible, to reduce the inflammatory response and prevent rejection of the device. The proposed GDD must also be easy to manufacture and surgically implant into the eye. The history and the development of the passive GDD will first be introduced in the following few sections.

### ***1.3.2.1 History of the development of glaucoma drainage devices***

The history of the development of the glaucoma drainage devices until 1997 is shown in Table 1-2. The earliest attempt at implanting a GDD can be dated back to 1907. Rollet first proposed the idea of implanting a horse-hair thread connecting anterior chamber to the subconjunctival space, trying to drain out the excess eye fluid [12, 19, 20]. Subsequently, other people tried many different kinds of materials, such as silk [21], gold [22], tantalum [23], glass rod [24], platinum [25], and polythene tube [26]. These previous hollow tubes were not successful because of bio-incompatibility and migration of the implants. In addition, the hollow tube, with neither threshold pressure constraint nor high-pressure protecting mechanism, causes excess fluid to leak out of the eye and leads to hypotony.

In 1969, Molteno introduced the GDD with the concept of utilizing an extra-thin plate with large surface area, based on his hypothesis that the previous filtration failure was primarily attributable to subconjunctival fibrosis [27]. Molteno's GDD has an acrylic tube attached to a thin acrylic plate implanted subconjunctivally. With no pressure regulating mechanism designed, the plate expands the conjunctival space to help distribute aqueous and prevent the "thinning of the bleb" [28]. With not too much success owing to plate exposure, tube erosion, and scar tissue formation, in 1973,

Molteno proposed a revised version of his previous GDD by placing the thin plate farther from the cornea with a longer acrylic tube to gain a higher success rate [29]. Although the Molteno GDD has no resistance valve embedded, the Molteno GDD utilized the deflection of the conjunctival layer to control the aqueous flow-rate and the final IOP.

With the higher success rate of the Molteno GDD, the tube-and-plate structure had become one of the benchmarks of GDD design. Since then, two major concepts have also been adopted for the GDD developments:

1. Built-in resistance, usually fulfilled by introducing a valve within the GDD, is introduced to GDD design to reduce postoperative hypotony. For example, in 1976, Krupin introduced the GDD with a slit valve to prevent early, postoperative hypotony [30]. The slit valve was designed to open at a pressure of 11 mmHg and close at a pressure of 9 mmHg. In 1993, Ahmed introduced a GDD with a valve utilizing Venturi's effect to reduce the friction within the valve system and help drain away the aqueous humor [31–34]. The Ahmed glaucoma valve (AGV) is designed to open at a pressure of 8 mmHg.
2. The large end plate or the explant becomes one of the paradigms. GDD developers tend to incorporate larger surface area to promote the bleb formation and therefore acquire lower IOP [35–39]. For example, Molteno introduced a double-plate GDD in 1981 [38] in contrast to the previous single-plate GDD in 1973. In 1992, Baerveldt also introduced a nonvalved silicone tube attached to a large barium-impregnated silicone end plate [40–42].

Table 1-2: History of glaucoma drainage device development [12]

Year	Investigator	Type	Material	Method	Flow control	Drainage site
1907	Rollet [43]	seton	Horse hair	Paracentesis	None	Anterior subconjunctival
1912	Zorab [21]	seton	Silk thread	Translimbal	None	Anterior subconjunctival
1925	Stefansson [22]	seton/tube	Gold	Translimbal	None	Anterior subconjunctival
1934	Row [44]	seton	Platinum	Cyclodialysis	None	Suprachoroidal
1940	Troncoso [23, 45]	seton	Magnesium	Cyclodialysis	None	Suprachoroidal
1942	Gibson [46]	tube	Lacrimal canaliculus	Transcleral	None	Anterior subconjunctival
1949	Bick [47]	seton/tube	Tantalum	Cyclodialysis	None	Suprachoroidal
1951	Muldoon [25]	seton	Platinum	Translimbal	None	Anterior subconjunctival
1952	Losche [48]	tube	Supramid	Cyclodialysis	None	Suprachoroidal
1955	Bietti [49]	tube	Polyethylene	Cyclodialysis	None	Suprachoroidal
1958	La Rocca [50]		Polyvinyl	Translimbal	None	Anterior subconjunctival
1960	Ellis [51]	tube	Silicone	Translimbal	None	Anterior subconjunctival
1967	Mascati [52]	tube	Plastic	Translimbal	None	Lacrimal sac
1969	Molteno [27]	tube-and-plate	Acrylic	Translimbal	None	Anterior subconjunctival
1974	Lee [53]	tube	Collagen	Translimbal	None	Vortex vein
1976	Krupin [30]	tube	Silicone and supramid	Translimbal	Slit valve	Anterior subconjunctival
1979	Honrubia [54]	tube	Silicone	Translimbal	None	Anterior subconjunctival
1982	Schocket [55]	tube and band	Silicone	Translimbal	None	Posterior subconjunctival
1985	White [56]	tube-and-plate	Silicone	Silicone	Valve and pump	Posterior subconjunctival
1986	Joseph [57]	tube and band	Silicone	Translimbal	Slit valve	Posterior subconjunctival
1990	Krupin [58]	tube-and-plate	Silicone	Translimbal	Slit valve	Posterior subconjunctival
1990	Baerveldt [59]	tube-and-plate	Silicone	Translimbal	None	Posterior subconjunctival
1993	Ahmed [32]	tube-and-plate	Silicone and polypropylene	Translimbal	Venturi valve	Posterior subconjunctival
1995	OptiMed [60]	tube-and-plate	Silicone and PMMA	Translimbal	Microtubules	Posterior subconjunctival
1995	Smith [61]	seton	Hydrogel	Translimbal	None	Intrascleral
1996	Pandya [62]	tube-and-plate	Silicone and hydroxylapatite	Translimbal	None	Posterior subconjunctival
1997	Glovinsky and Belkin [63]	tube	Stainless steel	Translimbal	None	Anterior subconjunctival
1997	Helies [64]	artificial meshwork	PTFE	Transcleral	None	Anterior subconjunctival

### 1.3.2.2 Contemporary passive glaucoma drainage device

Table 1-3 summarizes some of the current glaucoma drainage devices. The first category shows the commonly used tube-and-plate GDD design, which has dominated the GDD market since 1969. This type has an end plate located underneath the conjunctiva layer acting as the base for the bleb to form.

Table 1-3: Contemporary glaucoma drainage devices (GDDs) [12, 20]

<b>Design</b>	<b>Drainage location</b>	<b>Commercial available examples</b>
Tube-and-plate GDD	7–10 mm from limbus	Molteno, Baerveldt, Ahmed, Krupin, Optimed
Translimbal GDD	At the limbus	Ex-PRESS shunt
Trabecular bypass devices	Channel of Schlemm	GMP Eye pass, Glaukos trabecular bypass shunt
Trabecular bypass devices	Suprachoroidal space	SOLX system

The second type is translimbally implanted and drains the aqueous humor to the subconjunctiva. The most recently introduced GDD is EX-PRESS, made of stainless steel. The implantation concept of this type GDD resembles the concept of trabeculectomy surgery.

The third type involves implanting the GDD in such a way as to mimic the function of the trabecular meshwork, which helps drain away the aqueous humor through the channel of Schlemm. The GMP eye pass and Glaukos trabecular bypass shunt are examples of this type of GDD.

The fourth type of GDD drains the aqueous humor to the area of suprachoroidal space, and is still under clinical trials.

### 1.3.2.3 Glaucoma drainage devices with no resistance

Seen in Table 1-3, Molteno and Baerveldt are tube-and-plate GDDs with no resistance designed. This type of GDD has an end plate implanted underneath the conjunctival layer, which turns into the controlling membrane of the implants.

As for the translimbal GDD, Ex-PRESS shunt has no resistance designed as well. However, the small diameter (50  $\mu\text{m}$  [20]) makes it still possible to have a pressure drop of 4.78 mmHg within in the tube while draining out the aqueous humor.

For the trabecular bypass type GDD, GMP Eye pass, and Glaukos trabecular bypass shunt are designed with no resistance incorporated. The main reason is likely due to the fact that their small tube sizes have already provided a certain amount of pressure resistance for the drainage devices. Because a proper flow resistance designed in the GDD system is required to prevent postoperative hypotony, the contemporary GDD usually comes with a mechanism designed to regulate the flow-rate and the IOP. To estimate the required flow resistance of the entire GDD, the flow resistance of a hollow tube is introduced in the following section.

#### 1.3.2.3.1 Flow resistance of a hollow tube

The flow resistance is defined according to the relationship between the pressure drops versus the flow-rate. Assume that the volume flow-rate,  $\Phi$ , is proportional to the pressure difference,  $\Delta p$ , then the relation can be expressed in a simple form as [65]:

$$\Delta p = R \cdot \Phi, \quad (1-1)$$

where  $R$  is defined as the channel flow resistance. If the liquid flow in the circular hollow tube is a laminar flow, the pressure difference,  $\Delta p$ , across a circular hollow tube can be calculated by Hagen–Poiseuille equation, which is expressed as:

$$\Delta p = \frac{128\mu l}{\pi d^4} \Phi, \quad (1-2)$$

where  $\mu$  is the viscosity of the fluid,  $l$  is the tube length,  $d$  is the tube diameter.

Therefore, the flow resistance of a circular hollow tube can be found as:

$$R = \frac{128\mu l}{\pi d^4}. \quad (1-3)$$

The Reynolds number,  $Re$ , is used to identify whether the flow is a laminar flow. For a laminar flow,  $Re$  must be less than 2300. The Reynolds number is represented as:

$$Re = \frac{\rho \bar{v} d}{\mu}, \quad (1-4)$$

where  $\rho$  is the fluid density, and  $\bar{v}$  is the average velocity of the fluid, which can be calculated by

$$\bar{v} = \frac{4\Phi}{\pi d^2}. \quad (1-5)$$

Take the Ex-PRESS shunt as an example. To calculate its pressure drop across the shunt, the Reynolds number is first calculated. The aqueous humor density is assumed to be  $1000 \text{ kg/m}^3$ , the volume flow-rate is taken as  $2 \text{ }\mu\text{l/min} = 3.3 \times 10^{-11} \text{ m}^3/\text{sec}$ , and the diameter of the Ex-PRESS shunt is reported as  $50 \text{ }\mu\text{m}$  [20]. The viscosity of the aqueous humor,  $\mu$ , is found to be approximately similar to that of the saline, and therefore  $\mu$  is equivalent to  $1 \times 10^{-3} \text{ Pa}\cdot\text{s}$  [2, 66, 67]. The Reynolds number is then calculated as 0.84, which is much smaller than 2300, and therefore the aqueous humor flow can be assumed as laminar flow in the shunt, and eqn. (1-2) can be applied to estimate the

pressure drop of the Ex-PRESS shunt. Because the length of the Ex-PRESS shunt is reported as  $2.96 \times 10^{-3}$  m [20], the pressure drop can be found as  $636.77 \text{ Pa} = 4.78 \text{ mmHg}$ .

If the inner diameter of the Baerveldt and Molteno GDD shown in Table 1-4 as  $0.635 \times 10^{-3}$  m is considered, the length of the silicone tube is taken as  $1 \times 10^{-2}$  m, as shown in Table 1-3, the Reynolds number is obtained as 0.066, and the pressure drop is calculated as  $0.0827 \text{ Pa} = 6.2 \times 10^{-4} \text{ mmHg}$ , which is relatively too small for practical GDD to use.

#### ***1.3.2.4 Glaucoma drainage devices with resistance***

Two main tube-and-plate glaucoma drainage devices have been developed with micro valves as the flow resistance. The Ahmed glaucoma valve's silicone tube is connected to a silicone sheet valve, with the inlet section is made wider than the outlet. This special "Venturi shaped" chamber design introduces a pressure drop from inlet to outlet based on the Bernoulli principle. The Ahmed glaucoma valve is designed to open at 8 mmHg. Krupin developed another valved tube-and-plate GDD, with a silicone tube consisting of the cross-slit element. The Krupin GDD is designed to open at 11–14 mmHg. The other possible valved tube-and-plate GDD is the Optimed model-1014 GDD. The Optimed GDD is made of a "flow-restricting" unit consisting of multiple microtubules, each of which provides pressure drop governed by the Hagen–Poiseuille equation, as expressed in eqn. (1-2).

### ***1.3.2.5 Comparison of current “tube-and-plate”-type glaucoma drainage devices***

As the current dominant benchmark in the GDD development market, tube-and-plate structure are explored more and discussed at length in this section.

#### **1.3.2.5.1 End plate size comparison**

Table 1-4 shows the comparison of some geometry factors of the tube-and-plate. The GDD developers had been focusing on increasing the size of the end plates, as larger end plate size was believed to have more effective IOP regulating capabilities. However, the long-term implantation follow-up shows that there is no statistical difference between the surface areas ranging from 130 mm<sup>2</sup> (Molteno single plate) to 350 mm<sup>2</sup> (Baerveldt) among all different GDDs [19, 68, 69].

As for the comparison of the single-plate and double-plate Molteno GDD, although Heuer et al. concluded that the double-plate implants resulted in a statistically significant lower IOP and higher overall surgical success compared to single-plate GDD, the double-plate Molteno success and final IOP were only slightly better than the results with the single-plate implant [19, 36]. Lloyd et al. also found no statistical difference in the overall surgical success rate or IOP control comparing the Baerveldt's end plates' area with 350 mm<sup>2</sup> vs. 500 mm<sup>2</sup> [19, 40]. In addition, Smith et al. did a comparison of implantation results of 350 mm<sup>2</sup> Baerveldt GDD with 270 mm<sup>2</sup> double plate Molteno GDD. They found out that the mean IOP was similar at the 11.3 months of follow-up [19]. This may imply that end plate's area of 270 mm<sup>2</sup> might be large enough for the GDD and the improvement is not obvious once the area size is large than 270 mm<sup>2</sup>. In summary, it is found by many researchers that the size of the end plate does influence the

IOP regulating capabilities to a certain point. However, the effect is not linear proportional and also not the overall success rate of the operation.

Table 1-4: A comparison of some of current commercially available “tube-and-plate”-type glaucoma drainage devices (GDDs) [12, 20]

<b>Product name and Manufacturer</b>	<b>Product</b>	<b>Year of first introduction</b>	<b>Tube dimension *</b>	<b>Surface area (mm<sup>2</sup>)</b>	<b>Biomaterial</b>	<b>Valved /nonvalved</b>
Ahmed Glaucoma Valve (New World Medical, CA, USA)	model S3	1993	0.635 mm OD 0.305 mm ID, [70]	96	Polypropylene	Valved
	model S2			184	Polypropylene	Valved
	model FP8			96	Silicone	Valved
	model FP7			184	Silicone	Valved
	model B1 (Bi-plate)			364	Silicone	Valved
Baerveldt Glaucoma Implant (Abbott Medical Optics, Inc.)	BG 103–250	1990	0.63 mm OD 0.30 mm ID, [71]	250	Silicone	Nonvalved
	BG 101–350			350	Silicone	Nonvalved
	BG 103–425			425	Silicone	Nonvalved
Molteno Glaucoma Implant (IOP Inc., CA, USA)	Molteno single plate	1979	0.64 mm OD 0.34 mm ID, [72]	135	Polypropylene	Nonvalved
	Molteno double plate			270	Polypropylene	Nonvalved
Hood Laboratories, Pembroke, MA	Kruping with disc	1990	0.58 mm OD 0.38 mm ID, [12]	180	Silicone	Slit valve
Optimed (Manufacturer not available)	Model-1014	1995	0.56 mm OD 0.30 mm ID, [12]	140	Silicone drainage tube with PMMA matrix	Microtubules

\*OD: Outer diameter; ID: Inner diameter

### 1.3.2.5.2 Results of clinic trials comparison

Table 1-5 lists the results of five different GDDs' clinical trials summarizing from systematic literature reviews. The Pearson chi-square test was used to compare the incidence of surgical outcomes and complications among the GDDs. P value shown in Table 1-5 represents the paired *t*-test, which indicates how significantly different within a variable among the five GDDs. A two-tailed  $p < 0.05$  was considered with statistically significant difference. As can be seen from the table, there is no statistically significant difference in the postoperative follow-up time among the five GDDs. The pre-op IOP shows a statistically significant difference as the pre-op IOP of Molteno with no modification shows a higher value. The post-op IOP and % change in IOP, which both can be deemed as the regulating capabilities of the GDD, show no statistically significant differences and therefore it implies that these five GDDs have very similar regulating capabilities. This is verified by the p-value of the surgical success as 0.94. As shown, all five GDD can lower IOP within the normal pressure range with successful rate between 72–79%.

There are no statistically significant differences found for the incidence of decrease in visual acuity (0.9), transient hypotony (0.17), chronic hypotony (0.51), and suprachoroidal hemorrhage (0.47). For the pre-op and post-op medication numbers, all five GDDs had no statistically significant differences, meaning five GDDs were all capable of reducing the post-op medication numbers. The diplopia occurrence of Baerveldt implant and Krupin valve show relatively high numbers compared to other three GDDs. Therefore  $p = 0.01$  is obtained. The possible reason causing this high diplopia occurrence will be discussed in Section 1.3.2.6.2.

Table 1-5: Literature review of glaucoma drainage devices (GDDs) (1969–2002) [19, 20, 73, 74]

Variable	Molteno with no Modification	Molteno with surgical Modification (e.g., ligature)	Baerveldt Implant	Ahmed Glaucoma Valve	Krupin Valve	P value
Mean follow-up (Months)	23.1±10.8	27.1±14.2	18.6±7.8	16.0±7.5	21.3±11.2	0.72
Pre-op IOP, mmHg	42.1±2.1	34.1±4.8	30.8±4.2	33.9±4.5	36.3±1.5	0.02*
Post-op IOP, mmHg	17.1±1.3	16.6±2.1	14.3±1.8	16.6±1.8	13.8±1.6	0.32
% change in IOP	59±3	51±6	54±8	51±8	62±5	0.20
Surgical success, %	75±12	77±13	75±10	79±8	72±11	0.94
Decrease in visual acuity, %	33±18	30±13	27±10	24±7	28±4	0.90
Pre-op meds, no.	NR	2.3±0.3	2.2±0.3	2.7±0.3	2.7±0.3	0.40
Post-op meds, no.	1.5±1.0	1.1±0.6	0.8±0.2	1.0±0.3	1.0±0.2	0.86
Transient hypotony, %	26±14	12±7	15±8	14±8	17±12	0.17
Chronic hypotony, %	5±3	6±5	6±3	2±1	2±2	0.51
Diplopia, %	NR	2±2	9±5	3±1	7±5	0.01**
Suprachoroidal hemorrhage, %	NR	4±3	5±3	3±3	8±7	0.47

NR: Not reported

\*Pre-op IOP was significantly higher in “Molteno with no modification” group

\*\*Diplopia rate was significantly higher in Baerveldt group compared to Molteno and Ahmed glaucoma valve groups.

### 1.3.2.6 Postoperative complications of current glaucoma drainage devices

Table 1-5 reveals that these five GDDs can all successfully regulate the IOP and possibly treat the refractory glaucoma. However, several complications are generally found with GDDs.

#### 1.3.2.6.1 Hypotony

It can be seen from Table 1-5 that the occurrence of post-op chronic hypotony of Ahmed glaucoma valve and Krupin Valve is obviously lower than the rest three GDDs. This implies the function of the incorporated valves of these two GDDs, which are claimed to close at the IOP of 8–9 mmHg. However, the transient hypotony occurrence

of these two GDDs does not show any impressive hypotony improvement as claimed by the manufacturers. It is likely due to the insertion site of the GDD's silicone tube that aqueous humor might leak through before the incision heals, causing the early hypotony. As for the nonvalved Molteno GDD, it clearly shows that the modified Molteno GDD has a better performance in terms of the early transient hypotony.

#### 1.3.2.6.2 Diplopia

It is found from Table 1-5 that the occurrence of diplopia of Baerveldt is higher than the rest four GDDs. It is likely due to its special design that the device is implanted underneath the recti muscles. It is suggested that diplopia may be related to the height of the bleb or due to the adhesions to the recti muscles as the Baerveldt end plate is inserted under the muscle belly [40]. The problem is suggested to be solved by modifying the end plate such as fenestrating the end plate. However, there is still no quantitative reports regarding this improvement yet [75].

In addition, it is also reported that up to 30% of the patients receiving GDD implantation surgery might have corneal decompensation [19]. The complexity of these complications proves the difficulties of developing a final successful glaucoma drainage device.

#### ***1.3.2.7 Long-term failure of the GDD: Bleb fibrosis***

Apart from the immediate postoperative complications after the GDD implantation, the GDD could fail after a long-term operation. Bleb fibrosis is one of the major problems that lead to the GDD failure. The fibrous reaction around the end plate may encapsulate the end plate and eventually influence the final IOP.

The fibrosis is believed to happen due to the introduction of outside biomaterials such as the end plate of the GDD which could cause a fibrovascular response in the subconjunctival space [19]. In addition, the introduction of the aqueous humor into the subconjunctival space can stimulate fibrovascular proliferation in the episcleral tissue as well [26]. The intensity of the fibrous reaction may vary with respect to several factors such as the biomaterial, size, and/or design of the end plate and the individual patient's immune reaction to the operation, the GDD itself, and the presence of aqueous humor in the subconjunctival space, and also some factors that have not been understood.

Several suggestions are proposed to overcome the fibrosis problem. First of all, GDD made of more biocompatible material to reduce inflammation around the end plate, resulting in less scar tissue formation and promote longer GDD lifetime. The inert biomaterial should not attract fibroblast or protein deposits as well, which in turn could lead to cytokine release, chronic low-grade inflammation, and bleb failure [19]. The rigidity, flexibility, and shape design of the end plate is also believed to influence the fibrosis occurrence. The rigid plates might exhibit less to-and-fro micro motion with ocular movement leading to less chronic inflammation.

It is reported that the bleb fibrosis following the trebeculectomy operation can be successfully alleviated by medications such as mitomycin C and 5-fluorouracil. However, the effect of these medications on GDD implantation is still under debate and more clinical trials need to be done to get a clear picture.

### **1.3.3 Proposed glaucoma drainage device design**

Summarizing all the advantages and disadvantages of current GDDs, an ideal GDD should have the following key elements:

1. There must be a micro valve designed in the GDD to provide the necessary resistance to regulate the IOP in a proper range. It is desirable to have a device to regulate the IOP to be in the range of 10–20 mmHg.
2. The biomaterial of the GDD must be totally inert so as to reduce the occurrence of the inflammation and the fibrosis reactions.
3. The GDD needs to have a reliable fixation anchor to prevent it from dislocation after it is implanted.
4. The previously developed GDD focused only on how to drain out the excessive aqueous humor to lower the IOP to a proper range. However, when at a sudden eye pressure increase such as bumping or rubbing the eyes, those GDDs cannot prevent the unwanted aqueous humor drainage. Therefore, an ideal GDD should have a protecting mechanism to prevent hypotony in the case of transient unexpectedly high eye pressure (e.g., > 50 mmHg).
5. An easy implantation procedure is needed to implant the GDD within 10 minutes, without cutting the conjunctival layers. Therefore, a translimbal type of GDD without an end plate is chosen.

Micromachined check-valves have long been used in microfluidic devices for flow controls in micro-total-analysis systems ( $\mu$ TAS) [76, 77]. Those check-valves are used for the control of flow direction, flow-rate, and even pressure distribution. Practically, micromachined check-valves can operate either actively or passively. In terms of human body applications, passive device are generally preferred due to the simpler structure design and no power consumption needed, that is, less complicated circuits embedded in the check-valves.

In our newly developed GDD, the key component of the GDD is one normally closed (NC) check-valve designed to open at 10–20 mmHg. The NC check-valve allows extraneous aqueous humor to flow out of anterior chamber when the IOP is higher than the designed cracking pressure. On the other hand, the NC check-valve remains closed as long as eye pressure is lower than the designed cracking pressure. It restricts eye fluid from leaking out of the anterior chamber to prevent hypotony. The NC check-valve will be introduced in chapter 2. To fulfill the concept that the GDD closes at a sudden unexpected high IOP, one normally open (NO) check-valve is also developed. This NO check-valve opens during the normal operation, but closes when it encounters a sudden high IOP. The NO check-valve will be introduced in Section 3.2. In addition, the development of the fixation anchors, the integration, *in vitro* characterization, and *ex vivo* experiments of the whole GDD system will all be introduced in chapter 3.

## **1.4 Intraocular Pressure Monitoring**

Because there could be no symptoms of pain in open angle glaucoma and the human eye tends to compensate a small peripheral vision loss, open angle glaucoma patients are usually diagnosed in the late stage of the disease. Thus an early stage diagnostic becomes also important in glaucoma management.

### **1.4.1 Current clinical IOP monitoring approaches**

One of the current clinical IOP monitoring approaches is implement applanation tonometry [78]. The fundamental working principle is by applying a force onto the corneal surface, which is flattened by the sensing probe surface. The applied force is balanced with the deflection of the corneal and IOP, and therefore the IOP can be calculated given the flattened cornea's mechanical properties and its surface area.

Goldmann applanation tonometry (GAT) and tonopen (Reichert, Inc., Depew, NY) are two examples utilizing this contact approach to measure the IOP. The noncontact approaches such as pneumotonometry (i.e., air-puff tonometry) [79, 80], however, are currently more popular. The pneumotonometry blows an air-puff, which serves the applanation force in this case, onto the eye to flatten the corneal surface. The deformation of the corneal surface is measured by optical approach. Similar to the contact tonometry approach, the applanation force is balanced with IOP and the corneal surface, and therefore the IOP can be calculated given the measured flattened corneal surface and the applied force. Compared to contact tonometry, the pneumotonometry provides more accurate readouts as it has less refractory responses from the targets during the measurement.

#### **1.4.2 Wireless telemetric sensing technology**

Even though the applanation tonometry can provide quite useful information of patients' IOP, the readout, however, can be seriously affected by many unpredicted parameters such as the cornea thickness, the orientation of the instruments during the measurement, or variation in the corneal mechanical properties' from person to person [81–83]. Besides, the applanation tonometry requires skillful operation, which can only be performed by well-trained professionals such as ophthalmologists, making continuous IOP monitoring impractical.

Furthermore, it is reported that the IOP spikes that happen within the daily IOP fluctuations could also risk optic nerve damage [84–86], and therefore IOP is suggested to be monitored continuously with a long period of time. Nowadays, continuously monitoring of IOP still cannot be achieved *via* current applanation approach. Therefore,

a wireless IOP sensing technique is required to accomplish a direct, convenient and reliable continuous IOP sensing technology.

The concept of utilizing passive telemetric sensing technique to monitor IOP has been developed yearly to achieve the ideal sensors capable of noncontact and continuous in situ IOP measurement [87, 88]. A transensor is the key component of this technique that is implanted into the anterior chamber. The IOP signal is wirelessly obtained by an external coil reader which wirelessly interrogating the implanted sensor. Although the active devices were developed to demonstrate its capability of monitoring the IOP, its size and the power transfer are always the concerns and restrict them from practical usage [87, 89]. On the other hand, passive devices shows a more compact and flexible design which is more suitable for anterior chamber implantation [90].

The first passive device consisting of a capsulated electrical LC resonant circuit was reported in 1967 [91]. The transensor was implanted in the anterior chamber and the concept became the paradigm of current telemetric sensing technology. In recent years, many passive telemetric sensors were developed with the help of MEMS (microelectromechanical systems) technology [92–96]. However, those MEMS transensors usually used wafer bonding technique to create a chamber for the pressure-sensitive device. This process could increase the overall thickness of the device and make the implantation impractical due to the small space of the anterior chamber. In 2008 and 2010, Chen reported parylene-C-based passive IOP sensors featuring the biocompatibility and flexibility of parylene-C as the structural material [97, 98]. The variable capacitor of Chen's IOP sensor was monolithically fabricated by integrating the parylene-C fabrication techniques, and hence no wafer bonding is required. The

completed transensor is small enough for minimally invasive implantation into the anterior chamber.

Although Chen's IOP sensor has demonstrated its successful monitoring the IOP wirelessly, the quality factor reduces after the sensor implantation. This is attributed to the high loss tangent of the aqueous humor surrounding the device. The low quality factor degrades the performance of Chen's sensor, decreasing the sensing distance. In the thesis, two solutions are proposed to solve the problem. One is attaching a capillary tube on the bottom of the device serving as the pressure transducer connecting the anterior chamber and the variable capacitor. The other approach is to protect the sensing coil by covering protective materials with lower loss tangent than aqueous humor. These two new concepts provide new possibilities to skip or isolate the aqueous humor to preserve the quality factor of the sensor, and therefore make the passive IOP sensor implantation practical.

### 1.5 Biocompatible Material, Parylene-C, Usage

Parylene-C, poly(chloro-para-xylylene) is chosen to fabricate all the devices developed in this thesis. The molecular structure of parylene-C is shown in Figure 1-1. Parylene-C has been proved by Food and Drug Administration (FDA) to be the biocompatible material and complies with United States Pharmacopeia's (USP's) class VI plastics requirements, meaning it is totally implantable in the human body [99].

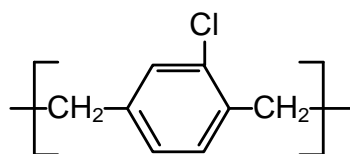


Figure 1-1: Molecular structure of parylene-C

Parylene-C is prepared by the vapor phase deposition at room temperature. To prepare the parylene-C film, the parylene-C dimer is first vaporized at 150°C to the gaseous dimer, and then pyrolyzed at 690°C, turning into the monomer gas. The monomer gas goes into the deposition chamber, conformally coating onto the targets. The deposition temperature is normally kept as room temperature (20°C), and the deposition pressure is in the range of 20–100 mTorr, which is unlike the metallic deposition chamber with deposition pressure as  $\sim 10^{-5}$  torr. In the pressure range of 20–100 mTorr, the mean free path is about 1 mm and therefore the monomer gas can uniformly distributed in the chamber and conformally coats the targets.

Parylene-C is a very good dielectric material with dielectric strength of 5600 V/mil and dielectric constant of about 3 [100]. Parylene-C has very low moisture permeability, and very inert to chemicals. In addition, parylene-C can be easily prepared in the clean room and can be patterned by normal oxygen plasma. Therefore, parylene-C fabrication is very compatible with CMOS/MEMS processes and has been widely used in BioMEMS research in recent days.

## **1.6 Characteristics of Parylene-C**

Properties of parylene-C, such as mechanical, thermal and polymer properties, etc, have long been studied in the literature for years [101, 102]. The results are now very available and widely used in many aspects [100]. In many years, people have been using those numbers in designing the insulation layer of printed circuit boards, the modification of implantable medical devices, or any parylene-C-based biomedical devices. In the past few years of our experiences of fabrication of parylene-C film, however, several main concerns are raised.

Most of the properties' numbers were measured at parylene-C film as-deposited state, which means the parylene-C was never treated thermally, mechanically, or any other kinds of treatments, before it was tested. In our fabrication experiences, however, it showed that the mechanical property is seriously affected by its processing histories. For example, after a series of fabrication processes in the clean room, Young's modulus was obtained as 4.75 GPa as compared to 2.78 GPa provided by the vendor of parylene-C dimer [103]. Therefore, it is necessary to understand the final influences that every fabrication process could cause during the device manufacturing.

More specifically, parylene-C is one type of thermal plastic polymer and temperature is a key controlling parameters of its properties. Therefore parylene-C properties are different between room temperature and the human body temperature; i.e., 37°C. The current available parameters cannot ideally represent the behavior of parylene-C in human bodies and needs to be further studied and updated.

For all of the micro check-valves designed in chapter 2, a certain amount of residual tensile stress is always required to pre-stress the tethers so that the check-valves can behave as designed. Due to the natural property of the polymer, however, stress usually relaxes after a period of time, called stress relaxation. To predict the lifetime of these micro check-valves, the rheological properties, that is, creep and stress relaxation, of parylene-C need to be understood. On the other hand, it is also required to know the rheological properties of the parylene-C film to properly design the fabrication procedures. For example, in order to either make the parylene-C-based devices flat or mold it into a certain shape, the proper processing temperature and the information of the time constant of the stress relaxation is required. Viewing back several decades of

parylene-C research history, however, there is still a lack of the viscoelastic-viscoplastic properties of parylene-C film and it will be studied in the thesis.

In addition, MEMS process usually involves different elevated temperatures without the isolation of the oxygen. In such processes, the parylene-C film is likely to get oxidized without a proper treatment, and deteriorates the device properties and performance. Therefore, oxidation must be considered during the fabrication and its behavior is studied in this thesis to understand its influence after different thermal treatment.

Hassler et al. had done a series of uniaxial tensile tests to study the effect of annealing, steam sterilization, deposition pressure and saline soaking on parylene-C's mechanical effect [104]. The results showed that the mechanical properties are very temperature sensitive and seriously affected by the temperature-related process such as annealing and steam sterilization. After high temperature thermal treatment, the parylene-C became more rigid, more brittle, and harder. Hassler suggested that the parylene-C polymer chains grow to a crystal-like structure and make the parylene-C stronger. This is also confirmed in our uniaxial tensile and crystallinity tests.

## **1.7 Summary**

A broad view of the motivations and contents of the whole thesis is introduced in this chapter. The histories of the GDD and the IOP sensors are explored, compared and discussed. It shows that the previously developed GDD led to many complications such as diplopia and hypotony. In addition, there was no mechanism among those GDD to prevent over drainage of the aqueous humor under the unexpected high IOP. As for IOP sensor review, previous telemetric IOP sensors experience a decreased quality factor

after implantation. New GDD design and IOP sensor improvement are therefore required to make glaucoma management efficient and practical.

Rheological properties of parylene-C play an important role in designing the medical devices, especially implantable ones. However, there are very few studies of the rheological properties of parylene-C can be found in the past decades of parylene-C research. In addition, parylene-C was reported as a very temperature-sensitive material. Therefore, a complete knowledge of parylene-C properties helps researchers use the materials properly and it will be discussed in the thesis.



---

# CHAPTER 2

---

## PASSIVE NORMALLY CLOSED MICRO CHECK-VALVES

### 2.1 Overview

Normally closed (NC) micro check-valve is used to stop liquid flow when liquid pressure difference across the membrane is lower than the designed cracking pressure. As shown in Figure 2-1, when the applied pressure  $P$  is lower than the designed cracking pressure,  $P_c$ , the NC check-valve is closed, and vice versa. Generally the cracking pressure can be introduced electrically such as electromagnetic force, mechanically such as MEMS springs, or other physical approaches such as stiction force. Passive check-valves usually use mechanical approaches to reduce complexity and thus no controlling circuit is needed. To mechanically implement controllable cracking pressures onto the NC micro check-valves, many different types of pre-stress technique have been developed, such as cantilever type, diaphragm type, and bivalvular type, etc. [105]. These NC check-valves use deformation of covering materials geometrically designed to provide the desired controlling force based on the requirements of applications. The material selection would also depend on the application of the micro check-valves. For example, if high cracking pressure is necessary, materials with large Young's modulus are used to provide the required pre-stressed force. Moreover, if the device is for human body implantation use, the biocompatible material such as parylene-C is needed to

fabricate the device. However, parylene-C has lower Young's modulus than general stiff MEMS materials such as poly silicon or silicon nitride. Therefore, parylene-C is not appropriate to construct a high-cracking-pressure NC check-valve using traditional configuration and a new design needs to be explored.

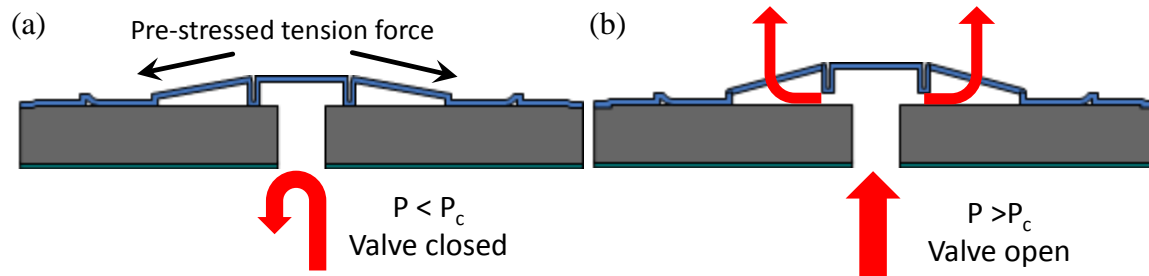


Figure 2-1: Concept of the normally closed (NC) check-valve: (a) The check-valve is closed when the applied pressure  $P$  is lower than the cracking pressure  $P_c$ ; (b) the check-valve is open when the applied pressure  $P$  is higher than the cracking pressure  $P_c$ .

Several different passive parylene-C micro check-valves have been developed in the past. For example, to generate a zero crack pressure NC check-valve, Wang developed a parylene-C micro check-valve with twist-up tethers to reduce membrane-induced flow resistance to a negligible level in 1999 [106]. On the other hand, to have a NC check-valve with a certain level of cracking pressure, Wang also developed in 2000 another type of NC micro check-valve with which a sealing plate is center-anchored by vacuum-collapse anchoring to achieve 20 kPa (2.9 Psi) of cracking pressure [107]. Xie developed another type of ideal NC micro check-valves with simpler check-valve structure than Wang's [108]. Xie's check-valve has nearly zero cracking pressure using the self-assembled monolayer (SAM) coating gold, which was found by the authors capable of reducing the adhesion of parylene-C and the silicon substrate so as to achieve the zero cracking pressure.

Among all the parylene-C NC check-valves mentioned above, only one check-valve is designed to be capable of providing the necessary cracking pressure, which is still limited in a certain low pressure range due to parylene-C's Young's low modulus of 3-4 GPa. This would restrict the NC check-valve to be used in high pressure applications. In addition, although the gas permeability of the parylene-C has been found to be very small, e.g., oxygen permeability of parylene-C is  $2.8 \text{ cm}^3 \cdot \text{mm} \cdot \text{m}^2 \cdot \text{day}^{-1} \cdot \text{atm}^{-1}$  [100], the parylene-C vacuum-collapse anchoring can still be in vein after a long time of usage as the gas can still permeate through the parylene-C film into the cavity.

In this chapter, the theoretical flow-rate of micro check-valves and the amount of the necessary pre-stress force are first investigated. Then a simple passive NC check-valve structure is proposed and developed to be a standard MEMS NC check-valves paradigm. NC check-valves with different level of cracking pressure are designed, fabricated and characterized to cover a broad pressure range of applications. With very similar structures, all of them consume no power, and are made of parylene-C to guarantee the biocompatibility. The cracking pressure is obtained by stretching the parylene-C using residual tensile stress introduced after thermal quenching (high pressure applications), or by stiction and pop-up structure (low pressure applications). Although with only 3-4 GPa of the parylene-C Young's modulus, these pre-stress approaches can still overcome the inefficiency by providing larger strain and thus make high cracking-pressure parylene NC check-valve possible.

## 2.2 Theoretical Analysis of NC Micro Check-Valves

### 2.2.1 Thin-film-flow theory of the check-valve

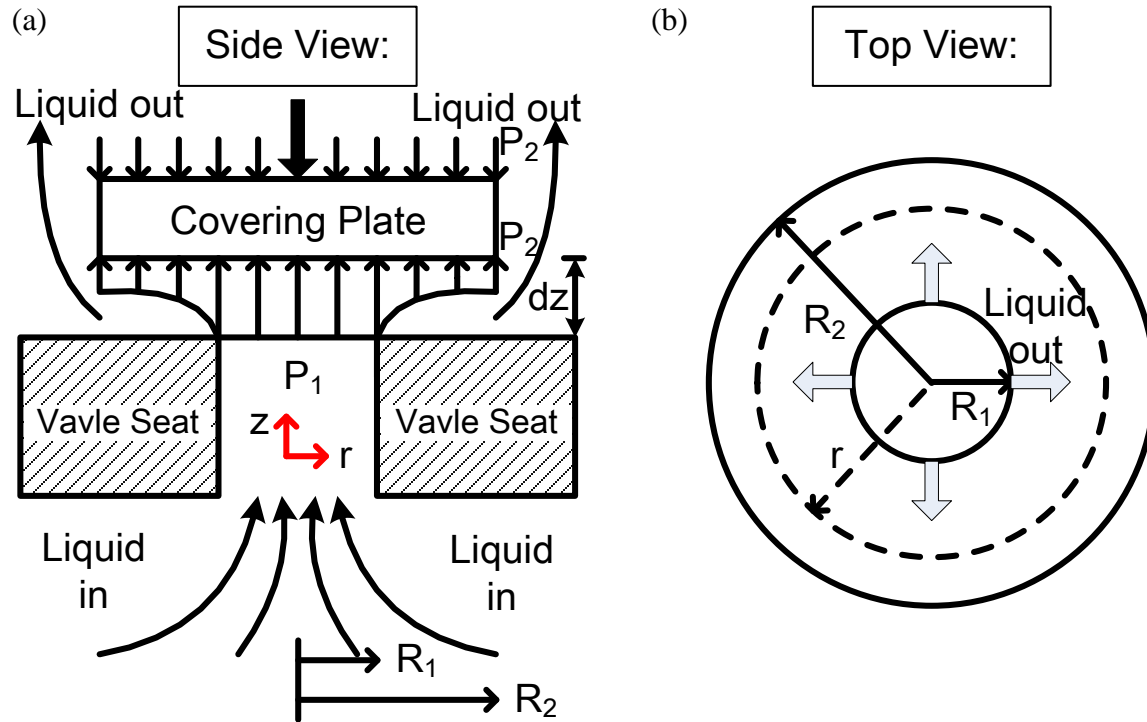


Figure 2-2: Check-valve model for unsteady flow analysis: (a) side view, and (b) top view

A simplified check-valve configuration is shown in Figure 2-2. The check-valve is normally closed owing to a pre-stressed downward force. The covering plate opens when the forwarding force of the liquid becomes higher than the downward force. After the covering plate pops open, the liquid flows in between the covering plate and the valve seat, forming a very thin capillary flow layer. The flow-rate equation in such case has not been fully developed so that the problem needs to take into account some unsteady flow effects. Several assumption are made to simplified the calculations: (1) The flow is incompressible, and asymmetrical; (2) the upstream pressure,  $P_1$ , is uniformly applied on

the covering plate within the range of  $r \leq R_l$ , the radius of the opening, and so is the downstream pressure,  $P_2$ , which is the pre-stressed downward force; (3) the weight of the liquid is negligible; (4) the opening gap,  $g$ , is much smaller than  $R_l$ .

At low Reynolds numbers found in this thin film flow, the Navier-Stokes equation can be reduced into the Reynolds equations of hydrodynamic lubrication as follows [109]:

$$\frac{\partial p}{\partial z} = 0, \text{ and } \frac{\partial p}{\partial r} = \mu \frac{\partial^2 u_r}{\partial z^2}, \quad (2-1)$$

where  $p$  is the pressure in the liquid film,  $\mu$  is the dynamic viscosity and  $u_r$  is the radial velocity component. From the integration of eqn. (2-1), we can get radial velocity as:

$$u_r(z) = \frac{1}{2\mu} \frac{dp}{dr} z(z - g). \quad (2-2)$$

Therefore, the volume flow-rate can be represented as:

$$Q(r) = \int_0^g u_r(z) 2\pi r dz = -\frac{\pi r}{6\mu} \frac{dp}{dr} g^3. \quad (2-3)$$

By conservation of mass, the volume flow-rate can be also shown as:

$$Q(r) = Q(R_1) - \pi(r^2 - R_1^2) \frac{dg}{dt}, \quad (2-4)$$

where  $\pi(r^2 - R_1^2) \frac{dg}{dt}$  represents the volume increase within  $R_l$  and  $r$ . Equal eqns. (2-3)

and (2-4), yields

$$r \frac{dp}{dr} = \frac{6\mu}{g^3} \frac{dg}{dt} (r^2 - R_1^2) + R_1 \left( \frac{dp}{dr} \right) \Big|_{r=R_1}. \quad (2-5)$$

Let  $\frac{r}{R_1} = \lambda$  and  $\frac{R_2}{R_1} = M$ , and integrate equation (2-5) with respect to  $\lambda$ , then yields

$$p = \frac{3\mu}{g^3} \frac{dg}{dt} R_1^2 (\lambda^2 - 2\ln\lambda) + \ln\lambda \left( \frac{dp}{d\lambda} \right) \Big|_{\lambda=1} + C. \quad (2-6)$$

To solve the constant  $C$  and  $\left( \frac{dp}{d\lambda} \right) \Big|_{\lambda=1}$ , substitute the boundary conditions with  $p=P_1$  at  $\lambda=1$  and  $p=P_2$  at  $\lambda=M$  and we can get:

$$C = p_1 - \frac{3\mu}{g^3} \frac{dg}{dt} R_1^2, \quad (2-7)$$

and

$$\left( \frac{dp}{d\lambda} \right) \Big|_{\lambda=1} = \frac{1}{\ln M} \left[ p_2 - p_1 + \frac{3\mu}{g^3} \frac{dg}{dt} R_1^2 (1 - M^2 + 2\ln M) \right]. \quad (2-8)$$

Substitute eqns. (2-7) and (2-8) into (2-6) and yields

$$p = p_2 + (p_1 - p_2) \left( 1 - \frac{\ln\lambda}{\ln M} \right) + \frac{3\mu}{g^3} \frac{dg}{dt} R_1^2 \left[ \lambda^2 - 1 + \frac{\ln\lambda}{\ln M} (1 - M^2) \right], \quad (2-9)$$

and hence the volume flow-rate of eqn.(2-3) becomes

$$Q(r) = (p_1 - p_2) \frac{\pi}{6\mu \ln M} - \frac{\pi r}{2} \frac{dg}{dt} R_1^2 \left( \frac{2r}{R_1^2} + \frac{1 - M^2}{r \ln M} \right). \quad (2-10)$$

The total force that the liquid applied on the covering plate can be expressed as:

$$\begin{aligned} F_{Total} &= (p_1 - p_2) \pi R_1^2 + F_{plate} = (p_1 - p_2) \pi R_1^2 + \int_1^M p 2\pi R_1^2 \lambda d\lambda \\ &= \left[ (p_1 - p_2) \pi R_1^2 \left( \frac{M^2 - 1}{2 \ln M} \right) \right] \\ &\quad + \frac{\mu}{g^3} \frac{dg}{dt} \frac{3\pi}{2} R_1^4 \left[ 1 - M^4 + \frac{1 - 2M^2 + M^4}{\ln M} \right] \\ &= F_{steady} + F_{unsteady}, \end{aligned} \quad (2-11)$$

where  $F_{steady}$  represents the applied force in steady state flow due to the pressure difference,  $P_1 - P_2$ , while  $F_{unsteady}$  represents the unsteady state condition. The second term

becomes zero if the covering plate's gap is fixed, i.e.,  $\frac{dg}{dt} = 0$ , or  $R_1=R_2$ , or the dynamic viscosity,  $\mu$ , is zero.

### 2.2.2 Calculation of the necessary pre-stress force

The liquid starts to flow when the upstream force is equivalent or higher than the downstream force. The force balance at this moment can be used to find the necessary pre-stress tensile stress and can be mathematically represented as:

$$p_1\pi R_1^2 \geq p_2\pi R_2^2, \quad (2-12)$$

or

$$p_1 \geq M^2 p_2 = p_c, \quad (2-13)$$

where  $p_c$  is defined as the cracking pressure of the check-valve. Assume the tensile stress of the slanted tethers is  $\sigma_t$ , the tethers' number, thickness, width, and angle are  $n$ ,  $t$ ,  $w$ , and  $\theta$ , respectively, then the required tensile stress can be derived as

$$\sigma_t = \frac{\pi R_1^2}{twn\sin\theta} p_c. \quad (2-14)$$

As the tensile stress is generated by annealing the check-valve in high temperature  $T_1$  and quenched to room temperature  $T_r$ ,  $\sigma_t$  can also be represented as:

$$\sigma_t = E_p \alpha (T_1 - T_r), \quad (2-15)$$

where  $E_p$  and  $\alpha$  are the Young's modulus and the thermal coefficient of expansion of parylene-C, respectively. The annealing temperature can be determined by eqn. (2-15).

## 2.3 Pre-Stressed Slanted Tether Micro Check-Valves

### 2.3.1 Slanted tether NC check-valve configuration

A simple NC check-valve structure schematic is proposed and shown in Figure 2-3. The check-valve is composed of single layer of parylene-C with several slanted tethers. The slanted tethers are reinforced to provide the necessary downward force which introduces the designed cracking pressure of the NC check-valve. With this simple slanted tether NC check-valve design, the downward force can be controlled by several parameters: the number of the slanted tethers, the sloping angle of the slanted tethers ( $\theta$ ), the geometry of the slanted tethers (the width and the thickness), and also the residual stress of the slanted tethers which can be controlled by annealing temperatures. The structure design greatly simplifies Chen's multi-layer parylene-C micromachining process into single-layer parylene-C deposition.

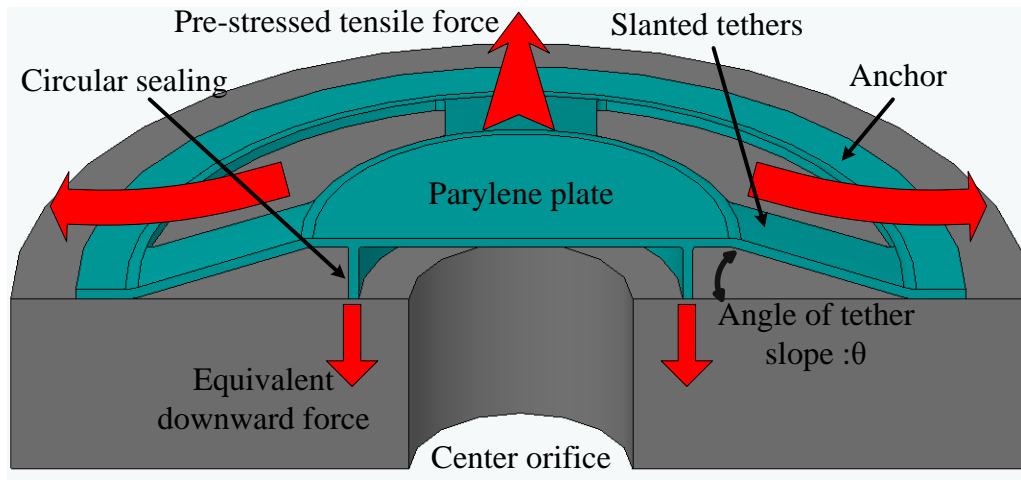


Figure 2-3: Schematic of cracking-pressure-controlled parylene-C check-valve using the residual tensile stress in parylene-C after thermal annealing

### 2.3.2 Thermal annealing pre-stressed NC check-valves

With the structure designed as in Figure 2-3, the slanted tethers are thermally annealed at predetermined temperature after the sacrificial photoresist is released and quenched down to room temperature afterwards. Since the residual tensile stress of the thermally annealed parylene-C can be as high as 34 MPa at 250°C [110], this approach allows the parylene-C tethers to provide a high downward force while it does not require any post-fabrication manual manipulation.

In order to utilize the residual tensile stress in parylene-C after thermal annealing, we need to make parylene-C tethers slanted with an angle,  $\theta$ . After the check-valves are processed with sacrificial photoresist releasing, they are annealed at a desired temperature and then quenched quickly to room temperature. Because the thermal expansion coefficient of parylene-C is much bigger than that of the silicon substrate, this process generates a residual tensile stress in the slanted tethers. This residual tensile stress then provides a net downward sealing force on the parylene-C NC check-valve's covering plate against the silicon orifice. The final cracking pressure can be mathematically represented as:

$$P_c = \frac{t \times w \times n \times \sigma_t \times \sin\theta}{\pi r^2}, \quad (2-16)$$

where  $P_c$  is the cracking pressure of the valve;  $t$  is the thickness of the parylene-C;  $w$  is the width of the tethers;  $n$  is the number of the tethers;  $\sigma_t$  is the residual stress of thermally annealed parylene-C; and  $r$  is the radius of the parylene-C covering plate. With the thermally annealing residual tensile stress at 250°C as 34 MPa, the cracking pressure of this check-valve can be achieved as high as several psi even for a small size check-valve.

### 2.3.3 Sloped photoresist

#### 2.3.3.1 One-time-exposure gray-scale photo-mask

The technique of using one-time-exposure gray-scale lithography to create the sloped photoresist [111–117] is introduced in this section. The one-time-exposure gray-scale lithography technique was originally invented to fabricate the diffractive optical elements (DOE) [113]. Due to its capability of generating sloped photoresist, the technique has also been used as the etching mask to create the sloped shape MEMS devices [112, 117]. In this work, the technique is used to make sloped sacrificial photoresist in the check-valve fabrication process.

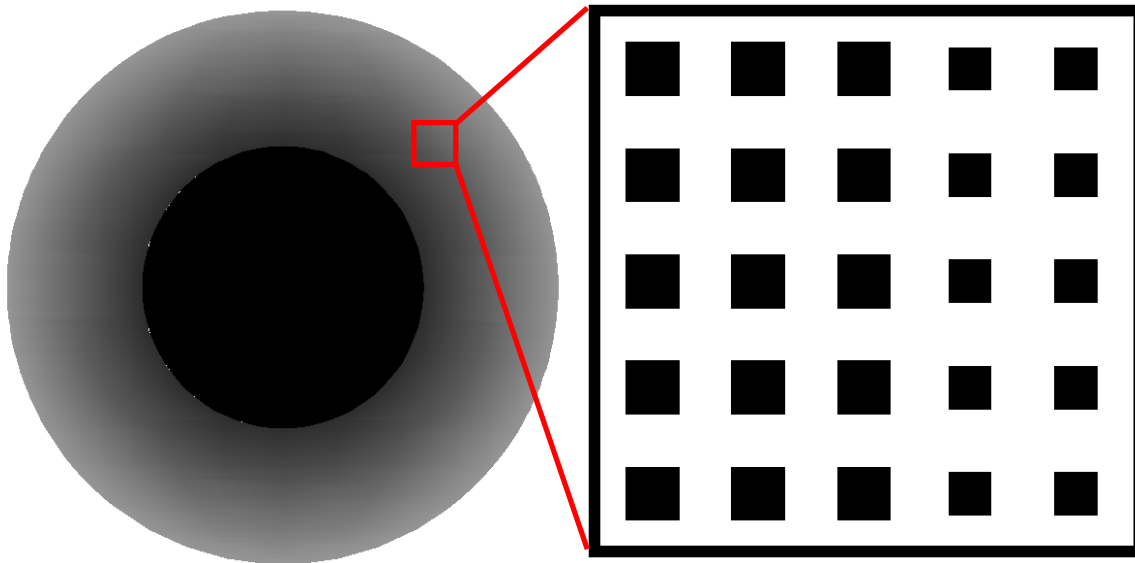


Figure 2-4: A closer view of designed gray-scale photo-mask for the creation of sloped photoresist. The right pattern magnifies part of the pixel structure of the ring.

Such a typical photo-mask is shown in Figure 2-4. To make photoresist partially exposed, an array of small dark squares with pitch,  $P$ , smaller than the diffraction limit of

the UV exposure system,  $P_c$ , are designed onto the photo-mask. Dark squares with pitch smaller than the diffraction limit can actually make the first order diffraction light blocked by the numerical aperture of the exposure system, making the light transmittance of the photo-mask proportional to the coverage area of these dark squares [117].

The maximum allowable square pitch size which will not get resolved by the optical system can be expressed as:

$$P \leq P_c = \frac{1}{1 + \sigma} \times \frac{\lambda}{NA}, \quad (2-17)$$

where  $\sigma$  is the coherence factor of the optical system,  $\lambda$  is the UV wavelength, which is 436 nm in our optical exposure system.  $NA$  is the numerical aperture of the optical exposure system. According to the specification of our exposure stepper, the diffraction limit is about 1  $\mu\text{m}$ . In the transmittance design, “pulse width modulation” approach is used, in which a constant square pitch with various dark square sizes as shown in Figure 2-4. With the 10:1 optical image reduction, we can have dark squares  $> 10 \mu\text{m}$  on our photo-mask. Therefore, it is relatively low-cost to perform the gray-scale-mask lithography using the regular commercially available transparency slides [115].

### ***2.3.3.2 Linearization of the sloped sacrificial photoresist***

It is well known that most photoresists have nonlinear response to UV light exposure. Therefore, a gray-scale photo-mask pattern with linear transmittance distribution will not give us a linear photoresist profile, as shown in Figure 2-5 (a). A mathematical model is adopted here to characterize and linearize our final photoresist profile [111]. In the model, the original total percentage of unexposed photoresist is normalized as 1, and the percentage of exposed photoresist is denoted as  $E(t)$ , which is generated after exposure to UV light within a period of time,  $t$ . It is further assumed that

the changing rate of exposed photoresist,  $E(t)$ , is proportional to the remaining unexposed photoresist,  $1 - E(t)$ , and the exposed light intensity  $I_0T$ , where  $I_0$  is the stepper light intensity and  $T$  is the transmittance of the photo-mask. Therefore, the overall exposure system can be represented as an ordinary differential equation with the initial condition as follows,

$$E(0) = 0, \quad (2-18)$$

and

$$\frac{dE(t)}{dt} = \alpha[1 - E(t)]I_0T, \quad (2-19)$$

where  $\alpha$  is the proportional constant. The constant is an optical property of the photoresist's sensitivity to UV light. The solution of eqns. (2-18) and (2-19) can be obtained as

$$E(t) = 1 - \exp(-\alpha I_0 T t). \quad (2-20)$$

Therefore, to have a linear distribution of exposed photoresist,  $E(t)$ , we can use eqn. (2-20) to design the corresponding transmittance distribution on the photo-mask. Figure 2-5 (b) shows the scanning result of the characterized and then linearized photoresist profile.

Figure 2-5 (b), the gray-scale photo-mask is composed of 16 levels with increasing transmittance from left to the right of the sloping area with each level translating into a photoresist height proportional to  $\exp(-\alpha I_0 t)$ . In order to create a true linear slope, a test photoresist strip was first fabricated for characterization. Then, the transmittance of each ring is adjusted according to the resulted photoresist height from

the test strip. It was shown in literature that larger  $\alpha I_0 t$  produces more reliable results [111]. In our case,  $I_0$  is measured as 200–250  $\text{mw}/\text{cm}^2$  in the stepper, which is one order of magnitude higher than the published literature. With  $t$  taken as 4 seconds, our exposure energy is within the right regime suggested in the literature.

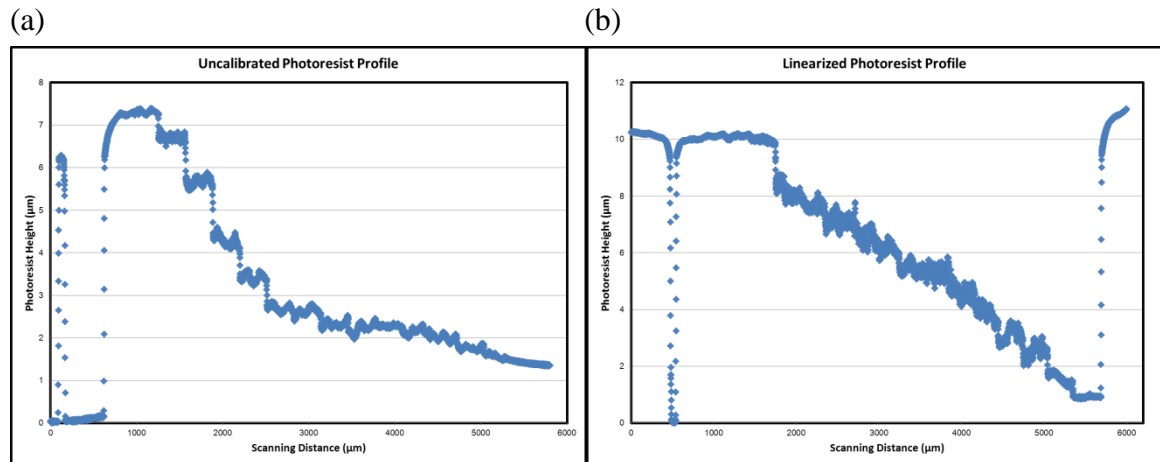


Figure 2-5: One-time-exposure gray-scale sacrificial photoresist profile: (a) before linearization, and (b) after linearization

### 2.3.4 Fabrication

Fabrication procedures are outlined in Figure 2-6. The process started with thermally growing silicon dioxide on both sides of double-side-polished wafers. After a back side oxide patterning, DRIE was used to etch the backside orifices with 100  $\mu\text{m}$  in diameter and also the releasing trench, until a thin silicon membrane of 50  $\mu\text{m}$  was left. A 100  $\mu\text{m}$  deep thin circular trench was etched on the front side followed by coating and patterning parylene-C as an anchor to help hold the parylene-C check-valve in place during valve operation. A 10  $\mu\text{m}$  photoresist AZ4620 was then coated on the front side and patterned using a gray-scale photo-mask. A two-step exposure technique with different exposure times was utilized to make the center photoresist to have variable

heights serving the mold of the valve sealing ring. After 10  $\mu\text{m}$  of parylene-C coating and patterning, the through holes and trenches were completed by DRIE etching. The sacrificial photoresist was then removed by acetone and IPA.

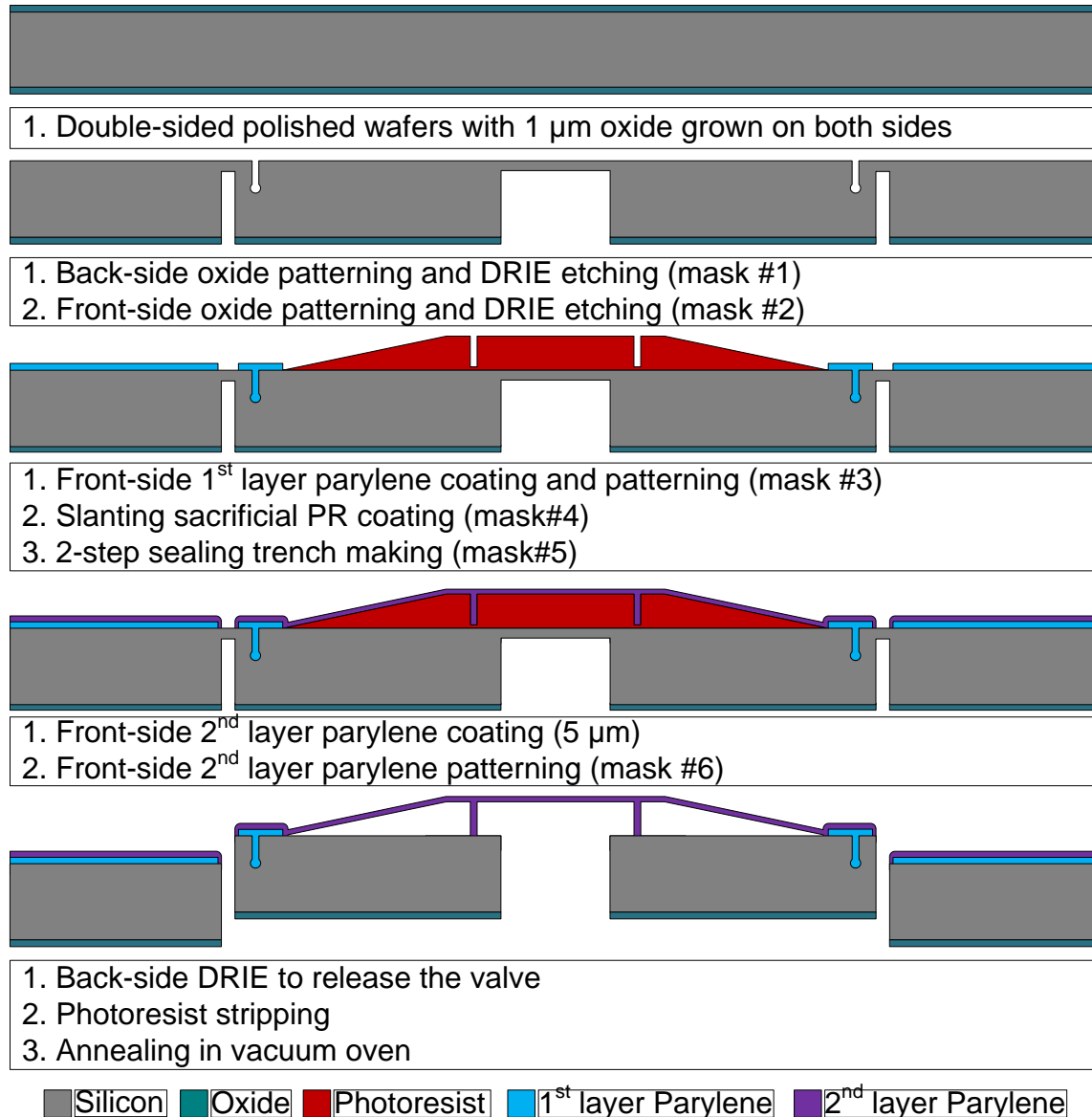


Figure 2-6: Fabrication procedures. Slanted sacrificial photoresist is achieved using a one-time-exposure gray-scale photo-mask photolithography approach.

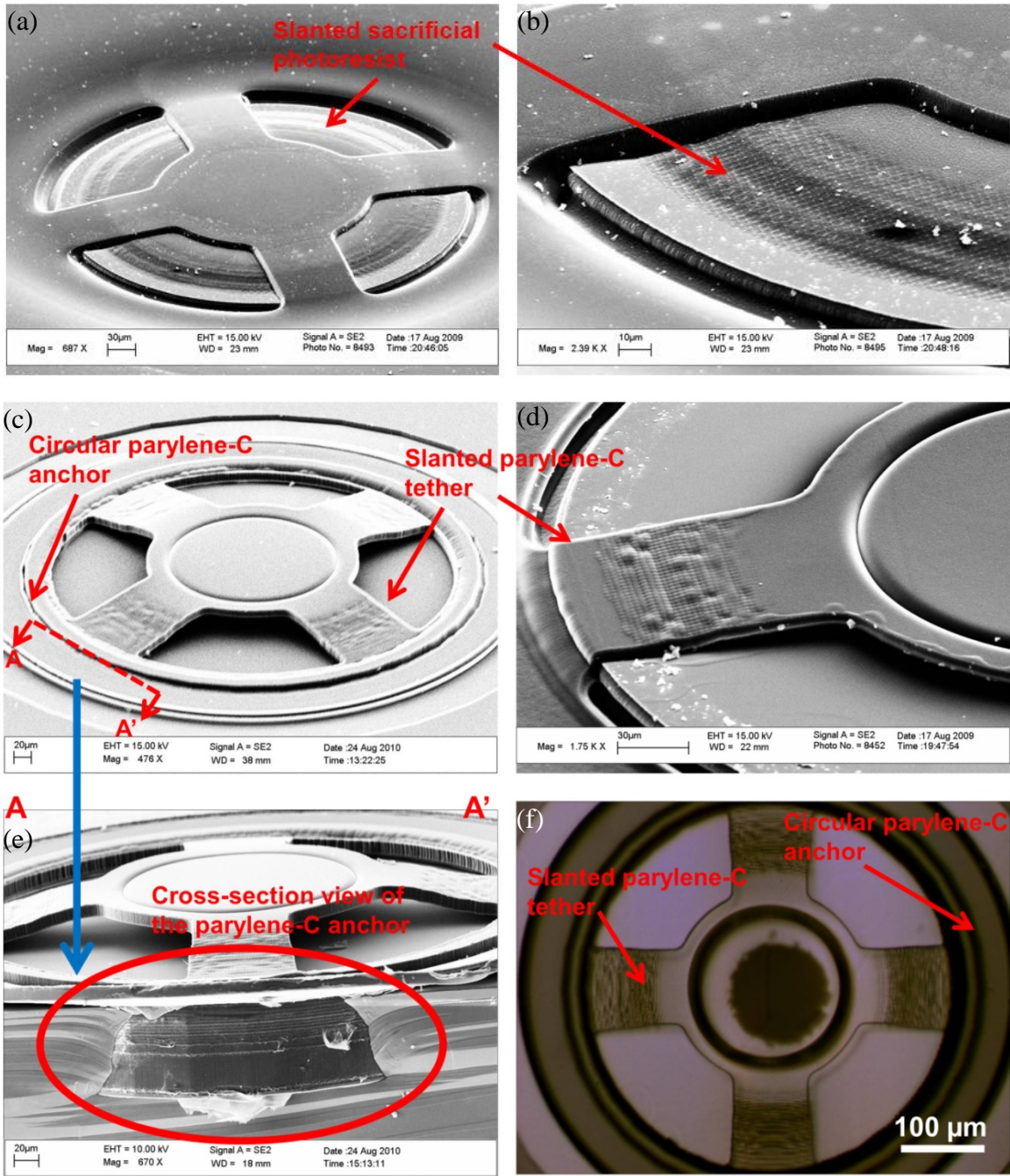


Figure 2-7: SEM pictures of fabricated check-valves: (a) check-valves before photoresist removal, (b) a closer view of a tether and the sloped photoresist, (c) check-valves after photoresist removal, (d) a closer view of a tether after photoresist removal, (e) the cross-sectional view of the parylene-C anchor, and (d) micrograph of the top view of the check-valve

SEM images of fabricated devices before and after photoresist stripping are shown in Figure 2-6 (a) to (e). Figures 2-6 (a) and (b) illustrate the successful creation of the slanted sacrificial photoresist profile by the one-time-exposure gray-scale lithography. Figures 2-6 (c) and (d) demonstrate the resulted linearly slanted parylene-C tethers after removing the photoresist. Figure 2-6 (e) shows the cross sectional view of the successful parylene-C anchor. Figure 2-6 (f) is the micrograph of the top view of the check-valve.

### 2.3.5 Device testing and discussion

After sacrificial photoresist was stripped by acetone and IPA, a thermal annealing of the NC check-valves was performed. Different temperatures were used to create different residual tensile stresses. The testing setup is shown in Figure 2-8. Water was chosen as the testing fluid. Working fluid flowed into a customized jig with specially designed channels conducting water to fluidic ports of the tested check-valves. Pressure was conducted to the check-valves through the backside orifices and flow-rate was recorded by measuring the marching speed of the testing fluid front inside the testing tubes.

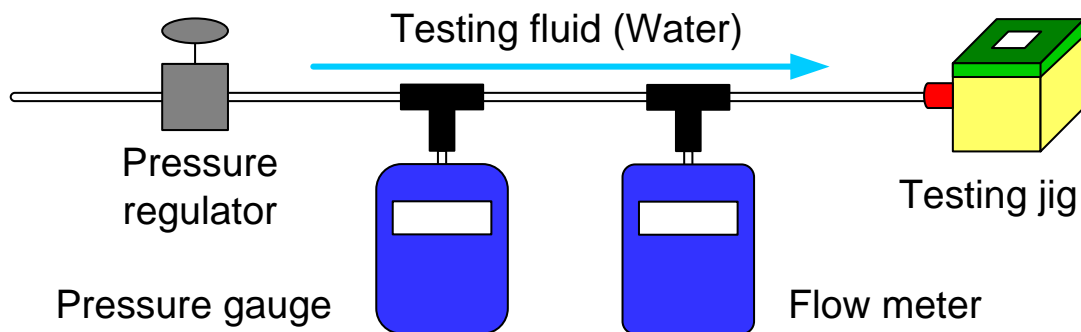


Figure 2-8: Testing setup for MEMS micro check-valves

Two cracking pressure controlling factors were considered and tested: parylene-C tether width and the annealing temperature. To study the influence of the parylene-C tether width, check-valves with 3 different tether widths (50  $\mu\text{m}$ , 70  $\mu\text{m}$ , 100  $\mu\text{m}$ ) were all annealed at 100°C for 1 hour and then quenched to room temperature to generate the necessary residual tensile stress. The pre-annealed check-valves were characterized by the proposed testing setup and the cracking pressures were measured to be 0.3 psi, 1.5 psi, and 2.9 psi, respectively as shown in Figure 2-9. It is shown that the check-valve's cracking pressure increases as the tethers widen. This agrees with our expectation because increased width means increased pre-stressed force.

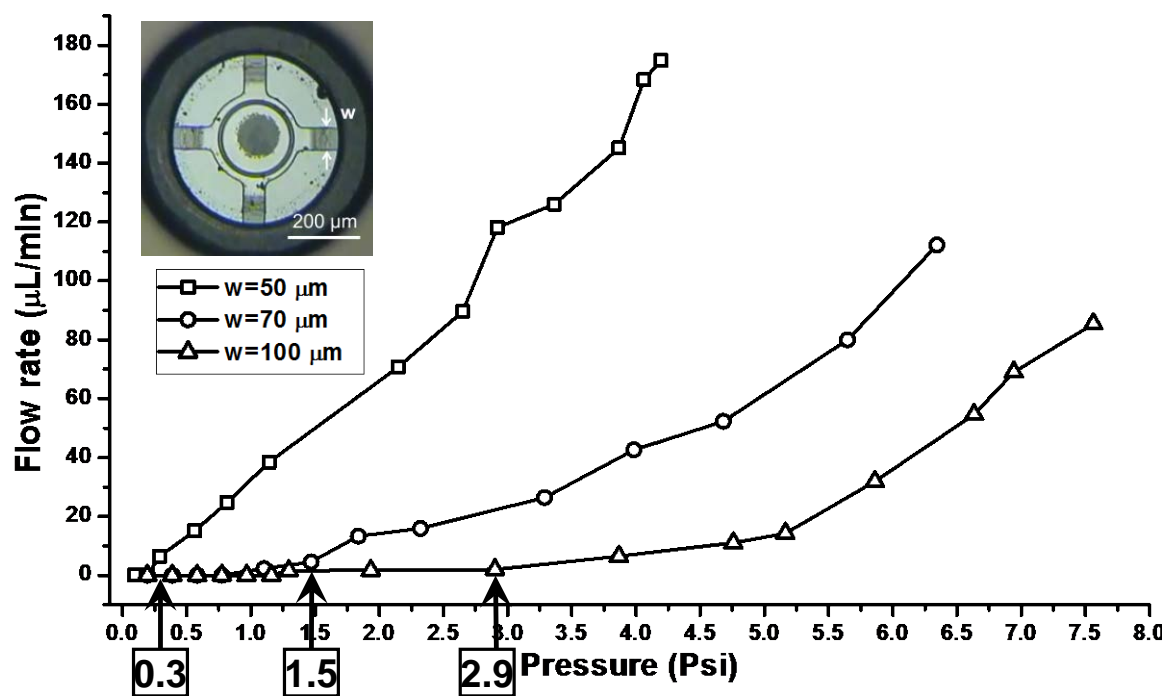


Figure 2-9: Parylene-C tether width effect of the characterization results of thermally pre-stressed slanted tether micro check-valves: different tether widths but with the same annealing temperature at 100°C

To study different annealing temperature effect, check-valves with 50  $\mu\text{m}$ -wide-tether were annealed at 100°C and 140°C, quenched to room temperature, and then characterized. The process of annealing check-valves at 140°C was performed in vacuum to prevent the oxidation of parylene-C. The flow-rates are shown and compared in Figure 2-10. The cracking pressures were obtained as 0.3 psi and 1.3 psi for 100°C and 140°C, respectively. It is found that the cracking pressure increased as the annealing temperature increases. This is attributed to the increased residual tensile stress of parylene-C after annealed at higher temperatures.

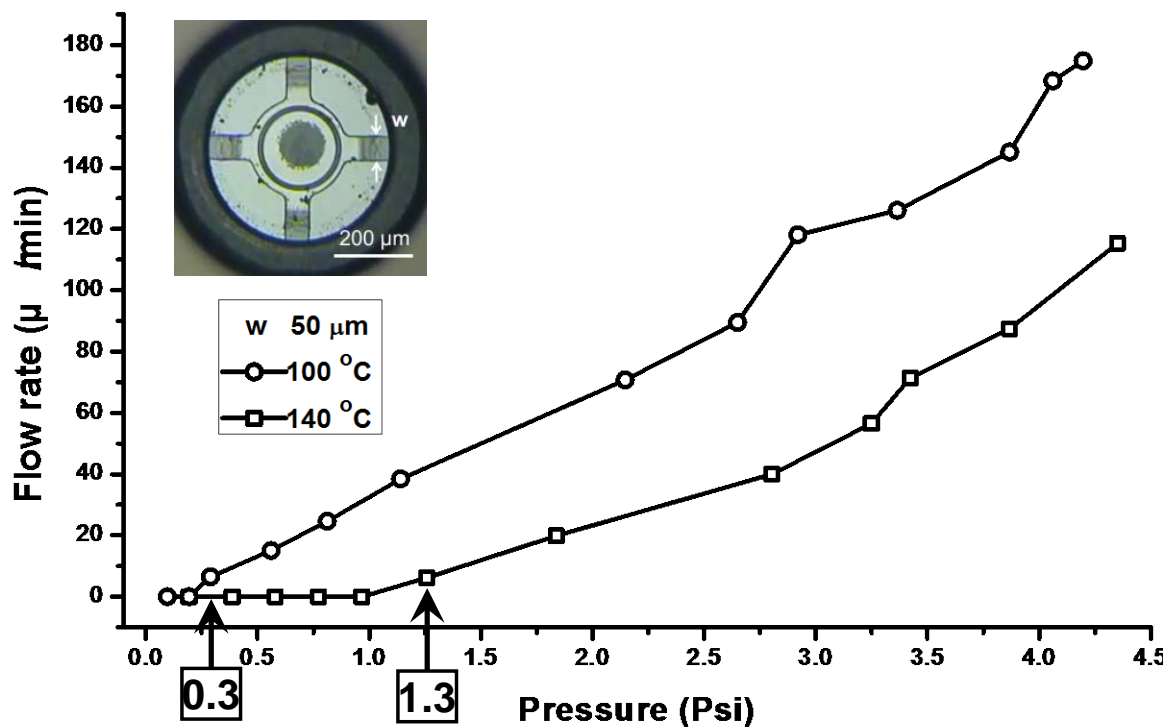


Figure 2-10: Temperature effect of the characterization results of thermally pre-stressed slanted tether micro check-valves: different annealing temperatures but with the same tether widths of 50  $\mu\text{m}$

To summarize, the cracking pressures of NC check-valves consistently increase with the increasing tether width and the annealing temperature. However, experimental data also showed that the cracking pressure could deviate from the theoretical value. This is likely because the flexibility of the parylene-C covering plate which cannot provide a strong fixed boundary condition. Therefore, the induced thermal stress cannot be as high as calculated. In addition, it is also found that, even at the room temperature, the cracking pressure tends to decrease at the early measuring stage after annealing. This is due to the stress relaxation of the parylene-C tethers right after annealing. The phenomenon of stress relaxation of parylene-C will be discussed more in detail in Section 5.8.3.

## **2.4 Integration of Slanted Tether Check-Valves for High-Pressure Applications**

The thermally pre-stressed slanted-tether micro check-valves has been proved to be capable of delivering cracking pressures as high as 2.3 psi in Section 2.3. The check-valves' tethers are reinforced by quenching check-valves to room temperature after the stress-relaxation annealing process to induce high residual tensile stress in the tethers. However, even though the cracking pressure of this slanted tether check-valve can be adjusted by annealing at different temperature, the maximum cracking pressure achievable with a single check-valve is still limited by the bonding strength between parylene-C and silicon in the anchor region, and also the ultimate tensile strength of the parylene-C tethers.

In this section, multiple slanted tether check-valves are integrated in series to achieve even higher cracking pressures. In a series construction, each slanted tether

check-valve could be modeled as a diode, where pressure and flow-rate are analogous to voltage and current respectively. Using this model, multiple check-valves can be easily analyzed and connected in series to achieve a larger total pressure drop even though the pressure drop across each check-valve is smaller. This situation is similar to using a series connection of multiple diodes to achieve a higher total voltage drop.

#### 2.4.1 Electrical-equivalent diode model

As shown in Figure 2-2, the volume flow-rate,  $Q$ , at  $r = R_2$  equals the final exit flow-rate of the check-valve.  $Q$  can be calculated and rearranged from eqn. (2-10) as

$$Q(r)|_{r=R_2} = (p_1 - p_2) \frac{\pi}{6\mu \ln M} - \frac{dg}{dt} \left( \pi R_2^2 + \frac{\pi R_1^2 - R_2^2}{2 \ln M} \right). \quad (2-21)$$

Therefore, in order to successfully generate the flow-rate, the applying pressure of the liquid  $p_1$  needs to be higher than the cracking pressure,  $p_c$ , shown in eqn. (2-13) with the flow-rate presented eqn. (2-21). The whole system can be equivalently modeled as a diode shown in Figure 2-11 with cut-in voltage as  $p_c$ . The flow-rate in eqn. (2-21) can be modeled as the electrical current after the cut-in voltage.

#### 2.4.2 Multiple check-valve integration

The check-valves were first annealed at 140°C and quenched to room temperature to introduce the residual tensile stress in tethers. To assemble the device, each check-valve was first inserted into a thin glass capillary tube, whose inner diameter is 530 μm, and sealed with epoxy as shown in Figure 2-12 (a). These individual assemblies were then characterized to obtain their cracking pressure and flow profile. Photoresist was used to seal the gap between the assembly and the testing tube so that the assembly can be released for later integration, as shown in Figure 2-13 (b). Afterwards, each pair of

assemblies were coupled together with a wider capillary tube (inner diameter of  $660\ \mu\text{m}$ ) to form an assembly of multiple check-valves, as shown in Figure 2-12 (b), then sealed with epoxy, and tested as shown in Figure 2-13 (c).

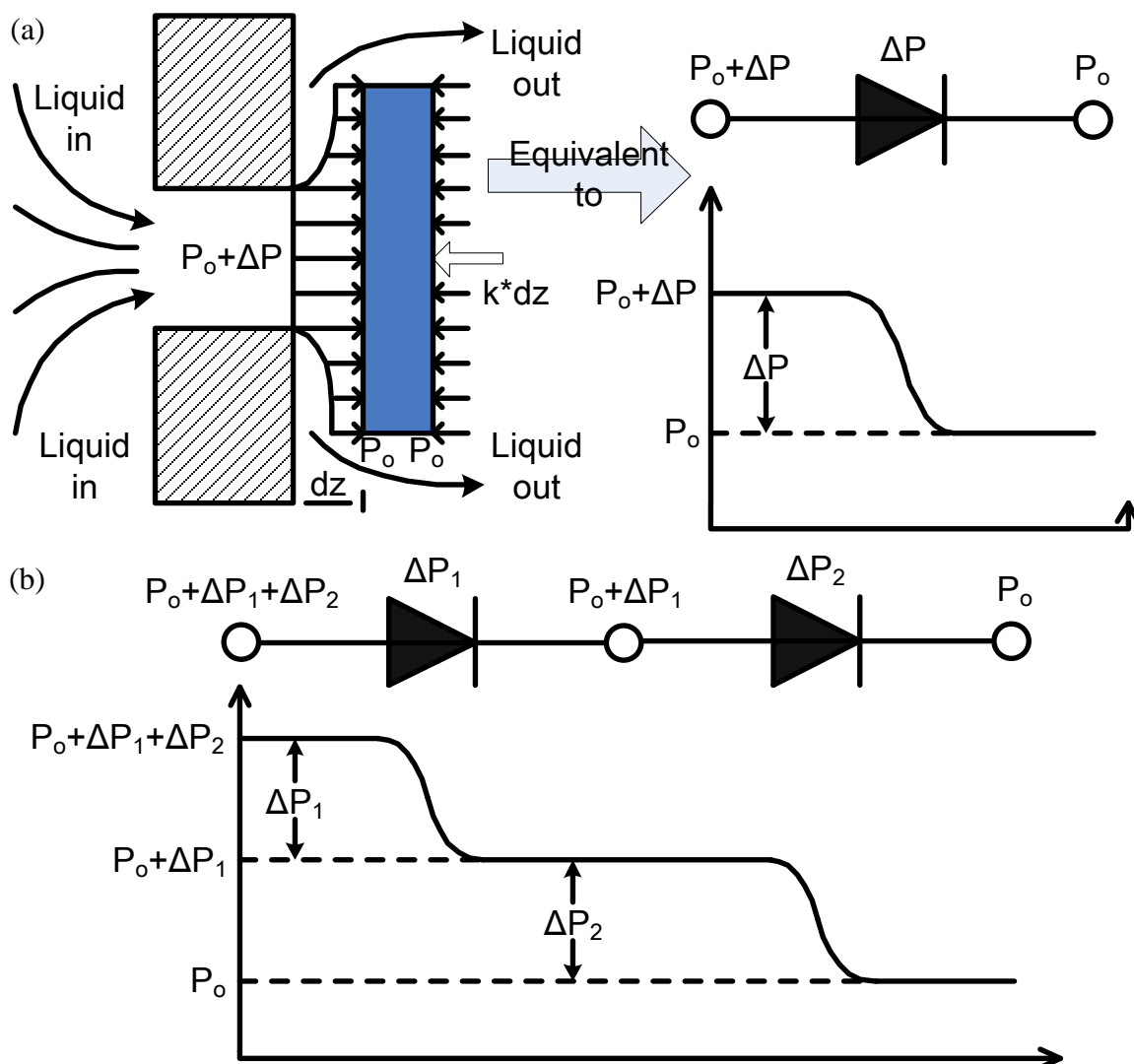


Figure 2-11: Equivalent electrical circuit component model of check-valves: (a) one-diode model of one check-valve.  $k$  and  $dz$  are the spring constant of the tethers and the covering plate displacement, respectively. (b) In-series diodes model of in-series check-valves

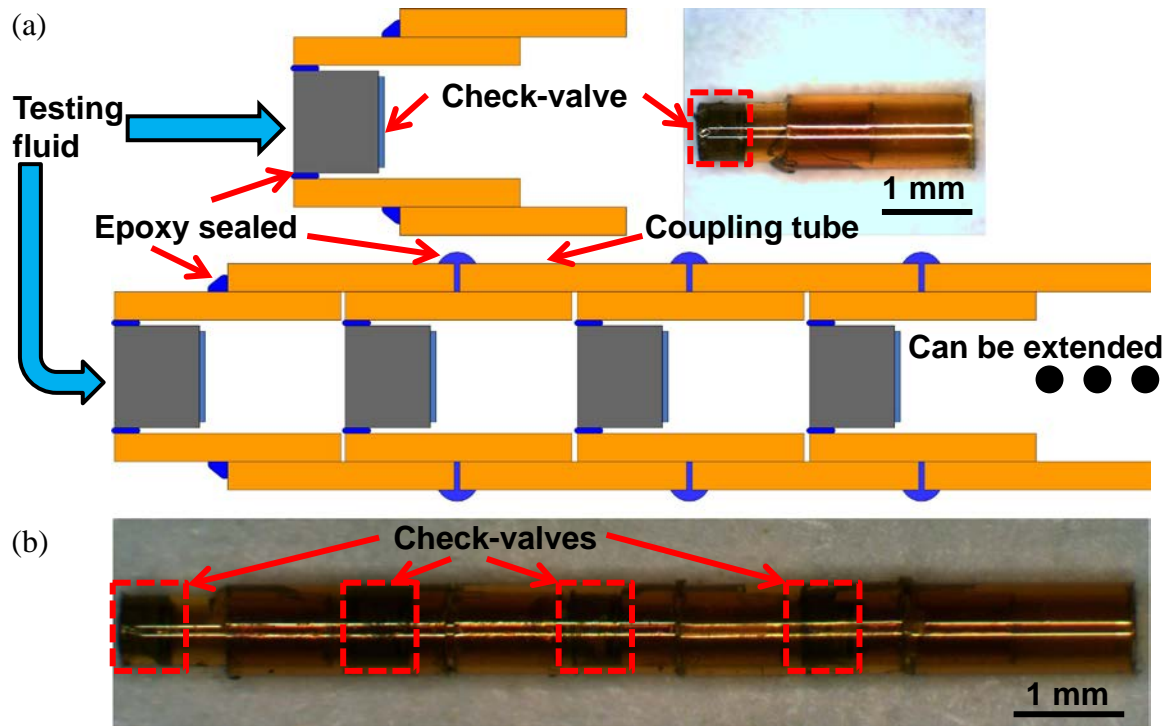


Figure 2-12: Valve packaging: (a) A single valve packaged in capillary tubes and (b) four individual modules integrated using coupling tubes

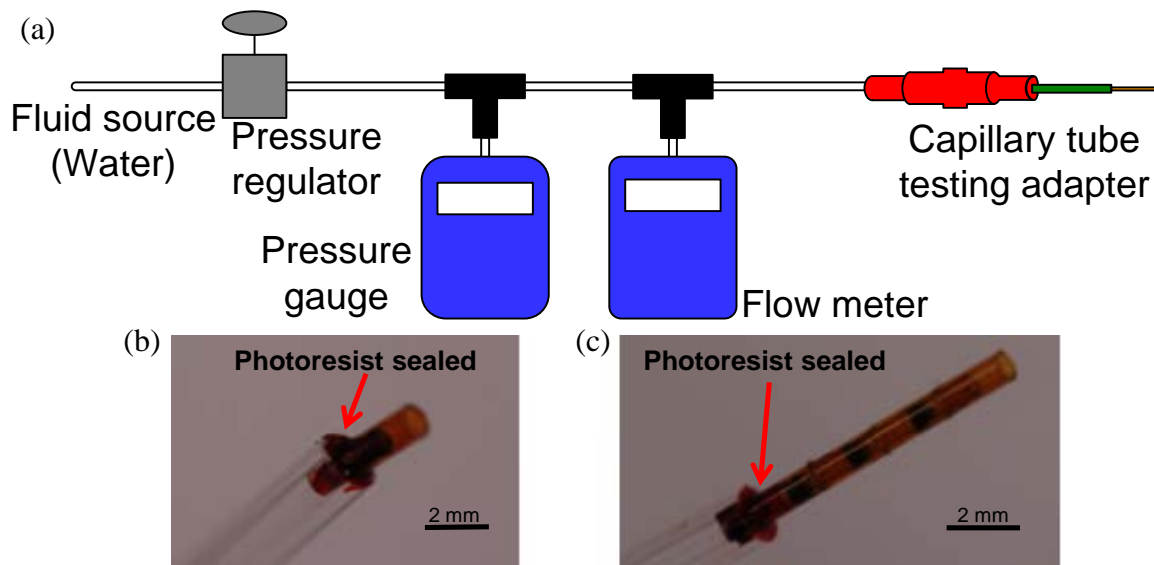


Figure 2-13: (a) Modified device testing setup, (b) the characterization of single valve, and (c) the characterization of four check-valves in series

### 2.4.3 Characterization results and discussion

The measured cracking pressures of each check-valve and the check-valve assembly are listed in Table 2-1. The flow profiles comparison between a single check-valve and a four-check-valve assembly is shown in Figure 2-14. The results show that the cracking pressure of a single valve falls between 0.42 psi and 0.49 and achieves 2.06 psi with four integrated check-valves. The parylene-C check-valves remain intact after many tests with inspection shown in Figure 2-14 (b). This proves the durability of the parylene-C anchors of the check-valve, which are to prevent de-bonding due to both the high tensile stress within the parylene-C layer after annealing process and the high pressure during the entire characterization process. The results verify the concept of integrating multiple slanted tether check-valves in series to create a high cracking pressure device for high-pressure microfluidic applications.

Table 2-1: Measured cracking pressures of four single check-valves and the assemblies of multiple check-valves

<b>Single valve</b>	<b>1</b>	<b>2</b>	<b>3</b>	<b>4</b>
<b>Cracking pressure</b>	0.49 psi	0.43 psi	0.47 psi	0.42 psi
<b>Multiple valves</b>	2 valves	3 valves	4 valves	
<b>Cracking pressure</b>	1.01 psi	1.48 psi	2.06 psi	

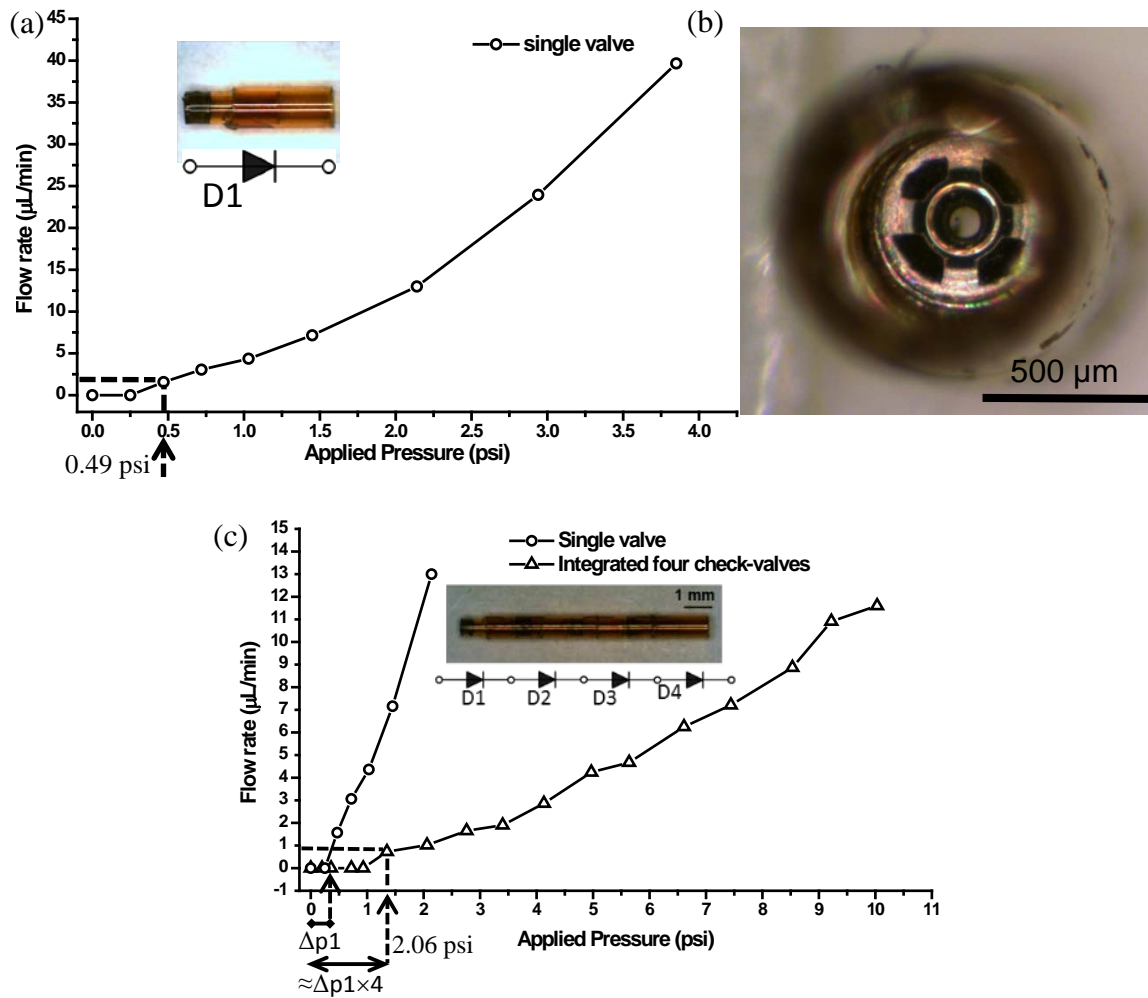


Figure 2-14: (a) Flow characteristics of a single valve, (b) micrograph of a check-valve in tube after testing, (c) flow characteristics of a four-check-valve assembly

## 2.5 Pop-Up Micro Check-Valve

The NC check-valves developed in Section 2.3 and the integrated multiple check-valves assembly in Section 2.4 have successfully demonstrated their capability of regulating pressure in a broad range (0.3 psi to several psi). However, it is found not simple enough to be integrated inside a channel so as to enable integrated microfluidics. In this section, a releasable all-parylene-C microfluidic device incorporating innovative

surface micro-machined NC pop-up check-valve is designed to regulate the cracking pressure of microfluidic flow. An undercut parylene-C foot is generated by first spin-coating a layer of LOR30B on silicon surface and then developed to create undercut after the first layer parylene-C film deposition and patterning. The cracking pressure is created by residual tensile stress built within the tethers introduced by post-fabrication pop-up process and can be enhanced by thermal annealing. This newly-designed micro check-valve can also be encapsulated within the all-parylene channel. The zigzag appearance along the channel edge makes it easy to anchor in any kind of implantation environments.

### **2.5.1 Pop-up micro check-valve device design**

The design of the pop-up check-valve is shown in Figure 2-15. The structure requires an undercut beneath the first layer parylene-C, which is created by developing LOR30B, using the first parylene-C as the mask. The 2nd layer of parylene-C then fills into these undercuts during deposition and creates an interlocking structure between the two parylene-C layers and the covering plate which is made of the second layer of parylene-C. Before the check-valve's usage, the covering plate is popped up from the back side by flowing liquid through the through hole. Once popped, the covering plate will stay on top of the first layer parylene-C due to the undercut parylene-C foot and will no longer return to the original interlocked position. The popping first creates an amount of mechanical tensile stress within the tethers connecting the covering plate and valve's anchor because of the extension. The tethers can then be thermally pre-stressed with thermal tensile stress by annealing/quenching to further control the cracking pressure. The cracking pressure can still be predicted by eqn. (2-16). The proper length of the

undercut is determined to be 10  $\mu\text{m}$  experimentally so that the covering plate can be popped up by injecting liquid into the back side through holes.

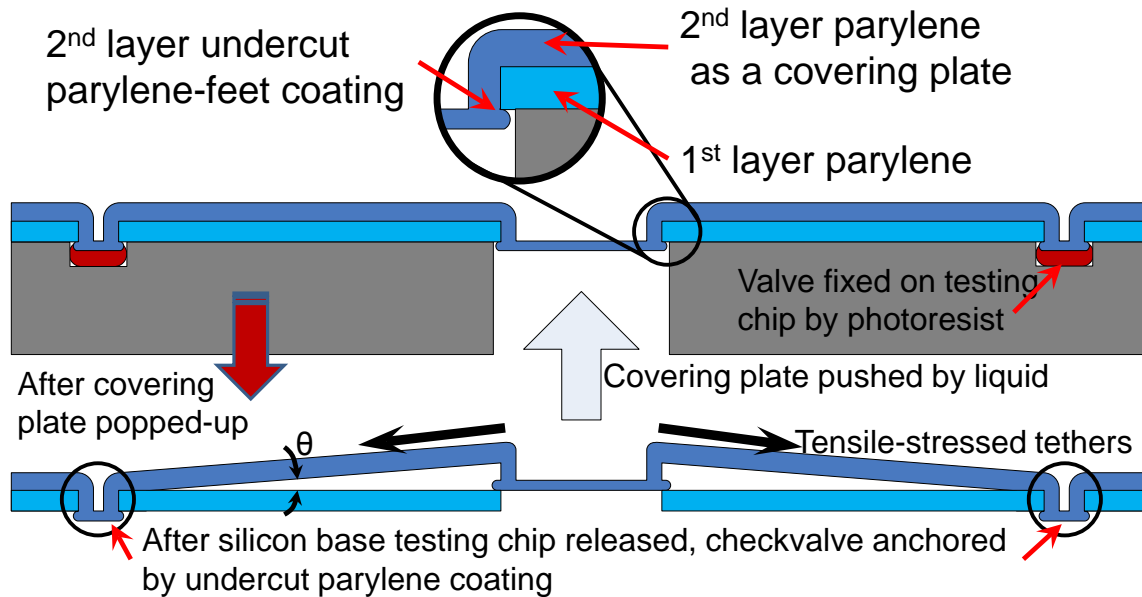


Figure 2-15: The configuration of a pop-up check-valve. A close-up of the undercut parylene-C foot is shown in the circular area.

### 2.5.2 Device fabrication

Both fabrication procedures of in-channel check-valves and testing chips were designed and are shown in Figure 2-16. The check-valve fabrication started with coating LOR30B on silicon wafers. A thin layer of aluminum was thermally evaporated onto LOR30B and then patterned to protect LOR30B from the possible hard baking during the following parylene-C layer plasma etching. The first layer of parylene-C was coated onto LOR30B and patterned. LOR30B undercut was developed after aluminum striping. The wafer was then coated with soap before the second layer of parylene-C deposition. After soap soaking on the parylene-C surface, the hydrophilic head of the soap was exposed

that changed the parylene-C surface to hydrophilic. This would benefit the popping process as the parylene-C would be easier to delaminate from the hydrophilic surface. The second layer of parylene-C was deposited, filling the undercut, and then patterned. A thick sacrificial layer of photoresist was coated, patterned and encapsulated with the third layer of protection parylene-C membrane. The whole device was released by acetone after patterning. On the other side of the parylene-C channel, an outlet port was fabricated using the same procedures as the check-valve, as shown in Figure 2-16 (a). The covering plate was etched away to make the through hole of the outlet port.

The testing chip fabrication started with double-side oxide wafers, with front side first patterned and etched by DRIE twice to create necessary cavities and then the back side DRIE followed to create through holes, as shown in Figure 2-16 (b).

The fabrication results are shown in Figure 2-17. Figure 2-17 (a) shows the successful undercut creation of LOR30B under the first layer of parylene-C; Figure 2-17 (b) is the micrograph of the check-valve after the second layer parylene-C patterned; Figure 2-17 (c) shows the micrograph of the top view of the outlet port after the second parylene-C patterned, and Figure 2-17 (d) demonstrates the final devices shown in 6 mm long. The zigzag features along the devices' sides facilitate the anchoring during the device implantation.

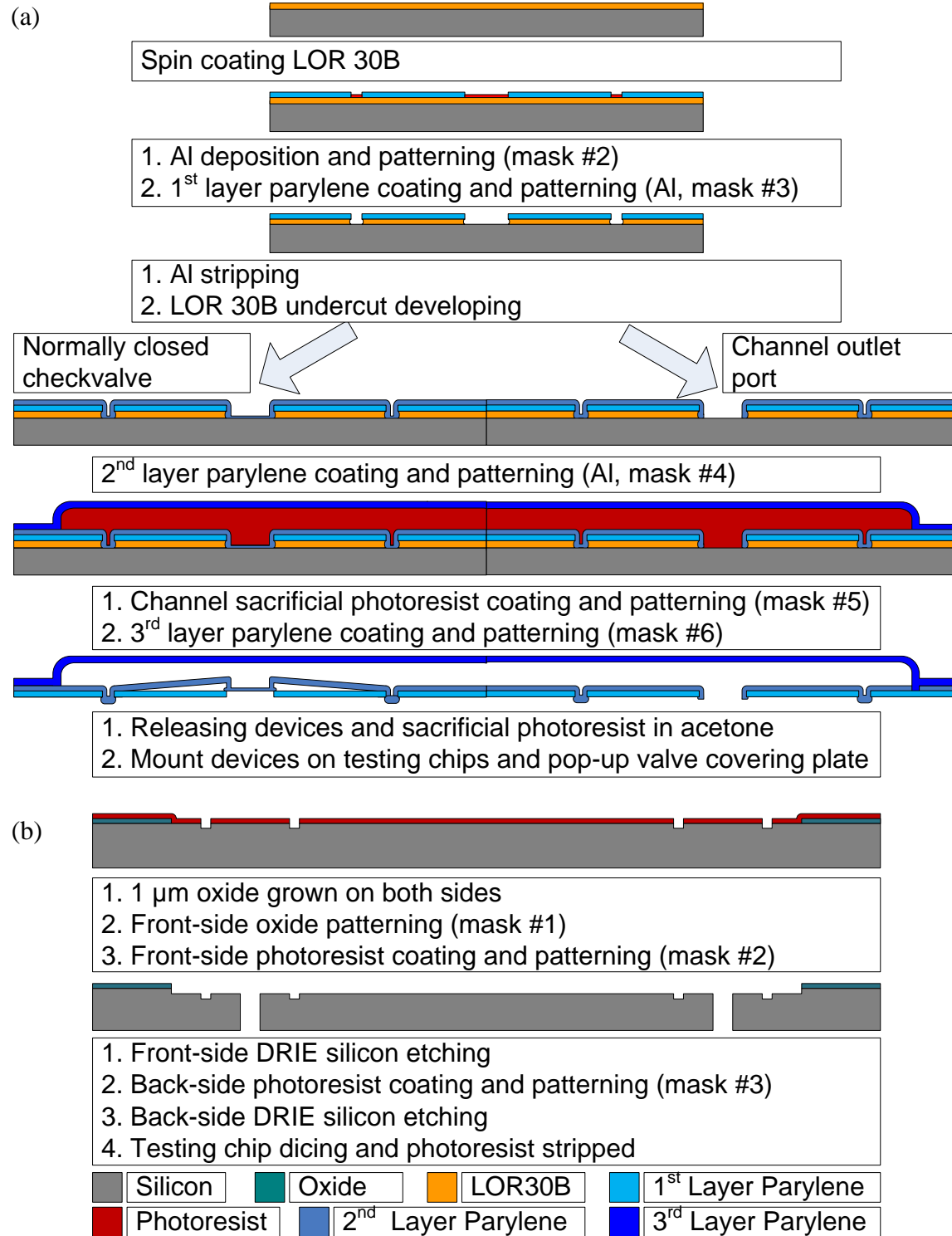


Figure 2-16: Fabrication procedures of (a) the pop-up micro check-valve, and (b) the testing chips

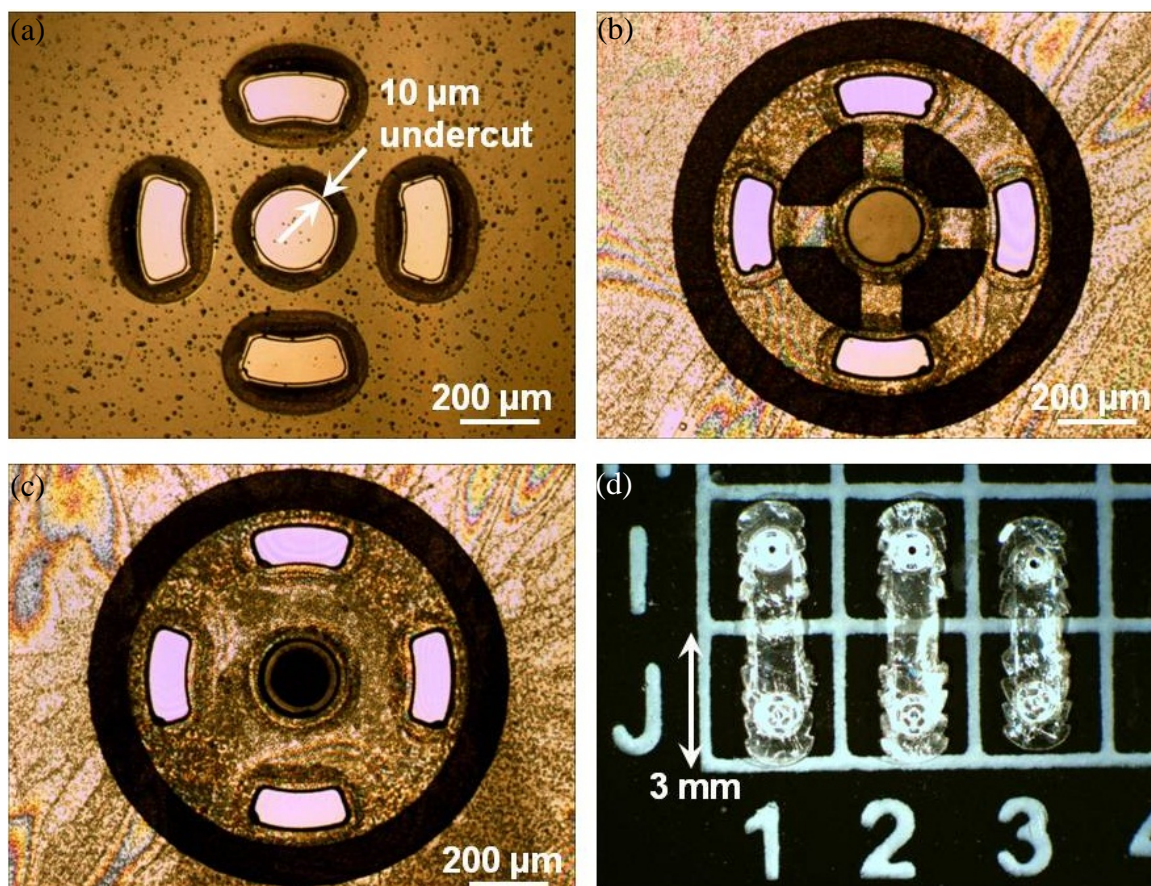


Figure 2-17: Micrograph of (a) 10  $\mu\text{m}$  undercut of the LOR30B, (b) top view of the NC check-valve, (c) top view of the outlet orifice, and (d) final device appearance

Figure 2-18 shows a series of SEM pictures of the fabricated check-valves. Figure 2-18 (a) shows the backside view of the check-valve, presenting the successful undercut parylene-C-foot coating; Figure 2-18 (b) represents a close view of about 10  $\mu\text{m}$  wide undercut coating; Figure 2-18 (c) is a top view of the check-valve before pop-up, and (d) is a close view of the tethers after pop-up. As shown in Figures 2-18 (a) and (b), four undercut parylene-C-foot not only work to anchor the check-valves onto the first layer parylene-C, but also behave as the posts preventing the device from stiction to the application surface.

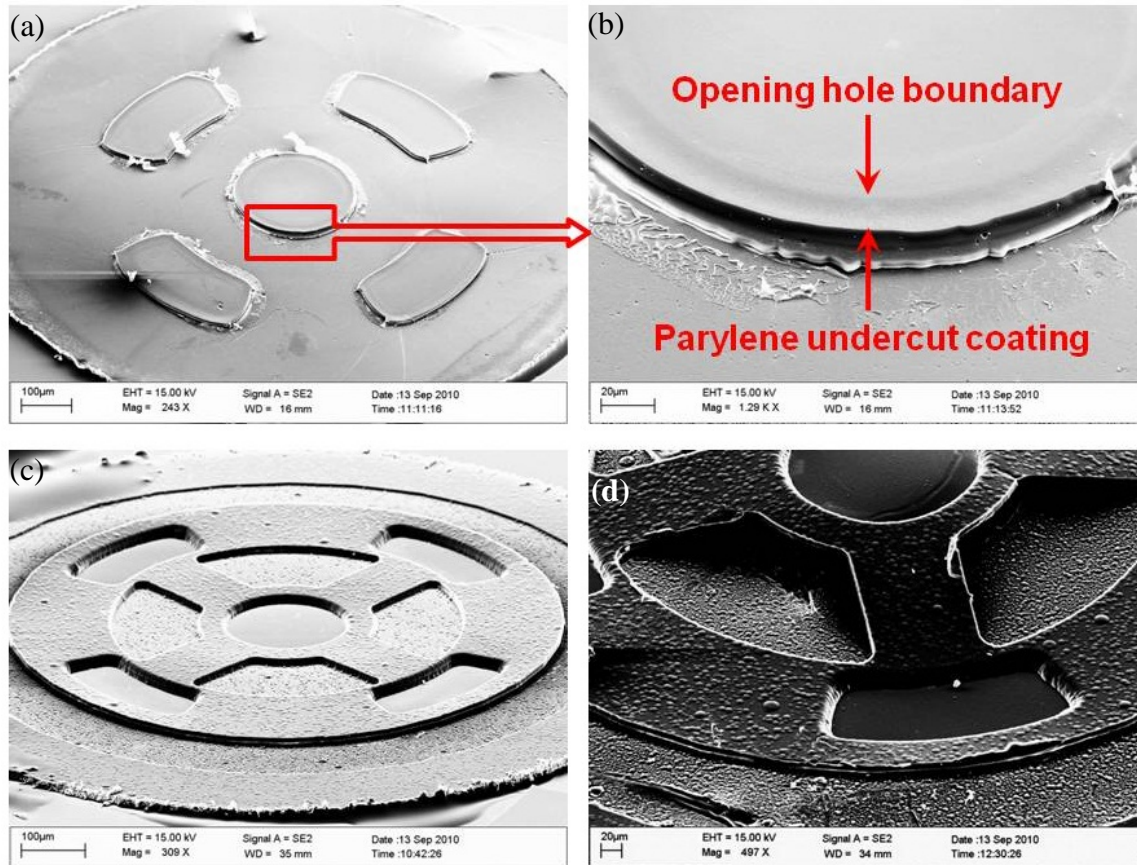


Figure 2-18: SEM pictures of (a) undercut parylene-C foot coating (back side view), (b) close view of undercut parylene-C foot coating, (c) normally closed check-valve, and (d) covering plate after pop-up

### 2.5.3 Device characterization setup

A complete testing chip is shown in Figure 2-20 (a). The size of the indentation on the testing chip is designed a bit larger than the device so that the through holes of the check-valves can be aligned with the holes of the testing chips. Circular trenches with the same width as check-valves' posts are fabricated to accommodate the posts so as to ensure the flatness of the check-valves and the complete sealing during the testing.

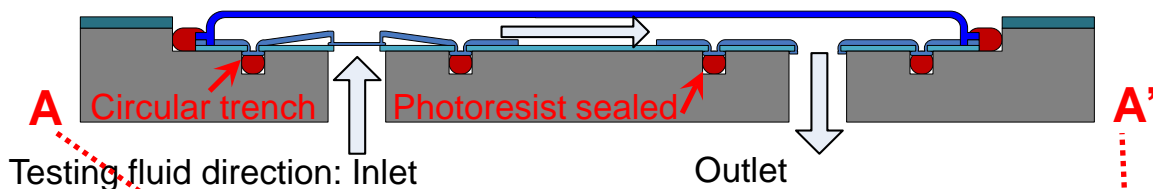


Figure 2-19: Cross section view of the testing chip with mounted in-channel check-valve

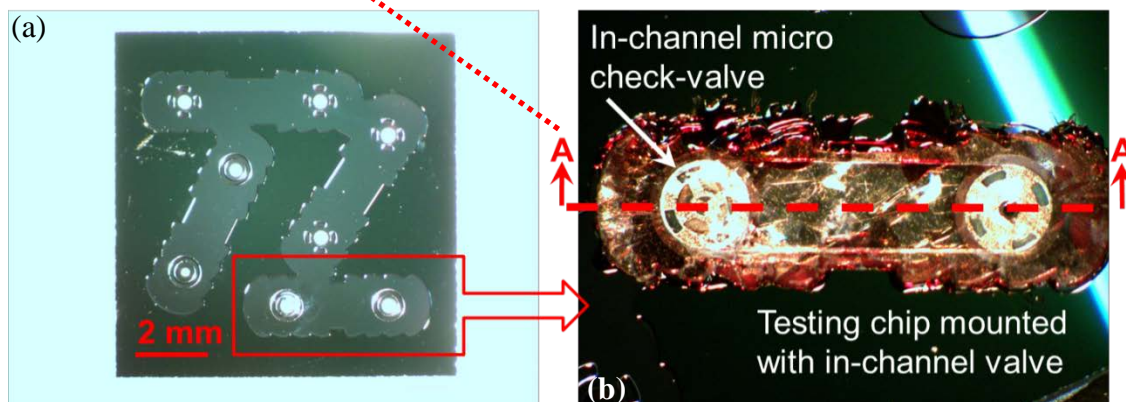


Figure 2-20: (a) Top view of the fabricated testing chip. (b) A close view of mounted device on top of the testing chip, sealed with dried photoresist

To test the in-channel check-valves, devices released from photoresist were first soaked in 5% HF solution. HF solution penetrates the top parylene-C layer into the boundary between two parylene-C layers and cleans the boundary. This makes it easier to separate the first and the second parylene-C layers during the popping-up. To enhance the check-valves' cracking pressure, devices were first annealed in high temperature in the oven to release all inherent residual stress, and then quenched to room temperature to build the necessary residual tensile stress. Rather than unpredictable residual stress, the stress achieved this way can be more controllable. Devices were then mounted onto the testing chip which was aligned and fixed on top of the testing jig as shown in Figure 2-20 (b). Photoresist was applied to seal and anchor the posts in the circular trench. The

surroundings of the device were also sealed by photoresist to ensure complete sealing. The testing setup shown in Figure 2-8 was used to characterize single check-valve. The check-valves were first popped up by pushing water into the back holes, and then microfluidically characterized. As shown in Figure 2-19, the testing liquid was sent into left NC check-valve. The liquid flew through the channel and exit to the right outlet port. The tested and qualified devices were then released in acetone to remove the photoresist for later implantation applications, as shown in Figure 2-17 (d)

#### **2.5.4 Device characterization results**

The popping process was filmed to observe its transition behavior. During the popping process, a syringe was used to inject the liquid into the through holes to gradually increase the applied pressure. When the applied pressure was higher the confining pressure of the interlock of the covering plate and the first layer parylene-C, the liquid burst out flowing. The applied pressure was released afterward, and the covering plate stayed on top of the first layer parylene-C due to the undercut parylene-C-foot. Figure 2-21 shows a sequence of pictures captured from the video: (a) shows the situation when applied pressure almost reached the confining pressure. Liquid is still covered by the covering plate; (b) demonstrates the time when applied pressure is just right over the confining pressure. The covering plate is suddenly popped over the confinement hole and liquid can be clearly seen to burst flowing out the NC check-valve; (c) shows the liquid over flooded right after the popping-up.

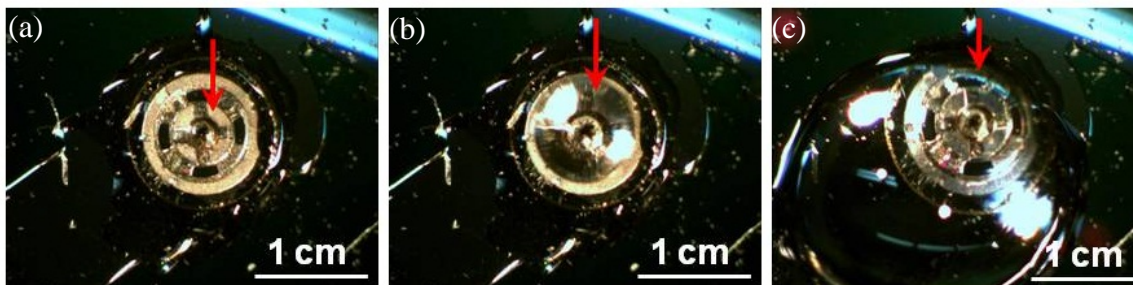


Figure 2-21: Captured pictures of normally closed pop-up check-valve during popping-up process (shown in arrow): (a) right before pop-up, (b) during pop-up, and (d) after pop-up. (Top parylene-C membrane is peeled off for clarity.)

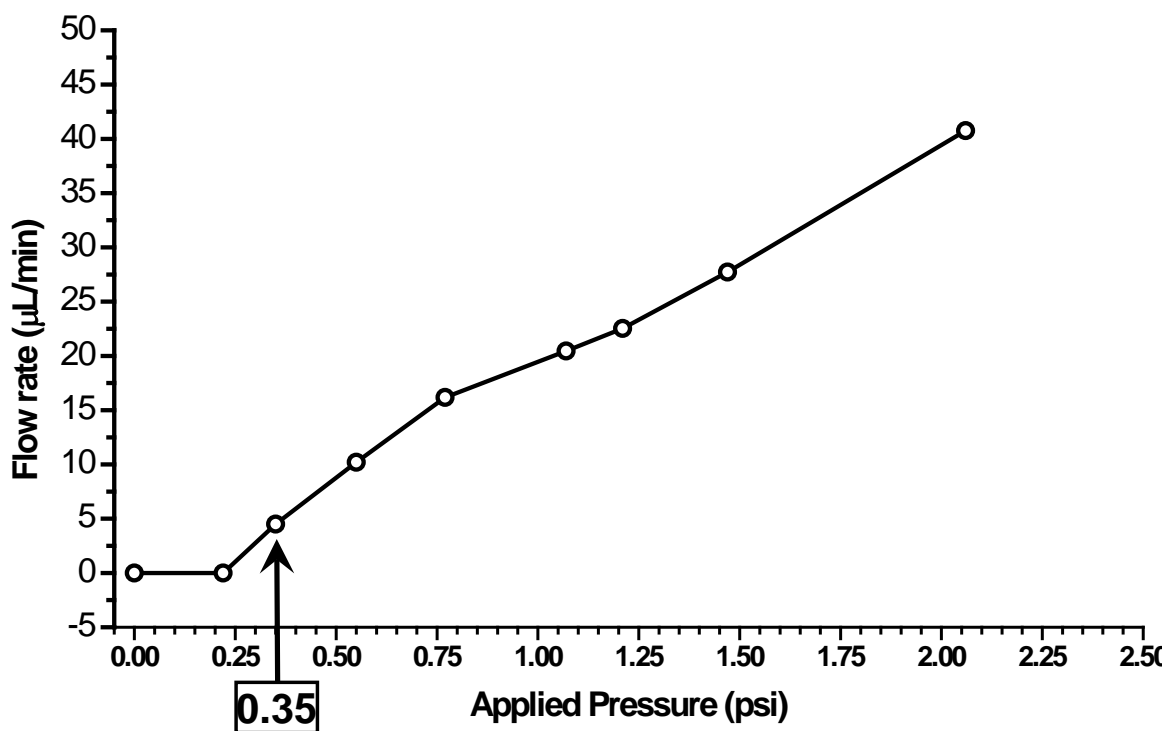


Figure 2-22: Testing result of the pop-up check-valve

After the popping process, a check-valve can be further annealed at  $140^{\circ}\text{C}$  to enhance the pre-stressed parylene-C tethers. Figure 2-22 shows the experimental result.

The cracking pressure of the check-valve is determined by the time when the liquid starts to flow. The flow characteristic is obtained with cracking pressure of 0.35 psi, verifying the feasibility of the pop-up check-valve. It is found that the flow-rate is similar to the check-valve shown in Figure 2-10, but with a lower cracking pressure in the pop-up check-valve. It is likely that the parylene-C base (the first layer parylene-C) is very easily damaged during the popping process. Besides, because the 10- $\mu$ m thick parylene-C base is still very flexible, the pre-stressed parylene-C tether would cause the parylene-C base to deform downward after the popping and thermal annealing. This causes smaller angle of the parylene-C tethers and therefore reduces the check-valve cracking pressure. Depositing thicker parylene-C base can solve the problem. In addition, coating a layer of metal would increase the Young's modulus of the parylene-C base and reduce the deformation amount caused by the pre-stressed parylene-C tethers.

## **2.6 Self-Stiction-Bonding Micro NC Check-Valves**

### **2.6.1 Design concept of the self-stiction-bonding NC check-valve**

Although the NC check-valve developed in Sections 2.3 to 2.5 has demonstrated the promising results of their capability of regulating the flow-rate, there still drawbacks exist in these NC check-valves. For the slanted check-valve utilizing the sloped sacrificial photoresist, it is more pricy to make the key gray-scale photo-mask. On the other hand, for the pop-up NC check-valve, the pop-up process might damage the parylene-C base easily and thus the yield rate is low. In this section, a NC check-valve is developed by manipulating the stiction phenomenon to create the necessary cracking pressure.

As shown in Figure 2-23, the self-stiction-bonding NC valve utilizes a stiction process that inevitably takes place after the drying process. According to theory [118–123], the parylene-C tether's length can be accurately designed for enough stiction while keeping the appropriate size of the micro NC check-valves. To generate enough stiction, the length of the parylene-C tether must be longer than the critical length of a cantilever beam which can be predicted as:

$$l_{crit} \geq \sqrt[4]{\frac{3}{16} \frac{Et^3 g^2}{\gamma_{la} \cos \theta_c}}, \quad (2-22)$$

where  $E$ , and  $t$  is the Young's modulus and the thickness of parylene-C, respectively.  $g$  is the gap spacing,  $\gamma_{la}$  is the surface tension of the liquid–air interface.  $\theta_c$  is the contact angle between the drying liquid and the parylene-C.

This self-stiction effect facilitates spontaneous anchoring of the NC check-valve with predetermined cracking pressure by pre-stressing the center sealing part of the check-valve through straight tethers connecting to the anchoring part, as shown in Figure 2-23. The built-in stress of the parylene-C tethers comes from both the residual tensile stress remained after thermal annealing, and stretching due to stiction bonding. Cracking pressure can be controlled by many parameters as described in Section 2.3.1. Similar to the NC check-valve structure aforementioned, flow-rate is defined by the size of the opening orifice and the opening gap of the parylene-C membrane. Furthermore, few holes are designed on the stiction-bonding parts where epoxy can be used to further ensure bonding strength and to prevent parylene-C from de-lamination after repeated operations, as shown in Figure 2-25 (b).

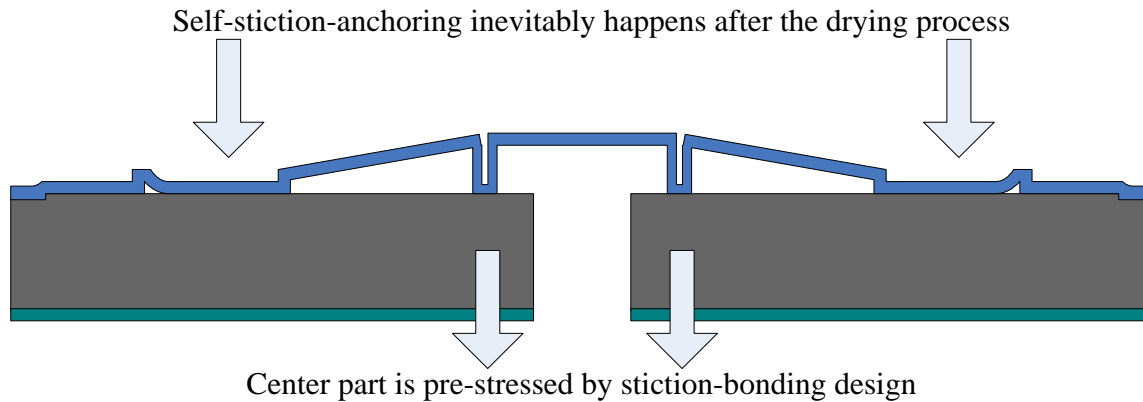


Figure 2-23: Schematics of the self-stiction-bonding NC check-valve

### 2.6.2 Fabrication of the self-stiction-bonding NC check-valve

The fabrication process started from growing thermal oxide on silicon wafer, as shown in Figure 2-24. Through-wafer holes and releasing trenches of the check-valves were etched using back-side DRIE until 50  $\mu\text{m}$  silicon membranes was left. The circular boundary of the valve seats were defined here with diameter to be 500  $\mu\text{m}$ , which can be fit into parylene-C protective tube's I.D. smoothly.  $\text{XeF}_2$  was used to roughen the front side surface encircling the check-valve area to improve the adhesion between deposited parylene-C and the silicon valve seat. The three-step exposure lithography was performed to create three different heights of sacrificial photoresist for the NC check-valve. After parylene-C deposition, RIE was used to pattern the coated parylene-C and then through holes and the releasing trenches were opened by completely etching away the remaining silicon membrane by DRIE so as to strip the sacrificial photoresist with acetone and IPA.

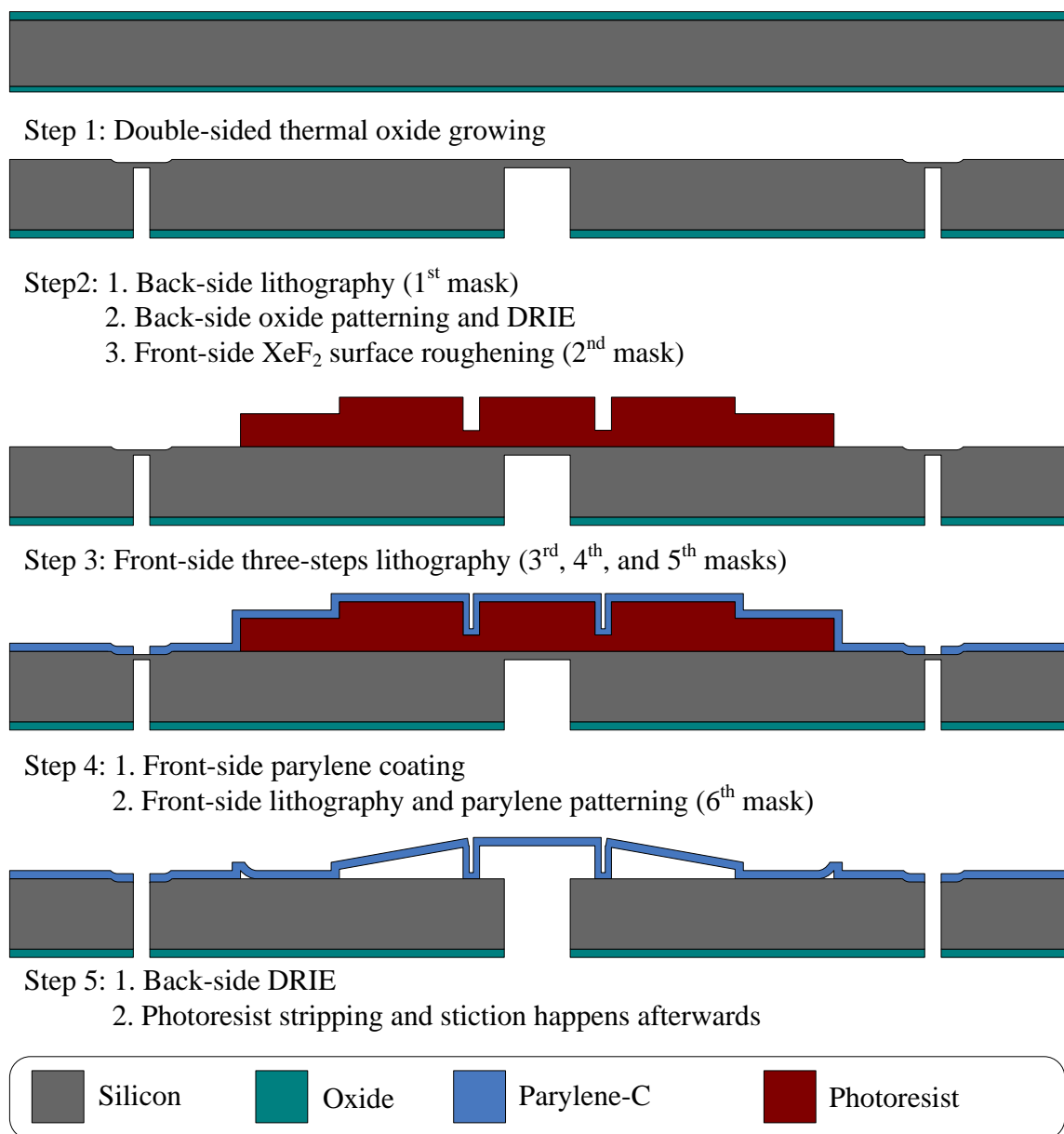


Figure 2-24: Fabrication procedures of the self-stiction-anchoring NC check-valve

Figures 2-25 (a) and (b) demonstrate the successful creation of the slanted parylene-C tethers through the self-stiction-bonding approach after the drying process. After photoresist stripping and air drying of the devices, stiction takes place on NC check-valves and the anchoring parts bonded onto silicon wafer surfaces, providing the necessary pre-stressed force through stretching the parylene-C tethers. The micrograph

of the fabrication result of the completed micro NC check-valve is illustrated in Figure 2-25 (c). To further enhance the bonding strength, tiny epoxy drops were then manually applied onto these NC check-valves' stiction-bonding parts to make sure the parylene-C won't de-laminate after several repeated operations, as shown in Figure 2-25 (d).

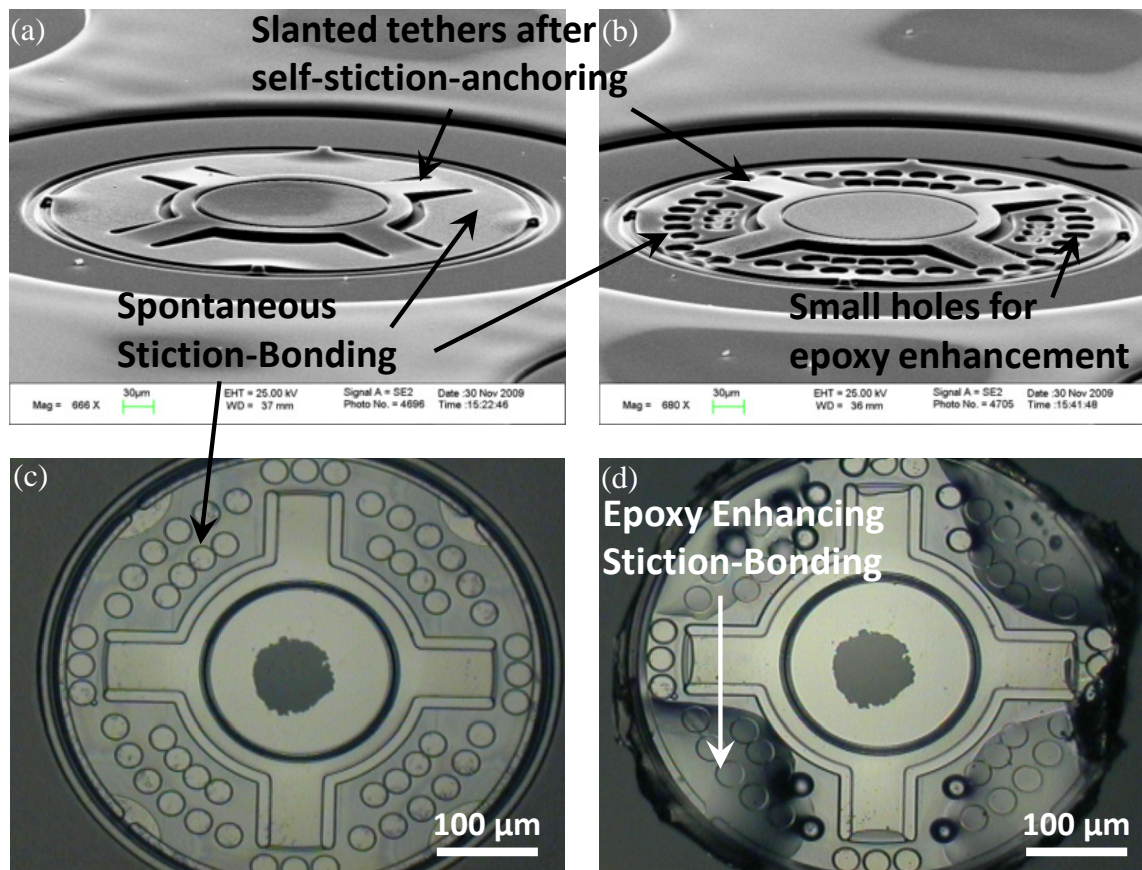


Figure 2-25: Fabrication results of the self-stiction-anchoring NC check-valves: (a) SEM picture showing the regular NC check-valve, (b) SEM picture showing the NC check-valve with small holes for epoxy enhancement, (c) top view of the NC check-valve, and (d) NC check-valve with epoxy bonding enhancement

### 2.6.3 Characterization of the self-stiction-bonding NC check-valve

To characterize the completed self-stiction-bonding NC check-valve, the same single check-valve packaging procedure as Figure 2-12 was adopted to accommodate

single NC check-valve in the capillary tube. On the other hand, the characterization setup represented in Figure 2-13 was also utilized to measure the NC check-valve's flow-rate profile. The pressure/flow-rate characteristic profile is shown in Figure 2-26. Liquid starts to flow at 0.2–0.3 psi (10–15 mmHg), and no obvious flow-rate is observed before the cracking pressure, showing that the sealing is well pressed by the four straight tether arms with the predetermined snapping force. This result meets our simulation expectation and provides the evidence that stiction does provide the required pre-stress force to create the cracking can secure the gap between the check-valve and the capillary tube opening.

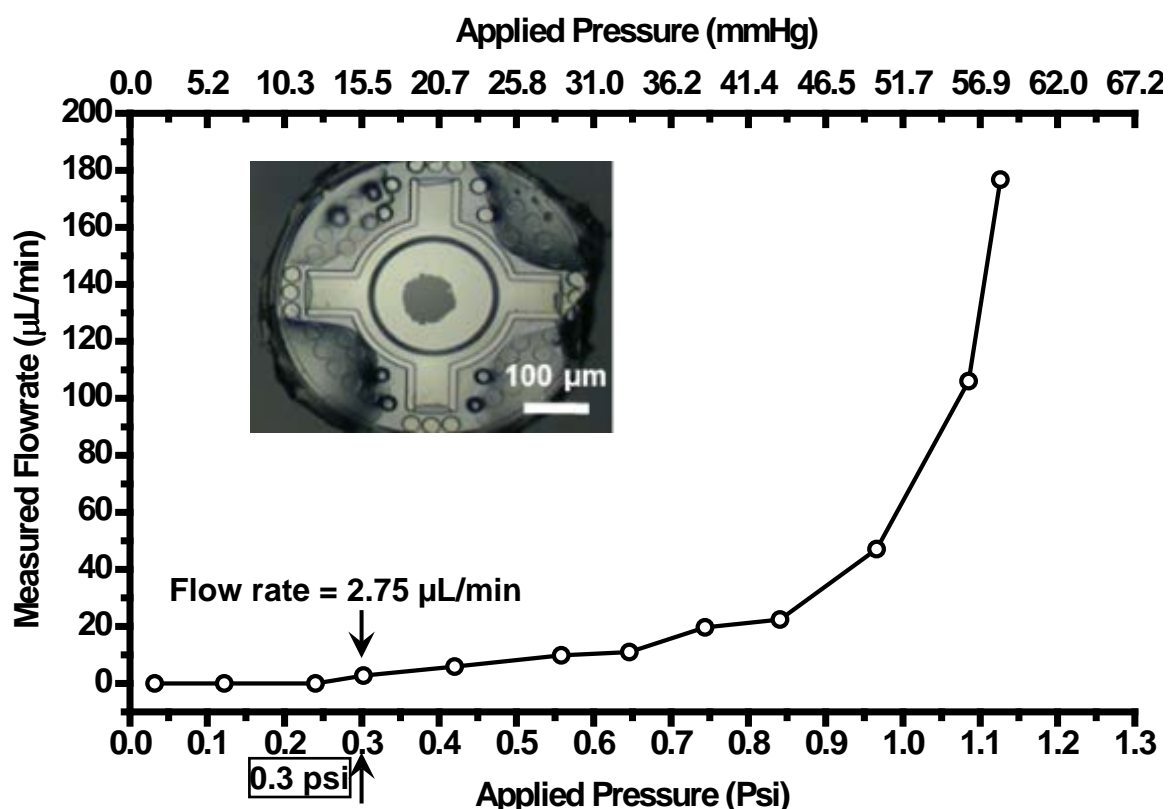


Figure 2-26: Pressure/flow-rate profile characterization results of the self-stiction-bonding NC check-valve

## 2.7 Blister Test of Stiction of Parylene-C Film

The self-stiction-bonding check-valve developed in Section 2.6 has demonstrated its successful regulating the microfluidic flow. However, since the cracking pressure of this check-valve is governed by stiction between the parylene-C film and the underlying substrate, a comprehensive study of stiction between parylene-C and different surfaces is required in order to understand, design, and create valves with specific cracking pressure and desired flow-rate profiles.

Stiction is an attraction that occurs between free standing micro-machined features and the substrate after the release of sacrificial photoresist [124]. Even though stiction is often an undesirable phenomenon, it can be employed to control the operation regime of thin film parylene-C check-valves. Attempts have been made to reduce stiction for specific check-valve geometries. For example, the cracking pressure of a polyimide check-valve with  $C_4F_8/Ar$  non-stiction coating changed from 210 kPa to 59 kPa [125], and SAM (self-assembled monolayer) is also used to reduce stiction [126].

The study in this section presents a comprehensive investigation of stiction between parylene-C and a variety of different surfaces using blister test. Blister test has been sophisticatedly used to measure the adhesion of two different materials and is capable to provide measurable results [127–137]. The surfaces under investigation include Au, Al, Si, parylene-C,  $XeF_2$  treated Si, and silicon dioxide. After quantifying surface stiction, possible mechanisms that lead to stiction between parylene-C and various materials are explained. In addition, different recipes for sacrificial photoresist release that may affect the resulting stiction are also explored. Stiction results for different surfaces under different photoresist releasing methods show that surface coating

and releasing procedures used in this investigation can be used to control characteristics of parylene-C check-valves.

### 2.7.1 Experimental approaches

An outline of the fabrication procedure for stiction test devices is depicted in Figure 2-28. A backside circular trench 300  $\mu\text{m}$  in diameter is created using DRIE until only a thin silicon membrane remains. Front side surface treatment is performed. These treatments include  $\text{XeF}_2$  roughening, gold (0.2  $\mu\text{m}$ ) and aluminum (0.25  $\mu\text{m}$ ) deposition, parylene-C coating (2.5  $\mu\text{m}$ ), and silicon dioxide growth (1  $\mu\text{m}$ ). After surface treatment, sacrificial photoresist and 5  $\mu\text{m}$  parylene-C layers are coated. Finally, DRIE is used again to remove the thin silicon film from the backside etching. Top views of the finished valves are shown in Figure 2-27.

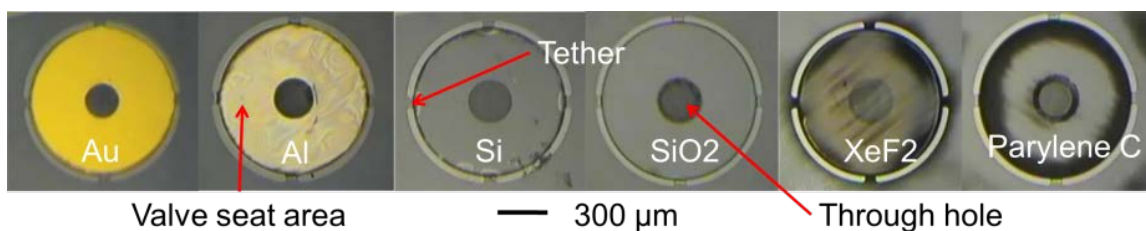


Figure 2-27: Top view of finished parylene-C check-valves fabricated for blister test

After dicing the wafer, different photoresist releasing methods are used. The sacrificial photoresist of all devices is released using ST-22, after which acetone is used to remove the ST-22 residue. Then, some valves are dipped in IPA (isopropyl-alcohol) and air dried. These valves are used for surface stiction characterization. Some valves are dipped in a mixture of acetone and 5 ml of silicone oil before air drying. These devices are used to study the effect of oil coating on parylene-C stiction. In addition, to

test the hypothesis of stiction mechanisms, some devices are subjected a 30 second HF (hydrofluoric acid) dip followed by a quick rinse in water to remove the acid. All devices are characterized using blister test.

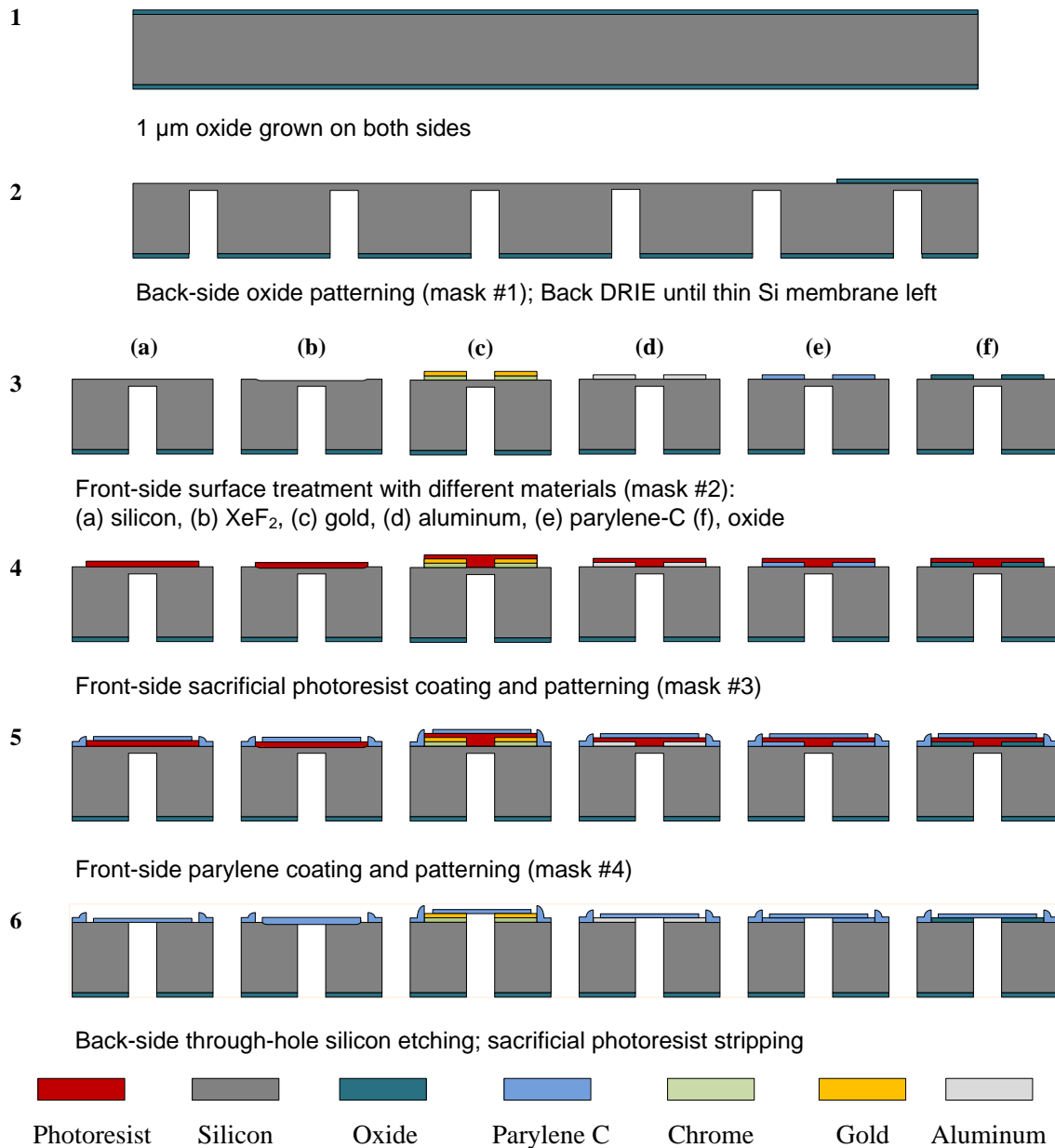


Figure 2-28: Fabrication procedures for circular parylene-C check-valve with different valve-seat surface treatments

### 2.7.2 Theory of blister test

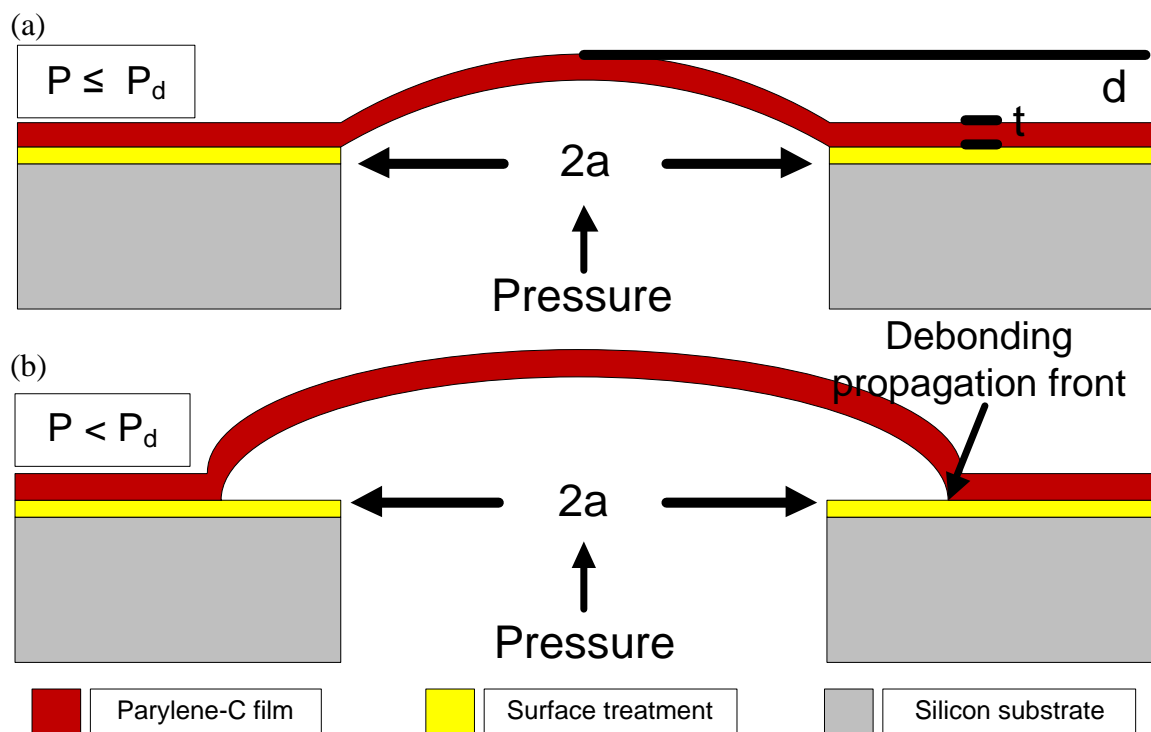


Figure 2-29: Theoretical blister formation during experimentation: (a) The applied pressure is less than or equal to the critical debonding pressure,  $P_c$ . (b) The applied pressure is higher than the critical debonding pressure,  $P_c$ ; the parylene-C film starts to propagate.

Blister test is usually performed on thin films overlying a solid substrate. Through holes are used to apply pressure to the film from the back side, as shown in Figure 2-29. When the applied pressure is less than the critical debonding pressure,  $p_d$ , the blister only buds up without any debonding. However, when the applied pressure is larger than  $p_d$ , parylene-C debonds from the silicon surface and propagate along the surface radially. For parylene-C check-valves, when pressure is applied, plastic deformation occurs in the parylene-C film that causes it to bulge to a distance  $d$  that is

dependent on the Young's modulus,  $E$  (~ 4 GPa), Poisson's ratio,  $\nu$  (~ 0.4 [138]), geometry of the substrate opening, and thickness of the parylene-C film,  $t$ .

Due to the circular *via* in silicon, it can be assumed that the blister has a semispherical profile. With this assumption, the critical debonding pressure can be first calculated as [137]:

$$p_d = \frac{3.56Et}{a^4} d_c^3 + \frac{4\sigma_o t}{a^2} d_c, \quad (2-23)$$

where  $d_c$  is the maximum vertical displacement of the parylene-C film,  $t$  is the thickness of the parylene film (3  $\mu\text{m}$  in our experiment),  $a$  is the radius of the blister (100  $\mu\text{m}$ ). With the obtained critical debonding pressure, the stiction between parylene-C and silicon surface,  $\gamma$ , can be derived by

$$\gamma = 2.22Et \left(\frac{d_c}{a}\right)^4 + 2.00\sigma_o t \left(\frac{d_c}{a}\right)^2, \quad (2-24)$$

where the constant  $\sigma_o$  represents residual stress within the parylene-C film. For this particular experiment where parylene-C is annealed at 100°C, 37.8 MPa is used as the residual stress [138]. As the pressure inside the blister exceeds the critical pressure,  $p_d$ , parylene-C film debonds from the silicon surface and the obtained  $p_d$  from eqn. (2-24) is used to calculate the stiction,  $\gamma$ .

### 2.7.3 Blister test experimental setup

During experimentation, each die is placed in a testing jig that allows fluid ( $\text{N}_2$  gas) to apply pressure to the parylene-C membrane. The jig is then connected to a fluidic setup consisting of a valve, a pressure regulator, and a pressure gauge, as shown in Figure 2-30. Figure 2-30 (a) shows the cross section view of the testing jig and Figure 2-30 (b) illustrates the overall view of the testing setup. The testing jig is placed under a

microscope for observation. Pressure inside the tubing is gradually increased by adjusting the pressure regulator. The pressure gauge reads out the current pressure inside the blister. The critical pressure is recorded when debonding occurs.

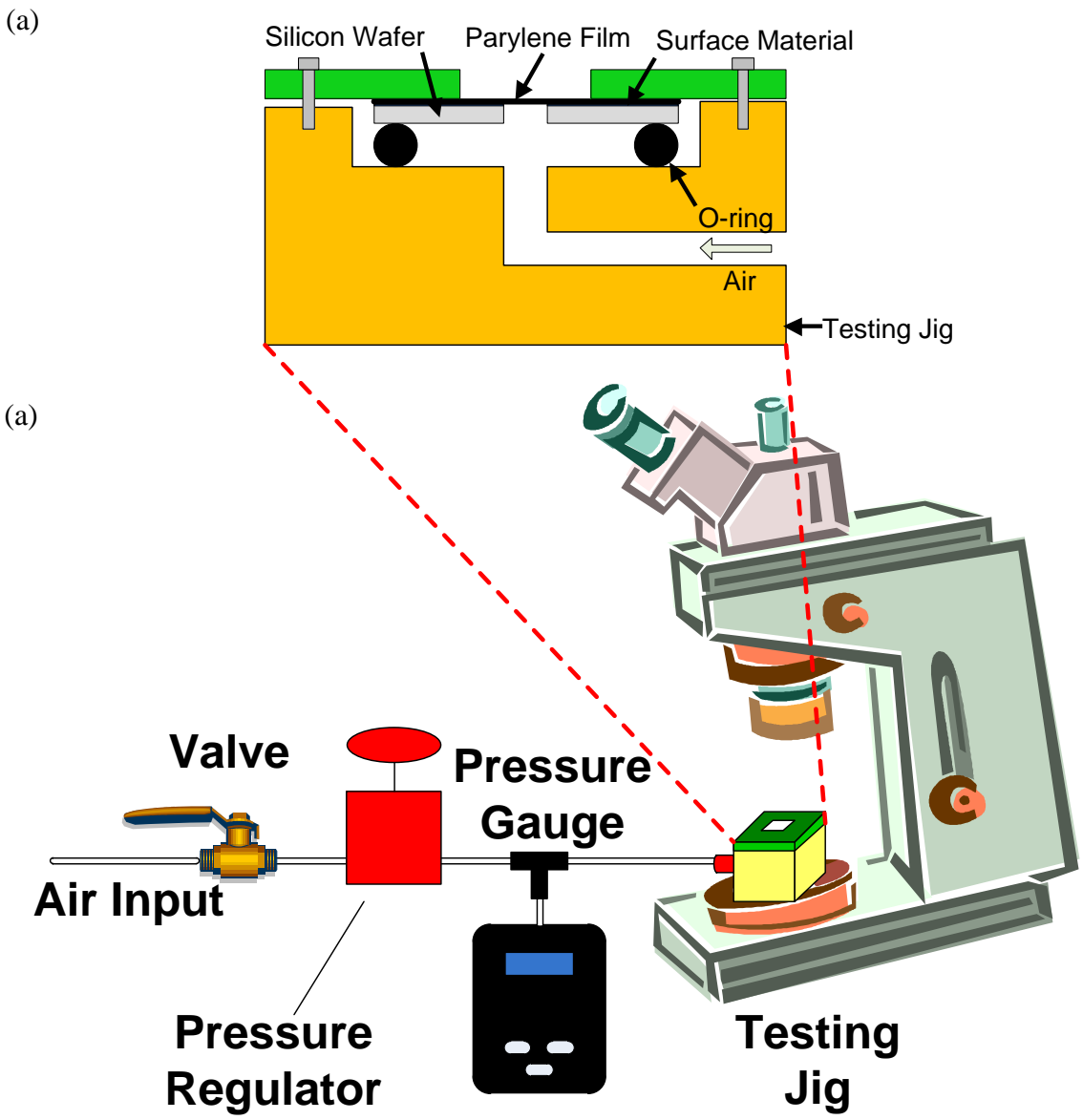


Figure 2-30: Experimental setup of the blister test: (a) the cross-section view of the test jig, and (b) schematic diagram of the testing setup

### 2.7.4 Testing results and discussion

A typical testing curve showing the relationship between the blister pressure and the passing time is shown in Figure 2-31. The parylene-C film starts to debond when the applied pressure is higher than the critical debonding pressure.

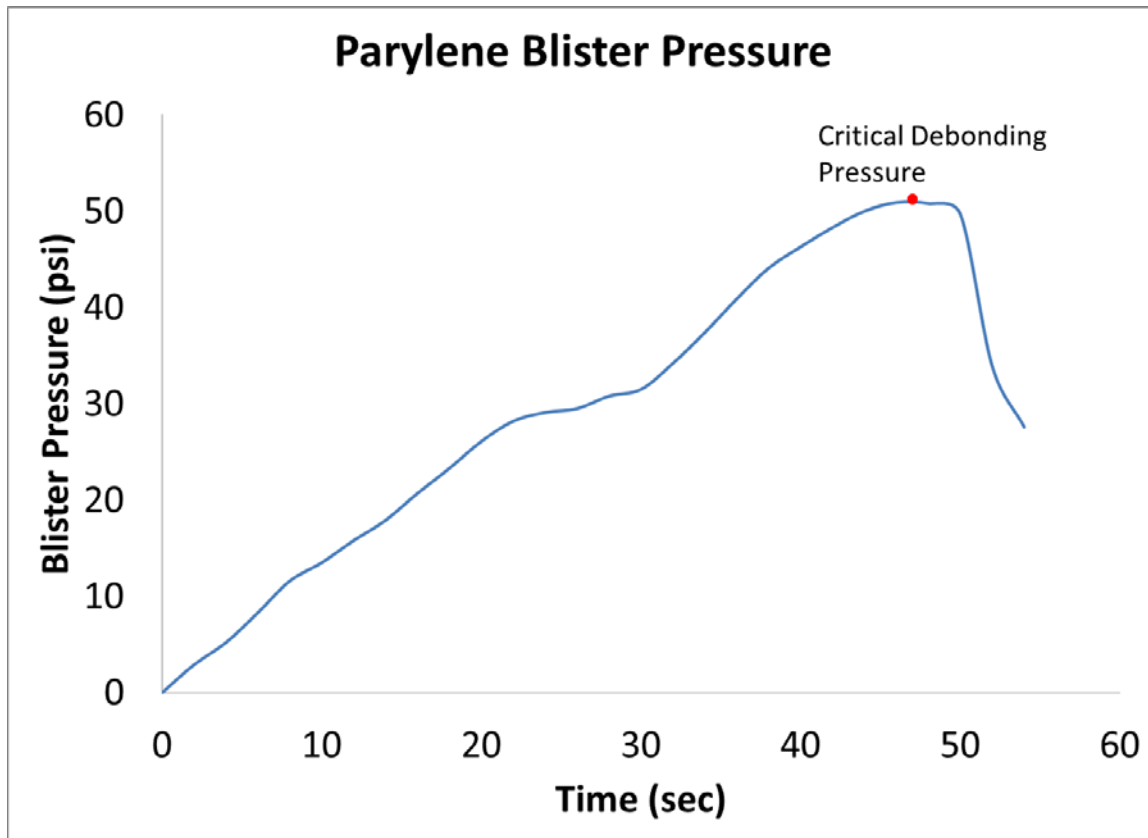


Figure 2-31: A typical curve of the blister test. The parylene-C film starts to debond when the applied pressure is higher than the critical debonding pressure.

Figure 2-32 illustrates the stiction between parylene-C and different surfaces after each device is soaked in acetone, IPA, and allowed to dry in air. In addition, the average cracking pressure of the valves is also recorded and listed in Table 2-2. The results show that Si has the greatest tendency to stick to parylene-C after drying ( $2.59 \text{ J/m}^2$ ). The high stiction of silicon to parylene-C can be explained by surface passivation. Even though

silicon and parylene-C are inherently hydrophobic, when they are subjected to water during photoresist release, the dangling bonds on the surface of the materials tend to bond to OH- groups in water. Such bonds make surfaces slightly hydrophilic. As the device dries, decreasing water content between the parylene-C film and silicon surface pulls the two surfaces together through hydrogen bonding, as illustrated in Figure 2-33. When the surfaces are extremely close from each other, Van der Waal's forces result in adhesion.

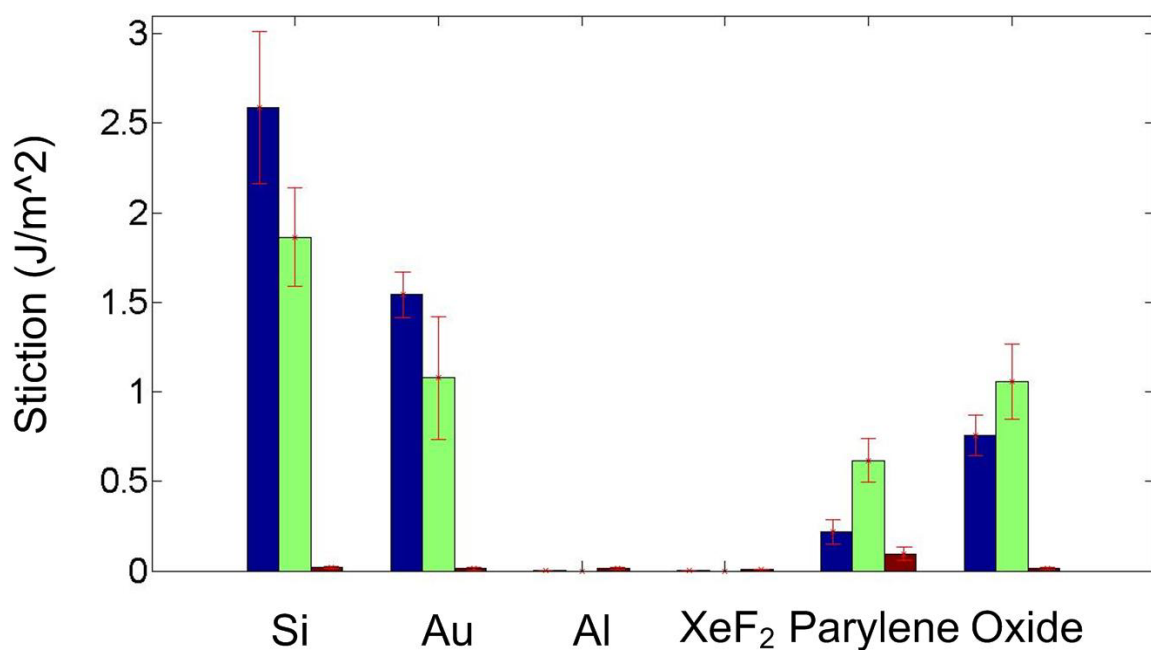


Figure 2-32: Stiction of parylene-C with different substrate surfaces after three kinds of releasing processes. Blue: acetone soak followed by IPA and water soak. Green: acetone soak followed by HF dip and water rinse. Red: soaking in mixture of acetone and silicone oil followed by direct air drying

Compared to Si, Au, oxide, and parylene all had gradually decreasing stiction to parylene-C. The decreasing values could be attributed either to increasing surface roughness or decreasing reactivity to OH- groups. Al and XeF<sub>2</sub> treated Si surfaces show almost no stiction to parylene-C. The former result can be attributed to the high surface

energy of aluminum, which precludes effective adhesion to most materials. On the other hand, XeF<sub>2</sub> treated Si surface display huge surface roughness. As a result, very little silicon surface actually come into contact with parylene-C. Thus, Van der Waal's force is not great enough to cause significant stiction.

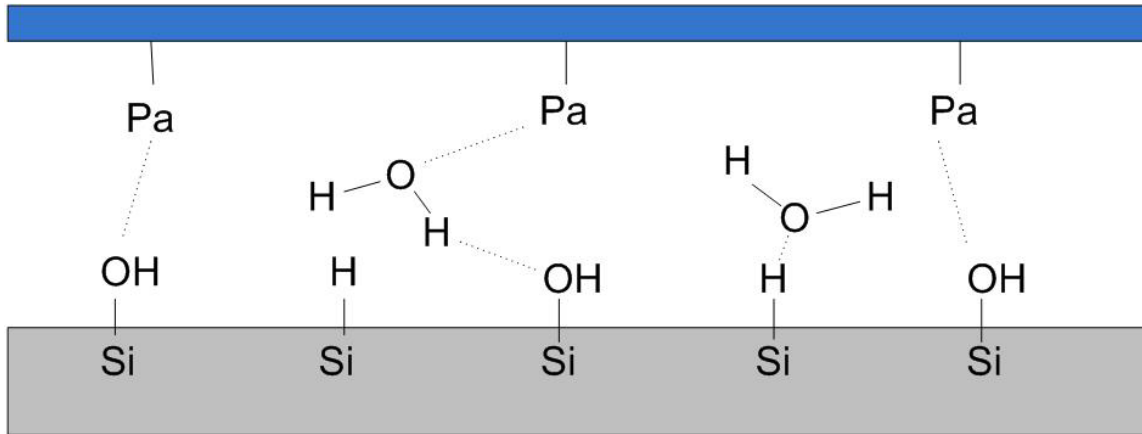


Figure 2-33: Hydrogen bonding that occurs between water molecules and the passivated silicon surface. As the device dries, decreasing water content between the parylene-C film and the silicon pulls the two surfaces together through hydrogen bonding.

Table 2-2: Cracking pressure of parylene check-valves under different releasing procedures: (1) acetone and IPA soak followed by air drying, (2) HF dip, water rinse, followed by air drying, (3) soak in a mixture of acetone and silicone oil before air drying. Zero stiction means that the stiction is too small to be measured effectively.

Release method	1 (J/m <sup>2</sup> )	2 (J/m <sup>2</sup> )	3 (mJ/m <sup>2</sup> )
<b>Si</b>	2.59	1.86	18.5
<b>Au</b>	1.54	1.07	12.5
<b>Al</b>	0	0	13.2
<b>XeF<sub>2</sub></b>	0	0	8.2
<b>Parylene</b>	0.22	0.62	95.6
<b>Oxide</b>	0.76	1.06	13.9

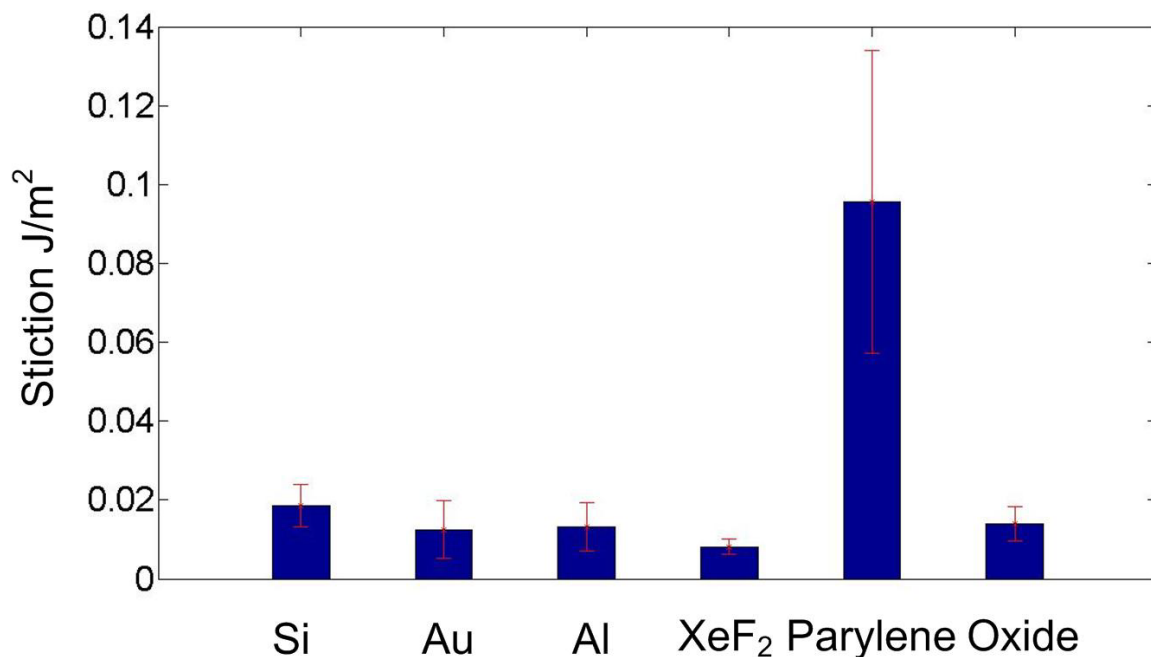


Figure 2-34: Stiction between parylene-C and various surfaces after releasing in a mixture of acetone and silicone oil

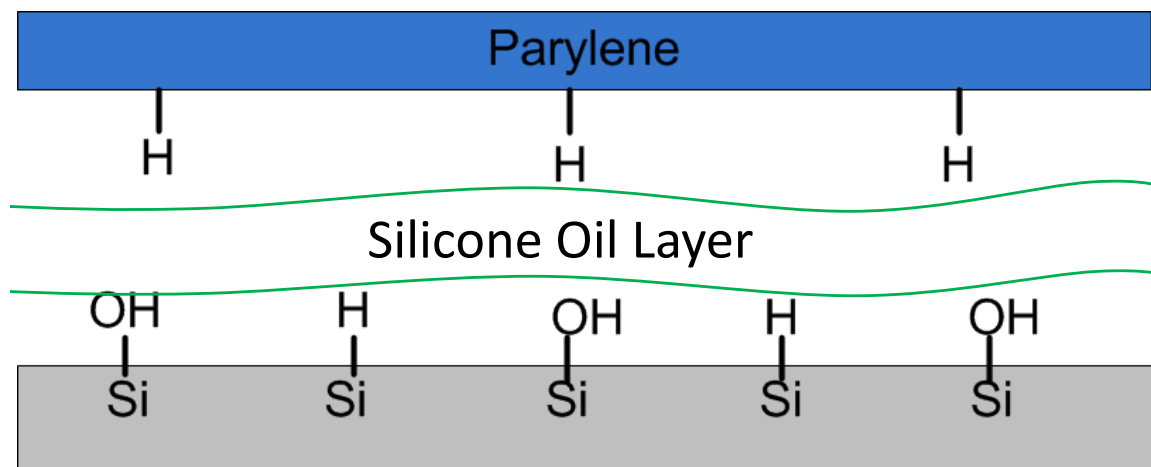


Figure 2-35: Stiction between the parylene-C and the silicon surface is reduced due to the silicone oil layer, which reduces surface passivation and the proximity between surfaces.

Following the second photoresist releasing method where devices are air dried after soaking in a mixture of acetone and silicone oil, stiction between parylene-C and all

surfaces are reduced, as shown in Figure 2-34. Results show that, other than parylene-C, all stiction values are between 0.01 and 0.02 J/m<sup>2</sup>. These results suggest that, after silicone oil coating, stiction is no longer caused by the interaction between parylene-C and substrate surfaces but by the adhesion between parylene-C and the oil layer. Since this oil layer reduces surface passivation and the proximity between surfaces, stiction is decreased, as shown in Figure 2-35. The relatively high stiction value between two parylene-C surfaces can be explained by the roughness of the parylene surface, which increases its effective area to interact with silicone oil.

In order to verify the proposition that surface passivation contributes to stiction, some devices are subjected to a short HF dip before drying. This HF dip should remove some surface –OH bonds and thus reduce stiction. Results from blister tests done on these valves reveal that for certain material surfaces (i.e., Si and Au), HF dip does decrease stiction slightly, as shown in Figure 2-32. Even though HF dip removes much of the hydroxyl groups, the ensuing rinse in water probably introduces some –OH groups back. As a result, stiction still remains.

### **2.7.5 Summary**

This study successfully quantifies stiction between thin film parylene-C and various surfaces. Devices with valve configurations were fabricated and released using various procedures. After performing blister tests, stiction values were recorded. The mechanisms that lead to stiction or the reductions thereof include surface passivation with hydroxyl groups, surface roughness, and surface proximity. Experiments show that mechanisms that can reduce the proximity between parylene-C and other surfaces during drying will likely reduce stiction. In addition, since different surface treatments result in

different stiction, all processes and photoresist releasing methods from this study can be used to design parylene-C check-valves with different cracking pressures.

## **2.8 Summary and Conclusion**

### **2.8.1 Comparison of different types of micro check-valves**

In this chapter, a parylene-C-based NC check-valve paradigm was proposed and developed. The standard NC check-valve structure consists of slanted parylene-C tethers with built-in residual tensile stress. These pre-stressed slanted parylene-C tethers provide the necessary downward force, giving the desired cracking pressure of the NC check-valve.

Three different methods were developed to create the slanted tethers. The first method adopted the gray-scale photolithography to generate the sloped sacrificial photoresist as the mold of the following deposited parylene-C film. The second approach utilized the post-fabricated pop-up structural design to generate the desired slanted tethers. The third method adopted the stiction phenomenon that inevitably takes place after the drying process to create the slanted slope created using height differences of the parylene-C structure. The residual stress built in the parylene-C tethers can be achieved by stretching the tether, thermal annealing and quenching afterward, or combination of both. The cracking pressure can be manipulated by several parameters such as the number of the slanted tethers, the sloping angle of the slanted tethers, the geometry of the slanted tethers (the width and the thickness), and also the residual stress of the slanted tethers which can be controlled by the annealing temperatures. Table 2-3 shows the comparison of all different check-valves introduced in this chapter. It can be seen that thermal annealing are capable of providing the highest cracking pressure (2.9 psi) among

the three kinds of slanted tether NC check-valves. Therefore, NC check-valves pre-stressed by thermal annealing is suitable for high-pressure applications. In addition, to obtain even higher cracking pressure system, multiple NC check-valves can be integrated in series to meet the request of the extremely high cracking pressure applications. The characterization results demonstrated the additivity property of the integration of multi NC check-valve's cracking pressure. On the other hand, NC check-valves pre-stressed only through pop-up mechanism or self-stiction bonding mechanism are appropriate for the applications where low cracking pressure usage is needed.

Table 2-3: Comparison of different slanted tether parylene-C NC check-valves introduced in this chapter. Water was used as the working fluid.

<b>Check-valve type</b>	<b>NC</b>	<b>NC</b>	<b>NC</b>	<b>Integration of multiple NC in series</b>
Creation of slanted tethers	Gray-scale lithography	Post-fabrication pop-up	Self-stiction bonding	---
Cracking pressure (psi)	0.3–2.9	0.35	0.3	2.06 (Combining for four NC check-valves)
Breakdown pressure (psi)	> 25	> 25	> 25	> 25

In addition, a study of parylene-C stiction to several different kinds of surfaces was performed by utilizing the blister test in this chapter as well. Experimental results showed that the stiction strength of parylene-C to other surfaces would be influenced by the surface with hydroxyl groups, surface roughness, and surface proximity.

### **2.8.2 Lifetime of the slanted tether NC check-valves**

Because parylene-C served as the main structural material of the NC check-valves developed here, it begs the question of how long the residual tensile stress would last within the parylene-C tethers. The question is actually related to the viscoelastic/viscoplastic properties of parylene-C, which has rarely been explored in the past. Therefore, the creep and stress relaxation behavior and other types of viscoelastic/viscoplastic properties of the parylene-C will be discussed at length in chapter 5.



---

# CHAPTER 3

---

## INTEGRATION AND APPLICATIONS OF MICRO CHECK-VALVES FOR GLAUCOMA TREATMENT

Glaucoma drainage device (GDD) has been developed as an alternative solution to treat glaucoma patients who are resistant to normal glaucoma medications. This chapter presents the integrated parylene-C-tube-type micro-valved glaucoma drainage device incorporating micro-flow regulatory assembly, parylene-C protective tube and anchors. All components are designed to fit in a needle-implantable form factor for suture-less minimally invasive implantation through subconjunctival hypodermic needle injection.

A successful GDD can continuously drain out excess aqueous humor accumulated inside the anterior chamber and lower the intraocular pressure (IOP) to the range of 10–20 mmHg. On the other hand, to prevent hypotony happening, aqueous humor should be preserved inside the anterior chamber when a spike of high eye pressure happens (due to external impact). To accommodate these functions, a dual-valved GDD system capable of creating a “band-pass” pressure/flow-rate profile is proposed in this chapter. The parylene-C-tube-type GDD paradigm is developed to incorporate one normally closed (NC) and one normally-open (NO) valve that can regulate intraocular pressure (IOP) passively with no power consumption. The self-stiction-bonding NC check-valve which

has been introduced in Section 2.6 is adopted in this chapter to form the GDD due to its appropriate cracking pressure range. The NO valve will be further developed in Section 3.2 to complete the form factor of the proposed GDD system.

In addition, two types of “band-pass” micro-flow control assemblies are designed and developed to explore the different possibilities of the check-valve positions. The basic GDD type has both NC and NO valves fixed at the both ends of the parylene-C protective tube, while the modified GDD has a micro-flow regulating assembly which has adjustable distance of NC/NO valves. The adjustable NC/NO valves’ distance enables ophthalmologists to optimize the check-valve positions in the GDD through *ex vivo/in vivo* implantation tests. In this section, a NO valve will be first introduced for later dual-valved GDD development.

In terms of the clinical implantation, the subconjunctival implantation with needle-inserted and suture-less surgical procedures is proposed for the new parylene-C-tube GDD. The biocompatible parylene-C-tube-type GDD can be minimally-invasively implanted under the conjunctiva using a #19-gauge hypodermic needle. A parylene-C fixation anchor is also developed to help the GDD anchor subconjunctivally after the implantation. The integrated GDD is first bench-top characterized and then delivered to the hospital for further *ex vivo* test to understand its biomedical feasibilities. Both bench-top *ex vivo* implantation results are shown and discussed in Sections 3.5 and 3.6, respectively.

### 3.1 Configuration of the “Band Pass” Flow-Rate Profile Dual-Valve GDD System

As shown in Figure 3-1, an ideal glaucoma drainage device should be capable of regulating the IOP to be below 20 mmHg while not causing hypotony (i.e., IOP < 5 mmHg) with time. Besides, the device should be closed if high IOP (e.g., > 50 mmHg) happens due to normal external interferences like eye rubbing or bumping. To realize the concept of this “band-pass” pressure/flow-rate profile, a dual-valve GDD system is proposed with an innovative micro-flow control design: one NC check-valve is chosen to achieve the necessary low-pressure-off response and one NO valve is chosen to behave as a high-pressure stopper.

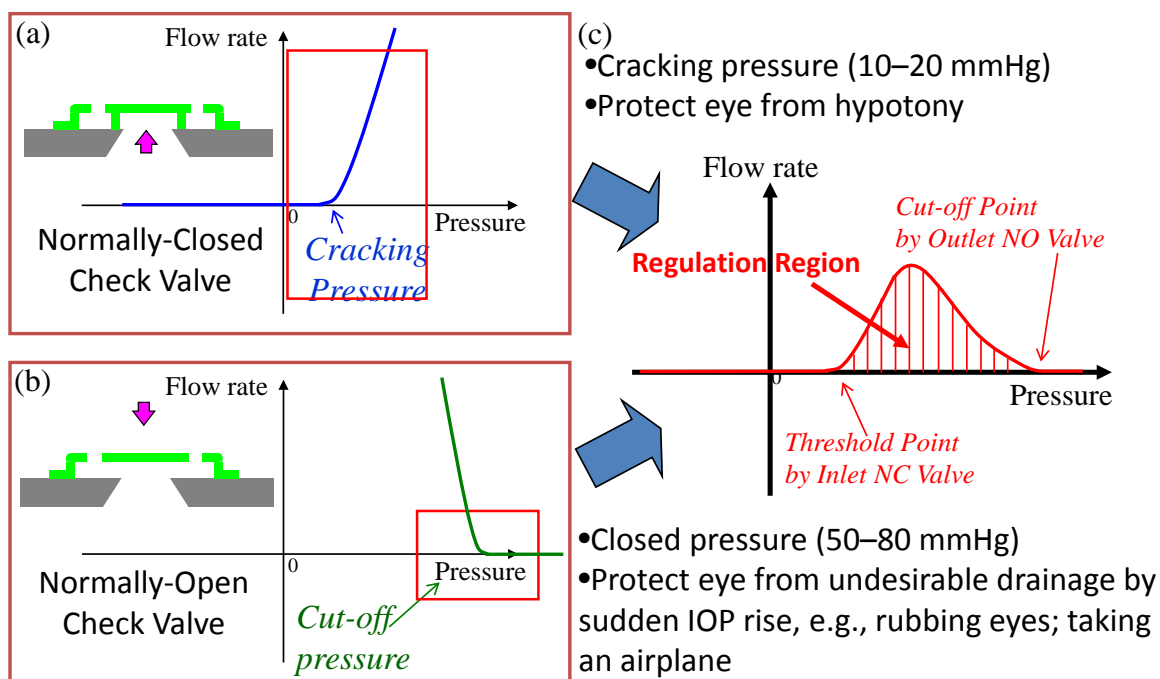


Figure 3-1: Concept of the “band pass” flow-rate profile of the proposed GDD system comprising (a) an NC check-valve, and (b) an NO valve to achieve (c) a band pass flow-rate profile

### 3.1.1 Dual back-to-back valves design

The dual NC/NO parylene-C-valves system artificially regulate the intraocular fluid drainage without any external power consumption, thus controlling the IOP drainage profile of glaucoma patients. Therefore, it is ideal to have dual back-to-back valves consisting of an opened normally closed (NC) check-valve above 20 mmHg and a closed normally-open (NO) valve above 50 mmHg in series in order to realize the desirable pressure/band-pass flow regulation. The back-to-back configuration also prevents the GDD from water leakage if the fluid flows in the opposite direction.

To regulate the flow as a “band-pass” flow profile, Chen had demonstrated an on-chip surface-micromachined parylene-based dual-valve system which can achieve the flow regulation in the required ranges compatible with IOP regulation specification [139]. Besides, another approach also reported by Chen to regulate the flow as the same flow profile by a single parylene-C micro-valve adopting the floating-disk mechanism with a two level valve seat design [140]. However, these approaches required complicated processing. In the case of vacuum-collapsed sealing check-valve, the cracking pressure might drift with time because of gas permeation into the vacuum cavity. In addition, to accomplish a stand-alone implantable device, the micro check-valves must be extensively released and packaged into a capillary tube to become a real valve-in-tube system for real device implantation.

Furthermore, their integration with appropriate surgical components for fixation is also necessary for its practical applications. In 2007, Chen also reported the concept and successful experiments of using the surgical features in the proposed device in MicroTAS07 to anchor the biomedical device in human body tissue [141]. Therefore, the

new GDD system would attempt to integrate the dual-valved tube with the surgical features as the fixation anchor to address the dislodging problem after the device implantation.

### **3.1.2 Numerical simulation of the glaucoma drainage device**

To define the geometry of the check-valves, the mechanical properties and the pressure/flow-rate characteristics of the check-valves were simulated using COMSOL Multiphysics™ to select the appropriate thickness and tether lengths of the NC check-valve. The check-valve outer diameter is restricted to be within 500  $\mu\text{m}$  so that the overall GDD size can be fit into gauge #19 needle, which inner diameter is 690  $\mu\text{m}$ . The cracking pressure of the NC check-valve is defined as 15 mmHg during the simulation. The flow-rate is also assigned as 2–3  $\mu\text{L}/\text{min}$  to meet the required drainage rate of the aqueous humor [1].

The optimization of the check-valve flow characteristics is a complicated multiphysics simulation problem, which originally has to find out the linking equation between solid mechanics and fluidic dynamics. To overcome the problem, therefore, the simulation was separated to two easier simulations. One solid mechanics simulation is performed to understand the deflection of the covering plate versus the applied pressure, as shown in Figures 3-3 (a) and (c) for NC and NO valves, respectively. The other fluidic dynamics simulation was followed to understand the flow-rate versus different gap of covering plate openings, as shown in Figures 3-3 (b) and (d) for NC and NO valves, respectively. Once the geometry had been defined, the flow-rate of GDD system combining both NC and NO valves was simulated, as illustrated in Figure 3-3 (e). The simulations are iterated to verify the optimal geometry. The optimal design can be

selected for later fabrication based on the obtained simulation flow-rate results, as demonstrated in Figure 3-3 (f).

## 3.2 Design, Fabrication, and Test of the Normally Open Valve

### 3.2.1 Design of the NO valve

In this section, a NO valve is developed to accomplish the GDD's requirement of automatically off when the IOP is higher than the designed pressure. A cross section view of the NO valve design is shown in Figure 3-2. In NO valve design, the twisted-arm tether length is carefully designed while considering stiction to guarantee free-standing valve membrane after photoresist releasing [119–121]. The critical radius,  $r_{crit}$ , that the parylene-C membrane will not adhere to the substrate surface after the drying process can be predicted as:

$$r_{crit} = 1.7 \sqrt[4]{\frac{3 Et^3 g^2}{16 \gamma_{la} \cos \theta_c}}, \quad (3-1)$$

where  $E$ , and  $t$  is the Young's modulus and the thickness of the deflection material, respectively.  $g$  is the gap spacing;  $\gamma_{la}$  is the surface tension of the liquid–air interface, and  $\theta_c$  is the contact angle between the drying liquid and the deflection material. In addition, sealing trenches are added in the free-standing membrane of the NO valves to avoid stiction and also to improve its high pressure sealing behavior.

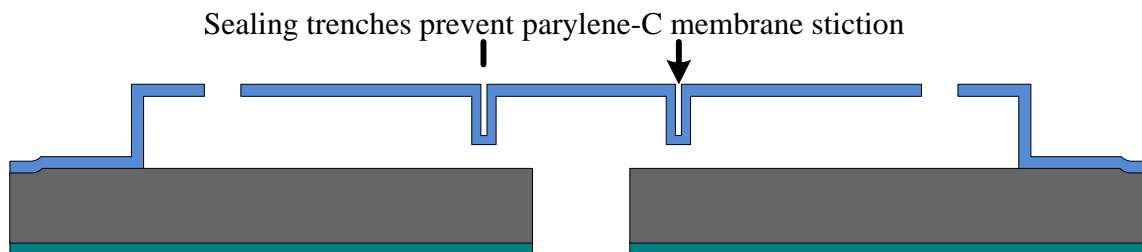


Figure 3-2: The cross section of a normally open check-valve

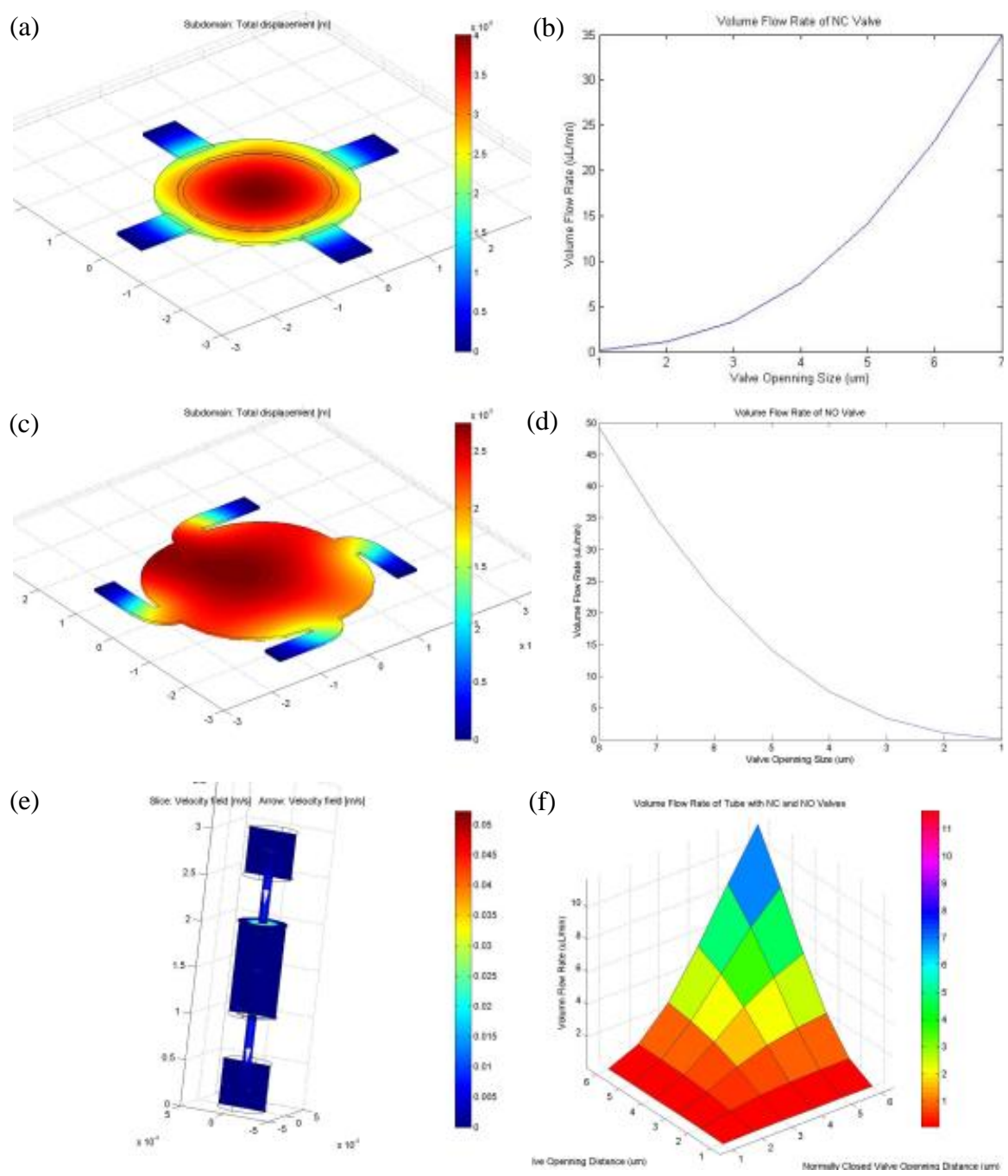


Figure 3-3: COMSOL Multiphysics™ simulation of the dual-valved GDD system: (a) deflection simulation of the NC check-valve, (b) flow-rate simulation results of the NC check-valve, (c) deflection simulation of the NO valve, (c) flow-rate simulation results of the NC check-valve, (e) flow-rate simulation of the dual-valved GDD system, (f) flow-rate simulation results of the dual-valved GDD system

### 3.2.2 Fabrication of the NO valve

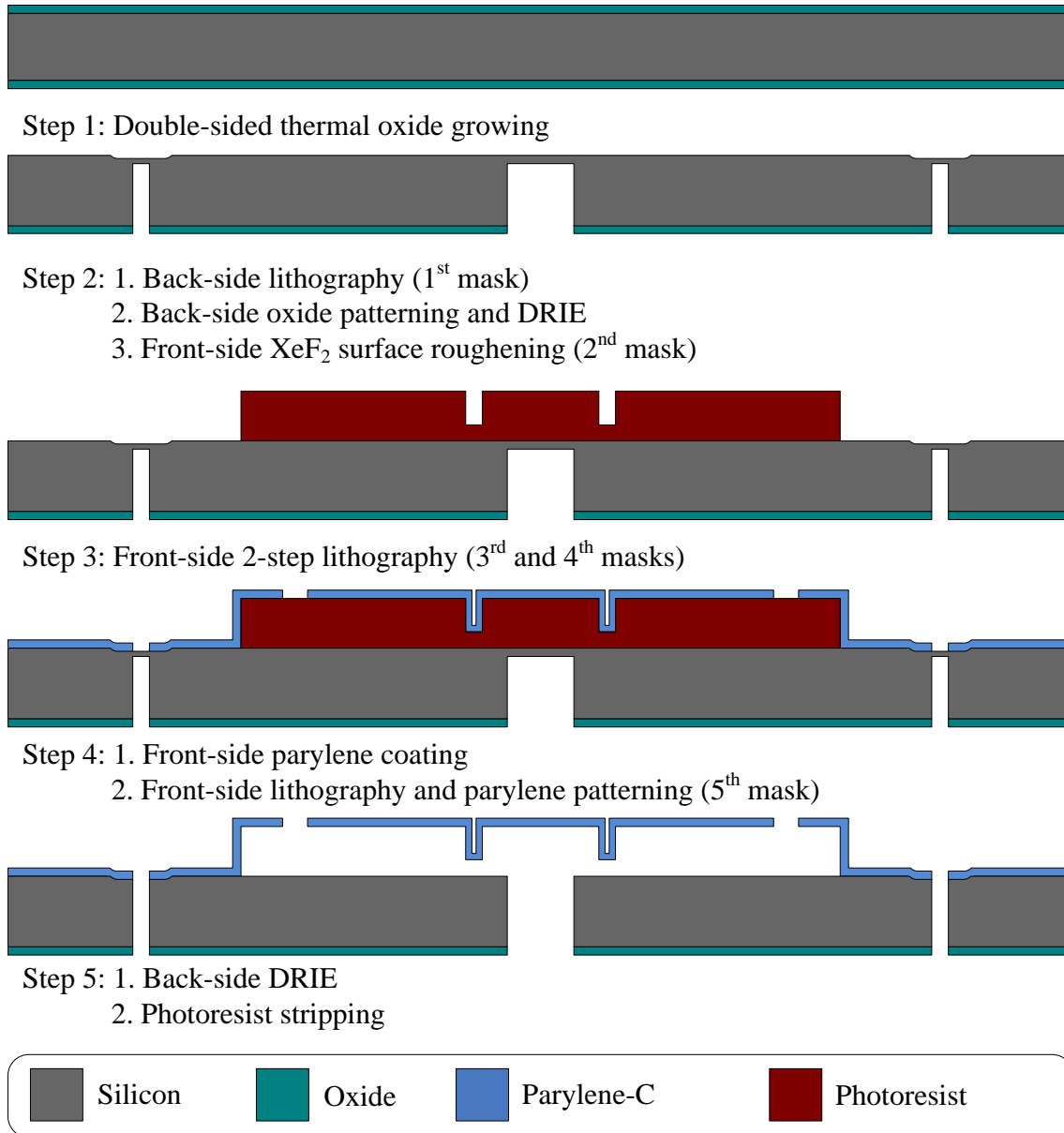


Figure 3-4: Fabrication procedures of the NO valve

The fabrication process started from growing thermal oxide on the silicon wafer surface, as shown in Figure 3-4. Through-wafer holes and releasing trenches of the check-valves were etched using backside DRIE until 50  $\mu\text{m}$  silicon membranes was left. The circular boundary of the valve seats were defined here with diameter to be 500  $\mu\text{m}$ ,

which can be fit into parylene-C protective tube's I.D. smoothly.  $\text{XeF}_2$  was used to roughen the front side surface to improve the adhesion between parylene-C and the silicon valve seat. Two-step exposure lithography was performed to create two different heights of sacrificial photoresist for the NO valve, where the lower photoresist was the location of the sealing trench of the parylene-C membrane. After parylene-C coating, RIE was used to pattern the coated parylene-C and then through holes and the releasing trenches were opened by completely etching away the remaining silicon membrane using DRIE to strip the sacrificial photoresist with acetone and IPA. The fabrication results are shown in Figure 3-5.

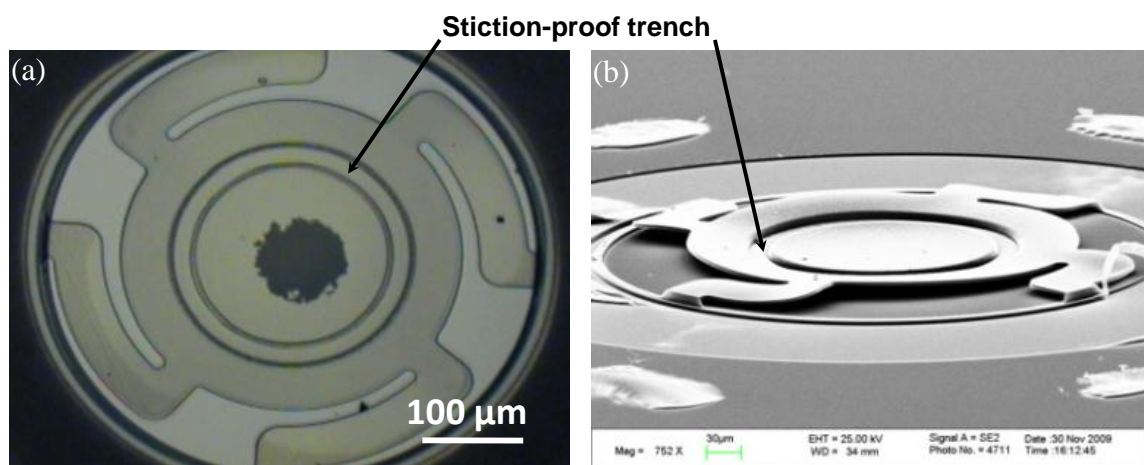


Figure 3-5: Fabrication results of the NO valve: (a) top view of the NO valve, and (b) SEM picture of the NO valve

### 3.2.3 Characterization of NO valve

Similar to the characterization procedures for the NC check-valves aforementioned in chapter 2, single NO valve was first packaged by the packaging procedure as Figure 2-12, and then characterized by the setup shown in Figure 2-13. The

pressure/flow-rate characteristic profile is demonstrated in Figure 3-6. It is found that no significant cracking pressure was obtained during tests, and fluid in NO valve flows smoothly before pressure reaches the high limit. The flow-rate starts to decrease when the pressure goes up to 0.5 psi (~ 25 mmHg) and almost closes after 1.12 psi (~ 56 mmHg). The leak rate is less than 5  $\mu\text{L}/\text{min}$ . This result proves that the sealing trench designed on NO valve does seal the NO valve orifice. The small amount of leak rate may be due to the non-flat bottom under the sealing trench which comes from the top surface of the sacrificial photoresist layer.

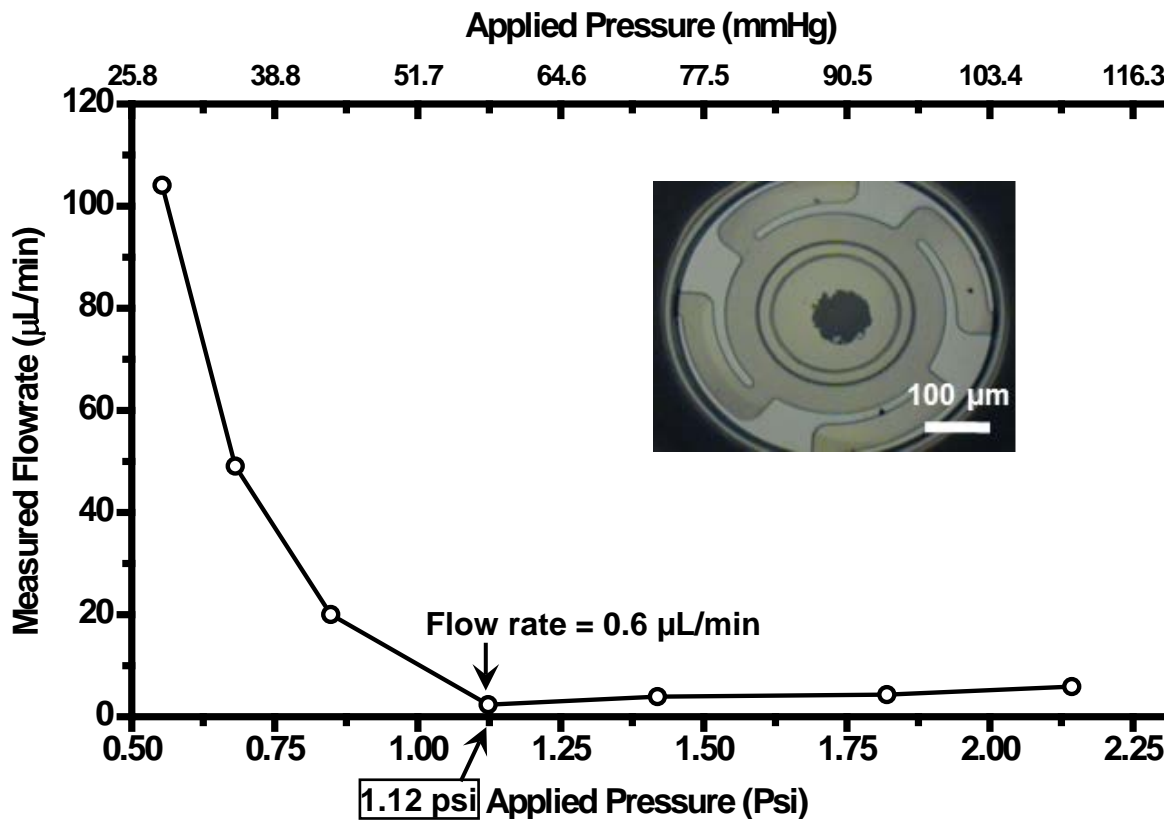


Figure 3-6: Pressure/flow-rate profile characterization results of the NO valve

### 3.3 Sutureless, Minimally Invasive Implantation of the Dual-Valved GDD

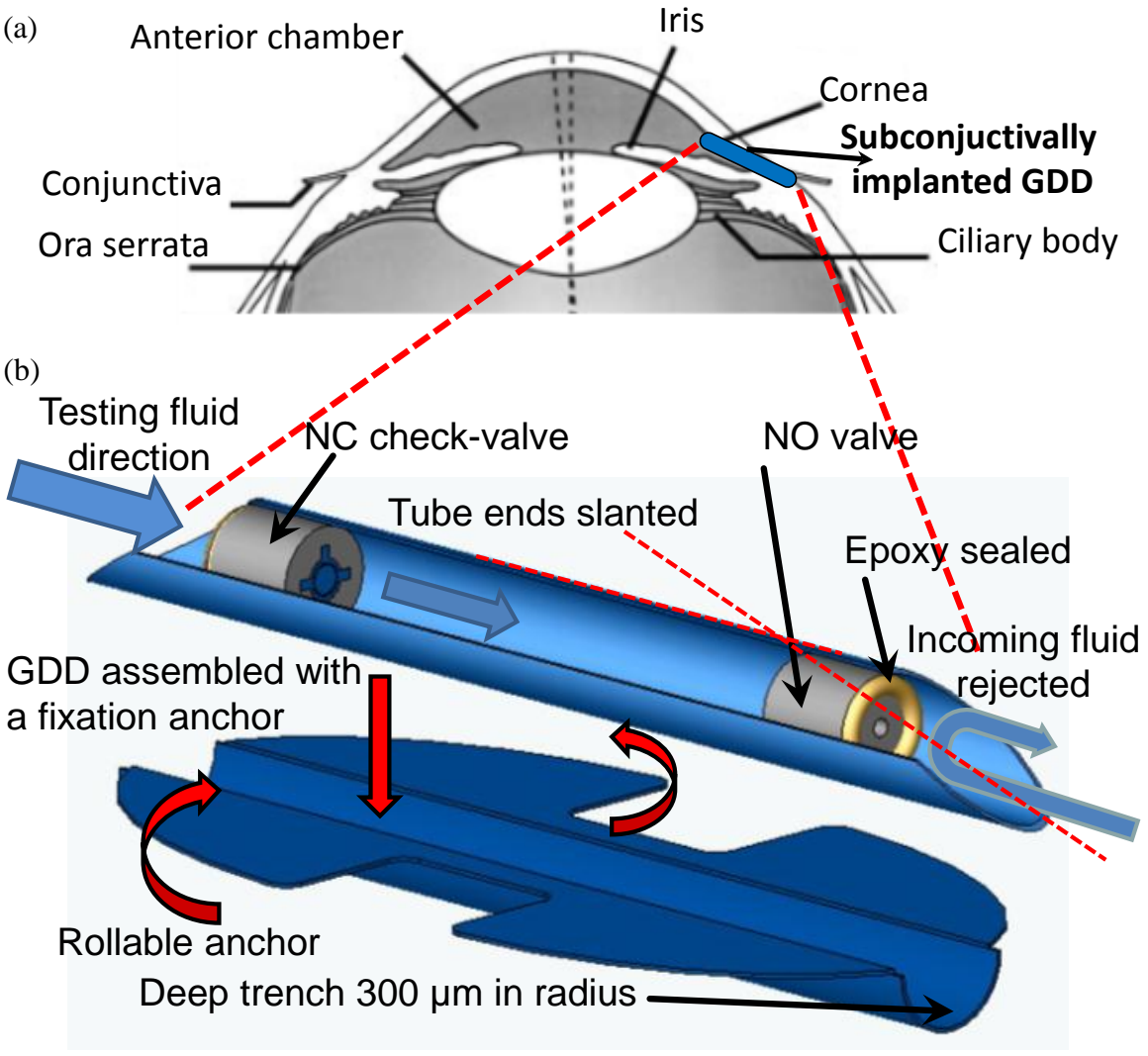


Figure 3-7: Concept of the minimally invasive implantation: (a) Subconjunctival implantation idea of the (GDD) implanted through the anterior chamber of the eye. (b) A complete GDD system consisting of a dual-valve micro-flow regulation system (one NC check-valve at one end of the tube and one NO valve on the other end of the tube), a parylene-C protective tube carrier, and a rollable/foldable anchor

### 3.3.1 Dual-valved GDD out-shape

A subconjunctival needle implantation would be executed to mimic the normal aqueous humor drainage pathway, as shown in Figure 3-7 (a). As such, the shape and length of the capillary tubes are carefully designed so that the implantation can be performed using a specific plunger-in-needle introducer setup. As aforementioned, the outer diameter of the GDD must be designed smaller than the inner diameter of the implantation hypodermic needle. The front end of the tube is tapered for convenient device placement after injection. The length is chosen so that the back end of the tube is observable through cornea during surgery. This surgical procedure can be completed within 10 min. In addition, no suture is required after implantation is done, greatly simplifying surgery process.

### 3.3.2 Dual back-to-back valve configuration

As shown in Figure 3-7 (b), a complete implant comprises a dual-valve micro-flow regulation system in a tube with integrated flexible tissue anchors. Dual back-to-back micro valves system with one check-valve normally closed but open at 20 mmHg and the other valve normally open (NO) but closed beyond 50 mmHg is designed to fulfill the concept of “band-pass” flow regulation described in Section 3.1. A stiction pre-stressed NC valve developed in Section 2.6 is adopted here for its appropriate cracking pressure range for the glaucoma treatment. Owing to the inherent structure of the NC check-valve, fluid coming from the opposite way will be rejected, protecting the anterior chamber from exterior contamination while the fluid can flow from NC check-valve to NO valve until the pressure reaches the limit of NO valve. Every parts of the GDD, (micro-valves, parylene-C protective tube, and parylene-C anchors), is fabricated

separately and eventually integrated into one system. Except for the micro valves which have been introduced in the previous sections, the parylene-C protective tube and the parylene-C fixation anchor are first introduced in Sections 3.3.3 and 3.3.4, respectively. The packaging procedures of the whole GDD system will be presented in Section 3.3.5.

### 3.3.3 Parylene-C protective tube carrier

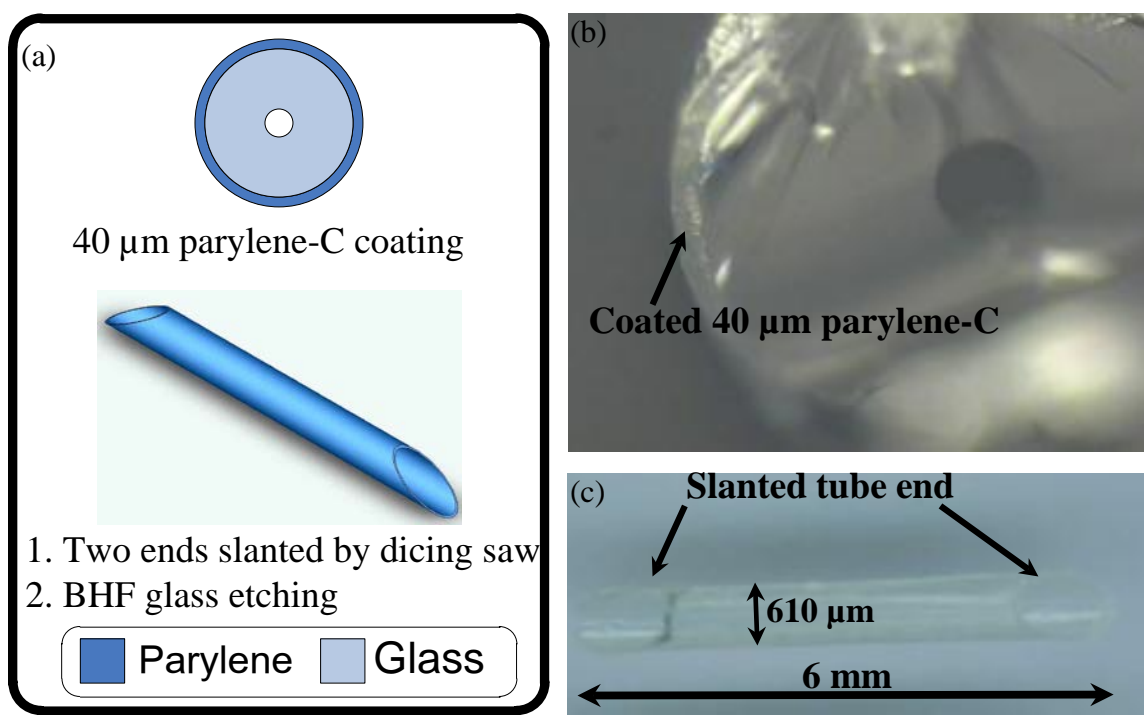


Figure 3-8: (a) Fabrication procedures of the parylene-C protective tube carrier, (b) coated 40  $\mu\text{m}$  parylene-C on the sacrificial capillary glass tubing, (c) slanted and completed parylene-C protective tube carrier

As previously shown in Figure 3-7 (b), to accommodate two micro valves, a hollow tube made of thick parylene-C is utilized and the length is chosen as 6 mm long. Both ends of these parylene-C protective tube carriers are slanted at 30 degrees to facilitate the surgical implantation and guard the GDD against iris retraction.

The fabrication procedures of the parylene-C protective tube are shown in Figure 3-8 (a). Parylene-C protective tube carrier was made by coating 40  $\mu\text{m}$  thick parylene-C onto capillary glass tubing with 530  $\mu\text{m}$  in O.D., which were then cut into desired lengths of 6 mm with slanted ends on both sides and later free-released in BHF. Figure 3-8 (b) shows the coated 40  $\mu\text{m}$  parylene-C on the capillary glass tubing while Figure 3-8 (d) shows the result of fabricated parylene-C protective tube carrier with two slanted ends.

### **3.3.4 Design and fabrication of the rollable/foldable parylene-C fixation anchors**

To prevent the implanted GDD from dislodging, rollable/foldable anchors with hemispherical recesses are designed (Figure 3-7 (b)). The anchor has a wingspan larger than the O.D. of #19-gauge hypodermic needles and can stretch out after needle retraction for robust fixation. A parylene-C recess is also fabricated together with the fixation anchor to facilitate the integration of the valved GDD tube system with the fixation anchor. The radius of hemispherical recesses is 300  $\mu\text{m}$ , fitting and covering the parylene-C protective tube carrier O.D. well during later integration.

During the fixation anchors' fabrication, the dry film photolithography technique was utilized to fabricate the connection between parylene-C recess and fixation anchor. The aluminum mask was patterned by Dry film photolithography prior to the parylene-C patterning to overcome the problem that regular liquid-based photoresist would not be possible to spin and cover over the recesses. Dry film photoresist is one kind of negative photoresist that is widely used in printed circuit board (PCB) industry. The process provides the capability of patterning circuit boards with small holes without any photoresist collapsing [142, 143]. Hence it becomes very useful in MEMS applications

to help pattern materials over cavities within the structures [144–146]. The high thickness of the dry film can also be transferred to the high aspect ratio sidewall fluidic channels in the microfluidics devices [147–151]. In our case, dry film was used to pattern the aluminum film on top of the parylene-C layer with a very deep trench. In addition, the dry film photoresist always comes as a large size sheet, rendering it a very good choice to fabricate large structures where regular liquid-based photoresist cannot be spun on, such as parylene-C MEMS wings [152, 153]. A laminator is required to laminate the dry film photoresist onto the parylene-C surface. The dry film photoresist is photo patternable by UV light with wavelength ranging from 360 to 420 nm, and developed by sodium carbonate ranging from 0.6% w.w to 1.2% w.w [154]. Being a polymer, the dry film photoresist can also be etched away during oxygen plasma etching, and can be stripped by potassium hydroxide after the entire process is completed.

Fabrication procedures for parylene-C fixation anchors are shown in Figure 3-9. The process started with growing thermal oxide layers on both sides of the silicon wafer. Front side oxide was first patterned for later  $\text{XeF}_2$  etching. Then the silicon wafer was isotropically etched to create semispherical recesses with radius to be 300  $\mu\text{m}$  in depth. A 20  $\mu\text{m}$ -thick parylene-C layer was then coated onto the wafer. A layer of 2000  $\text{\AA}$  of aluminum, used as the oxygen-plasma etching mask, was deposited on top of the parylene-C film and then patterned by dry film photolithography. The parylene-C layer was then patterned by oxygen plasma and then released by soaking in DI water. Different fixation anchor shapes can be designed and patterned to fit different surgical requirements. Results of the fabricated anchors are shown in Figure 3-10 (f).

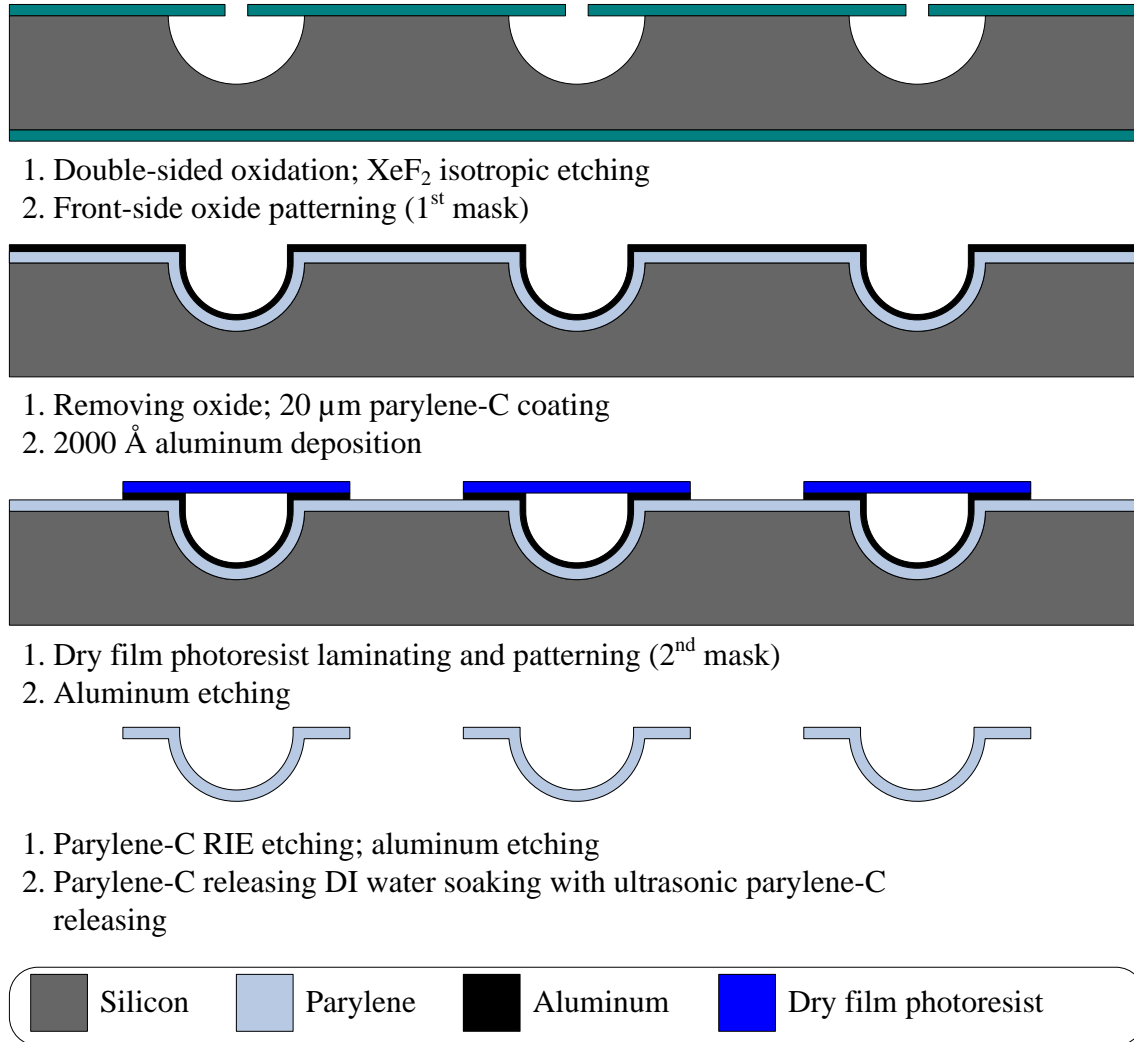


Figure 3-9: Fabrication procedures of the parylene-C fixation anchors

### 3.3.5 Dual-valved glaucoma drainage device packaging

The packaging procedure of the GDD is shown in Figure 3-10 (a) to (h). To package the entire GDD system, one NC check-valve and one NO valve were first released and then inserted into either ends of the parylene-C protective tube carrier, as demonstrated in Figure 3-10 (a) to (d). The NC check-valve is specifically manipulated by epoxy drops on the stiction-bonding area to enhance the anchoring adhesion, as illustrated in Figure 3-10 (b). The gap between the micro check-valves' seats and the

protective tube carrier inner wall was sealed by epoxy and the completed assembly is shown in Figure 3-10 (e). To mount the finished dual-valved tube onto parylene-C fixation anchors, tiny epoxy drops were first wiped on the semispherical recess. Then, the dual-valved tube was assembled onto the recess. Figure 3-10 (g) shows the final assembled GDD with different parylene-C fixation anchor shapes. Since the O.D. of the parylene-C protective tube carrier is  $600\ \mu\text{m}$  ( $530\ \mu\text{m} + 70\text{--}80\ \mu\text{m}$  parylene-C coating), it fits the recess of the parylene-C fixation anchor nicely after assembly. The anchor is flexible enough to be rolled/folded and insert into the testing Teflon tube thereafter, as shown in Figure 3-10 (h). The assembly is also suitable for the #19-gauge hypodermic needle implantation.

### **3.4 Valve-Position-Adjustable Dual-Valved GDD**

Even though the design concept of the dual-valved GDD system proposed in section 3.3 is easy and straight forward, ophthalmologists are also interested in exploring the possibilities of adjustable check-valve positions within the parylene-C protective tube. The GDD in Section 3.3 has two position-fixed check-valves at the two ends. If the check-valves' position has to be modified, the parylene-C tube length needs to be altered and thus shortens the overall length of the GDD system and might cause the difficulties of the implantation. As a result, another novel post-micro-fabrication tube packaging technology using an auxiliary glass capillary tube as a coupling tube in this section is developed to help us assemble the micro-flow regulating system.

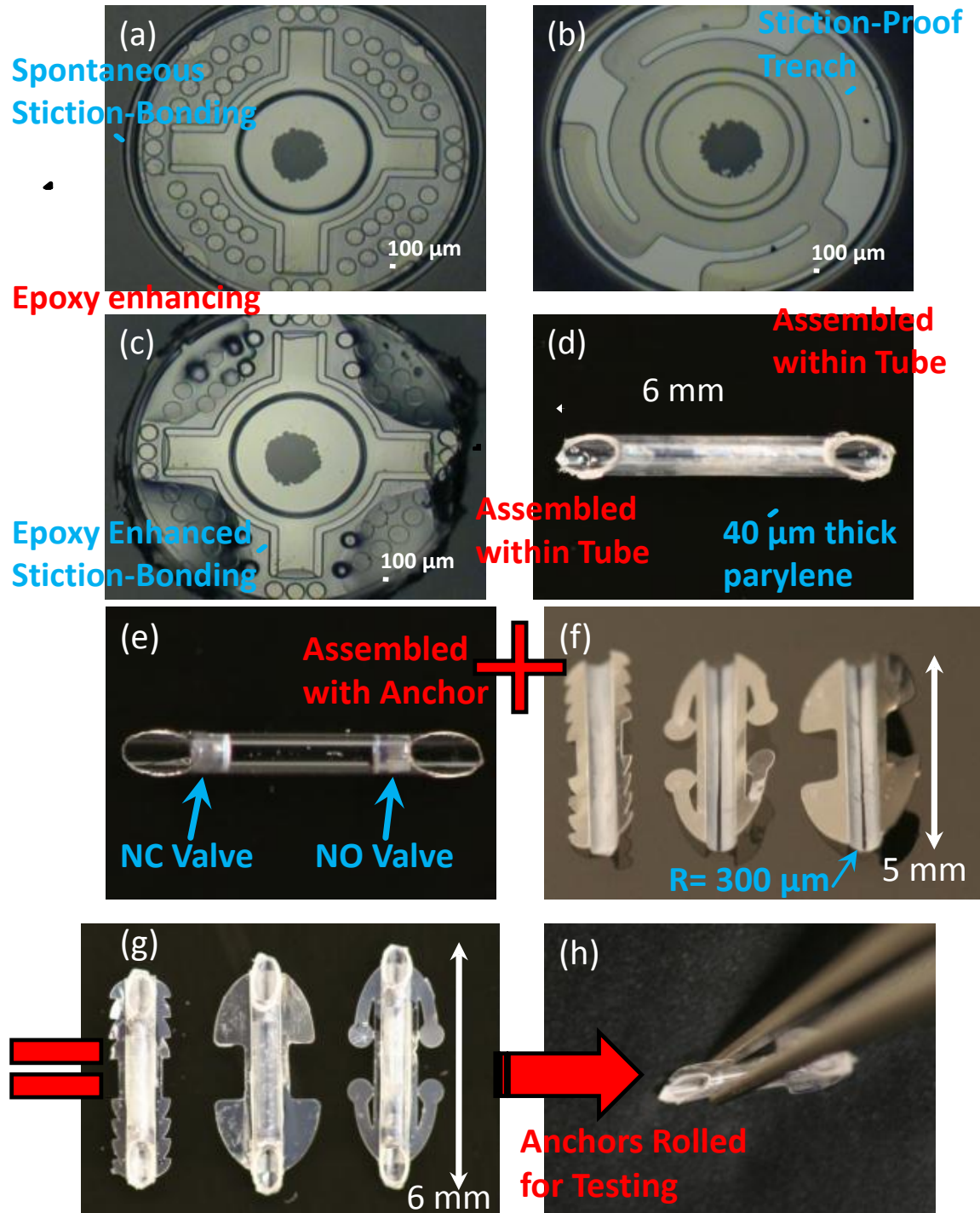


Figure 3-10: Packaging procedures of the dual-valved GDD system: (a) NC check-valve; (b) NO valve; (c) NC check-valve with stiction bonding enhanced by epoxy; (d) hollow parylene-C protective tube carrier; (e) one NC and one NO valve sealed in the parylene-C

protective tube carrier (transparent glass tube used here for clarity); (f) anchors with trenches of 300  $\mu\text{m}$  in radius, different anchor shapes designed to facilitate the surgical convenience, and future GDD fixation (left: ragged anchor; middle: foldable anchor; right: rollable squeeze-tail anchor); (g) completed assembled GDD in top view; (h) anchors can be rolled/folded for testing and implantation convenience. Check-valves are first sealed in the carrier, which is then assembled onto anchors.

### **3.4.1 Configuration of the valve-position-adjustable dual-valved GDD**

With the similar design concept described in Section 3.3, one NC check-valve and one NO valve are adopted here but attached to the two ends of the coupling tube with the valve surfaces facing to each other, as shown in Figure 3-11. The check-valves are fabricated with a ring groove for easier attachment. Both NC and NO valves are required to have smaller planar size than the inner diameter (I.D.) of the coupling tube so that the check-valves' surface can be inserted into the coupling tube and not be contaminated during packaging. The distance of the two micro check-valves can be adjusted by using different coupling tube with different lengths. In addition, the completed micro-flow regulating system makes it easier to load the check-valves into the protective tubes owing to its larger handling size. The parylene-C protective tube from Section 3.3.3 is still adopted in this design to accommodate the micro-flow regulating assembly and hence the finished GDD can still be perfectly fit into #19-gauge needle given its 610  $\mu\text{m}$  O.D. which makes the minimally invasive hypodermic needle implantation feasible. The completed GDD has the same regulatory function as in Section 3.3, but with more flexible valve position choices.

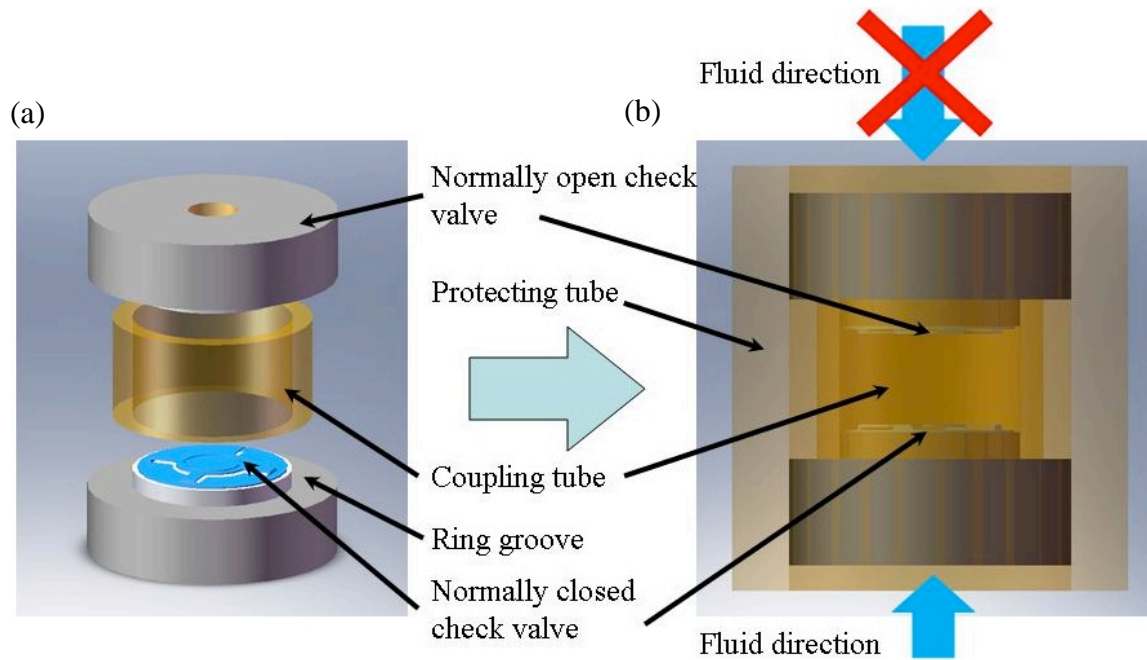


Figure 3-11: Schematics of valve-in-tube system: (a) Combination of one NC valve and one NO valve with a coupling tube to form the micro-flow regulating assembly. (b) Final finished valve-in-tube system

### 3.4.2 Grooved check-valves

As shown in Figure 3-12, in order to attached the check-valves onto the coupling tube, both NO and NC valves are further encircled by 65- $\mu\text{m}$ -wide, 150- $\mu\text{m}$ -deep grooves defined by DRIE on the top side for convenient assembly afterwards. The diameter of the valve's seat, however, is still designed as 500  $\mu\text{m}$ . The I.D. of the coupling tube is 320  $\mu\text{m}$ , which is slightly larger than the 300  $\mu\text{m}$  check-valves' surface diameter. The outer diameter (O.D.) of the coupling tube is 400  $\mu\text{m}$ , which is smaller than the I.D. of the outside parylene-C protective tube and can thus be packaged in the parylene-C protective tube.

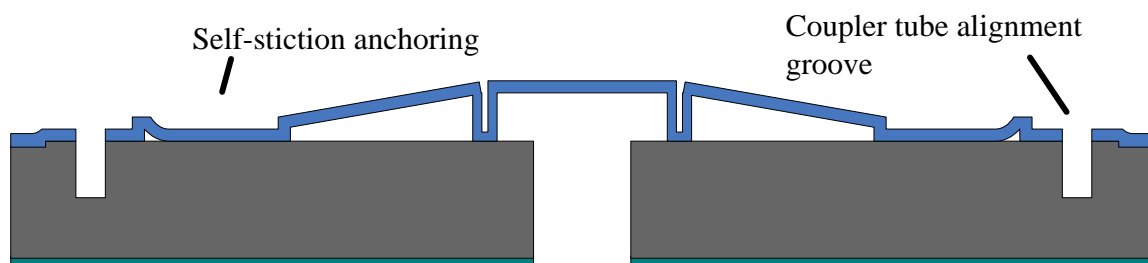


Figure 3-12: Cross section of the grooved self-stiction-bonding NC check-valve design

### 3.4.3 Grooved check-valve fabrication procedures

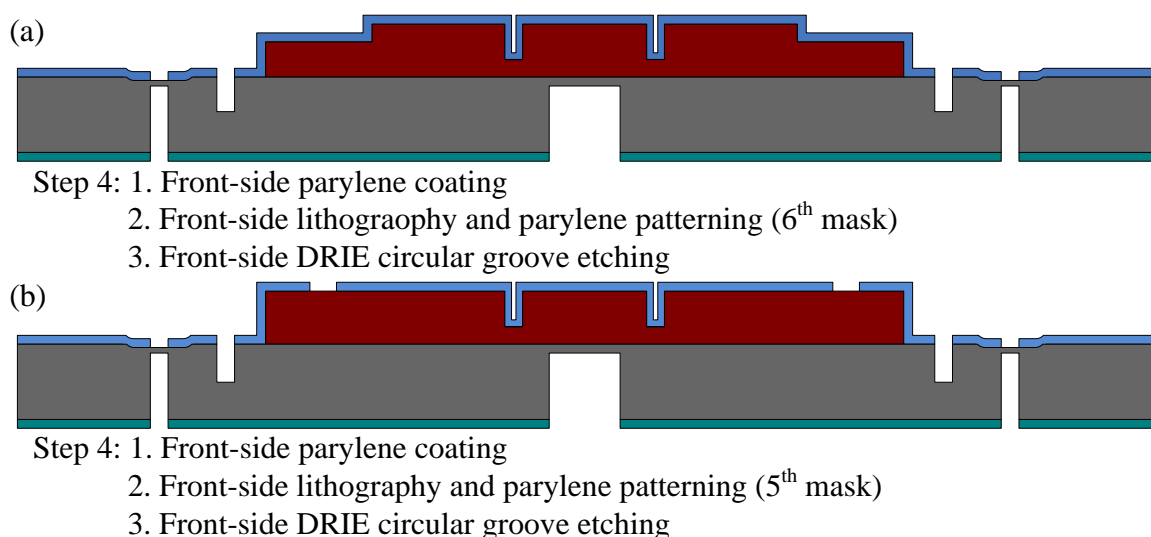


Figure 3-13: Modification of step 4 of the fabrication procedures of (a) NC check-valve and (b) NO valve by DRIE to incorporate a circular groove using the same photoresist mask for parylene-C patterning (photoresist mask not shown)

The grooved self-stiction-bonding NC check-valve and NO valve share very similar fabrication procedures shown in Figure 2-24 (NC check-valve) and Figure 3-4 (NO valve), respectively. However, in order to create the circular groove on top of check-valves, step four of the fabrication procedures in both Figure 2-24 and Figure 3-4 was modified to incorporate the usage of DRIE etching as shown in Figures 3-13 (a) (NC

check-valve) and (b) (NO valve). A 150- $\mu\text{m}$ -deep groove was created encircling the check-valves using additional DRIE after parylene-C coating and patterning for convenient coupling tube packaging alignment afterwards. The stiction happens in NC check-valves as expected after the photoresist stripping and the drying process. The fabrication result of the grooved NC check-valve is shown in Figure 3-14 (a).

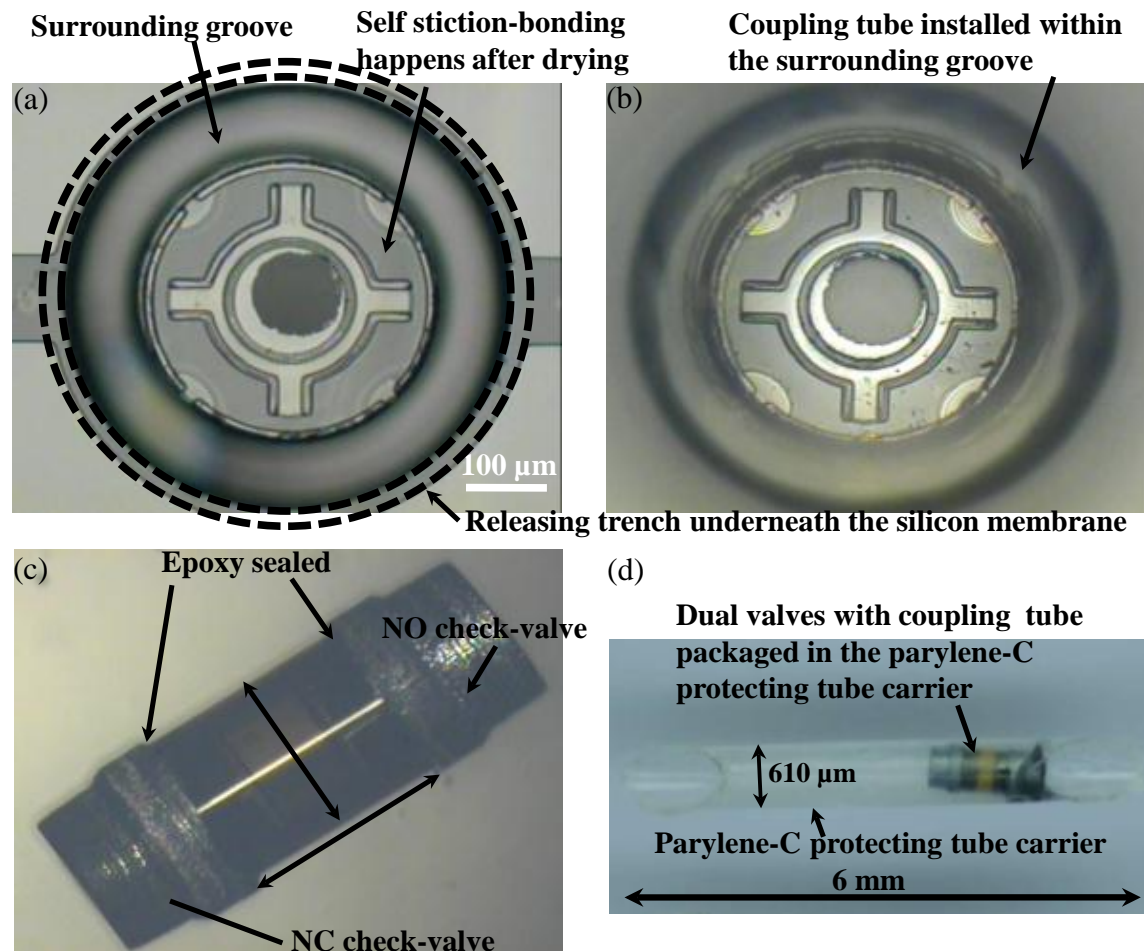


Figure 3-14: Micrographs of: (a) the fabrication result of an NC check-valve, (b) the top view of a NC check-valve packaged inside a coupling tube, (c) packaging results of the micro-flow regulating assembly, (d) the micro-flow regulating assembly packaged inside a tapered parylene-C protective tube carrier 610  $\mu\text{m}$  in diameter, suitable for a #19-gauge hypodermic needle

### 3.4.4 Grooved check-valve packaging procedures

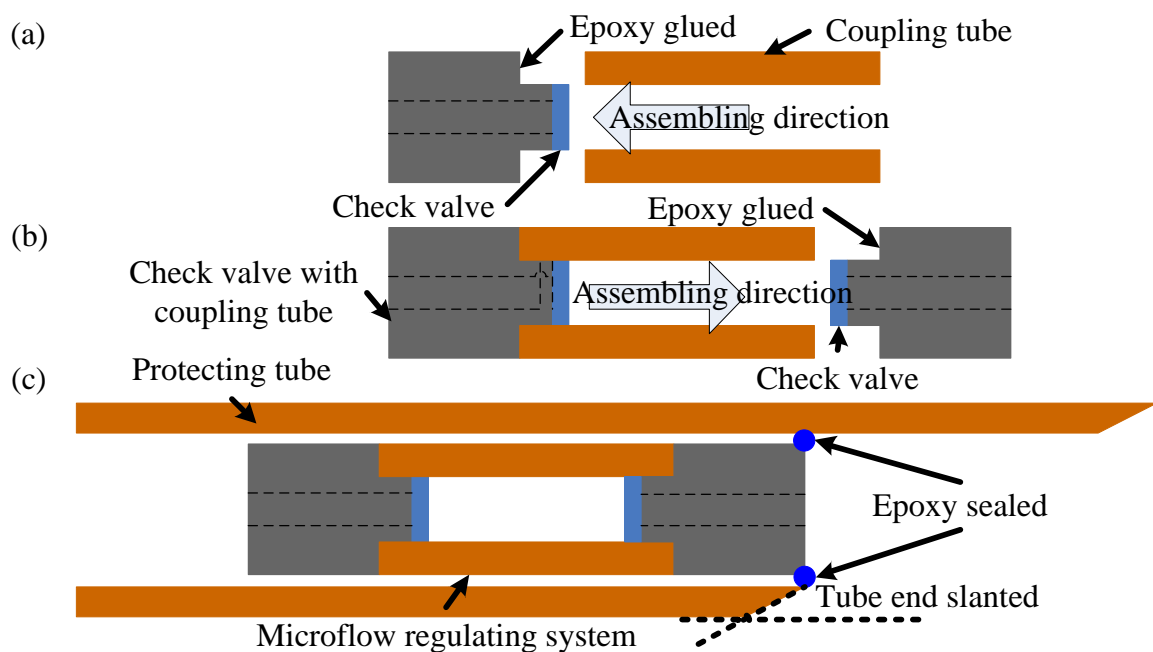


Figure 3-15: The packaging procedures: (a) one check-valve attached to one end of the coupling tube, (b) complete micro-flow regulating assembly, (c) final valve-in-tube system

As shown in Figure 3-15, the microfabricated valves were then packaged into a capillary protective tube to fulfill the valve-in-tube system. One microfabricated check-valve (NC or NO) was first attached to one end of the coupling tube with a tiny epoxy drop gently applied onto the alignment groove, as shown in Figure 3-15 (a). The other check-valve (NO or NC) was then attached on the other end of the coupling tube to form a micro-flow regulating assembly, as shown in Figure 3-15 (b). The micro-flow regulating assembly was then inserted into the protective tube which is first trimmed to 2–10 mm long and the entire tube-in-tube system was further secured by epoxy sealing, as shown in Figure 3-15 (c). The packaging results of the valve-in-tube system are

shown in Figure 3-14 (b) to (d). Figures 3-14 (b) and (c) shows the successful attachment of the check-valves onto the coupling tube with the help of the surrounding groove to form a micro-flow regulatory assembly. Figure 3-14 (d) demonstrates the complete valve-in-tube system which is suitable for #19-gauge needle implantation.

### **3.5 Bench-Top GDD Characterization**

#### **3.5.1 Bench-Top GDD characterization setup**

The completed GDD was first characterized to verify that its behavior meets the standard IOP regulation requirements *via* the bench-top testing. The testing setup is adopted from Figure 2-13 with the same working fluid chosen and the Teflon tubing was connected to the pressure gauge with turning resolution up to 0.01 psi (~ 0.5 mmHg). Prior to characterize the completed GDD, the Teflon FET tubing was first cut into 2 inch segments in advance. Then one wingspan of the GDD was folded by tweezers and inserted into Teflon FET tubing, which has I.D. of 750  $\mu\text{m}$ . The gap between the GDD and the Teflon tubing was sealed with photoresist and dried in the air, as illustrated in Figure 3-16. The characteristic curve of every assembly was generated and also filmed. In order to get a qualified working device, the result of the cracking pressure is required to fall in between 10–20 mmHg. It's also required that water drips should only be observed flowing out through the opening of valve-tubes, not the slits between valve-tubes and the FET tubing.

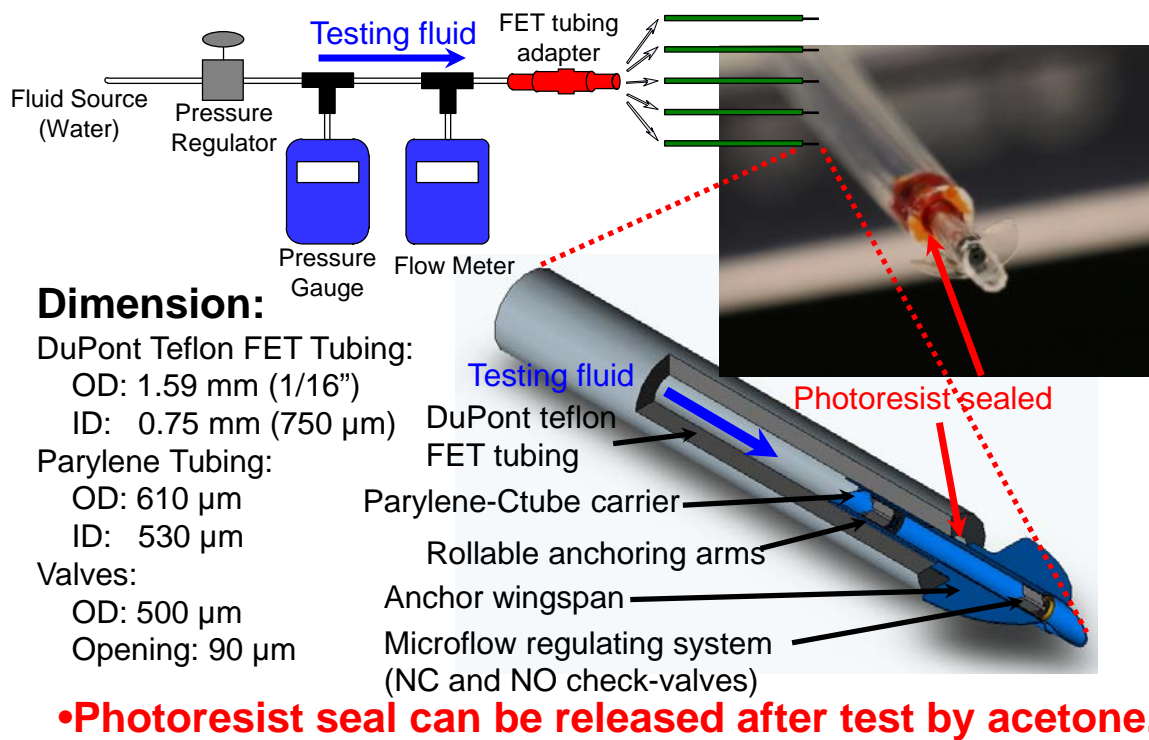


Figure 3-16: Testing setup of the GDD: Photoresist is painted in the gap between GDD and Teflon tubing for sealing.

### 3.5.2 Bench-Top GDD characterization results

Before every GDD is sent to animal surgical test, the devices are prepared and characterized first. One of the typical dual-valved GDD pressure/flow-rate profile characterization result is shown in Figure 3-17. The NC check-valve successfully opens at 0.33 psi (~ 17 mmHg) and NO valve starts to function at 1.1 psi (~ 57 mmHg), which is consistent with our simulation results. The off pressure of NO valve in the dual valve system is a bit larger than single NO valve system. It is likely due to the fact that part of the energy of the flowing fluid is consumed before the fluid reaching the NO valve by the friction and tether deformation of the NC check-valve. Therefore only part of the energy is left to push the NO valve membrane to close the valve orifice. This off pressure delay

makes the off pressure of the dual-valved GDD system right meet our design requirement to close after 50 mmHg. The testing flow-rate also show that our GDD system can perfectly satisfy the reported aqueous humor formation rate as 2–3  $\mu\text{L}/\text{min}$  [1]. *In vitro* testing results of the cracking pressure are shown in Table 3-1. Tested and qualified GDD systems were then released by acetone and IPA for further *ex vivo* implantation test to study their biomedical feasibilities.

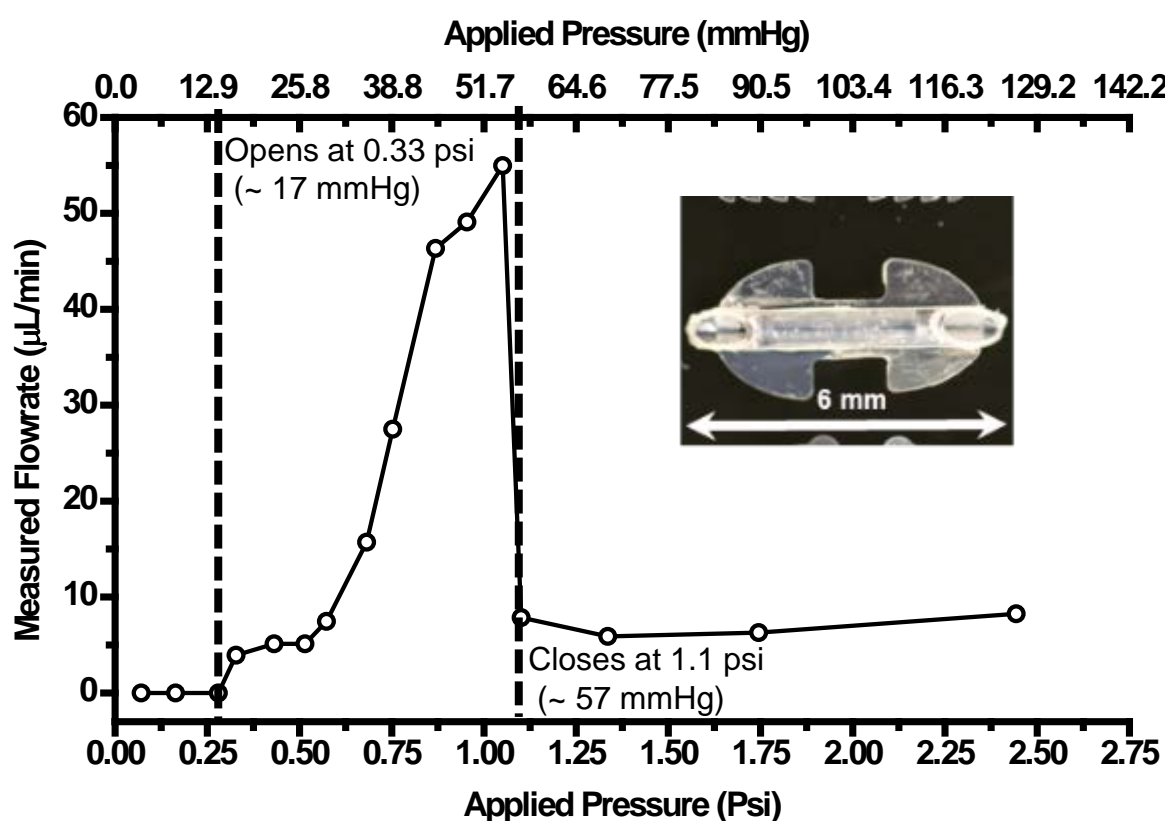


Figure 3-17: Dual-valved GDD characterization results: The fluid starts to flow after 0.33 psi (~ 17 mmHg) and closes at 1.1 psi (~ 57 mmHg). Water was chosen as the working fluid.

Table 3-1: Cracking pressures of two GDD systems obtained from *in vitro* and *ex vivo* tests

Measured Cracking Pressure (mmHg)	<i>In vitro</i>	<i>Ex vivo</i>
GDD in Section 3.3 (GDD 1)	17	15–25*
GDD in Section 3.4 (GDD 2)	12	24

\*Number is obtained by estimation from video timeline.

### 3.6 GDD *Ex Vivo* Test and Discussion

The photoresist sealing the gap of the GDD system and the FET testing tube was dissolved during device soaking in the acetone and IPA. The GDD was pulled out from FET testing tube and its wingspan stretched back to its original shape. After characterization and GDD released, the working device was then delivered for sterilization in order to prepare it for later *ex vivo/in vivo* functionality verification. An enucleated porcine eye was used as our implantation model in the process and a height-adjustable saline bottle is used as the working fluid to mimic eye fluid and simulate different eye pressure situations, as shown in Figure 3-18.

A customized plunger-in-needle introducer using #19-gauge hypodermic needle and a blunt-end plunger with wire size as AWG-22 (644  $\mu\text{m}$ ) in diameter, as shown in Figure 3-19 (a), was developed to facilitate the minimally invasive needle incision and device injection. The introducer was designed to avoid the device's dislodging during introducer retraction within the gauge #19 hypodermic needle while the blunt-end plunger are used as the GDD carrier and deliverer. Figure 3-19 (b) demonstrates a GDD with the folded zigzag type parylene-C fixation anchor inserted into the #19-gauge hypodermic needle.

An experiment demonstrating this subconjunctivally implantation concept was performed by using a tapered hollow tube as shown in Figures 3-19 (c) and (d). After the implantation of the hollow tube, as shown in Figure 3-19 (c), testing dye was injected into the hollow tube and it can be seen from Figure 3-19 (d) that the dye successfully drained out to the diffusive subconjunctival location as expected.

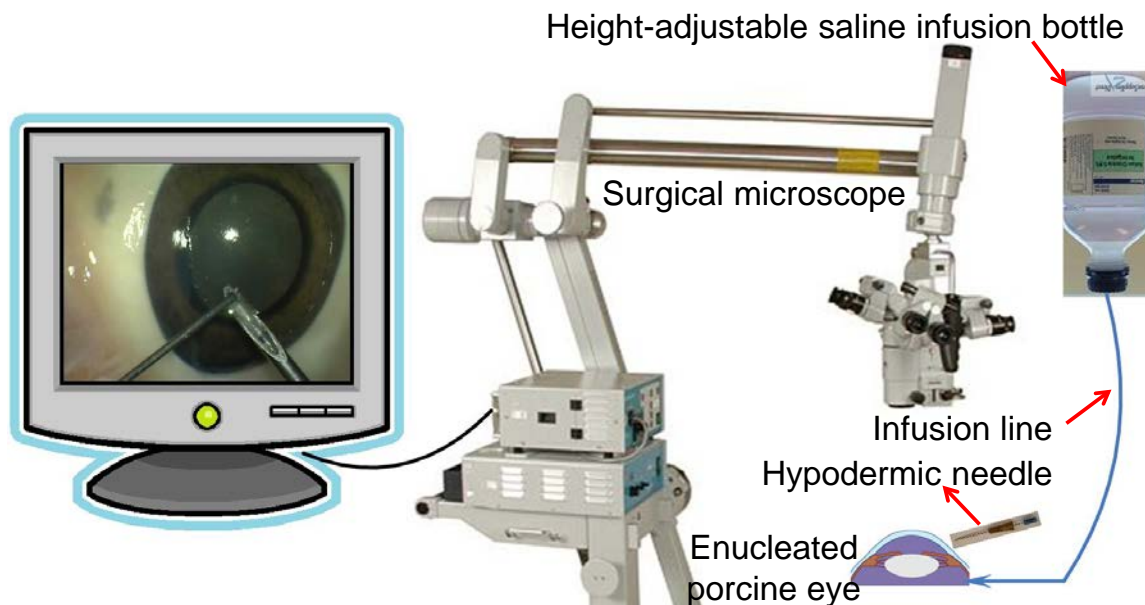


Figure 3-18: Testing setup of GDD *ex vivo* implantation test

### 3.6.1 GDD *ex vivo* implantation

Two *ex vivo* implantations are performed to understand the behavior of the two proposed integrated GDD systems implanted in enucleated porcine eyes and the function of the parylene-C fixation anchor. It can be shown Figure 3-20 (a) that the parylene-C fixation anchor helps the GDD stay firmly without moving successfully after needle retracted. Before the implantation started, the GDD was primed first, that is, inject saline through the GDD, to ensure no blockage within the tube.

### 3.6.2 Tapered hollow parylene-C protective tube mockup *ex vivo* implantation

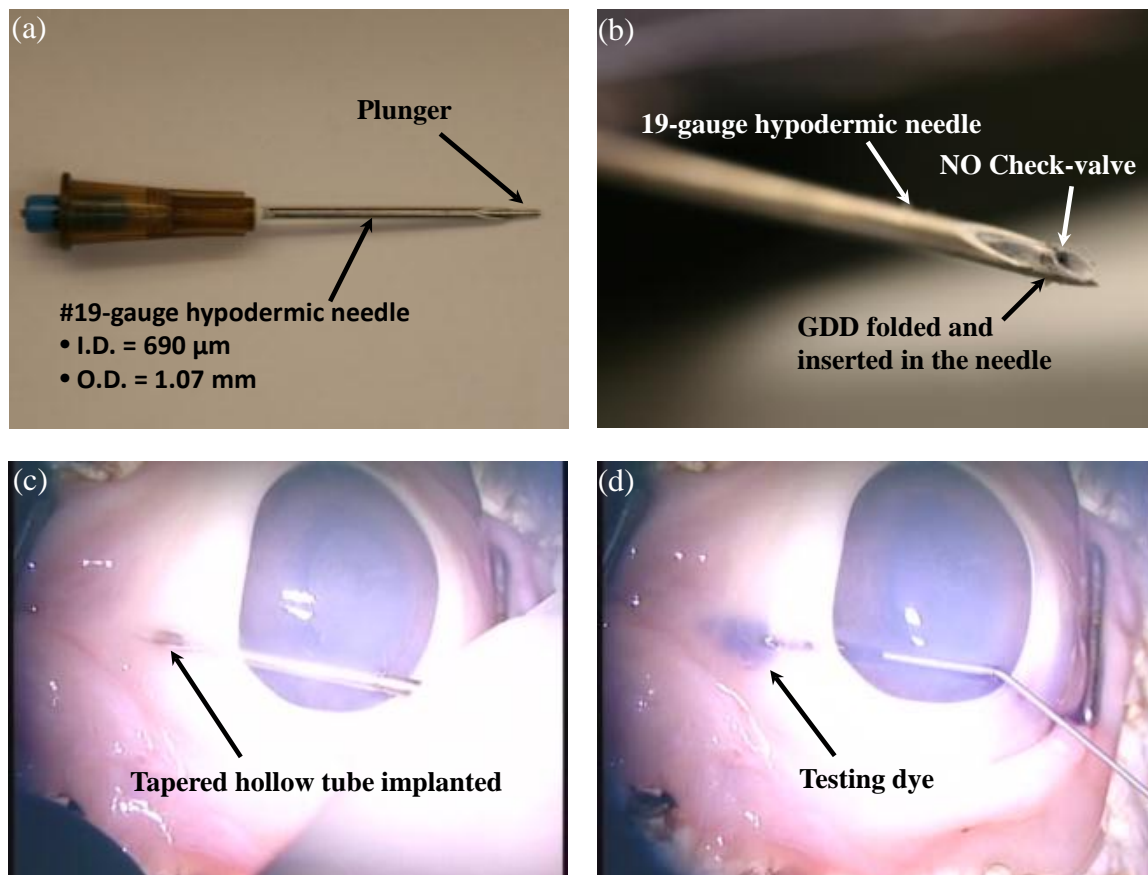


Figure 3-19: (a) The plunger in the needle introducer, (b) a GDD with folded zigzag type parylene-C fixation anchor inserted into a #19-gauge hypodermic needle, (c) a hollow parylene-C tube subconjunctivally implanted into an enucleated porcine eye, (d) testing dye shunted into the hollow tube. The drained-out testing dye is visible.

The *ex vivo* testing results of the first type of GDD developed in Section 3.3 are summarized in Table 3-1. The infusion line was connected to the vitreous chamber so that different pressures can be provided by raising the infusion bottle. After GDD implantation, a blue dye was injected into the anterior chamber, then the infusion bottle was raised up to increase the pressure. Soon after the infusion line was turned on, the dye

was seen to come out of the GDD, as shown in Figure 3-20 (a). After a few seconds, when the IOP reaches 52 mmHg, the infusion line is turned off. The video shows that GDD successfully opened to drain out testing dye well before the IOP reached its final 52 mmHg. From the timeline of the video, the turn-on pressure was around 15–25 mmHg.

Another implantation was also performed with the second type of GDD system introduced in Section 3.4. In this experiment, one end of the GDD was exposed to air in order to understand more about the behavior of the external end of the GDD. Unlike the previous setup, the infusion line and dye were both inserted and injected directly into anterior chamber to mimic the accumulation of aqueous humor during real glaucoma. Video recordings show that once saline and testing dye were both injected into the anterior chamber, GDD started to drain out the liquid due to the increased accumulated pressure, as shown in Figure 3-20 (b). We adjusted the saline flow-rate and observed that the GDD stopped to drain out fluids at 24 mmHg. The offset of the cracking pressure is possibly due to differences between *in vitro* and *ex vivo* testing environments. A hysteresis study was also executed at the end of the test to quantify the lowest pressure required to keep the GDD open. Using a cotton swab, capillary forces were introduced to continually pull eye fluids (saline, to be more accurate) out of the GDD. It was observed that the testing dye flow continued until the pressure reached 4 mmHg IOP for a few seconds. This result indicates that the response time of the valve's restoring force is in the order of several seconds.

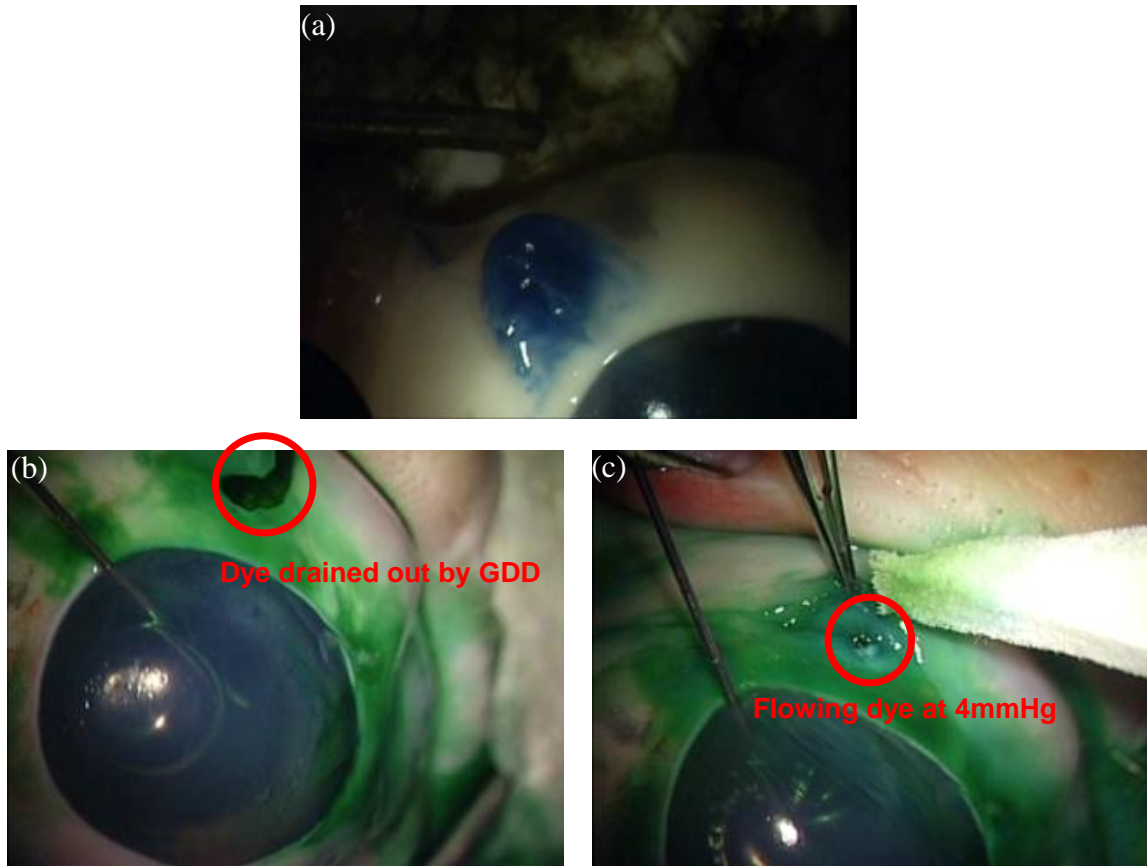


Figure 3-20: *Ex vivo* implantation results of: (a) GDD 1 and (b) GDD 2. The testing dye started to drain out after fluids were injected and stopped at 24 mmHg. (c) Residual dye kept flowing slightly at 4 mmHg.

After experimentation, the implanted GDD was retracted and investigated. Figure 3-21 (a) illustrates the situation of the NC check-valve retracted right after the implantation. Some residue is observed on top of the check-valve surface. The residue most likely comes from the eye fluid. After one week of soaking in DI water, the check-valve surface is cleaner, but some residues remained, as shown in Figure 3-21 (b). Future work would try to work out a solution to remove the residue and prevent GDD clogging after the implantation.

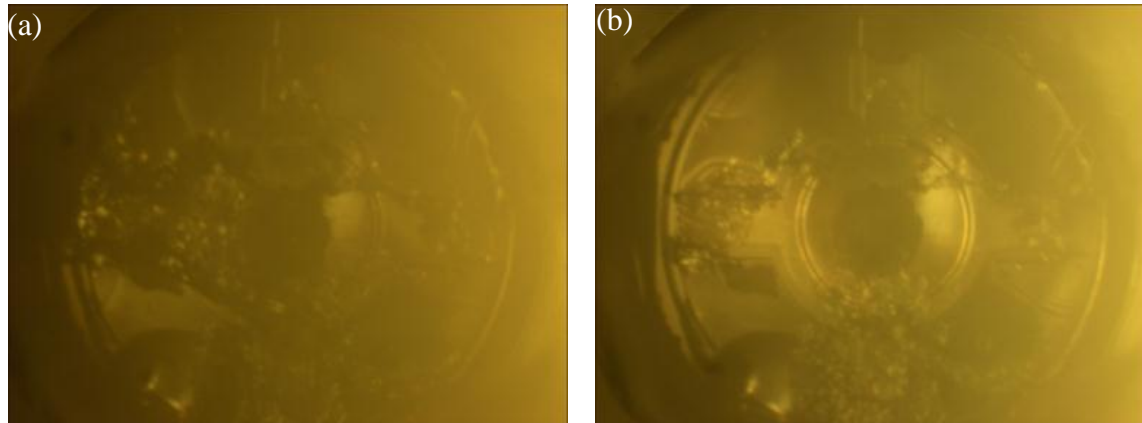


Figure 3-21: Inspection of the NC check-valve after *ex vivo* implantation: (a) right after the implantation, and (b) after one week of soaking in DI water

### 3.7 Summary and Conclusion

In this chapter, two types of glaucoma drainage devices are designed, developed, fabricated and tested: one has two valves integrated at both ends of the protective tube while the other allows position adjustments. Both GDD comprise of two types of valves (NC and NO) to accomplish the “band-pass” flow regulation. Two valves are packaged with valves’ surfaces facing interior to each other to protect the valves’ structure. For the selection of the NC check-valve, the self-stiction-bonding NC check-valve introduced in Section 2.6 is adopted here for the GDD system use due to its proper cracking pressure range. The NO valve is developed as the high-pressure stopper, which is one of the critical benefits of our GDD system. For the valve-position-adjustable GDD system, a coupling tube is involved into the system to realize the purpose of position-adjustable valve configuration. Aside from the valves development, the fabrication of the parylene-C protective tube is also developed. In addition, the parylene-C fixation anchors are fabricated by incorporating the dry film photolithography technique to overcome the

substrate recess problem. The packaging procedures of the entire GDD are developed to complete the final GDD system. Both bench-top characterization and *ex vivo* implantation test are performed to verify the functionality and the biomedical feasibility of the GDD. *Ex vivo* testing results show that the developed GDD can successfully regulate the eye fluid pressure down to ~ 24 mmHg. Some residues are found on top of the NC check-valve after the implantation. Future work would focus on the prevention of the accumulation of such residue.



---

# CHAPTER 4

---

## HIGH-QUALITY-FACTOR PARYLENE-C-BASED INTRAOCULAR PRESSURE SENSOR

### 4.1 Overview

Intraocular pressure (IOP) has been important information for the prevention and treatment of certain human eye diseases. For example, glaucoma is the second leading cause of blindness worldwide according to World Health Organization [6]. The majority of glaucoma patients have an IOP  $> 20$  mmHg (compared to a normal IOP of  $\sim 10$  mmHg), which could damage patients' optic nerves in the backside of the eye and cause the irreversible blindness. Currently, there is no cure for glaucoma, however, with early diagnosis and proper treatment, the visual loss can usually be slowed down or eliminated. Due to the lack of other symptoms or pain and the eye's ability to compensate for loss of peripheral vision, many glaucoma patients are unaware of the disease's development, until it is already severe. In fact, only half of the patients in the U.S are aware of having glaucoma. Therefore, early diagnosis and treatment are important to prevent blindness. Thus, a device to diagnose early-stage glaucoma is in demand.

As IOP is a convenient biomarker of glaucoma, it is generally measured in clinics to determine the presence of the disease. Current clinical IOP measurement is typically done with applanation tonometry. There are primarily two types of applanation

tonometers and both are non-implantable. The first type uses physical contact approach to touch the cornea and to estimate the area of the flattened portion. The IOP can then be calculated by the given applanation force and the flattened cornea area [155]. This approach requires well-trained ophthalmologists. The other type of applanation tonometers, named pneumotonometry, obtains the IOP by puffing an air jet onto the eye and measuring the flattened portion of the cornea optically [79]. Due to its non-contact characteristics and fine optical sensors, pneumotonometry can provide more accurate IOP information than the contact approach. However, the cornea's mechanical properties and thickness do vary from person to person, so the assumed cornea properties would always introduce errors. Interestingly, it's also reported that depending on daily activities, a person's IOP can actually go up to as high as 25 mmHg (i.e., above the glaucoma threshold IOP), while the IOP measured in clinic actually shows a normal value [84, 85, 156–158]. Therefore, the monitoring of a patient candidate's IOP should be 24/7 continuously. Unfortunately, current applanation tonometers, as clinical equipments, cannot provide this capability. Therefore, an implant sensor that can monitor the IOP continuously and wirelessly will be highly desirable [87].

Either active or passive approaches can be adopted to fulfill the telemetric pressure sensing [87]. Although the active devices are more likely to provide more functions, they tend to consume more power during the operation. Therefore power supply is a big issue. In addition, an active implant may require a significant size, which is of special concern for intraocular placement. However, with the infusion of MEMS (micro electro mechanical systems) technologies, miniaturized telemetric pressure sensors have already been developed for physiological pressure sensing applications such

as intracranial pressure monitoring by Leung [159]. For IOP measurement, McLaren's IOP sensor had a commercial transducer implanted on the dorsal neck of the rabbit under test with a catheter going to the anterior chambers [88]. Mokwa's IOP sensor was designed to be implanted in the lens [89]. Leonardi built a thin-microfabricated platinum-titanium strain gauge on a soft contact lens which can be worn directly on the cornea [160]; Chow designed a tadpole-shaped IOP sensor and would curve along the rim of the anterior chamber after the device implantation [161].

As seen from the above examples, there could be many different approaches for active IOP sensing; however, in any case one must consider collectively the implant size, the placement and the corresponding surgical procedures because eye is a small and delicate organ, and has very limited room inside. Passive IOP sensors may have many advantages over active ones in terms of smaller size, little or no power consumption, and easier surgery. One especially interesting passive IOP approach is to use LC-tank-based sensors with a pressure-dependent capacitor and/or inductor. This approach has also been studied for decades and is well established [90, 92, 93, 162]. Different physiological pressure monitoring has been achieved using passive telemetry. For examples, DeHennis has adopted the technique to monitor the transcutaneous pressure [94]; Fonseca also utilized it for pressure monitoring of abdominal aortic aneurysms (AAA) [95]. For IOP implants, Collins published the first passive wireless transensor implantable in the anterior chamber in 1967 adopting the LC-tank resonant circuit to measure the IOP [91]. Backlund et al. modified Collins' IOP sensor design using a capacitive sensor manufactured by silicon fusion bonding technique [96, 163, 164]. The capacitor was connected to a hand-wound coil made of 50  $\mu\text{m}$  gold wire to form a LC-

tank resonant circuit and the entire system was encapsulated by silicone for biocompatibility.

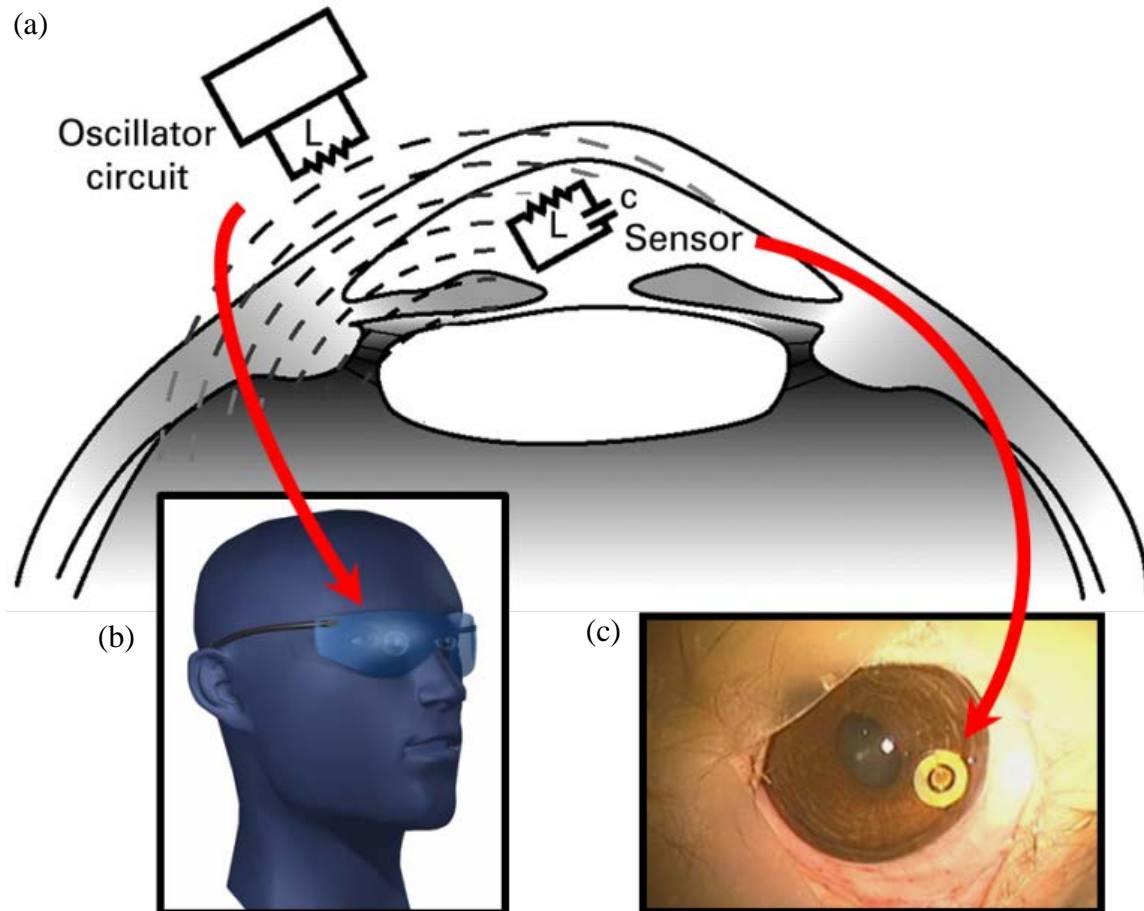


Figure 4-1: (a) Wireless sensing concept of implantable IOP sensor in the anterior chamber, (b) the glass reader paradigm, (c) a real IOP sensor *in vivo* tested in a rabbit eye

This work presents our effort to develop a telemetric implantable IOP sensor using an LC-tank resonant circuit. In fact, our group presented a flexible parylene-based IOP sensor by Chen et al. in 2010 [98]. The sensor had one inductor and one capacitor combined in series as a passive LC-tank resonance circuit. The IOP sensor was implanted into the anterior chamber and anchored on the iris, as shown in Figure 4-1(a).

Figure 4-1 (c) shows the *in vivo* test of Chen's IOP sensor in a rabbit eye. The resonant frequency shift was registered by an external oscillator circuit through a wireless inductive coupling link, whose concept is shown in Figure 4-2. The external interrogating circuit could be designed and even integrated into a pair of glasses as shown in Figure 4-1 (b). With the sensor's principle shown in Figure 4-3 (a), when the sensor's surrounding pressure increases, the capacitance increases due to the sensing plate's deforming concavely, introducing the resonant frequency shifts to the lower range.

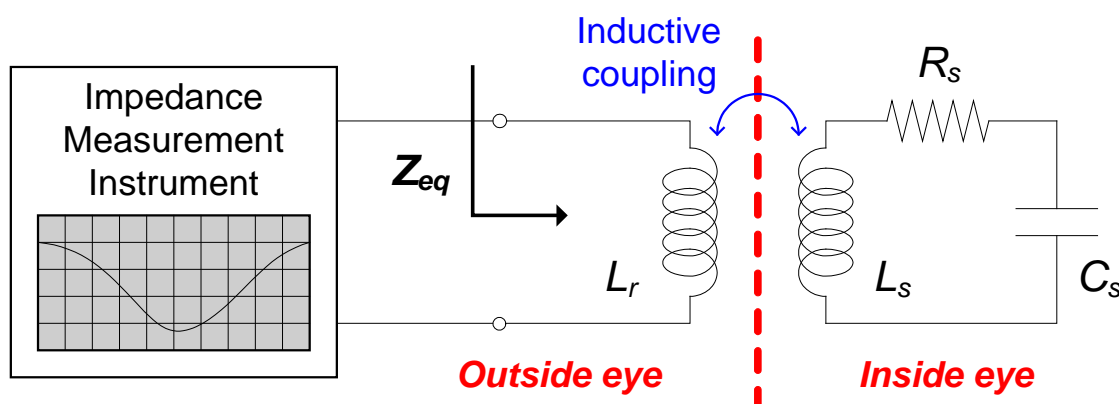


Figure 4-2: The concept of the wireless inductive coupling link: The frequency shift is registered through an external oil reader.

Although the IOP sensor could successfully measure the pressure information of the eye, the anchoring of the sensor was still an issue. In Chen's work, a modified iris retractor was attached to the bottom of the IOP sensor so that the sensor can anchor on top of the iris after the implantation. However, the iris would contract or expand very frequently and the iris retractor might get loose. In addition, due to the high loss tangent of the eye fluid in the anterior chamber, the LC tank's quality factor was degraded and

the sensing distance was reduced just as what have been reported in other wireless sensors [95, 97, 98].

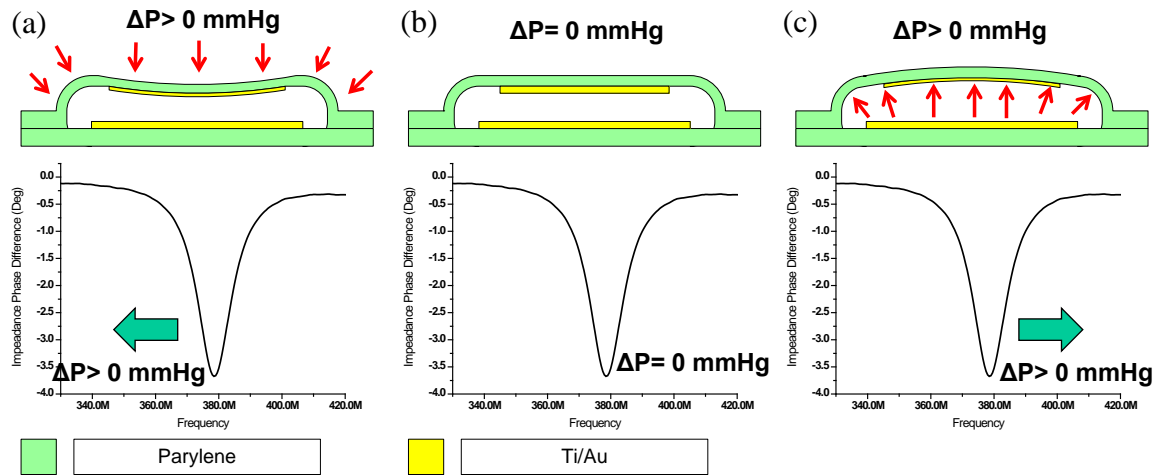


Figure 4-3: Resonant frequency shift corresponds to the applied pressure: (a) Frequency decreases as the capacitance increases; (b) No frequency shift is observed when no pressure difference exists; (c) Frequency increases as the capacitance decreases.

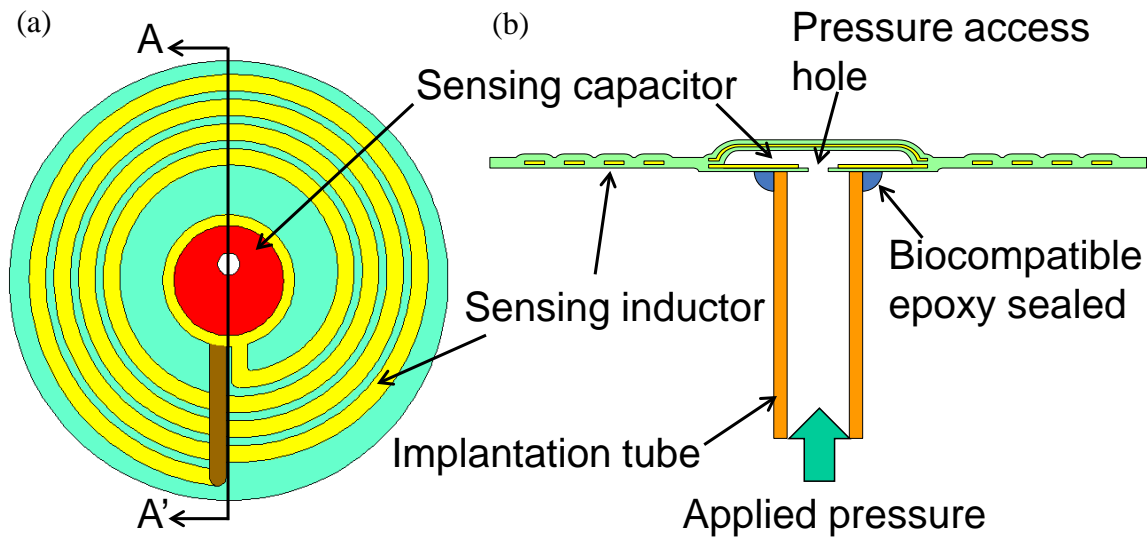


Figure 4-4: The new IOP sensor design: (a) Top view of the sensing part, (b) AA' cross-section view of the IOP sensor

To overcome these problems, a new IOP sensor structure is developed. We keep the sensing part design similar to our previous device, which is composed of a sensing inductor and a sensing capacitor as shown in Figure 4-4 (a). A pressure access hole connecting the chamber of the sensing capacitor and outside is created during device fabrication. The pressure access hole allows an implantation tube to be attached to the backside of the device to cover the access hole as shown in Figure 4-4 (b). During the device fabrication, a biocompatible epoxy is applied to seal the gap between the implantation tube and the sensing part to make it airtight, and also to ensure the device's biocompatibility.

The newly designed IOP sensor could be placed with an implantation tube penetrating the eyeball choroid through the pars plana while the sensing part remains outside the choroid and under the conjunctiva of the eye, as shown in Figure 4-5. This kind of placement is similar to that of [70].

In addition, this work also includes a designed passivation to retain the device's high quality factor. Although the sensing coil is kept outside the eyeball in this new implantation, the tissue under the conjunctiva can still cause the reduction of the quality factor induced by the tissue power absorption. To counter this, we adopted an approach of parylene-C passivation, in which enough parylene-C was deposited to contain the electric field in between different coil turns. By quantitatively measuring the effects of parylene-C passivation with different parylene-C thicknesses, the results have shown that the quality factors of the sensing coils immersed in the saline could indeed be recovered to the original values as in air. As shown in Figure 4-14, it was concluded that an extra 20  $\mu\text{m}$  parylene-C passivation layer applied on top of the original sensing coil helped

maintain sensor's high quality factor when it was covered by the human body tissues. Ultimately, the passivation will enable long sensing distance after the implantation.

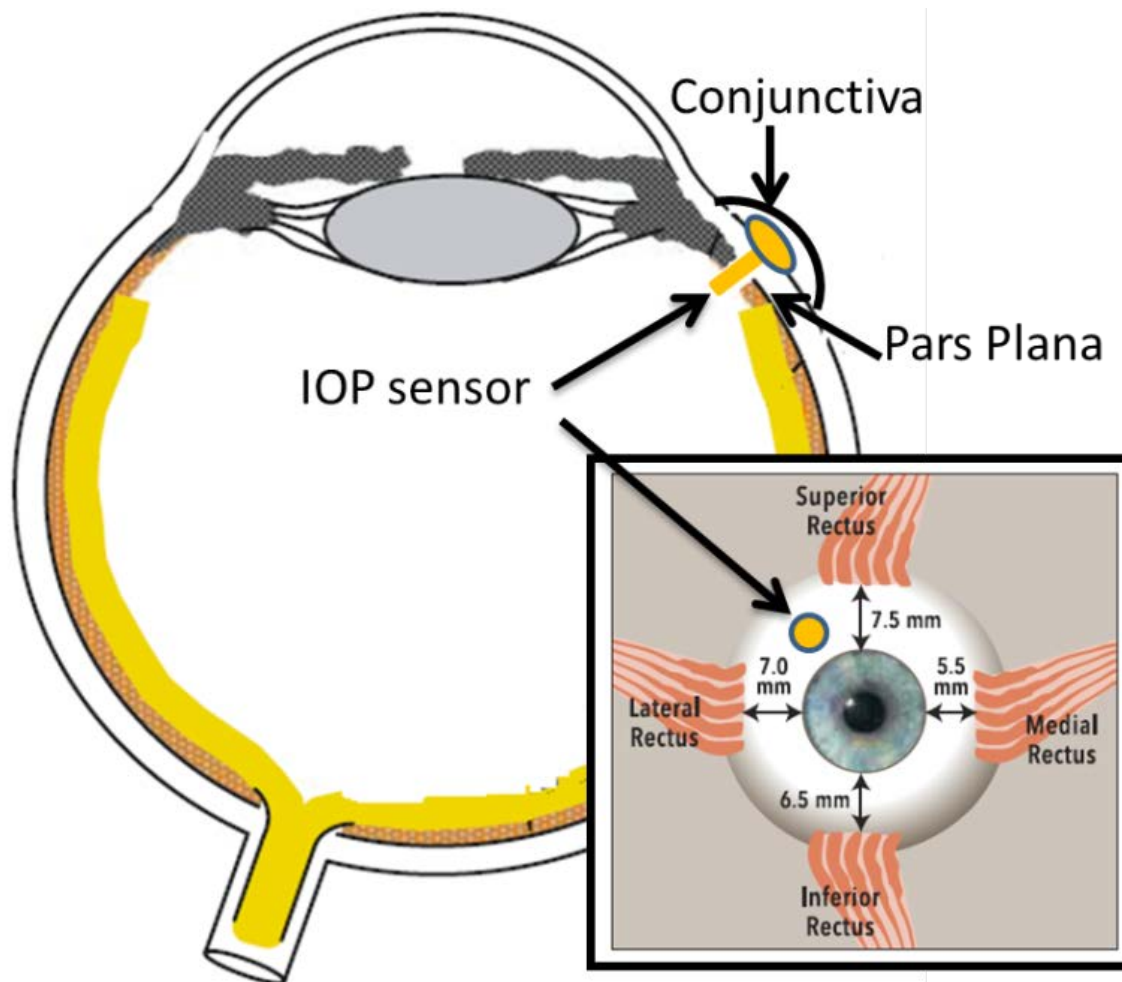


Figure 4-5: The newly designed IOP sensor is implanted at the pars plana with the implantation tube going through the choroid, while the sensing part still remains outside the choroid, but under the conjunctiva of the eye.

## 4.2 Sensing Theory and the Device Design

### 4.2.1 Sensing scheme

The wireless sensing scheme is shown in Figure 4-2. The right RLC circuit represents the implanted IOP sensor and its resonant frequency can be expressed as [97]:

$$f_s = \frac{1}{2\pi} \sqrt{\frac{1}{L_s C_s} - \frac{R_s^2}{L_s^2}} \cong \frac{1}{2\pi \sqrt{L_s C_s}} \text{ if } R_s^2 \ll \frac{L_s}{C_s}, \quad (4-1)$$

where  $R_s$ ,  $L_s$ , and  $C_s$  represent the sensor's resistance, inductance, and capacitance, respectively. The equivalent impedance viewed from the external coil reader and apparatus is derived as [95, 162, 165]:

$$z_{eq} = j2\pi f L_r \left[ 1 + k^2 \frac{\left(\frac{f}{f_s}\right)^2}{1 - \left(\frac{f}{f_s}\right)^2 + \frac{1}{Q_s} j \frac{f}{f_s}} \right], \quad (4-2)$$

where  $f$  is the excitation frequency,  $k$  is the coupling coefficient of the inductive link depending on the dimensions and separation of the coupled coils [93–95, 162, 165].  $Q_s$ , the quality factor of the sensor at the resonance, can be represented as:

$$Q_s = \frac{1}{R_s \sqrt{L_s C_s}}. \quad (4-3)$$

When the sensor is excited at the resonant frequency,  $Z_{eq}$ , eqn. (4-2), becomes

$$Z_{eq} = j2\pi f_s L_r (1 + jk^2 Q_s), \quad (4-4)$$

and its phase dip magnitude can be approximated as:

$$\Delta\phi \cong \tan^{-1}(k^2 Q_s). \quad (4-5)$$

when the capacitance of the IOP sensor changes, it can be shown from eqns. (4-3)–(4-5) that the impedance phase dip shifts to either lower or higher frequency which can be detected by a network analyzer.

#### 4.2.2 Electrical and mechanical design of the device

The electrical design of the IOP sensor can be explained by the well-developed equations as follows [92, 98, 166]. The inductance of the spiral coil can be represented as:

$$L_s \cong \frac{\mu_0 n^2 d_{avg} c_1}{2} \left[ \ln \left( \frac{c_2}{F} \right) + c_3 F + c_4 F^2 \right], \quad (4-6)$$

where  $n$  is the number of turns of the inductor,  $d_{avg}$  is the averaged diameter of the coil windings,  $F = (d_{out} - d_{in}) / (d_{out} + d_{in})$  is the fill factor of the coil windings, and  $c_1 - c_4$  are constants determined by the winding geometry. The coil winding inherently comes with a resistance and can be calculated as:

$$R_s = \frac{\rho l}{w \delta (1 - e^{-h/\delta})}, \quad (4-7)$$

where  $\rho$  is the electrical resistivity of the metal,  $w$  and  $h$  are the metal line width and height, respectively.  $\delta$  is the frequency-dependent metal skin depth which can be written as:

$$\delta = \sqrt{\frac{\rho}{\pi f \mu}}, \quad (4-8)$$

where  $\mu$  is the magnetic permeability of the metal. The capacitance of the IOP sensor is given by

$$C_s = C_{s,g} + C_{s,p}, \quad (4-9)$$

where  $C_{s,g}$  is the capacitance of the parallel metal plate capacitor at the center of the IOP sensor and  $C_{s,p}$  is the parasitic/stray capacitance introduced by other components in the entire device.

To have a detectable impedance phase dip shift, a deformable circular metal plate was designed at the center of the IOP sensor. Once the plate deforms either downward or upward, the capacitance of the parallel-metal-plate capacitor changes and the impedance phase dip shifts can be registered. The deformation of the metal plate corresponding to the pressure difference can be predicted as [167]:

$$w(r) = \frac{\Delta P a^4}{64D} \left[ 1 - \left( \frac{r}{a} \right)^2 \right]^2, \quad (4-10)$$

where  $\Delta p$  is the pressure difference,  $r$  is the radius calculated from the center of the plate,  $a$  is the diaphragm radius and  $D$  is the flexural rigidity of the diaphragm, which is calculated as:

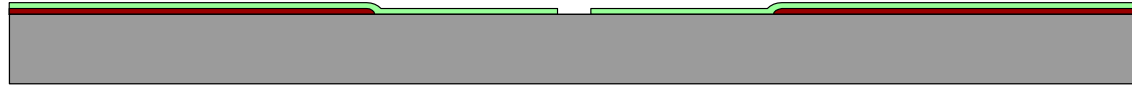
$$D = \frac{Et^3}{12(1-\nu^2)}, \quad (4-11)$$

where  $E$  is the Young's modulus,  $\nu$  is the Poisson's ratio of the parylene-C, respectively.  $t$  is the diaphragm thickness.

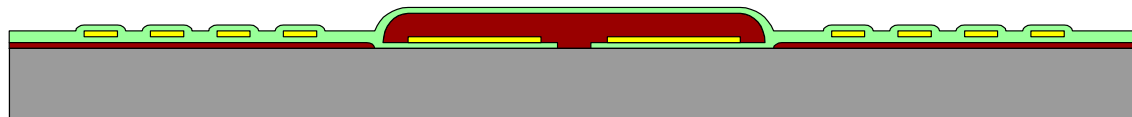
In our new sensor implantation approach, the sensing metal plate deforms convexly with higher surrounding pressure transmitted to the metal diaphragm capacitor chamber through the implantation tube. According to eqn. (4-1), this higher eye pressure causes the capacitance to reduce and thus the resonant frequency shifts to the higher range, as described in Figure 4-3 (c).

## 4.3 Device Fabrication and Characterization

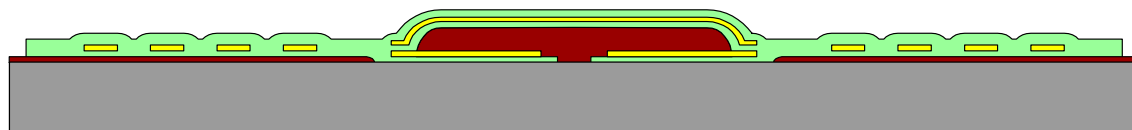
### 4.3.1 Device fabrication



1. Sacrificial photoresist coating and patterning
2. 1<sup>st</sup> layer parylene deposition and patterning (5  $\mu\text{m}$ )



1. 1<sup>st</sup> layer Ti/Au deposition and patterning (3  $\mu\text{m}$ )
2. Sacrificial photoresist coating and patterning (10  $\mu\text{m}$ )
3. 2<sup>nd</sup> layer parylene deposition and patterning (8  $\mu\text{m}$ )



1. 2<sup>nd</sup> Ti/Au deposition and patterning (0.5  $\mu\text{m}$ )
2. 3<sup>rd</sup> layer parylene deposition and patterning (7  $\mu\text{m}$ )



1. Device released in acetone



Figure 4-6: Fabrication procedures of the sensing part of the IOP sensor

The fabrication procedure of the sensing coil is shown in Figure 4-6. The sensing part was made of parylene-gold (3  $\mu\text{m}$ )-parylene sandwich structure. The first layer of 5  $\mu\text{m}$  parylene-C was first deposited on top of a layer of sacrificial photoresist. The pressure access hole with 180  $\mu\text{m}$  in diameter was opened by oxygen plasma. 3  $\mu\text{m}$  Ti/Au was deposited on top of the first layer parylene-C and patterned. The distance between two capacitor metal plates was designed as 10  $\mu\text{m}$  and was achieved by spin

coating and patterning a 10- $\mu\text{m}$ -thick sacrificial photoresist. A second layer of parylene-C was deposited to cover and protect the 3  $\mu\text{m}$  Ti/Au; followed by a 0.5  $\mu\text{m}$  Ti/Au deposition. The third parylene-C layer was then deposited and the configuration of the sensing part was patterned by oxygen plasma. The sensing part was finally released from the substrate by soaking in the acetone. The completed sensing part is shown in Figure 4-7 (a). After completing the fabrication of sensing part, the implantation tube was attached onto the backside of it, as shown in Figure 4-7 (b). The inner diameter of the implantation tube was chosen as 320  $\mu\text{m}$  to fully cover the pressure access hole. The outer diameter of the implantation tube was 450  $\mu\text{m}$ . The implantation tube was manually mounted onto the sensing part. A precision XYZ stage was used to control the position of the implantation tube which was maneuvered to be concentric with the pressure access hole. The implantation tube and sensing part were glued together with a few drops of biocompatible epoxy.

#### **4.3.2 Device characterization**

The completed IOP sensor was then integrated to a bigger testing capillary tube and sealed by photoresist, as shown in Figure 4-7 (c). The inner diameter of the testing tube was chosen as 500  $\mu\text{m}$  to accommodate the implantation tube. The completed sensor with testing capillary tube assembly was left overnight to dry the photoresist.

The device characterization setup is shown in Figure 4-8. The whole IOP sensor assembly was mounted onto a pressure characterization setup. During the characterization, a HP 4195A network/spectrum analyzer was hooked up with a 1.5-mm-diameter hand-wound coil serving as the reader coil. The characterization signal was accessed *via* a data acquisition system and then analyzed in personal computer. The

qualified IOP sensor was released by soaking the whole assembly in the acetone to remove the photoresist. The final IOP sensor is shown in Figure 4-7(d) and is ready for the next *in vivo/ex vivo* test.

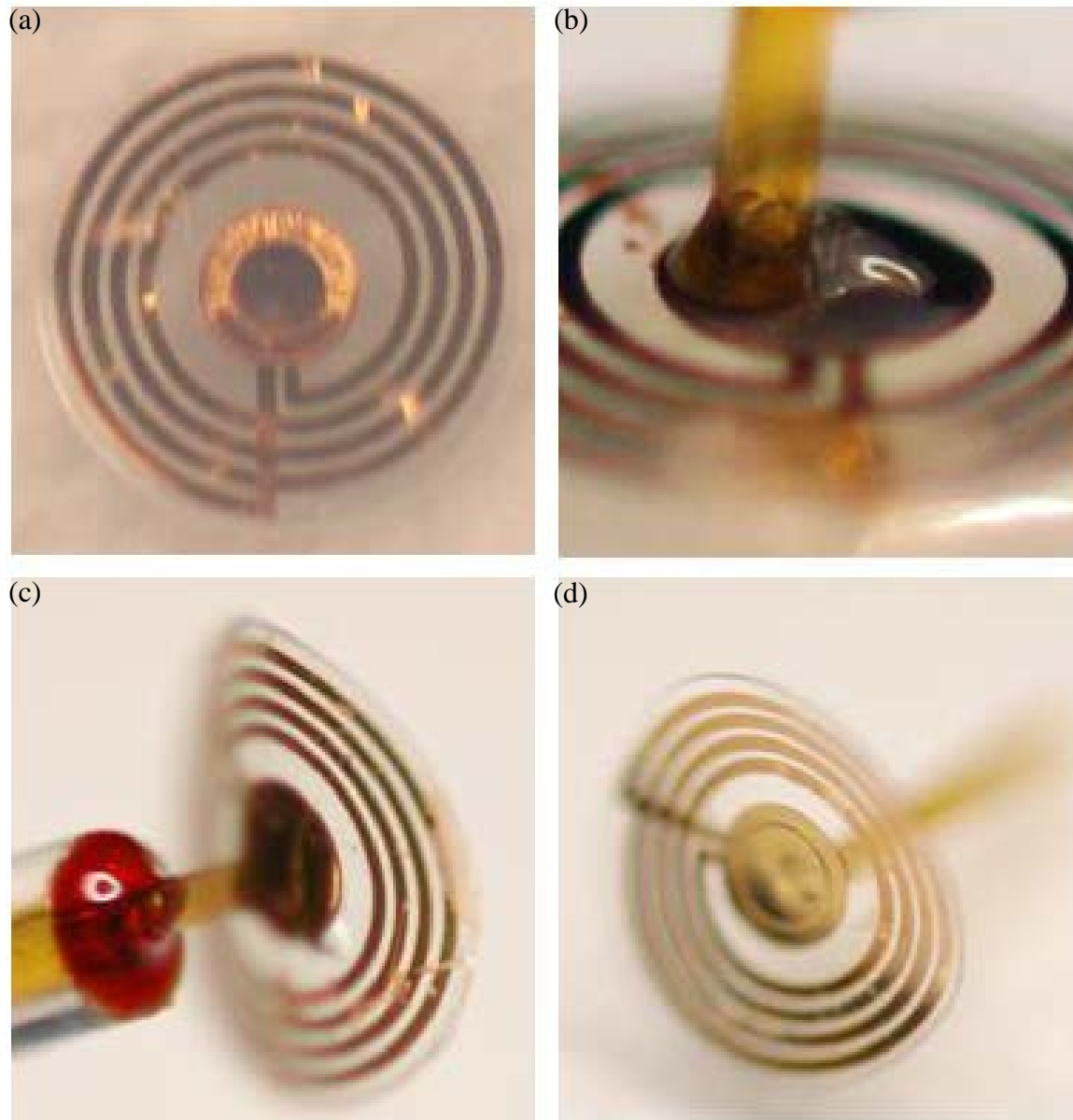


Figure 4-7: IOP sensor fabrication and assembling results: (a) Completed sensing part, (b) implantation tube attached onto the backside of the sensing part concentric with the pressure access hole, (c) IOP sensor mounted to the testing tube by photoresist, (d) final IOP sensor

#### 4.4 Characterization Results and Discussions

The benchtop characterization results are shown in Figure 4-9. The results show that the resonant frequency was 379 MHz when the applied pressure difference was 0 mmHg. When the applied pressure difference increased, the resonant frequency shifted to the right as expected because the metal plate deformed convexly. The IOP sensor's electrical parameters were obtained and shown in Table 4-1.

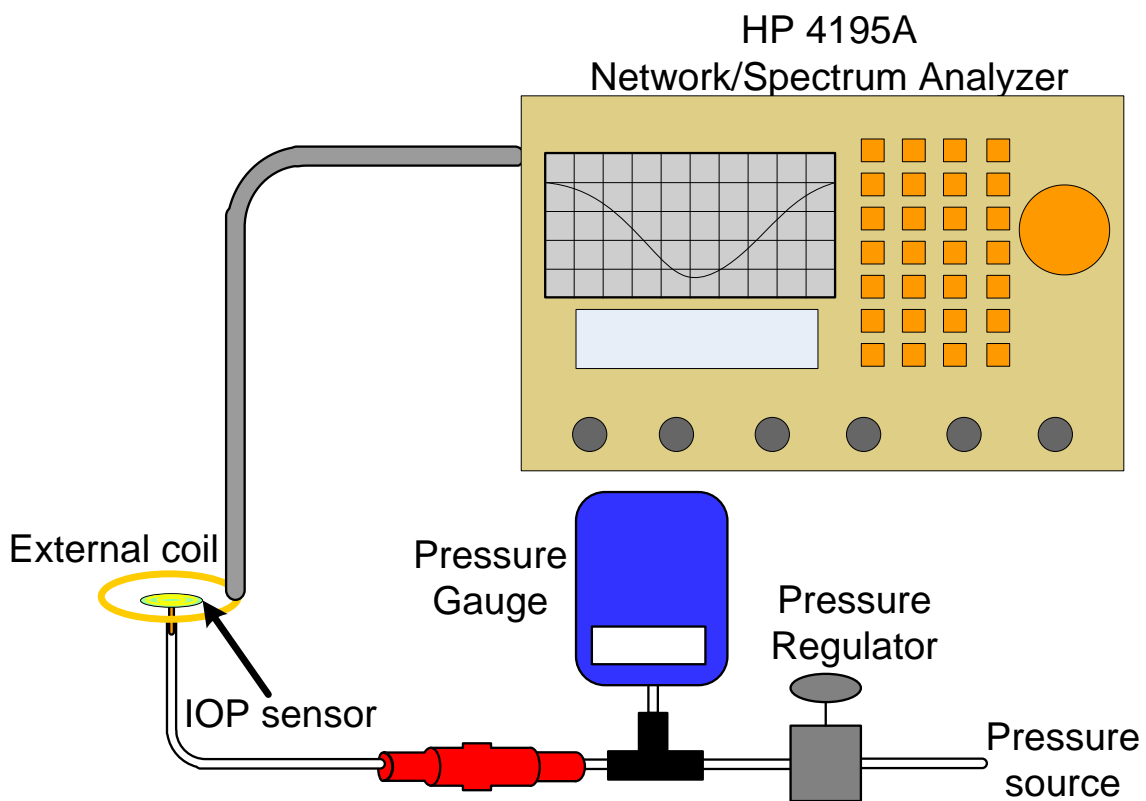


Figure 4-8: IOP sensor characterization setup: a 1.5-mm-diameter hand-wound coil served as the reader coil and a HP4195A network/spectrum analyzer was used to register the frequency shift of the phase dip.

Table 4-1: Dimension of the new IOP sensor and its measured electrical parameters

<b>Planar dimension</b>	4 mm (foldable)					
<b>Pressure (mmHg)</b>	0	20	40	60	80	100
<b>Frequency (MHz)</b>	379	381	385	390	395	402
<b>Q Factor</b>	27	27	28	30	28	29
<b>Sensitivity</b>	542 ppm/mmHg					
<b>Responsivity</b>	205 kHz/mmHg					
<b>Sensing distance</b>	2.5 cm					

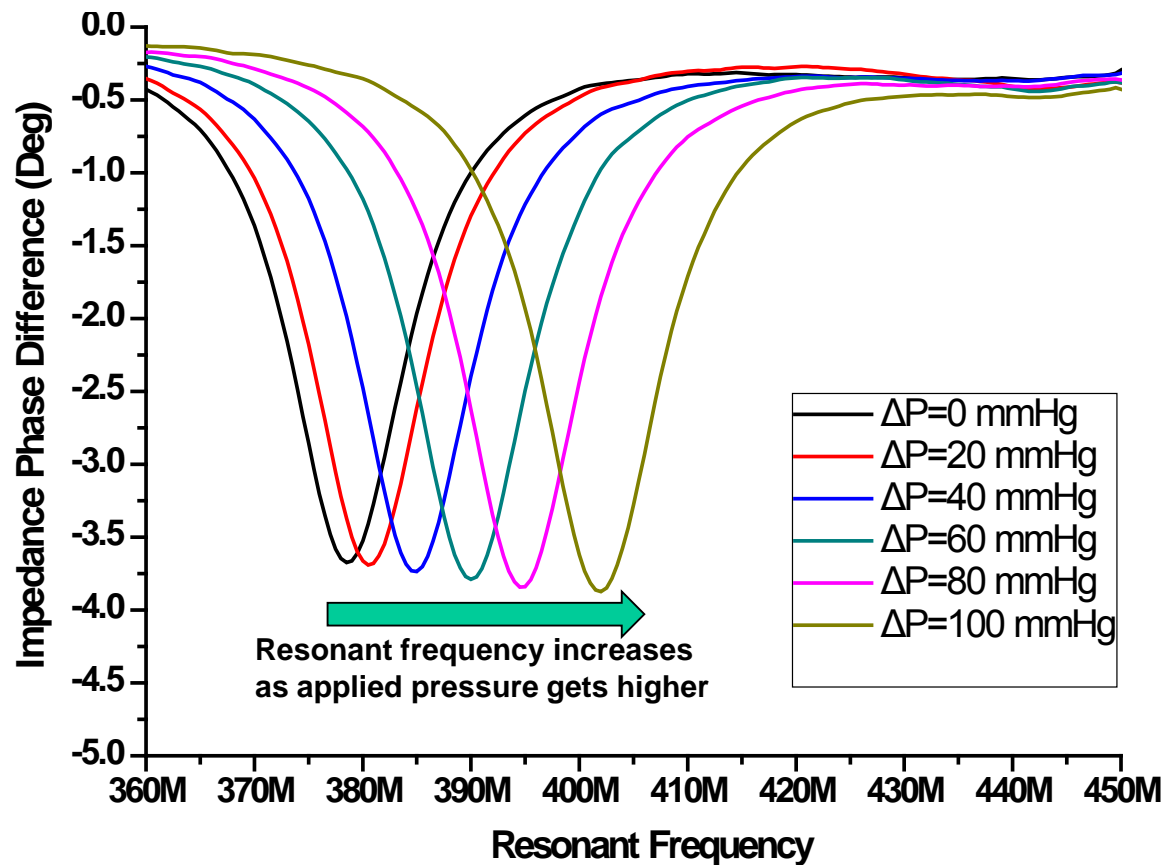


Figure 4-9: Bench-top characterization results of the IOP sensor: the resonant frequency was 379 MHz when the applied pressure difference was 0 mmHg, and shifted to higher frequency when the pressure difference increased.

As the sensing part can always be maintained exposed outside the anterior chamber, the quality factor drop caused by the lossy medium is largely alleviated in this work. Therefore, the new implant possesses farther sensing distance than the one implanted right in the anterior chamber, which was originally designed to have 2.5 cm sensing distance. The new design enables a glass reader paradigm to accomplish the autonomous, continuous, and wireless IOP monitoring.

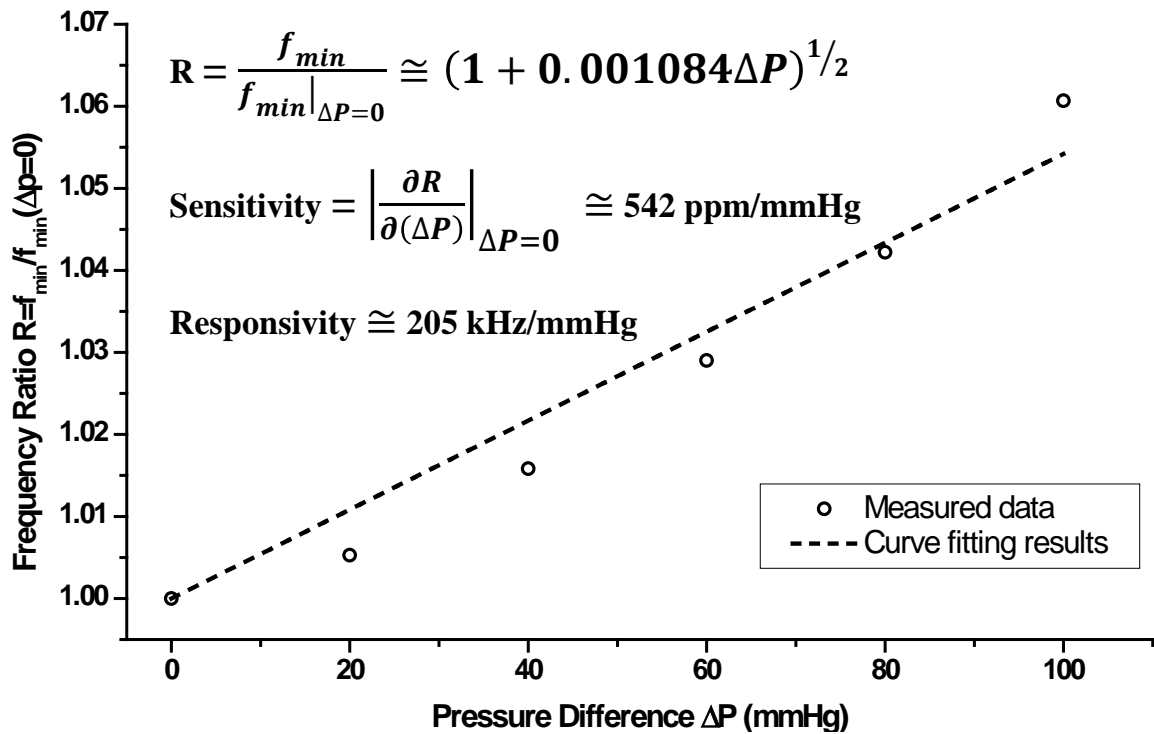


Figure 4-10: Sensitivity analysis of the IOP sensor

The result of sensitivity analysis is shown Figure 4-10. The sensitivity of the IOP sensor is defined as [97]:

$$\text{IOP sensor sensitivity} = \left| \frac{\partial R}{\partial(\Delta P)} \right|_{\Delta P=0}, \quad (4-12)$$

where  $R$  is the frequency ratio defined as:

$$R = \frac{f_{min}}{f_{min(\Delta P=0)}}. \quad (4-13)$$

A sensitivity of 542 ppm/mmHg was obtained for the IOP sensor, corresponding to the responsivity as 205 kHz/mmHg. With a proper designed high resolution external coil reader, the IOP sensor can resolve the pressure difference  $< 1$  mmHg, which is suitable for glaucoma diagnostics.

## 4.5 Quality Factor Recovery Study

### 4.5.1 Overview

As mentioned in [98], the quality factor of the transmitting coil, i.e. transmitting resonant tank, dropped a lot (from  $\sim 30$  down to  $\sim 6$ ) when implanted in the anterior chamber, which resulted in a great reduction of the sensing distance (from 2.5 cm to 1.5 cm). As the loss tangent represents the power loss in the medium, this quality factor drop is due to the high loss tangent of the eye fluid in the anterior chamber. For lossy medium such as saline, the permittivity,  $\epsilon$ , can be written in the complex form as [168–170]:

$$\epsilon = \epsilon' - j\epsilon'', \quad (4-14)$$

with the loss tangent defined as:

$$\text{loss tangent} = \frac{\epsilon''}{\epsilon'} \quad (4-15)$$

which represents the power loss in the medium. The loss tangent value of saline is reported as about 0.2 [95, 169], which is much higher than of the air, and close to that of body tissue and eye fluid. This means the electromagnetic energy of the IOP sensor dissipates more easily in the anterior chamber. Although in our work, only the implantation tube penetrates into the eyeball and leaves the sensing part under the conjunctiva, the quality factor can still drop due to the covering human body tissues.

#### 4.5.2 Q factor recovery by passivation layers of different materials

Except for modifying the implantation scheme as depicted in Section 4.2, another way to solve the problem is to try to strengthen the isolation between the sensor structure and the surrounding medium [95, 97]. In this section, three different materials: regular glass cover slip, photoresist, and regular 5 min epoxy, are used to cover the IOP sensors as the passivation layers to isolate the devices and the surrounding medium. The loss tangents of these covering materials are expected to be lower than the saline, and hence could improve the quality factor when the devices are immersed in the saline.

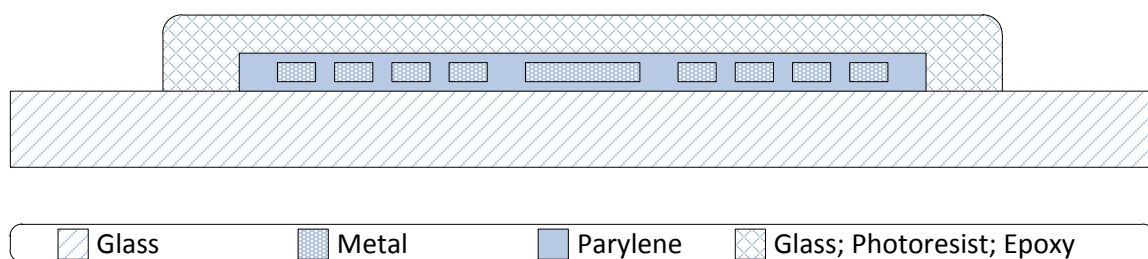


Figure 4-11: The idea of covering the device with different passivation layers: glass cover slip, photoresist, or epoxy. The IOP sensor is shown in gray in the figure.

The idea of covering the devices with passivation layers is shown in Figure 4-11. These testing samples as shown in light blue were first placed on top of the glass cover slips and characterized in the air before they were covered by the passivation layers. Only one passivation layer was then applied to the top of the device and the entire device was characterized again. Two examples of the completed devices are shown in Figure 4-12. The completed devices were tested both in the air and saline to study the efficiency of the covering of the passivation layers. For photoresist as the passivation layer, a

second layer of photoresist was painted on top of the first photoresist layer again followed by the same quality factor characterization procedures to study the thickness effects of the photoresist passivation layers.

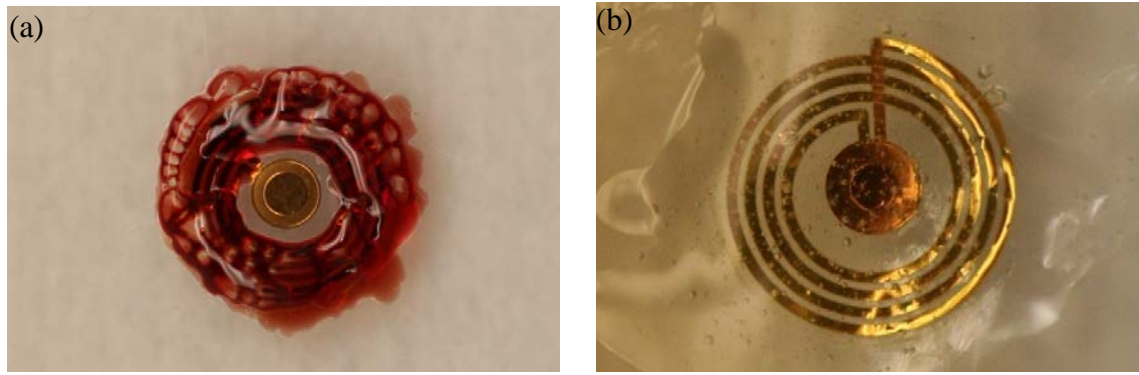


Figure 4-12: IOP sensors covered by two different materials with low loss tangent: (a) photoresist and (b) epoxy

The diameter of the reader coil was about 11 mm and the sensing distance was about 9 mm. The characterization results are shown in Table 4-2. The first device sample was covered by a regular glass cover slip with 0.2 mm in thickness. Sample 2 and 3 shared the same treatment of photoresist passivation layers. Sample 4 was covered by the regular 5-min dry epoxy. The results show that the quality factors of the original devices fell in the range of 23.6–28.76, and dropped from 23.6 measured in the air to 2.69 measured in the saline without any passivation layer (Sample 4).

For the device covered by the cover slip (Sample 1), however, the Q factor was kept almost unchanged and the Q factor was maintained at 15.74. For the two devices covered by the photoresist (Sample 2 and 3), the Q factors dropped from 28.76 (Sample 2) and 27.13 (Sample 3) to 25.37 (Sample 2) and 22.5 (Sample 3) when devices were exposed to the air. Furthermore, the Q factors of Sample 2 and Sample 3 dropped to 4.11

(Sample 2) and 5.07 (Sample 3) when the devices were immersed in the saline. The thickness of one layer of the photoresist was measured about 45  $\mu\text{m}$ . To study the thickness effect of the photoresist passivation layer, another layer of the same type of photoresist was painted on the device again. When the devices were exposed to the air, the obtained Q factors were recovered from 25.37 (Sample 2) and 22.5 (Sample 3) to 25.98 (Sample 2) and 29.48 (Sample 3). When the devices were immersed in the saline, the improvements of the obtained Q factors were more obvious: 4.11 to 10.54 (Sample 2) and 5.07 to 8.98 (Sample 3). Sample 4 was covered by regular 5-min dry epoxy and the result showed that the Q factor dropped from 23.6 to 18.84 (in the air) and 11.49 (in the saline).

Table 4-2: Measured quality factors with different isolation layers covered on top

	<b>Sample 1</b>	<b>Sample 2</b>	<b>Sample 3</b>	<b>Sample 4</b>
<b>No isolation layer Tested in the air</b>	25.47	28.76	27.13	23.6
<b>Isolation layer</b>	Glass cover slip	One side PR	One side PR	---
<b>Isolation layer thickness</b>	---	~ 45 $\mu\text{m}$	~ 45 $\mu\text{m}$	---
<b>In the air</b>	24.43	25.37	22.5	23.6
<b>In saline</b>	15.74	4.11	5.07	2.69
<b>2<sup>nd</sup> isolation layer</b>	----	PR paint again	PR paint again	Epoxy
<b>2<sup>nd</sup> isolation layer thickness</b>	----	~ 90 $\mu\text{m}$	~ 90 $\mu\text{m}$	NA
<b>In the air</b>	----	25.98	29.48	18.84
<b>In saline</b>	----	10.54	8.98	11.49

In summary, it is observed that, when the device is exposed to the air, the measured Q factor has very little change no matter what kind the passivation layer covered on top. In terms of the device characterization in the saline, the Q factors are always smaller than its original values even with the passivation layers. Even though, the characterization results still show that the passivation layers do preserve the Q factors after the passivation layers covering. Among all of the three passivation materials, the glass cover slip demonstrates the best restoring result according to Table 4-2. One of the reasons is because of its high thickness (0.2 mm). The thickness effect of the photoresist passivation layer is very obvious.

On the other hand, the isolation efficiency of the epoxy seems to be better than photoresist when the characterization is performed in the saline, but not in the air. It is likely attributed to the epoxy thickness is much higher than photoresist so that the coil is more effectively isolated from the saline. However, the isolation efficiency of the epoxy for device characterized in the air is not as good as others. It is also found that the two Q factors obtained of sample 4 (both in the air and in saline) are closer in comparison to other passivation materials. The assumption is that the loss tangent of the epoxy is higher than the photoresist, causing a lower Q factor when measured in the air. However, the higher epoxy thickness can more effectively isolate the device from the saline solution, and hence results in a higher Q factor than covered by photoresist.

#### **4.5.3 Q factor recovery by parylene-C passivation layers**

Section 4.5.2 has successfully demonstrated the concept of recovering the Q factor to a certain level by covering the devices with passivation layers. However, those materials used in Section 4.5.2 are either not flexible enough (glass cover slip) or not

biocompatible at all (photoresist and 5-min-dry epoxy). In order to recover the device's Q factor while still preserving its biocompatibility, a material needs to not only have a low loss tangent, but also to be flexible and biocompatible.

In addition to its superior flexibility and biocompatibility, parylene-C is also compatible with the most of the surface micromachining fabrication procedures and hence has very good machinability. Furthermore, parylene-C is found to have loss tangent with 0.1 [171], which is much lower than saline (0.2), implying that it can be a very good candidate for the passivation layers described in Section 4.5.2. Therefore, to restore the high quality factor, quantitative investigation has also been done by putting multi-layer parylene-C films on top of the sensing coil to regain its quality factor when it is submersed in the saline.

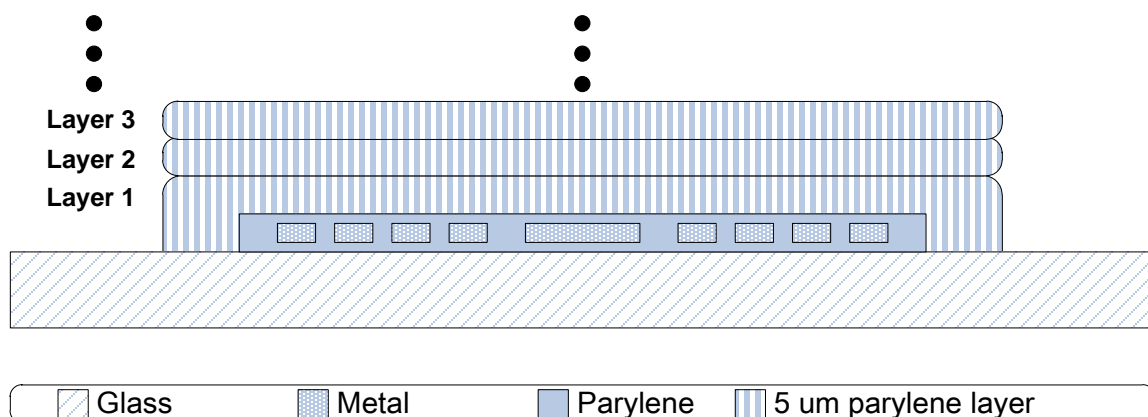


Figure 4-13: The idea of covering the device with several layers of parylene-C sheets. The IOP sensor is shown in gray in the figure.

The concept of the experiment is shown in Figure 4-13. An original sensing coil with the 7  $\mu\text{m}$  parylene-C deposited on top was first mounted onto a glass slide. Multiple 5- $\mu\text{m}$ -thick parylene-C films were put on top of the sensing coil layer by layer until 40

$\mu\text{m}$  parylene-C accumulated. Every time before the next 5  $\mu\text{m}$  parylene-C film was put on, the coil was characterized both exposed in the air and also submersed in the saline. The quality factors were calculated to investigate the quality factor recovery capability with respect to different parylene-C thicknesses.

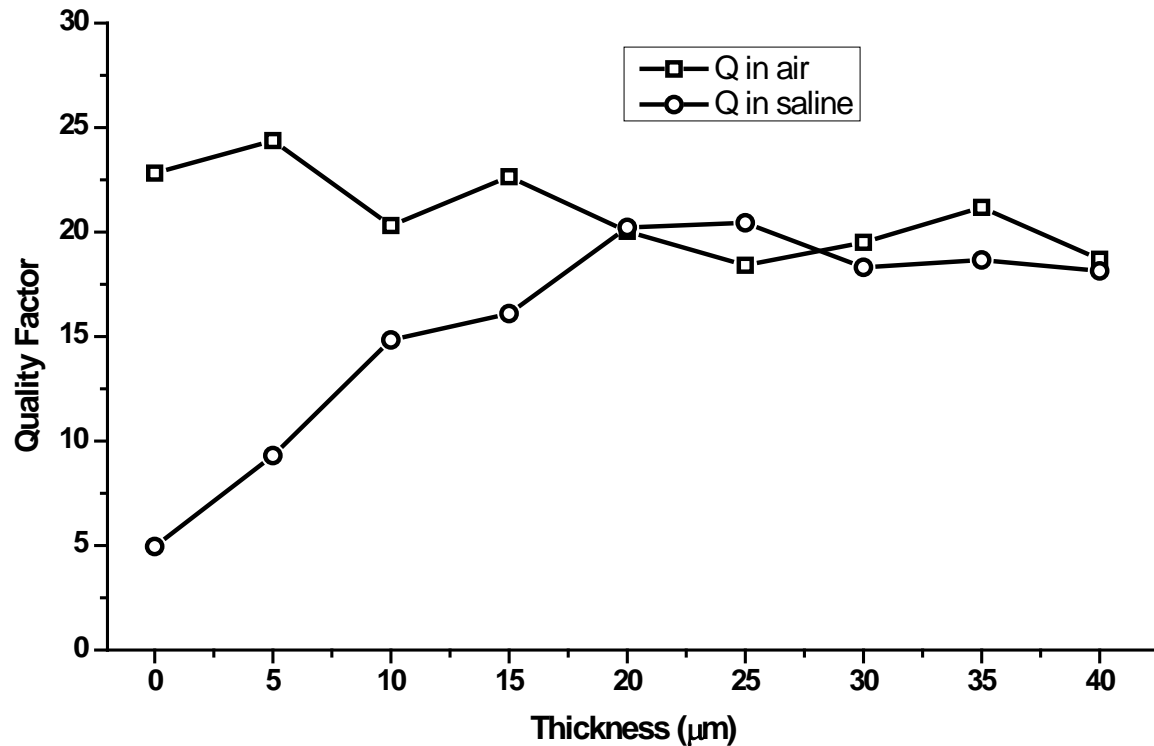


Figure 4-14: Quality factor recovering results versus parylene-C thickness by covering the IOP sensor with several parylene-C layers

The sensor's quality factor measuring result versus the parylene-C layer thickness is shown in Figure 4-14. When only 7- $\mu\text{m}$ -thick parylene-C covered on top of the sensing coil (the original sensing coil), the quality factor was measured only 4.95 in saline while it was measured as 22.83 in the air. The obtained quality factors (in saline) increased with the increasing parylene-C thicknesses, and saturates at about 17–20 when

the parylene-C thickness reached 20  $\mu\text{m}$ . In other words, the Q factor measured with the device immersed in the saline was noticeably recovered. As the recovered Q factor (device immersed in saline) reached the same level as the Q factor (device exposed to the air) when the parylene-C thickness reached 20  $\mu\text{m}$ , we concluded that the sensing coil would not be affected by the surrounding saline when the thickness of the covering parylene-C layer reached 27 (20+7)  $\mu\text{m}$ . It is therefore proved that a 30- $\mu\text{m}$ -thick parylene-C passivation layer is sufficiently thick to be deposited on top of the metal coil.

It is also found that the quality factor measured with the device exposed in the air dropped a bit from 22.82 to  $\sim 20$  as the parylene-C passivation layer increases. This is likely attributed to the fact that the loss tangent of the parylene-C, 0.1, is still higher than the air.

#### **4.5.4 Summary**

In summary, it is found that the Q factor can be recovered by covering the devices with at least extra 20  $\mu\text{m}$  parylene-C passivation layers. Theoretically, 20  $\mu\text{m}$  parylene-C can be easily created by standard parylene-C deposition process and then patterned by oxygen plasma. It needs to be noted that, however, during the parylene-C deposition, 20- $\mu\text{m}$ -thick parylene-C would also deposit onto the metal plates of the parallel metal-plates capacitor. This would increase the parylene-C thickness of the deformable plate, resulting in the loss of the capacitor sensitivity. To overcome this problem, one more process with oxygen plasma etching could be used to thin down the parylene-C layer right on top of the metal-plate capacitor, as demonstrated in Figure 4-15.

## 4.6 Summary and Conclusion

In this chapter, we have successfully demonstrated the feasibility of the new concept and design of the IOP sensor implant. A parylene-C-based sensing part with about 30  $\mu\text{m}$  in overall thickness was first fabricated, and then integrated with an implantation tube attached to the sensor's backside pressure access hole.

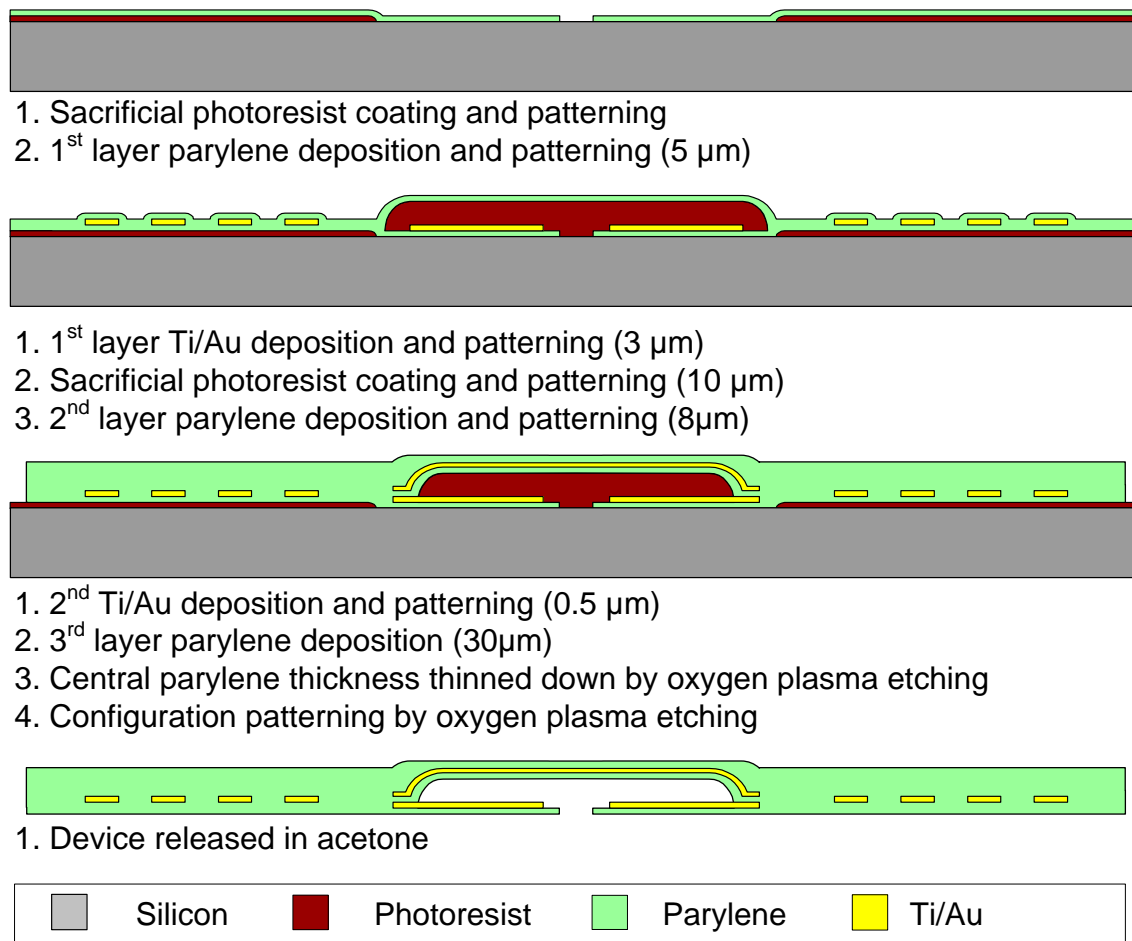


Figure 4-15: Modified sensing coil fabrication procedures: After 30  $\mu\text{m}$  parylene-C layer is deposited on top of the capacitor metal plate, an extra oxygen plasma etching process is executed to thin down the central parylene-C to retain the capacitor sensitivity.

A new surgical placement of the device was also proposed. The new IOP sensor was implanted at the pars plana with the implantation tube penetrating through the choroid, while the sensing part still remained outside the eyeball but covered by the conjunctiva. Without the influence of the surrounding aqueous humor, this implantation approach can maintain the high quality factor of the device and thus a 2.5 cm sensing distance can be fulfilled. This enables the glass reader paradigm concept, and therefore achieves autonomous, continuous and wireless IOP monitoring.

The sensitivity was obtained as high as 542 ppm/mmHg while the responsivity was about 205 kHz/mmHg. The characterized IOP sensor is ready for use, and the *ex vivo/ in vivo* test can be scheduled in the near future to verify the biological feasibility. In addition, the future work would also focus on the fixation of the IOP sensor. The possible solution would include enlarging the parylene-C area of the sensing coil of the device, enabling the possible suturing of the parylene-C sensing part.

Besides, the quality factor can be recovered also by covering the device by low loss tangent materials as passivation layers to isolate the device and the saline. It is found in Section 4.5 that parylene-C is a very good passivation layer to recover the Q factor due to its low loss tangent. Experimental results showed that the Q factor was mostly recovered by an extra 20  $\mu\text{m}$  parylene-C film. We demonstrated that a 30- $\mu\text{m}$ -thick parylene-C on the capacitor metal plate could maintain the sensor's high quality factor in saline or under human tissue.

Furthermore, parylene-C isolation layer can also be easily achieved by standard parylene-C deposition process, followed by oxygen plasma etching to remove the excess parylene-C on top of the capacitor to maintain the sensitivity of the IOP sensor.



---

# CHAPTER 5

---

## CHARACTERISTICS OF PARYLENE-C FILM

### 5.1 Overview

In this chapter, a systematical study of some parylene-C's properties is performed and discussed. To explore parylene-C's mechanical, rheological, and viscoplastic properties, the chapter starts with the introduction of parylene-C's polymer properties: polymerization, densification, and oxidation followed by a detailed study of crystallization/densification and discussions about them. It shows that the crystallization is one of the major effects causing parylene-C to behave differently after thermal treatment.

The mechanical properties, rheological properties and viscoplastic properties of the parylene-C film were studied using TA Instruments DMA Q800. Among many mechanical properties, Young's modulus, tensile strength and elongation are primarily concerning in terms of implantation applications and therefore were considered in this chapter. Mechanical properties can be known by many ways. For example, Young's modulus and residual stress can be obtained simultaneously by load-deflection approach [103, 138]. In our study, mechanical properties were obtained by uniaxial tensile test due to its simplicity and popularity.

Although it has been long since people started to use parylene-C in the implantable devices, its rheological properties and viscoplastic properties have not been

thoroughly studied yet. By using the same testing setup as mentioned above, creep and stress relaxation, and viscoplastic properties were measured as well. These properties provide very important information for parylene-C-based medical devices in terms of their fabrication and later implantation in human bodies. With the knowledge of these properties, the life-time of the devices is predictable, the device fabrication time could be reduced, and the residual stress generation by annealing the device at a proper temperature is avoidable.

It also shows that the rheological testing results of parylene-C film are highly temperature-dependent. To understand this, except the crystallization results, the glass transition temperature was measured by both dynamic mechanical analysis (DMA) approach and a ramping-temperature-dependent modulus experiment. Both obtained results were compared and discussed to explain the rheological testing results.

## **5.2 Introduction to Parylene-C Polymerization**

The current most common way to prepare Parylene-C film is done by chemical vapor deposition invented by W. F. Gorham in 1966 [172]. Gorham's approach is also commonly used to prepare other parylene (poly-para-xylylene) family members, such as parylene-N (poly-para-xylylene), parylene-D (poly-dichloro-para-xylylene), parylene-C (poly-chloro-para-xylylene), or parylene-HT (or parylene-F, poly-tetrafluoro-para-xylylene) to name a few. During the parylene-C preparation, the parylene-C dimer is sublimated at elevated temperature (180°C in our deposition process), and pyrolysed at 690°C. The parylene-C film can conformally deposit onto the substrate and also the temperature of the chamber wall could range from -196°C to room temperature [173,

174]. Because the parylene-C polymerizes right from the gaseous type, the process is also called vapor deposition polymerization (VDP) [175].

It is parylene-N polymerization which was first focused on and studied. Errede published the mechanism of polymerization of parylene-N in 1960 [176]. Rather than using Gorham's vapor deposition approach to get the parylene-N film, Errede prepared parylene monomer liquid solution at  $-78^{\circ}\text{C}$ . Polymerization happens when the solution is disturbed by momentary contact with a warm surface. Beach proposed a model for the vapor deposition parylene-N for the first time in 1978 [177]. Gaynor, Rogojevic and Fortin also developed different kinds of models to describe the vapor deposition of parylene-N thin film after Beach [178–180].

Some of previous researchers' important findings are summarized in this section. The molecular weight of parylene-N is found to be 200,000 to 400,000 g/mol, which corresponds to 2000–4000 units per chain length [178]. In addition, the deposition rate of parylene-C is found to decrease as the deposition temperature rises, which is opposite to the regular chemical vapor deposition reaction that shows higher deposition rate as the deposition temperature rises. It is suggested that the higher deposition rates of the parylene family at lower temperature are caused by increased monomer condensation rate on the substrate surfaces [181].

### **5.3 Densification**

Densification means the polymer chain becoming more compact than its original chain structure. Theoretically speaking, densification can be caused by thermal treatment which gives polymer chain energy to move, or by stretch force which causes the polymer chain to align closer. In densification, the polymer chains do not need to be well

organized to form a lamella, but the polymer chains are getting closer to fill in the voids of the material, which usually results in the reduction of the volume. Therefore, the densification can be observed by measuring the materials' dimension. There hasn't been too much research work done to study the densification of the parylene-C film to our best knowledge. The first related study could be found to be done by Wu in 1995 [182]. Wu and the coworkers measured in situ the thickness of parylene-N and parylene-F at elevated temperature up to the sample decomposing. Their results showed no thickness reduction or increment before the samples decomposed, regardless of whether the annealing was done in air, nitrogen or vacuum. In 2005, Huang et al. published a paper studying the glass transition temperature of ultra-thin parylene-C film (21 nm) deposited on silicon substrate by in situ measuring the film's thickness change [183]. They used an ellipsometer to measure the thickness of the sample from temperature at 0°C to 120°C. The results showed that the thickness increases monotonically, with a thermal expansion coefficient turning point occurring at the glass transition temperature or so. In spite of their successful findings of the glass transition temperature, the thermal expansion coefficients found from their results showed a value of 1190 ppm and 2143 ppm below and above the glass transition temperature, respectively. Because of the contradiction between Wu and Huang, it is of interest to measure the parylene-C film thickness change in the usage thickness range.

In this section, the densification of 20- $\mu\text{m}$ -thick parylene-C film is studied at 100°C. In addition, the parylene-C film's length change during thermal annealing at ramping rate of 3.33°C/min is measured as well.

### 5.3.1 Thickness-change measurement

To measure the thickness change of 20- $\mu\text{m}$ -thick parylene-C film, a layer of parylene-C film of 20  $\mu\text{m}$  thickness was first deposited on top of a clean glass plate. A parylene-C step was then created by stripping part of the parylene-C film for later thickness measurement. Parylene-C film was put in the convection oven which was preheated at 100°C for a targeted duration. When time was up, the parylene-C was taken out and cooled down to room temperature. A KLA-Tencor P-15 profiler was used to measure the parylene-C thickness. The measurement was performed before the thermal annealing and every time the parylene-C film was cooled down. 5 data points at different positions were obtained in each measurement corresponding to each annealing time.

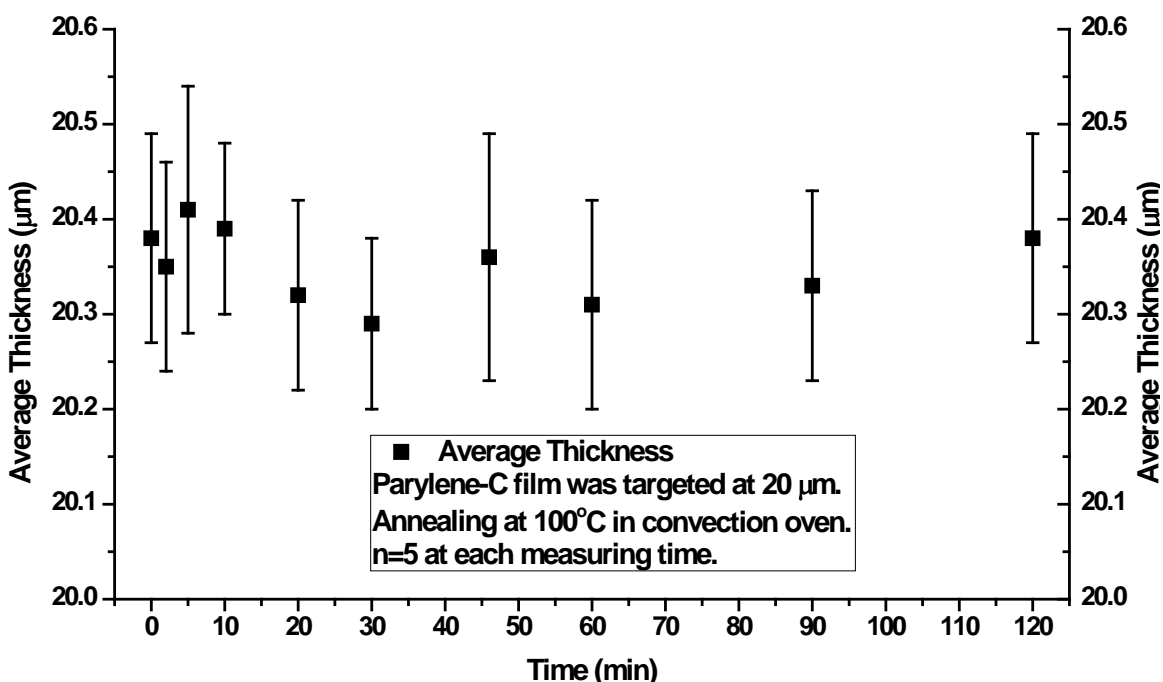


Figure 5-1: Measured thickness of 20  $\mu\text{m}$  parylene-C film annealed at 100°C in the convection oven

The obtained thickness data versus annealing time is shown in Figure 5-1. Although there is some variation (error bar) at each measurement, the average thickness falls in a constant range without too much change during the thermal annealing. The changing of the average thickness versus time cannot show any correlation between the thickness and annealing time as the thickness always lies in the error range. The results demonstrate that the parylene-C film thickness change is not detectable within the 2 hours of annealing at 100°C in convection oven with our current measuring capabilities. Our measuring data agrees well with Wu's results. It might be due to the thickness effect that Huang's parylene-C film behaves differently.

### **5.3.2 In situ length-change measurement during thermal annealing**

#### ***5.3.2.1 Length change under long-time thermal annealing process at 100°C***

An experiment monitoring the length change of the parylene-C film during the thermal annealing was also conducted. With the same sample thickness prepared as above (as-deposited parylene-C film), the free standing parylene-C film was cut into 5.3 mm (W) by 10mm (L) in dimension and mounted onto the clamps of the DMAQ800 with a tiny little force (0.0027N). The chamber temperature was ramped up to 100°C in the machine's fastest way and the length of the sample was monitored at the same time. After the chamber was thermally stabilized, the sample was annealed in this environment for eight hours to observe its length change. Once the annealing is done, the chamber was then fast cooled down to room temperature by blowing cool nitrogen gas into the chamber. The whole system was kept in room temperature for another two hours to observe the parylene-C film length change.

The obtained length change of parylene-C film annealed at 100°C is shown in Figure 5-2. All system response is corrected and thus the data shown represents the true parylene-C film response. Figure 5-2 (a) shows the length change of the whole annealing and cooling period. Figure 5-2 (b) shows the closer view of the length response of the parylene-C film between 0–2.5 minutes. Figure 5-2 shows that the as-deposited parylene-C film length actually shrinks when the environmental temperature increases higher than ~ 40°C. The rate of the length change reduces after the temperature reaches the target temperature, and slows down. In Figure 5-2 (b), it is observed that the sample length actually elongates before 0.25 minutes, which corresponds to 38.76°C in the raw data, and start to shrink afterward. It infers that the parylene-C starts to have some structural change at 38.76°C and thus the length shrinks. The hypothesis of this phenomenon is that the parylene-C is likely to start to crystallize at 38.76°C. As from the conventional wisdom of solid state thermodynamic transitions regarding the glass transition, no crystallization should be able to take place below the glass transition temperature [184, 185], plus the parylene polymer chain orientation is proved to lie in the plane of the film [186], Figure 5-2 could be treated as an evidence that the parylene-C film crystallization starts from temperature at 38.76°C, i.e., the onset of glass transition range. The concept and experiments regarding the glass transition temperature will be discussed more in detail in Section 5.6. It is postulated that the parylene polymer chain folds into several lamellae, constituting the spherulite of the parylene-C. Therefore, the parylene-C length reduces during this crystallization process. The slowly length shortening after thermally stabilized at 100°C is likely attributed to the slow isothermal crystallization behavior, which will be studied by XRD approach in Section 5.5.

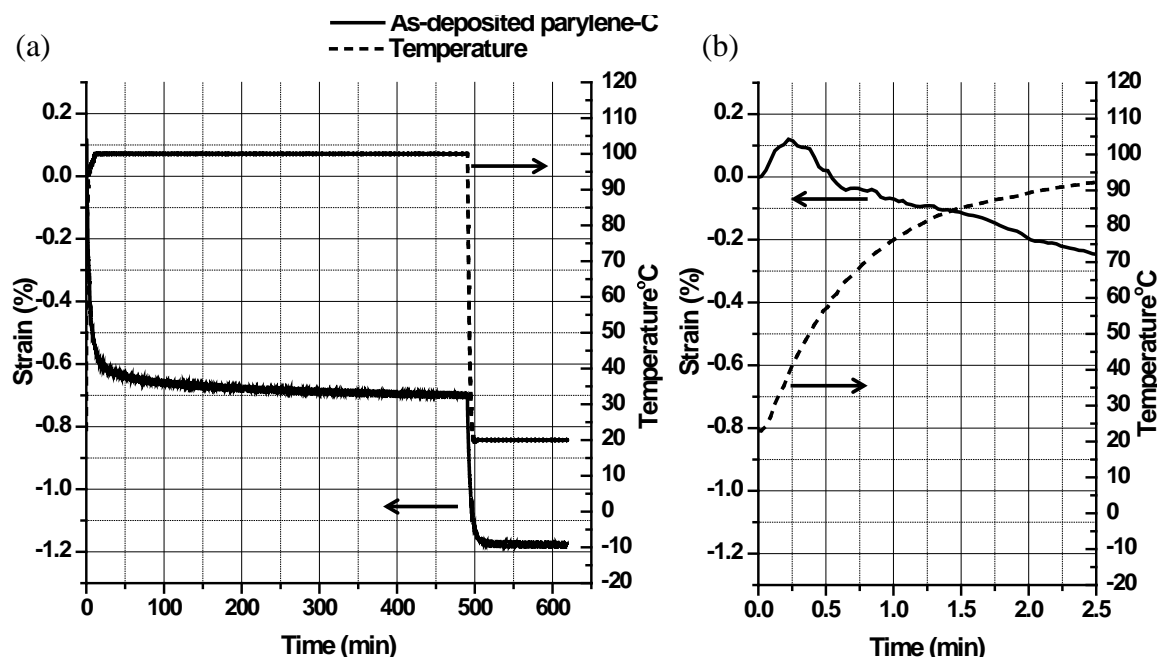


Figure 5-2: (a) Obtained length change of the parylene-C film annealed at 100°C in air for 8 hours, and (b) a closer view of the length change during the first 2.5 minutes

In order to further prove that the as-deposited parylene-C is crystallized during the annealing process, the parylene-C sample previously annealed at 100°C for eight hours was tested again in the same annealing condition for another two hours, and the testing results is shown in Figure 5-3. It can be clearly seen that, rather than length shrinkage, the parylene-C film expands during the early temperature ramping up period, which is totally opposite to the as-deposited parylene-C's results. Although the parylene-C is very likely still crystallizing during this period, the thermal expansion effect of the parylene spherulite dominates the length change. Thus the overall effect shows that the parylene-C film is expanding. After the chamber is thermally stabilized again, the parylene-C film has no (or very little) expansion and the crystallization mechanism dominates the length change again. The thermal coefficients of expansion (TCE) of as-deposited and annealed parylene-C film are also estimated from Figure 5-2 (a) and Figure 5-3. Three TCE

obtained from these two figures are shown in the first three columns of Table 5-1: TCE of the 8-hours-annealed sample cooled down, TCE of the annealed sample heated up, and TCE of the 10-hours-annealed sample cooled down.

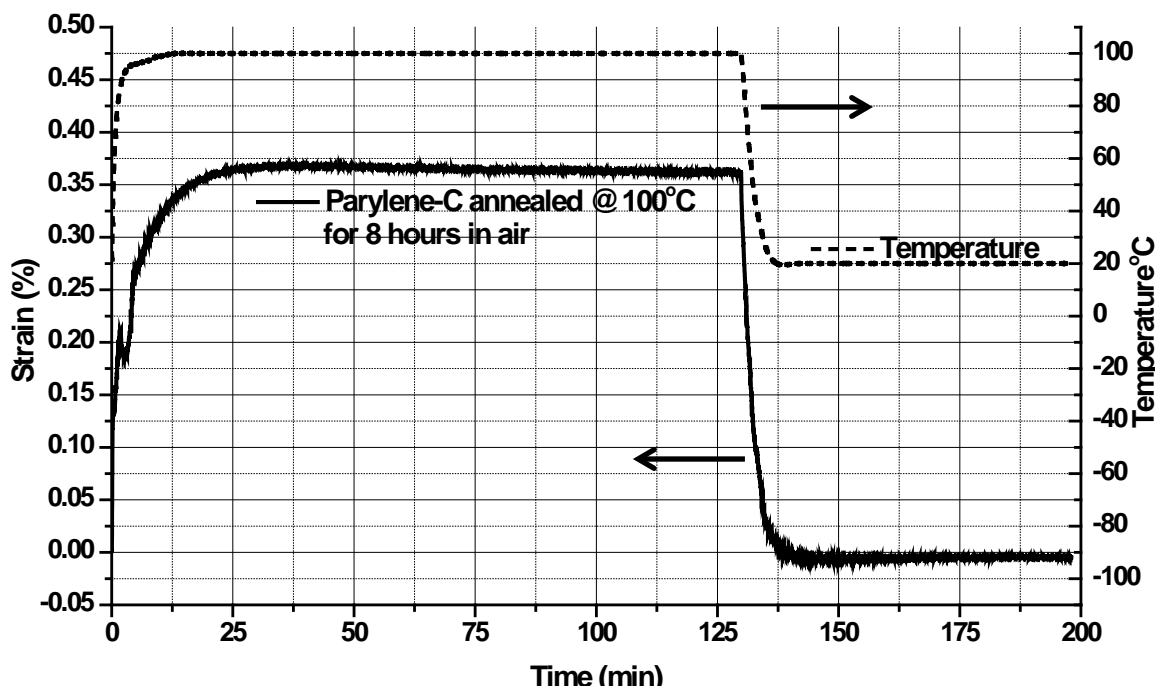


Figure 5-3: Length change of the parylene-C film which was annealed at 100°C in air for 8 hours in the previous test. The sample was annealed again at 100°C for another 2 hours.

Table 5-1: Table of thermal coefficients of expansions obtained in different states of the parylene-C film. The literature values are also listed for comparison.

	Annealed 8 hours at 100°C, cooled down to room temperature (Figure 5-2 (a))	Followed from the previous sample and heated up to 100°C (Figure 5-3)	Annealed another 2 hours and cooled down to room temperature (Figure 5-3)	As-deposited parylene-C heated up to transition (Figure 5-4)	Literature value by Beach [101]	Experimental value obtained by Dabral [110]
TCE (ppm)	60	56.3	58.8	35.5	35	50

### 5.3.2.2 *One cycle thermal annealing treatment*

Although the TCE below parylene-C's glass transition temperature can be obtained from the experiments described in Section 5.3.2.1, the temperature ramping, however, is extremely fast in that case. Therefore another test under a slower temperature ramping rate was performed to verify the expansion behavior below and above the glass transition temperature and the results are shown in Figure 5-4. It could be seen that in a slower temperature ramping profile, the sample expands until 53.75°C owing to the thermal expansion and starts to shrink afterward. The temperature, 53.75°C, actually agrees perfectly well with our glass transition found in Section 5.6 and therefore it is hypothesized that the parylene-C starts to crystallize at 53.75°C. The expansion phenomenon above 120°C is likely due to the dominating oxidation effect. The oxygen atoms are involved into the parylene-C structure and therefore expand the parylene-C sample again until it gets decomposed at 240°C.

The obtained TCE of each region is shown in Table 5-1. From Table 5-1, the TCE of annealed parylene-C usually lies in the range of 56.3–60 ppm. The TCE obtained before parylene-C's glass transition is 35.5 ppm, which agrees well with Beach's literature value measured at 25°C [101]. The difference of the TCE between annealed and as-deposited parylene-C can be explained on the basis of changes in the parylene-C's properties due to annealing which gives parylene-C higher crystallinity [110]. More discussion and study of crystallinity will be in Section 5.5. In addition, Dabral obtained TCE as 50 ppm from his annealing samples below 150°C. The difference between his result and our TCE result is about 11.2–16.7%. Apart from the measuring resolution errors, it is very likely that Dabral's parylene-C film has been annealed up to 250°C,

which could introduce another polymer structure transition from  $\alpha$  form to  $\beta$  form. Thus the Dabral's TCE could represent the property of  $\beta$ -form parylene-C film while ours could represent  $\alpha$  form as our sample annealed only up to 100°C.

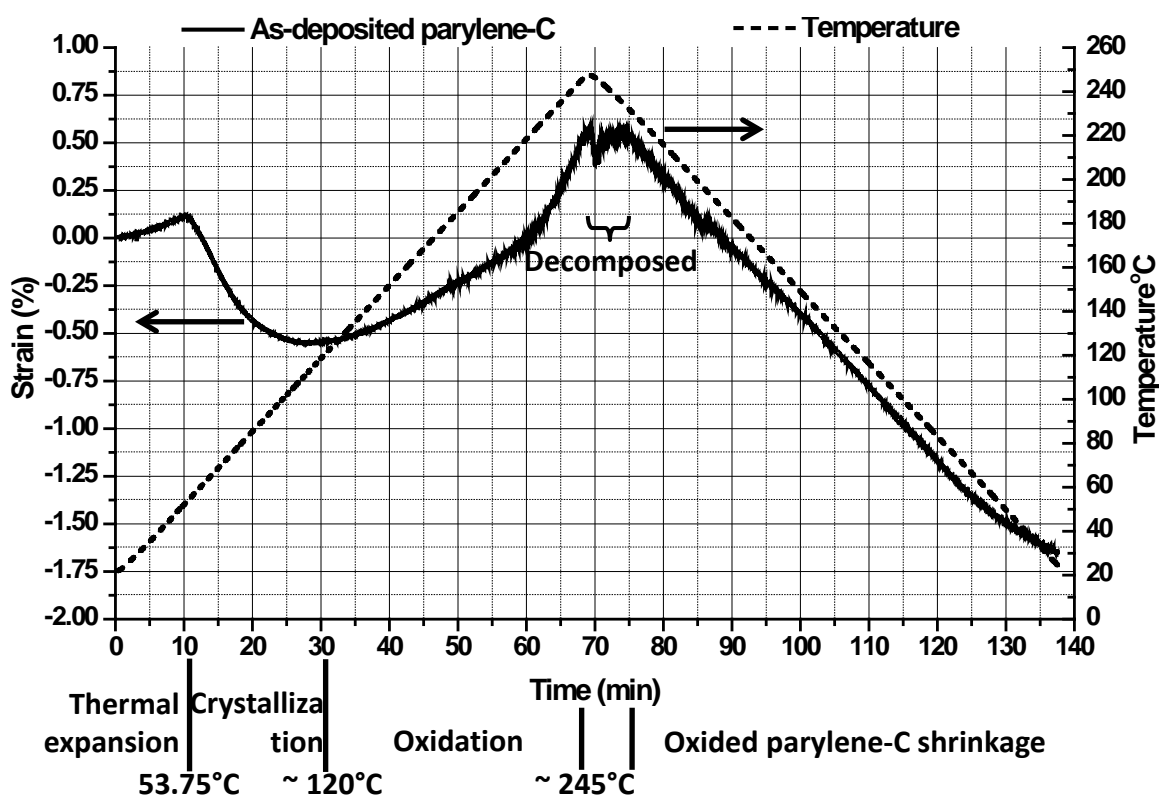


Figure 5-4: Length change of parylene-C film annealed under the temperature ramping rate at 3.33°C/min and its hypothesized phenomenon interpretation by dominant effect

### 5.3.2.3 Cyclic thermal annealing treatment up to 120°C

The experiment done in Section 5.3.2.2 shows only one cycle of parylene-C thermal annealing. The TCEs before and after the thermal annealing are found. Figure 5-4 also demonstrates that the parylene-C sample decomposed at  $\sim 240^\circ\text{C}$  in the normal air environment. In this section, another experiment was designed to study the behavior of the parylene-C sample annealed under cyclic thermal conditions. As-deposited

parylene-C film was still used during the tests. The annealing temperature ramped from 20°C to 120°C at the ramping rate of 3.33°C/min. Right after the temperature reached 120°C, it cooled down to 20°C at the rate of -3.33°C/min. The chamber temperature was then maintained at 20°C for another 30 min. Six cycles were executed in this experiment and the temperature profile is demonstrated in Figure 5-5.

The measuring results are shown in Figure 5-5 and Figure 5-6. It can be seen that the parylene-C first expanded as expected until temperature reached 60°C, which can be identified as the glass transition temperature. The strain decreased dramatically to  $\sim -1.4\%$  when the temperature reached 120°C, meaning the parylene-C sample was shrinking as annealing temperature increased over 60°C. The strain further decreased when the temperature decreased from 120°C to 20°C as well. However, the shrinkage showed more linear proportional to the temperature during this state than when the temperature-ramped from 60–120°C in the first state. The strain shrank to  $\sim -2\%$  when the temperature reached 20°C. Furthermore, the film expanded pretty linearly proportionally to the temperature when the temperature either ramped up from 20°C to 120°C or cooled down to 20°C again in the second and later cycles. More detailed quantitative results are shown in Table 5-2. The TCE was found as 29.2 ppm in the first expansion state until 60°C and -249.6 ppm in average when parylene-C shrank to -1.41% afterward until 120°C. The TCE became 59.8 ppm during the first cooling process. The obtained TCEs of the second and later cycles were always higher than the literature value, 35 ppm. It is evident that the parylene-C experienced either transition, transformation, or crystallization, etc. during 60–120°C. Therefore, after the first-time annealing, the parylene-C possesses different thermal properties than the as-deposited one.

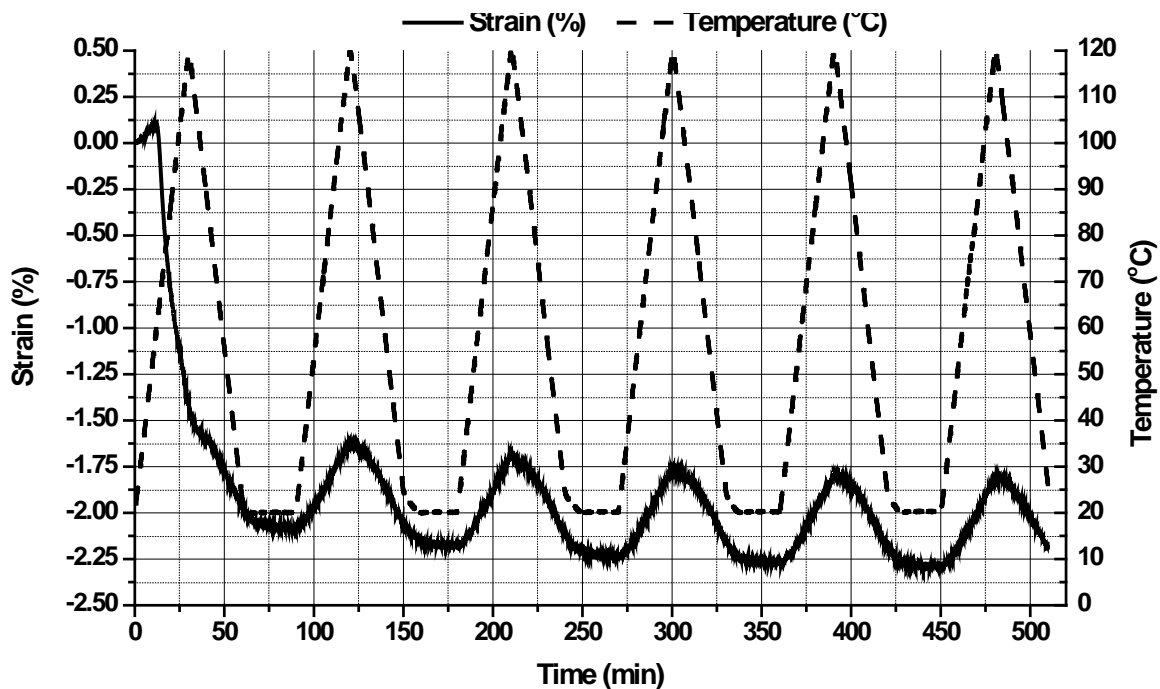


Figure 5-5: Six cycles of thermal annealing of parylene-C film up to 120°C: The length of the film never goes back to its original length after the first-time thermal annealing.

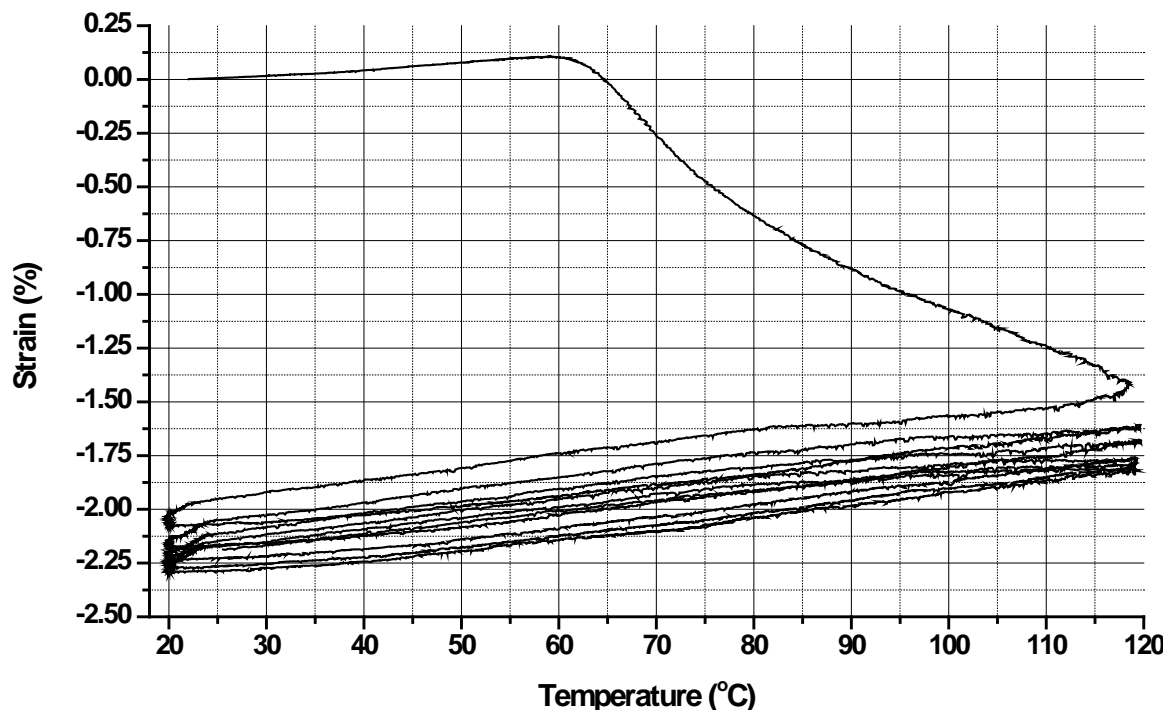


Figure 5-6: The parylene-C film behaves differently after the first-time thermal annealing.

Table 5-2: Derived TCEs from six cycles shown in Figure 5-5 and Figure 5-6

n <sup>th</sup> cycle		1			2			3			4			5			6		
Temperature range (°C)	From	22.0	57.9	118.6	20.0	119.7	20	119.7	20	119.3	20	119.3	20	119.3	20	119.4	25.5		
	To	57.9	118.6	20.0	119.7	20	119.7	20	119.3	20	119.3	20	119.3	20	119.4	25.5			
Strain variation (%)	From	0	0.105	-1.41	-2.08	-1.61	-2.18	-1.69	-2.23	-1.77	-2.27	-1.78	-2.29	-1.82					
	To	0.11	-1.41	2.0	-1.61	-2.15	-1.69	-2.20	-1.77	-2.23	-1.78	-2.25	-1.82	-2.19					
TCE (ppm)		29.2	249.6	59.8	47.4	53.9	49.1	51.2	46.3	46.3	49.3	47.3	47.3	39.4					

### 5.3.3 Summary

Three experiments measuring the length change during the parylene-C thermal annealing were done. In the past, it was generally believed that the parylene-C film expands when it is heated up. In our tests, however, the as-deposited parylene-C film actually expands only up to the glass transition temperature and shrinks afterward until the temperature reaches 120°C. It is likely due to the crystallization effect above the glass transition temperature. The experimental results also show that the parylene-C sample expands again after 120°C, which is believed that the oxidation dominates this stage and oxygen atoms get involved into the parylene-C structure. The sample decomposed at temperature higher than 245°C. The thermal coefficients of expansion of as-deposited and annealed parylene-C film are found to be different. The thermal coefficient of expansion of as-deposited parylene-C is found pretty similar to the literature value, but it becomes higher after the thermal annealing. This is likely attributed to the higher crystallinity of annealed samples. Due to the miniature size of the MEMS devices, this thermal expansion effect and difference can be a critical issue when designing the parylene-C related MEMS devices and thus should be considered in the devices' design to avoid unwanted cracks or residual stress.

## 5.4 Oxidation

Like many other kinds of polymers, parylene-C can get oxidized by either thermally heating [187–189] or by UV light photoluminescence [190–194]. Because parylene-C is transparent, colorless, and conformal well to all irregularities, and has low permeability to air and moisture, and pin-hole free material structure, it has been used for conservation materials [187]. Therefore, research about parylene-C oxidation should focus more on predicting the lifetime of the as-deposited parylene-C film. Nowlin et al. published a paper studying the thermal oxidation of parylene-C film at temperatures between 125 to 200°C [189]. Nowlin used neutron activation (NA) oxygen analysis to quantitatively analyze the oxidative degradation of the parylene-C film's mechanical properties. Their result indicates that the amount of oxygen incorporated into the parylene-C before a significant degradation in mechanical properties is 5000 ppm. The activation energy for the parylene-C oxidation is found to be  $27 \pm 3$  kcal/mole. The temperature for 100,000 hour lifetime use of parylene-C is predicted as 72°C. In addition, they used IR spectrometer to conclude that the oxidation took place throughout the entire sample, not just on the surface. By IR spectrometry, Nowlin also claimed that the oxidized species produced during the oxidation process should be in the form shown in Figure 5-7, which contained the carbonyl bond, rather than the cleavage of the carbon-carbon bond. Baker founded in 1977 that no aging effects of yield stress and tensile modulus were noted in the parylenec-C annealed at 71°C [195]. Monk also suggested in 1997 that 105°C is the recommended maximum annealing temperature where parylene-C will not crack in their encapsulation coatings [188], which infers very little oxidation happens at those temperatures. In this section, the oxidative behavior will be first studied

by XPS (photoelectron spectroscopy) and FTIR (Fourier transform infrared spectroscopy). The corresponding mechanical properties will be discussed in later sections.

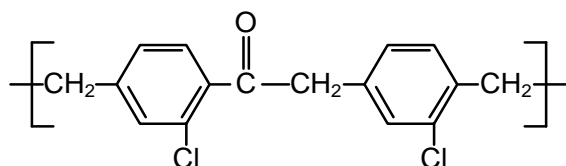


Figure 5-7: The oxidative species of parylene-C proposed by Nowlin [189]

#### 5.4.1 XPS

XPS (X-ray photoelectron spectroscopy) is widely used by chemists in surface chemistry analysis. In XPS, the high-energy x-ray photons are emitted onto the material surface and the material's electrons are excited and come out due to the "photoelectron effect". The escaped electrons are collected by the detector and their corresponding electron energy (or binding energy) is analyzed. Because electrons' binding energy are different from molecule to molecule, the material's surface compound can be derived according to these obtained binding energy data. The XPS machine we used is M-Probe XPS by Surface Science Instruments. Argon sputter was always on to calibrate the peak which represents carbon at 285 eV.

To measure the level of the oxidation of the parylene-C film versus the annealing time, several as-deposited parylene-C films were annealed at 200°C in convection oven for different time durations. A figure of typical XPS scanning results representing four different oxidation treatments is shown in Figure 5-8: as-deposited, 200°C for two minutes, 200°C for one hour, and 200°C for two days, all in the convection oven. The XPS faithfully displays the chemical contents of parylene-C. The chlorine is shown by

two peaks of 199.9 eV (2p) and 270 eV (2s), respectively, and carbon is shown at the peak of 284.6 eV. If the oxygen exists on the parylene-C surface, the XPS can find it as a peak located at 531.6 eV. To clearly see the difference of oxygen peaks between parylene-C films of different treatment, a closer view around the oxygen peak at 531.6 eV is also magnified in the top left of Figure 5-8. The contents of the three atoms (oxygen, carbon and chlorine) can be calculated by integrating over every peak representing the corresponding atom, and the percentage is shown in Table 5-3. From the XPS results of as-deposited parylene-C film, it can be found that the ratio of contents of chlorine to carbon is about 1:8, which agrees well with the parylene-C's chemical compound structure. The correct XPS-measured ratio demonstrates the accuracy of the XPS equipment.

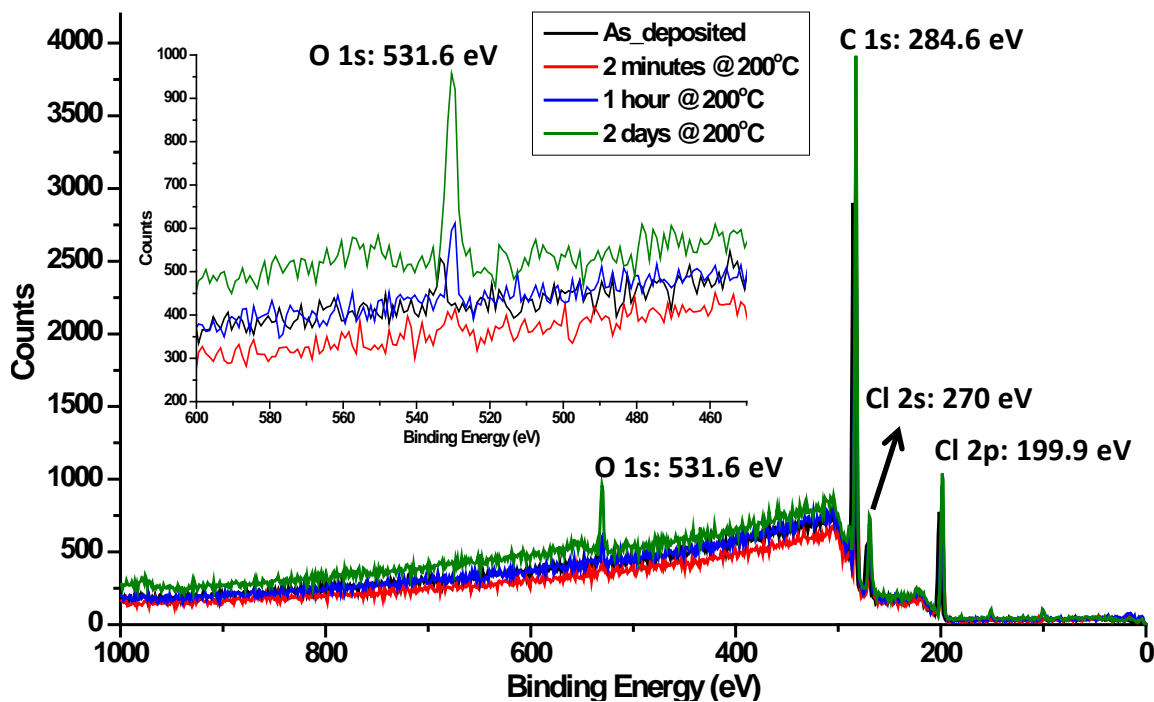


Figure 5-8: Typical XPS results of parylene-C samples. Top left: A closer view of the peak of 531.6 eV representing the content of oxygen

Table 5-3: Measured atom percentage of chlorine, carbon, and oxygen for different oxidative parylene-C films

Parylene-C treatment	Atom Percentage		
	Chlorine	Carbon	Oxygen
As-deposited	10.46	84.76	4.78
200°C 2 min. in air	13.00	87.00	Non-detectable
200°C 1 hour in air	12.57	84.44	2.99
200°C 2 days in air	11.41	82.03	6.56
200°C 2 days in vacuum	12.06	85.11	2.83

From Figure 5-8, and Table 5-3, it is observed that a small amount of oxygen signal can be originally found in the as-deposited parylene-C. After baking at 200°C in the air for the first 2 minutes, the oxygen peak becomes non-detectable by XPS. It infers that the oxygen found in the as-deposited parylene-C is likely from the moisture contamination, and it disappears after few minutes of baking. In terms of oxidation, the oxygen peak becomes detectable again after thirty minutes of annealing at 200°C in our experiments. The oxygen peaks shown in Figure 5-8 get higher when the annealing time gets longer, which means that parylene-C on the sample surface gets more oxidized during the annealing process.

Because oxidation can deteriorate the mechanical properties of the parylene-C [101], it is generally suggested to anneal the material in the vacuum system to avoid the oxidation. To verify that the vacuum environment can prevent oxidation, another parylene-C sample was annealed at 200°C for two days in vacuum and the result is shown in Figure 5-9. It clearly shows that the oxygen peak of the parylene-C annealed in

vacuum is much lower than in the air, meaning that the oxygen content in the annealed sample is much reduced by adopting this vacuum approach. The improvement can also be found in Table 5-3, the oxygen content is improved from 6.56% in air to 2.83% in vacuum. The little amount of oxygen detected can be explained by few oxygen residues remaining in the vacuum system.

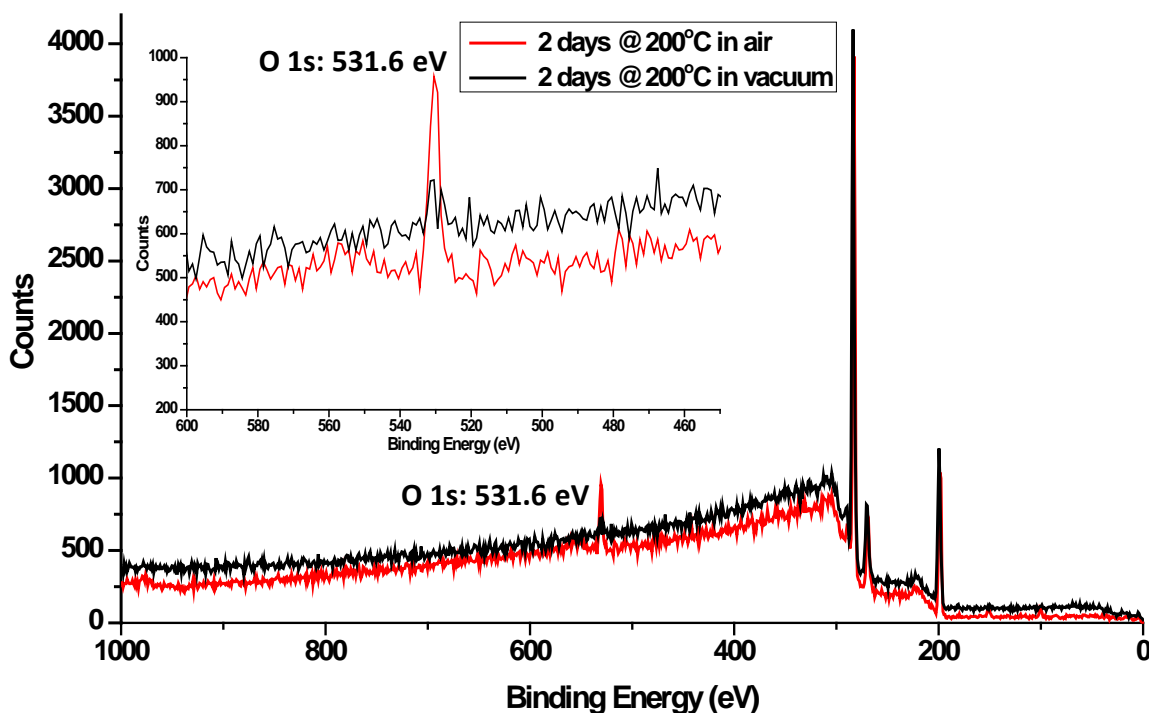


Figure 5-9: Comparison of two XPS results of parylene-C annealed at 200°C for two days in air and in vacuum

#### 5.4.2 FTIR

Although XPS can provide us with the content of atoms involved in the oxidative parylene-C film surface, it is generally believed that XPS can only measure the surface chemical compounds of the material. In addition, XPS cannot provide us with a correct prediction of the chemical bonding of the oxidative species. Therefore, another

experiment using FTIR (Fourier transform infrared spectroscopy) is performed here to study whether the oxidation happens throughout the samples, and also what the chemical bonding after the oxidation is.

FTIR uses a broad band of infrared light to obtain material's IR absorption (or transmission) spectrum. As different chemical functional groups absorb different wavenumbers of infrared, the IR spectrum tells the specific chemical bond and functional group inside the material, which can be used to analyze the intermediate oxidative species of the material.

The FTIR scanning results of the parylene-C annealed in different situations are shown in Figure 5-10 to Figure 5-12. In Figure 5-10, all parylene-C were annealed at 100°C in the convection oven, but for different time durations. Two curves representing as-deposited parylene-C and parylene-C annealed at 100°C in the vacuum are shown for comparison. It is more interesting to look at the wavenumbers of carbon-oxygen single bond located at 1100–1300 $\text{cm}^{-1}$ , and also carbonyl bond located at 1695  $\text{cm}^{-1}$  which show the clue of the oxidation. From Figure 5-10, it can be seen that no observable difference could be found among the five results within these two interested wavenumber ranges. No difference between the results of 100°C both in air and in vacuum means that the parylene-C gets oxidized very slowly at 100°C, which has also been pointed out by Monk in their real device parylene-C coating tests [188]. Same conclusion can also be obtained from Figure 5-10 that the annealing time of 4 days in the air makes no big difference to the as-deposited parylene-C film. The wave form variations between 1750–2750 $\text{cm}^{-1}$  and also among above 3250  $\text{cm}^{-1}$  is likely due to the thickness variations of different samples.

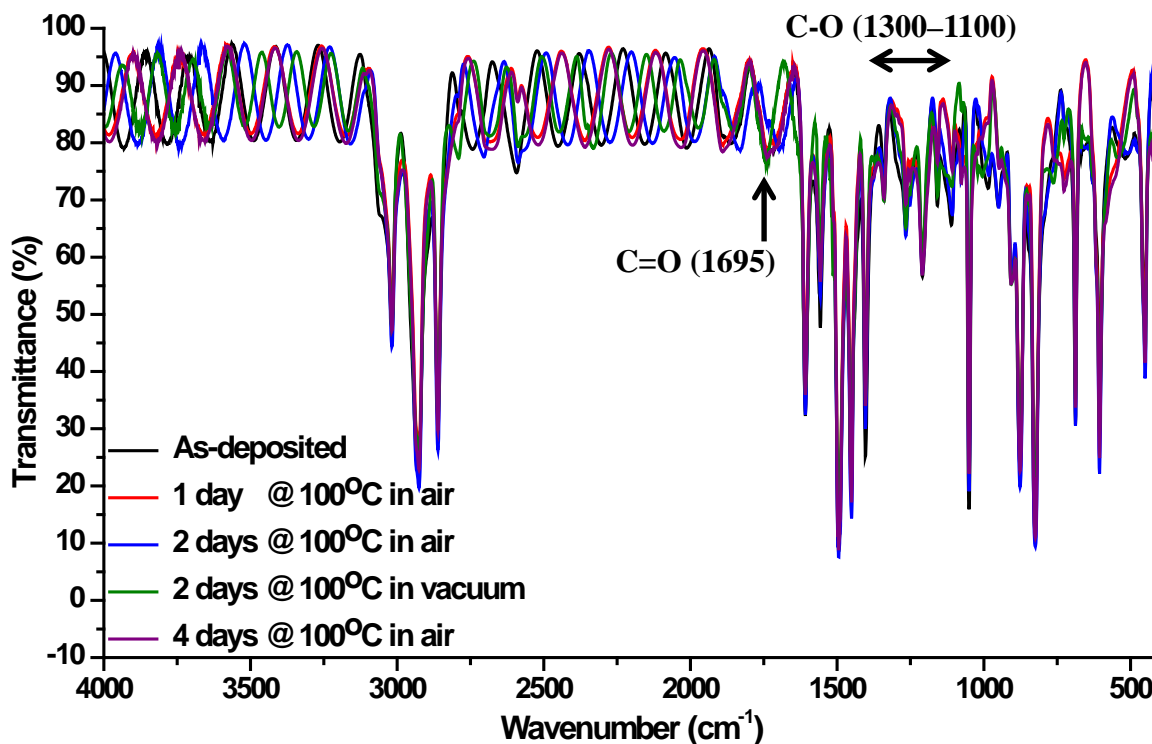


Figure 5-10: Typical FTIR results of parylene-C film. The black curve represents the as-deposited parylene-C film, while the others represent the results of annealing at 100°C.

Figure 5-11 shows the results of parylene-C annealed at 200°C in the convection oven. It can be clearly seen that the curves shift down more and more as the annealing time gets longer and longer. Both peaks representing carbon-oxygen single bond and carbonyl bond get deeper with the increasing annealing time, implying that more amount of parylene-C gets oxidized during the annealing. The peak growing at 1695  $\text{cm}^{-1}$  means that the intermediate oxidative species have carbonyl functional group, which was also found by Nowlin [189]. Except for the three sharp peaks representing the C-H stretching, it is also found that the curve between 2500–3550  $\text{cm}^{-1}$  gradually gets deeper as the annealing time gets longer. The regular FTIR database tells us that this range represents the OH functional group [196]. Therefore, the broader and deeper curve from 2500  $\text{cm}^{-1}$

to  $3550\text{ cm}^{-1}$  might infer that the parylene-C has started to decompose into some chemical compound after 1 day of annealing at  $200^\circ\text{C}$ , which has incorporated moisture to form the OH functional group.

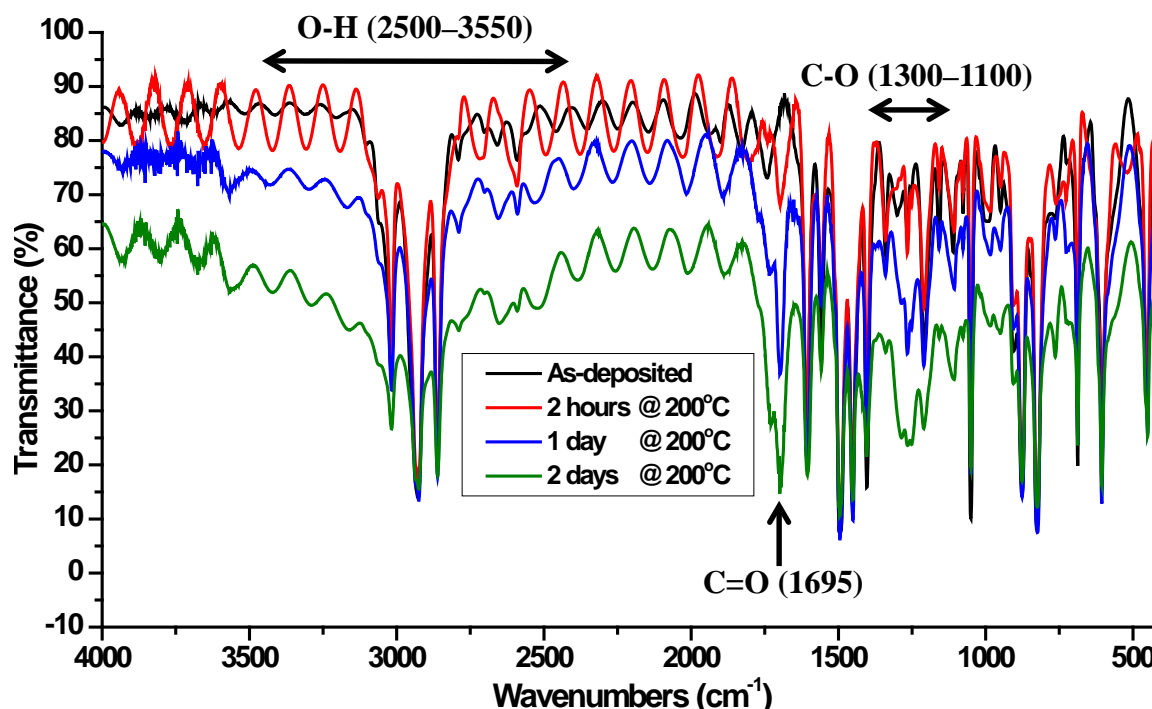


Figure 5-11: FTIR results of parylene-C annealed at  $200^\circ\text{C}$  in air for different times

To verify the vacuum improvement to the annealing, two results of parylene-C annealed at  $200^\circ\text{C}$  with one in the air and one in the vacuum are shown in Figure 5-12. It clearly shows that parylene-C annealed even at the temperature as high as  $200^\circ\text{C}$  in vacuum has no observable curve difference from the as-deposited parylene-C. It concludes that annealing in vacuum can preserve the parylene-C material and agrees well with what we found in Figure 5-9.

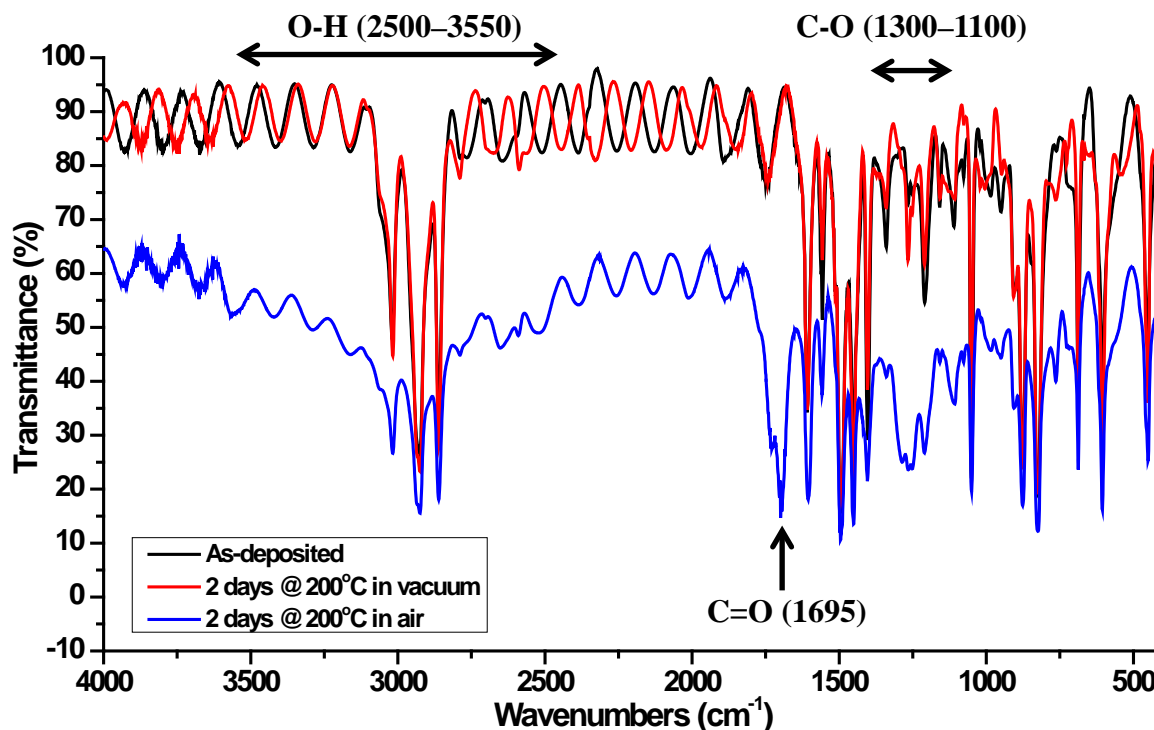


Figure 5-12: Comparison of the FTIR results of parylene-C annealed at 200°C in air and vacuum, all for two days

### 5.4.3 Summary and discussion

In this section, XPS and FTIR techniques have been used to study the oxidation behavior of the parylene-C film. Both techniques show that the parylene-C film has very little oxidation happening at 100°C. The results agree well with Nowlin and Monk's study, which is shown in Table 5-4. In Table 5-4, the oxidation rate is only found at the temperature higher than 125°C. If the oxidation rate at 125°C, i.e., 16 ppm [O]/hr, is taken for calculation, it can be estimated that it takes about 13 days for parylene-C to have a significant tensile strength degradation (5000 ppm). This demonstrates that parylene-C is still a very inert material at 100°C in the air.

Table 5-4: Measured initial (after 1 hour oxidation) oxygen uptake rate for parylene-C by Nowlin [189]

<b>Temperature (°C) (ppm [O]/hr)</b>			
<b>125</b>	<b>152</b>	<b>175</b>	<b>200</b>
16	290	1500	6600

Although XPS only qualitatively demonstrates the oxygen atom percentage of the parylene-C film, the oxygen found on parylene-C surface could either come from the real oxidation during the annealing or the moisture contamination. This measuring insufficiency of the machines is compensated by using FTIR in our experiments. FTIR tells the present bonds throughout the parylene-C thickness. Therefore, it can be used to determine whether the oxygen atom comes from the moisture or the oxidative species. It is found that the oxidative species of parylene-C have a lot of carbonyl functional group, which has been predicted by Nowlin. The carbon-oxygen single bond found at 1100–1300  $\text{cm}^{-1}$ , however, needs more studies to figure out its origin. By FTIR, it shows that the parylene-C might have already started to decompose after one day annealing at 200°C in the air. Both XPS and FTIR results provide strong evidence that annealing parylene-C at 200°C in vacuum does prevent serious parylene-C oxidation.

## 5.5 Crystallization

Crystallization is a process of phase transformation [197]. Like most of other polymers, parylene-C also has a certain degree of crystallization. It is reported that the crystallinity of the as-deposited parylene-C is about 60% [198–200], and is found to increase after post-fabrication thermal annealing [104, 184, 201]. On the other hand, however, parylene-C shares different paths of crystallization from other conventional polymers: it takes place during its chemical vapor deposition. Conventional polymers' crystallization is carried out by cooling the material from liquid type at higher temperature,  $T_m$ , to crystallization temperature,  $T_c$ , and hold at  $T_c$  until the crystallization is completed, which is called “isothermal crystallization”. The mechanism, model, and theory of the crystallization of conventional polymers such as polyethylene, poly(phenylene sulfide), nylon-11, etc., have been extensively described and discussed [197, 202]. In contrast, the mechanism of polymer crystallization occurring during the chemical vapor deposition in which the polymerization happens is relatively less studied and discussed. In the 70s, Wunderlich's group had done some researches on the crystallization of poly-para-xylylene (parylene or parylene-N) during its polymerization process [198, 199, 203, 204]. Their results qualitatively reveal that the parylene deposited at room temperature starts to crystallize subsequent to polymerization but before the molecule is complete. Although it was parylene-N that Wunderlich worked on, it is generally believed that the parylene-C shares the same crystallization mechanism as well.

Researchers used to focus more on parylene-N's crystal structures. In 1953, Brown and Farthing found two types of crystal structures of the parylene-N,  $\alpha$  form and  $\beta$

form, and transition from  $\alpha$  to  $\beta$  is achieved by thermal annealing (e.g., 220°C for parylene-N) [205, 206]. Iwamoto found that the parylene-N deposited at 80°C shows a mixture of  $\alpha$  and  $\beta$  forms, while parylene-N deposited between 0–60°C only shows  $\alpha$  form. Niegisch showed that the unit length of parylene-N is 6.58 Å and the orientation of parylene-N's polymer chains are aligned with lattice ac plane, which is parallel to the film plane [186, 207]. Iwamoto used x-ray diffraction technique to completely determine the structure of parylene-N's  $\alpha$  form, finding that the parylene's benzene ring is parallel to the b axis, which is preferentially oriented along the direction perpendicular to the substrate surface [208]. The parylene-N is also found to have a monoclinic unit cell with  $a=5.92$  Å,  $b=10.64$  Å,  $c$  (fiber axis)=6.55 Å, and  $\beta=134.7^\circ$ . L. You used x-ray pole figure technique to quantify the crystalline portion of the parylene-N film [200]. It was not until 1984 that, for the first time, Murthy used x-ray diffraction technique to figure out  $\alpha$  form structure of alkylated and chlorinated poly-p-xylylene, i.e., parylene-C [209]. Murthy claimed that the dimensions of lattice constants in the plane, which was a and c, did not change with the substituents, but lattice constant b changed from 10.64 Å for parylene-N to 12.8 Å for parylene-C.

The crystallinity and crystalline structure of parylene-C and parylene-N deposited at different temperatures have been studied by Surendran in 1987 [174, 210]. For parylene-C, several interesting findings are shown in Surendran's study:

1. The crystallinity of parylene-C increases as the dimer sublimation rate increases during the deposition process.
2. No polymorphism is observed either by decreasing the deposition temperature or by increasing the sublimation rate of the dimer.

3. Isothermal annealing increase brings the crystallization without any structural transformation.
4. At low temperature ( $< -60^{\circ}\text{C}$ ), all parylene-C depositions are all amorphous.

In this section, the parylene-C's crystallization was studied in more detail at  $100^{\circ}\text{C}$  in Helium to understand its crystallization kinetics. An in-situ temperature ramping annealing test was also performed to study its crystallization behavior at various temperatures. Several parameters of parylene-C's crystallite structure, e.g., d-spacing and crystallite size, are calculated and discussed. The time constant of the crystallization is evaluated in the last part of the section.

### **5.5.1 X-ray diffraction method**

X-ray diffraction technique (XRD) has been widely used to study materials' crystallinity, crystal orientation, fiber structures, and even the stress inside the materials. The technique is executed by emitting x-ray onto the sample's surface *via* different incident angles. The x-ray is scattered by materials atoms and the reflected light is collected by a light sensor. The structure of the tested material can then be figured out by the observed light information. The machine used in our study is X'Pert PRO MRD made by Philips. The x-ray anode source is copper and its wavelength is  $1.5406 \text{ \AA}$ .

#### ***5.5.1.1 In situ consecutive XRD scanning at $100^{\circ}\text{C}$***

Our first XRD experiment was performed to measure the crystallinity and crystallite size of the parylene-C annealed at  $100^{\circ}\text{C}$  consecutively for four hours. The parylene-C sample was held on the sample holder and the x-ray was scanning the sample with the angle from  $10^{\circ}$  to  $40^{\circ}$  continuously, which took 5.3 minutes to finish one scanning. The temperature was ramped from room temperature to  $100^{\circ}\text{C}$  at the rate of

3°C/min. An inert gas of helium was flushed into the chamber all the time during the scanning to eliminate any possible oxidation effect.

A typical XRD scanning results showing the curve from 10°–30° is shown in Figure 5-13. It can be seen that a clear peak happens at  $2\theta = \sim 14^\circ$ , which represents the (020) surface of the monoclinic unit cell. Lots of information can be obtained from the XRD results and they are introduced and defined as follows.

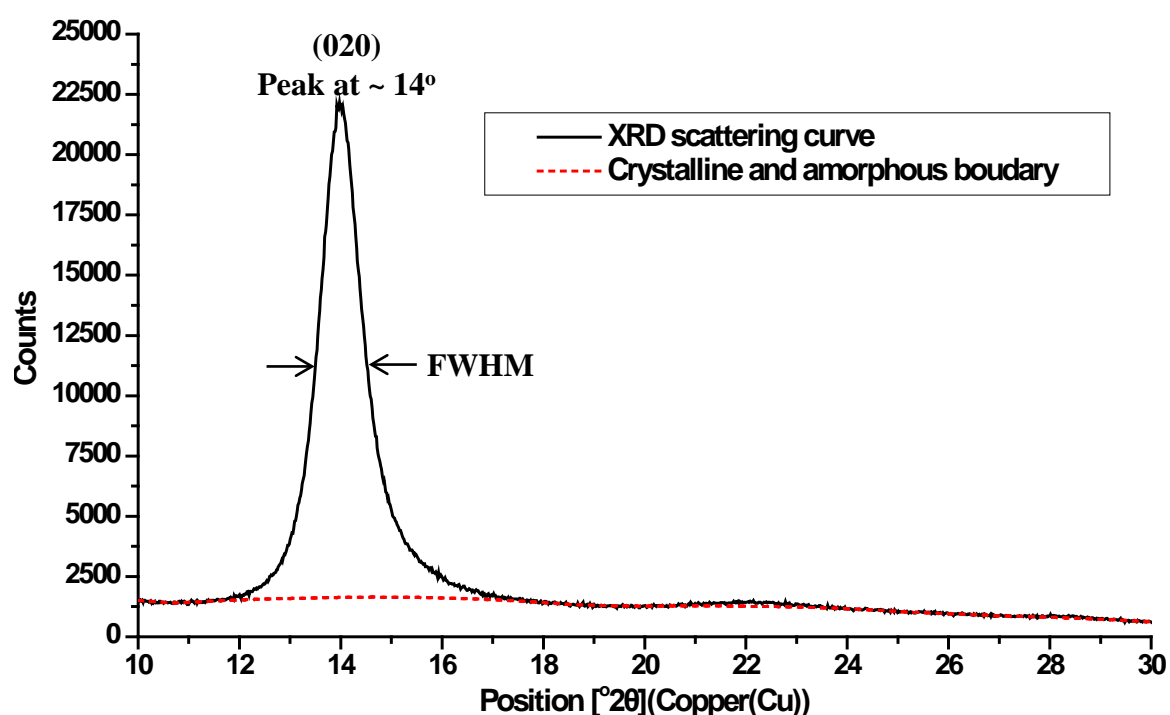


Figure 5-13: Typical XRD scanning results showing curve from 10°–30°C

#### 5.5.1.1.1 Crystallinity

Two fundamental approaches are usually utilized to calculate the material's crystallinity through the XRD scanning results. If either completely amorphous or crystallized state of the polymer under scanning exists, the XRD results can be calibrated according to them and the crystallinity at any state could be found [211–214]. Another

way to determine the crystallinity is using Hermans method [215–218], which resolves the curve into amorphous and crystallized portions, as shown in Figure 5-13. The crystallinity is then defined as the ratio of the crystallized portions, i.e., area bounded by the back and red lines in Figure 5-13, to the whole area under the black line.

Because the parylene-C shows as neither a completely amorphous nor completely crystallized polymer right after the deposition, Hermans method is adopted here to estimate the parylene-C's crystallinity [174, 210]. However, even though the boundary in Figure 5-13 can be determined by the commercial software, the estimated crystallinity still varies based on the algorithm of the boundary determinations. Since the crystallinity of the as-deposited parylene-C has been published as 60%, all our XRD results were calibrated to this crystallinity of the as-deposited parylene-C and then the crystallinity at any state was estimated based on this assumption. It is obvious that the crystallinity obtained in our experiments is not absolute, but only for comparison purposes.

#### 5.5.1.1.2 d-spacing

d-spacing represents the interplanar spacing of two crystallite planes. d-spacing,  $d$ , can be calculated by Bragg's diffraction law as

$$2d\sin\theta_B = n\lambda, \quad (5-1)$$

where  $\theta_B$  is the Bragg angle, which can be obtained from the location of the peak in Figure 5-13.  $\lambda$  is the wavelength of the emitting x-ray, which is 1.5406 Å. For the peak at  $2\theta_B = \sim 14^\circ$ ,  $n = 1$ .

#### 5.5.1.1.3 Crystallite size

The crystallite size,  $D$ , can be obtained using Scherrer's formula:

$$D = \frac{0.9\lambda}{B\cos\theta_B}, \quad (5-2)$$

where  $\lambda$  and  $\theta_B$  are the same as in eqn. (5-1).  $B$  is the full width at half maximum (FWHM), which can be found from the XRD results by commercial software.

Figure 5-14 shows the in situ XRD measurement results of the parylene-C consecutively annealed at 100°C in Helium. The first obtained curve was at the temperature of 30°C due to the machine's limitation. After the temperature reached 100°C, the machine scanned the sample every 5.3 minutes. It can be seen from Figure 5-14 that the height of the curve grows fast between 30° and 100°C. Once the temperature stabilizes at 100°C, the height keeps growing, but grows at a much slower rate. As the temperature ramp rate here is 3°C/min, the time constant of the parylene-C crystallization will be evaluated in Section 5.5.2 by individually annealing every sample.

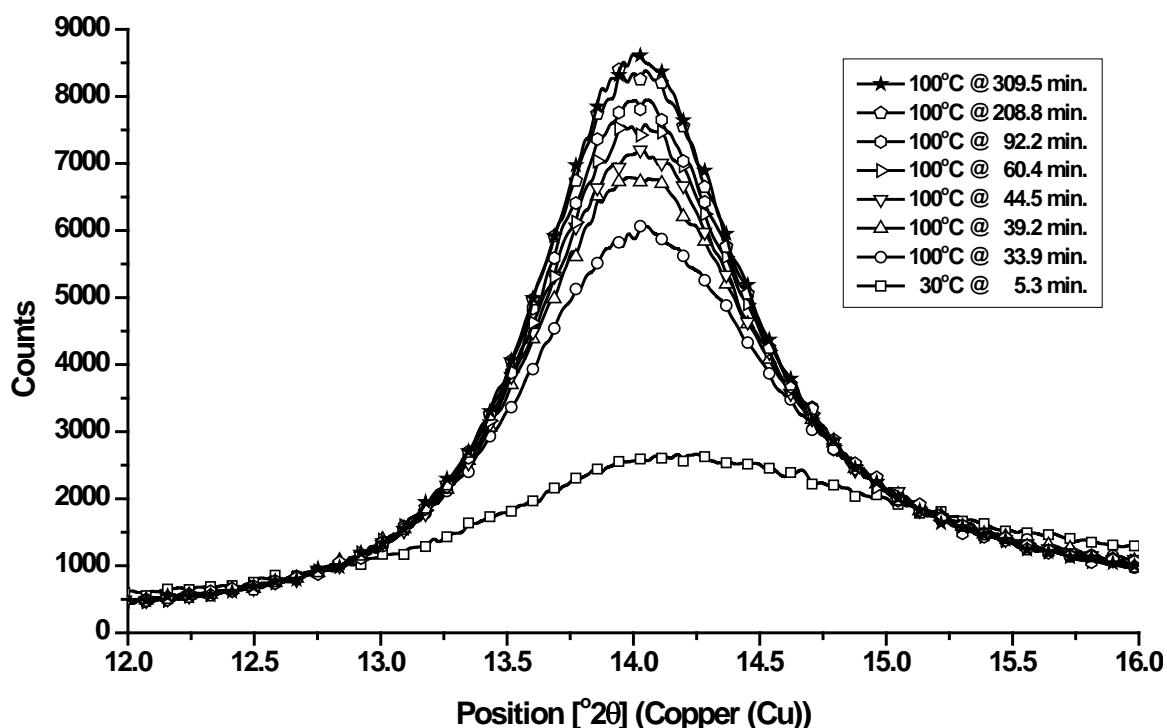


Figure 5-14: XRD results of in situ XRD measurement of parylene-C consecutively annealed at 100°C in helium

Table 5-5 is the list of the calculated parameters using the in-situ XRD measuring results of the parylene-C consecutively annealed at 100°C in helium. It can be seen that the crystallinity is growing up with the annealing time. The crystallinity does not go back after the parylene-C cools down to 30°C, meaning that the parylene-C structure has gone through crystallization and is irreversible. The position of the peak of  $2\theta$  is found to be at around 14°. The angle decreases to a bit less than 14.0194 during the annealing, but goes back to 14.1330. The varying  $2\theta$  position implies that d-spacing is changing during annealing. It can be found that the d-spacing increases more during 30–100°C than staying at 100°C. The d-spacing increase, therefore, could be explained by the thermal expansion of the parylene-C. Although the height is found to increase during the annealing, the FWHM, however, is also found to be narrower at the same time. The decreasing of the FWHM results in the increasing of the parylene-C crystallite size. As aforementioned, the crystallinity obtained through Hermans method for parylene-C is not absolute, it is more reasonable to use parylene-C crystallite size to analyze the level of the parylene-C crystallization behavior. The crystallite size of parylene-C annealed consecutively at 100°C versus annealing time is shown in Figure 5-15. It is found that the crystallite size saturates quickly once the temperature reaches 100°C, meaning that the crystallization of parylene-C responds spontaneously to the environmental temperature increase. The results show that the crystallite size saturates within 10 minutes. As the temperature ramping rate is slow, the time constant will be studied in Section 5.5.2 by annealing the samples in a pre-heated convection oven with different annealing time to mimic the step temperature change.

Table 5-5: A list of calculated parameters using the in situ XRD measurement results of parylene-C consecutively annealed at 100°C in helium

Time	Temperature	Crystallinity	Position	Height	FWHM	d-spacing	Crystallite size
min	°C	%	2 $\theta$	Counts	2 $\theta$	Å	Å
5.3	30	60.34	14.1755	2645.00	1.3382	6.2480	59.8226
33.93	100	86.39	14.0408	5985.00	0.9368	6.3076	85.4430
39.23	100	89.06	14.0277	6792.00	0.9368	6.3135	85.4418
44.53	100	89.81	14.0260	7146.00	0.8029	6.3143	99.6908
60.43	100	89.70	14.0261	7565.00	0.8029	6.3142	99.6908
92.23	100	90.45	14.0215	7944.00	0.8029	6.3163	99.6903
208.8	100	91.71	14.0199	8349.00	0.8029	6.3170	99.6901
309.5	100	90.45	14.0194	8476.00	0.6691	6.3172	119.6251
320.7	30	90.27	14.1330	8407.00	0.8029	6.2667	99.7023

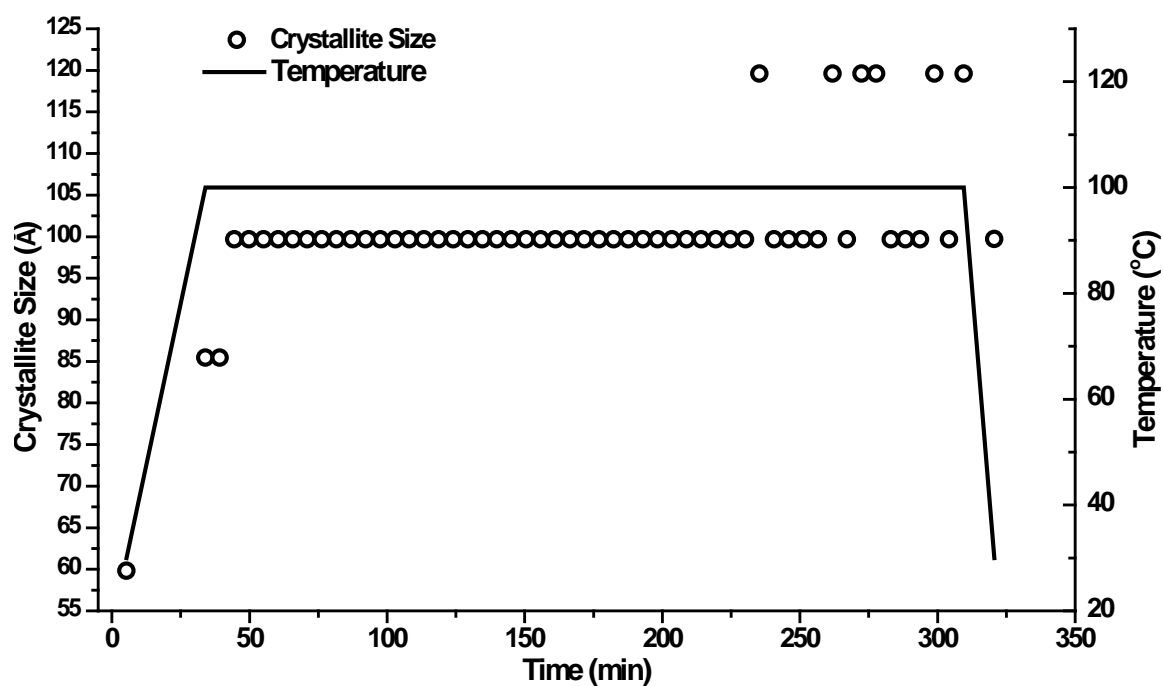


Figure 5-15: Crystallite size growing history of parylene-C annealed at 100°C in helium

### **5.5.1.2 In situ temperature ramping annealing study**

Another experiment was performed to study the crystallization effect at different temperatures. In this experiment, the environmental temperature of the parylene-C sample was ramped up at the rate of 3°C/min up to 300°C. Each scanning also took 5.3 minutes, and the machine kept scanning the sample 6 times after the machine reached the targeted temperature; hence the parylene-C sample would experience each annealing temperature for about 31.8 minutes. Helium was also used during the experiment to prevent the oxidation especially in the high temperature.

The XRD results of the annealing temperatures from 30° to 50°C are shown in Figure 5-16. For temperature from 80°–250°C, the results are shown in Figure 5-17 in comparison with the result for 30°C. For Figure 5-16 and Figure 5-17, only the sixth scanning results for each temperature was selected and drawn, which is believed to be closely enough to reflect the crystallization saturation at each temperature. The derived crystallization parameters are listed in Table 5-6, and the crystallite growing history is shown in Figure 5-18. It is found from Figure 5-16 that parylene-C show very little crystallization when the temperature is below (including) 50°C. Although the curve of 50°C in Figure 5-16 is higher than that of the lower temperatures, the calculated crystallite size at 50°C still does not show any clue of growing up, which would imply that the crystallization does not happen yet, but have a more organized structure at 50°C. This phenomenon agrees well with the measured length change in 5.3.2. The result again proves that the parylene-C does not crystallize (or crystallize very little) below 50°C, i.e., the glass transition temperature, which can be explained well by thermodynamics. After the temperature is over 50°C, the height of the XRD curve starts to grow up dramatically,

and also shifts to the left as the temperature increases. This shift results in the increase of the d-spacing, which can be explained as the thermal expansion. The crystallite size also starts to increase when the temperature ramps up higher than 50°C and keeps growing as the temperature increases until 250°C. When the temperature reaches 300°C, the crystallite size suddenly drops, because it is believed that the parylene-C has been decomposed or melted, as shown in Figure 5-18. The obtained parylene-C decomposing (or melting) temperature agrees well with the literature value of 290°C [100, 101]. Although the XRD curves of each temperature is always getting higher in the first scanning, the crystallite size shown Figure 5-18 demonstrates a flat line at most of the temperatures, except at 80° and 100°C. It reveals that the crystallization of parylene-C is very likely to have been done within the first 5.3 minutes scanning. The non-flat results at 80° and 100°C implies that the higher the annealing temperature, the shorter the crystallization time constant.

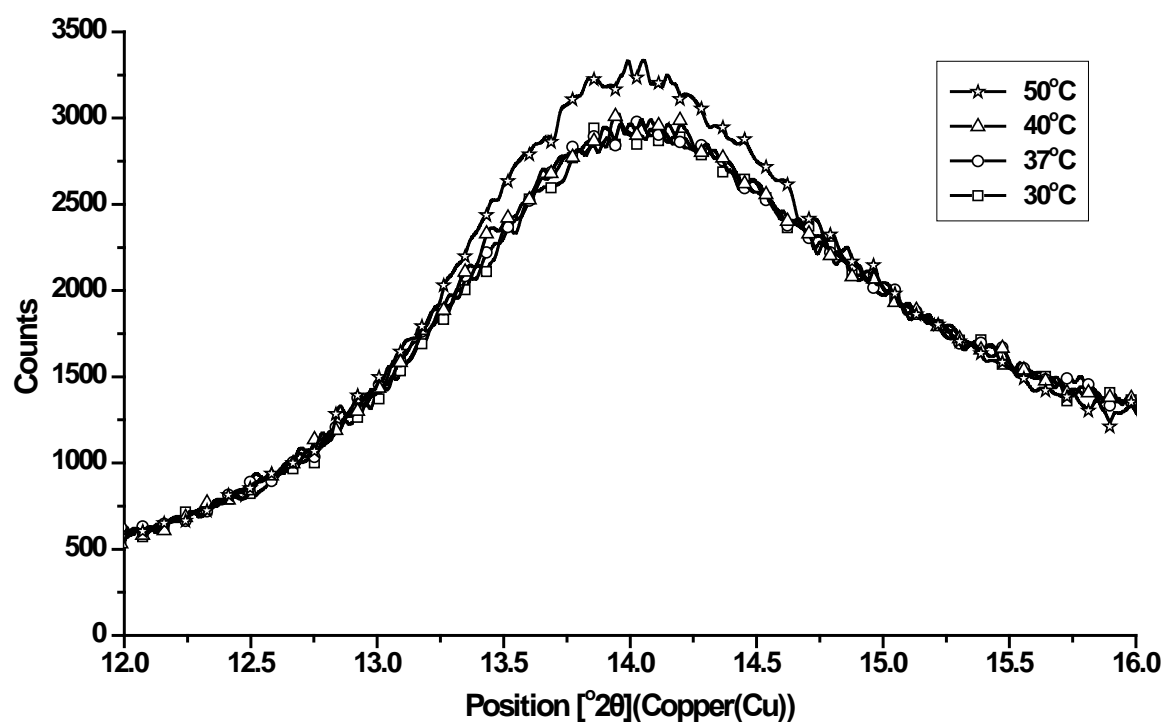


Figure 5-16: XRD results of parylene-C annealed at 30°, 37°, 40°, and 50°C

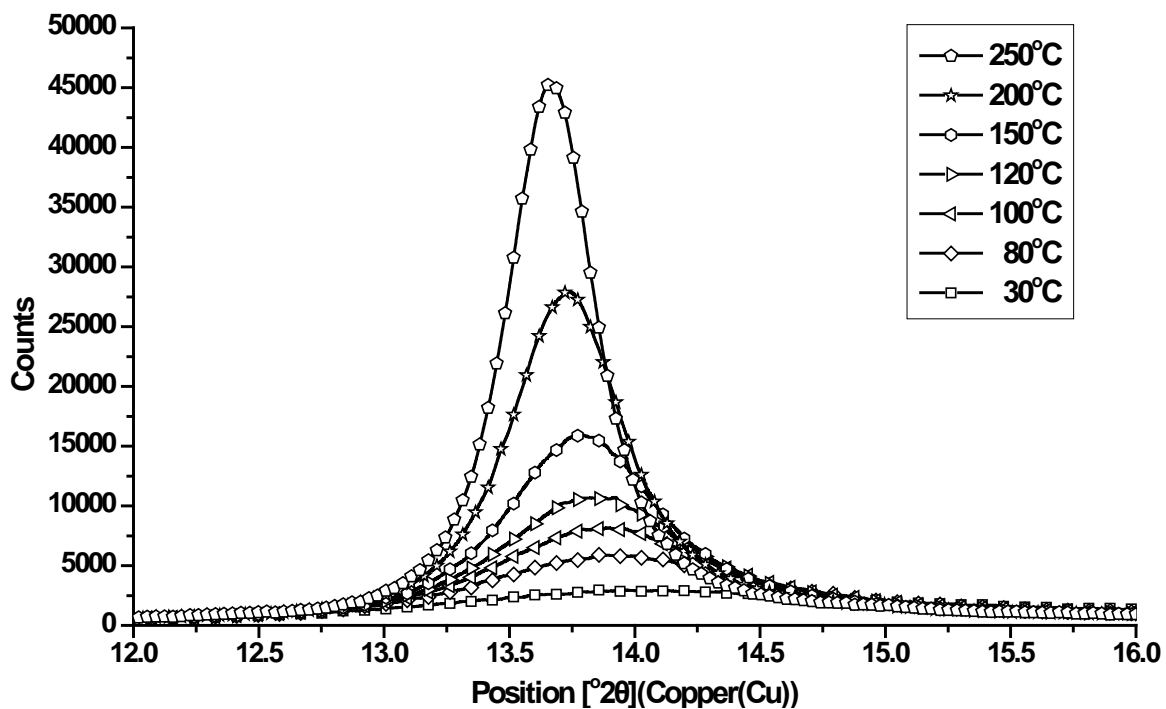


Figure 5-17: XRD results of in situ XRD measurement of parylene-C consecutively annealed at different temperatures in helium. Temperature ramping rate = 3°C/min.

Table 5-6: A list of calculated parameters based on the in situ XRD measurement of parylene-C consecutively annealed at different temperatures in helium

Time	Temperature	Crystallinity	Position	Height	FWHM	d-spacing	Crystallite size
min	°C	%	2θ	Counts	2θ	Å	Å
31.8	30	62.20	14.0482	2914.00	1.3382	6.3044	59.8144
65.7	37	60.74	14.0285	2935.00	1.3382	6.3132	59.8131
98.1	40	59.65	14.0473	2981.00	1.3382	6.3047	59.8143
133.0	50	58.11	14.0055	3273.00	1.3382	6.3235	59.8117
174.7	80	69.65	13.9203	5865.00	0.9368	6.3620	85.4320
213.1	100	75.04	13.8757	8117.00	0.8029	6.3823	99.6748
251.2	120	79.86	13.8393	10725.00	0.8029	6.3990	99.6709
292.6	150	81.64	13.7948	15898.00	0.6691	6.4196	119.5965
340.7	200	85.73	13.7270	27791.00	0.5353	6.4511	149.4794
388.8	250	86.21	13.6667	45185.00	0.5353	6.4795	149.4699

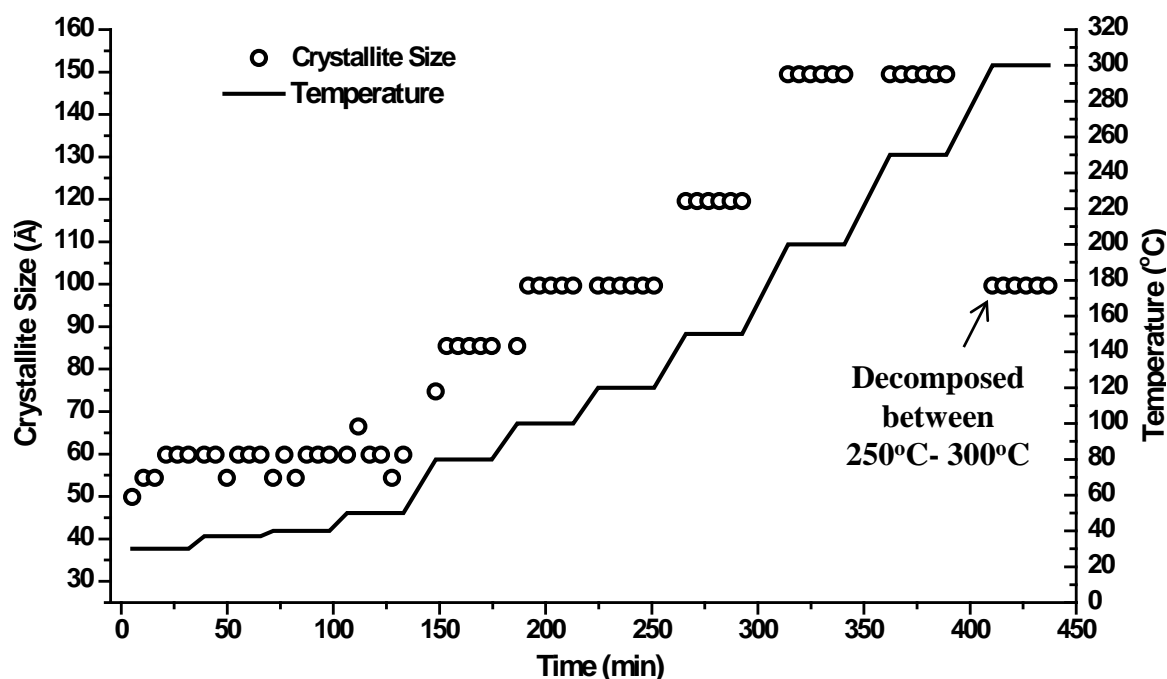


Figure 5-18: Crystallite size growing history of parylene-C annealed at different temperatures in helium

### 5.5.2 Time constant of parylene-C annealed at 100°C

Hsu has suggested in 2008 that the crystallization reaction is likely to be completed during the brief 20 min of annealing [201]. To find the time constant of the crystallization of the parylene-C at 100°C, several parylene-C samples were annealed at 100°C but for different annealing durations. To mimic a step-function temperature increasing profile, a convection oven was first pre-heated to 100°C before the samples were put in. The samples were taken out when the desired annealing time was up and then scanned separately by XRD machine.

The list of the XRD results of all parylene-C samples with different thermal treatment is shown in Table 5-7. It can be found that the crystallite size grows very fast in the early annealing process and saturates at 99.7 Å in two minutes. The crystallite size

as a function of the annealing time is drawn in Figure 5-19. The data points are curve fitted to the exponential equation as follows:

$$\text{crystallite size} = A + B \exp\left(-\frac{t}{\tau}\right), \quad (5-3)$$

where  $A$  and  $B$  are constants and  $\tau$  is the time constant. The curve fitting result shows that  $A$  is 99.98 Å,  $B$  is -40.50 Å and the time constant is 0.845 min. The short time constant means that parylene-C is very sensitive to heat and crystallization happens very fast at the annealing temperature. It is attributed to that the polymer chain motion is restricted during the vapor deposition polymerization (VDP), hence the as-deposited parylene-C is generally in a metastable state, which means parylene-C is not fully crystallized right after the VDP [101, 219]. It is postulated that the parylene-C's polymer chain tends to move immediately once the temperature reaches the temperature higher than the glass transition temperature and the crystallization takes place easily afterward.

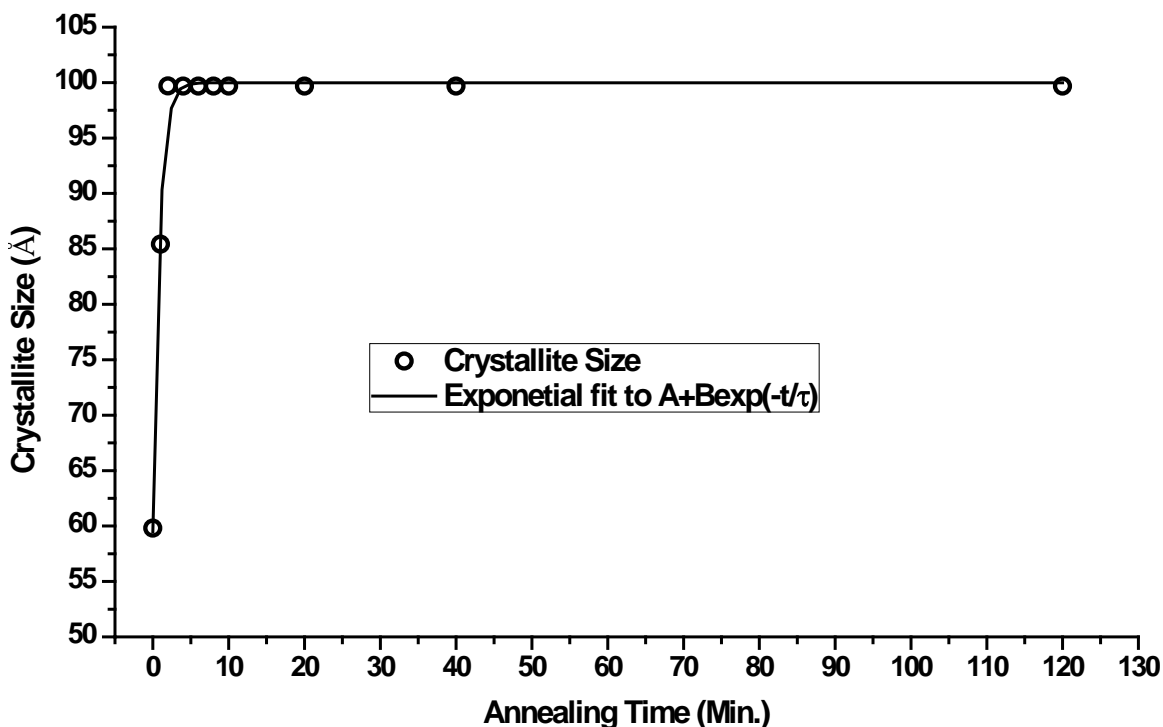


Figure 5-19: The crystallite size versus the annealing time

Table 5-7: The lists of the parameters of the crystallization of parylene-C individually annealed at 100°C for different annealing times

Time	Temperature	Crystallinity	Position	FWHM	d-spacing	Crystallite size
min	°C	%	2 $\theta$	2 $\theta$	Å	Å
0	Room Temperature	60.11	13.9535	1.3382	6.3469	59.8083
1	100	70.12	13.9141	0.9368	6.3648	85.4314
2	100	67.65	14.1324	0.8029	6.2670	99.7022
4	100	73.41	13.9785	0.8029	6.3356	99.6857
6	100	75.79	13.9886	0.8029	6.3311	99.6868
8	100	73.89	13.9729	0.8029	6.3382	99.6851
10	100	73.72	13.9776	0.8029	6.3360	99.6856
20	100	78.67	13.9615	0.8029	6.3433	99.6839
40	100	77.99	13.9894	0.8029	6.3307	99.6869
120	100	75.05	13.9910	0.8029	6.3300	99.6870

### 5.5.3 Effect of deposition pressure difference

In the previous research, it is found that increasing the deposition pressure will also increase the deposition rate [201] but decrease the crystallinity [104, 220]. When previous researchers were doing the parylene-C crystallization study, many of them usually used the height (or counts) signal of the XRD scanning results to represent parylene-C crystallinity [104, 201]. However, as has been discussed before, the FWHM

also narrows when the curve height increases, therefore the height might not be an adequate indicator to describe parylene-C's crystallization behavior.

Rather than using the height of the XRD results, the parylene-C's crystallite size is used to study the parylene-C's crystallization behavior in this section. Another as-deposited parylene-C film deposited at 35 mTorr was also prepared and scanned by the XRD machine. The calculated crystallization parameters are shown in Table 5-8 and the scanning results are shown in Figure 5-17 with the curve of 22 mTorr shown together for comparison. It is found that the peak of 35 mTorr curve is lower than 22 mTorr as expected. On the other hand, the obtained  $2\theta$  position, d-spacing, and the crystallite size are all very similar between the two parylene-C deposited at different pressures. Therefore it could be concluded that the crystallite structures of the two parylene-C films with different deposition conditions should be similar. The lower height (or intensity), and hence the lower crystallinity, of the parylene-C deposited at 35 mTorr is likely attributed to the fact that the percentage of amorphous phase is higher in parylene-C deposited at 35 mTorr than 22 mTorr. The corresponding mechanical properties will be discussed in detail in Sections 5.7–5.9.

Table 5-8: XRD results of two as-deposited parylene-C films deposited at 22 mTorr and 35 mTorr, respectively

<b>Deposition pressure</b>	<b>Crystallinity</b>	<b>Position</b>	<b>Height</b>	<b>FWHM</b>	<b>d-spacing</b>	<b>Crystallite size</b>
mTorr	%	$2\theta$	Counts	$2\theta$	Å	Å
22	60.27	14.0241	3979.00	1.3382	6.3151	59.8129
35	21.95	14.0507	1824.00	1.2044	6.3032	66.4595

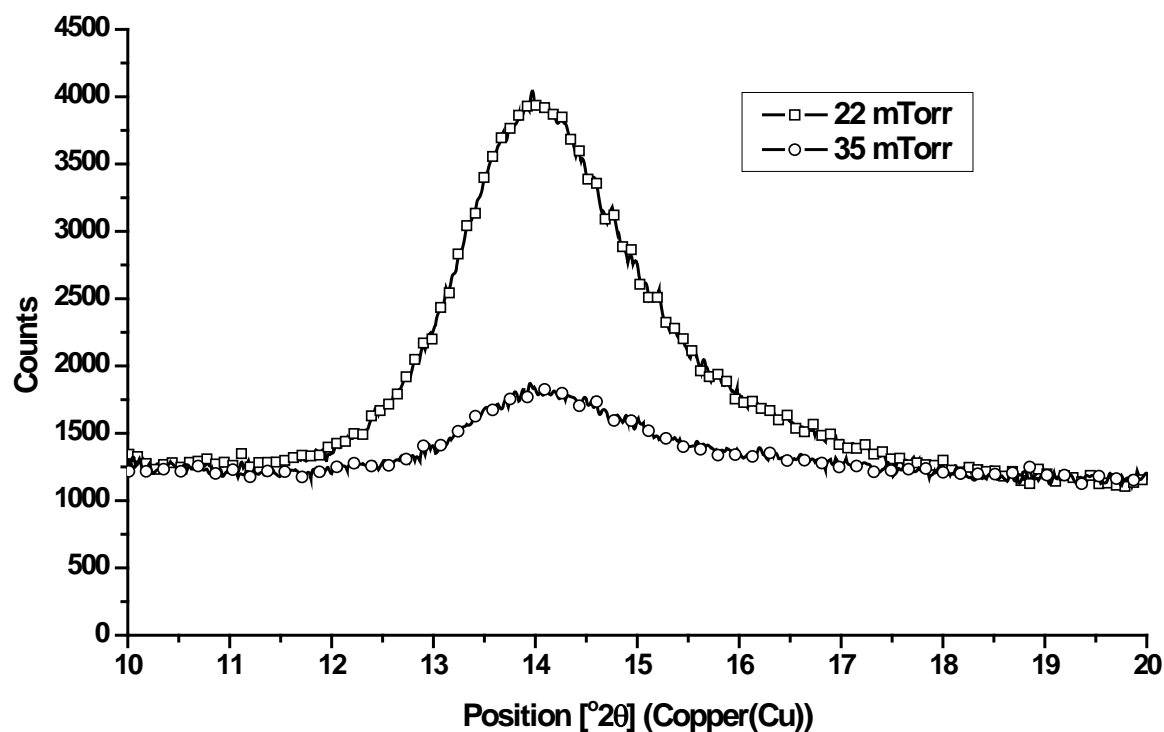


Figure 5-20: Comparison of the results of XRD measurement of parylene-C deposited at 22 mT and 35 mT

#### 5.5.4 Summary and discussion

In this section, the crystallinity of parylene-C annealed at various temperatures or deposited at different pressures is studied. The time constant of parylene-C annealed at 100°C is found to be around 0.845 minutes. It infers that as-deposited parylene-C is at a metastable state and is very sensitive to heat. The crystallization at 100°C could be done within only less than one minute. The in situ ramping temperature experiments show that the parylene-C starts to crystallize above the glass transition temperature, which is found to be 50°C in this section *via* XRD approach. In addition, the crystallinity, or crystallite size increases as the annealing temperature increases.

In our experiments, the crystallite size of as-deposited parylene-C is found to be  $\sim 59.8$  Å and increases to  $\sim 149.5$  Å at 250°C and parylene-C decomposes at 300°C. It is

pointed out in Section 5.2 that the molecular length of the parylene-N is about 2000–4000 units per chain. If the unit length of  $6.58\text{\AA}$  is used, the chain length could be about  $13160\text{--}26320\text{\AA}$ , or  $1.32\text{--}2.63\text{ }\mu\text{m}$ . Based on the crystallite size shown in this section, it can be concluded that the one parylene-C polymer chain is very likely to contribute to more than one single parylene-C crystallite. The hypothesis is that parts of the long parylene-C polymer chain are folded to form multiple ordered crystalline structures, or called lamella, which might happen irregularly in between single polymer chain [221]. The rest of the polymer chain remains in amorphous type. When the parylene-C is heated up, the parylene-C polymer gets enough energy to move, therefore more polymer chains become well-organized, and therefore results in the length shortening shown in Section 5.3. It has been reported that another XRD peak happens at  $28.2^\circ$  when the parylene-C is annealed at  $200^\circ\text{C}$ . The same phenomenon is also found in our XRD scanning results. It is very likely that another structure transformation takes place at this temperature. However, to our best knowledge, not too many papers have been working on the effect of the generation of this peak. The future work would focus on the cause of this peak and its corresponding crystallite structure. In addition, the future work would also focus on another interesting claim which was made by Shaw in 1970 [222]. They claimed that the free radicals buried in the parylene film would react with other radicals at other polymer chain ends when annealing directly after the film deposition. Therefore the annealing process would terminate the as-deposited parylene film radicals and the radicals would not react with the available oxygen. It might imply that the annealing of as-deposited parylene-C film could hinder the oxidation of the material, which is very worthwhile to look into.

## 5.6 Glass Transition Temperature

It is well known that viscoelastic behaviors of polymers differ below and above the glass transition temperature. To understand the mechanism of polymer transition, the concept of free volume is first introduced in the first part of this section. The free volume of the polymer is defined as the space a molecule has for internal movement [223]. The polymer chain cannot move freely if there is not enough space for a single C-C bond to rotate. It is believed that the typical free volume of the polymer is 2.5 Vol.-% and it requires free volume to be greater than 2.5 Vol.-% for macromolecules to start to move [185].

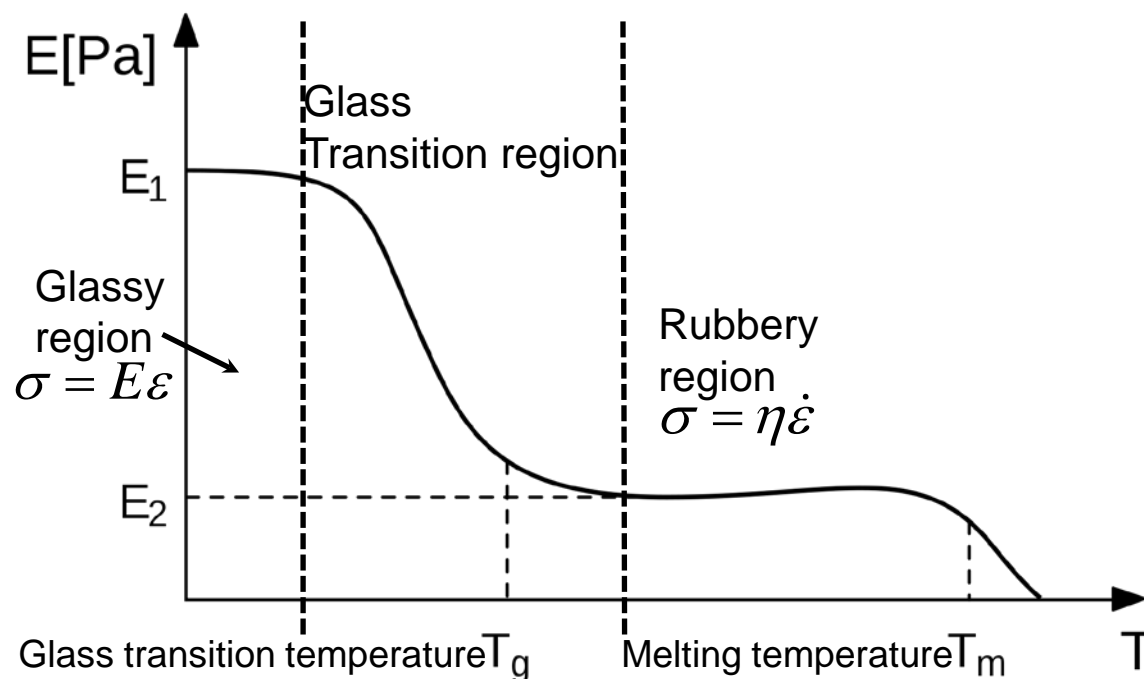


Figure 5-21: Elastic modulus response versus temperature change

As shown in Figure 5-21, the leftmost region is called glassy region. In this region, the material has relatively higher and flatter elastic modulus than others. The macromolecule is ceased in the glassy region and hence the polymer behaves like a

perfect elastic material at low temperature. It has been demonstrated that the free volume increases as the temperature increases [185, 223]. Therefore, as the temperature goes over a critical temperature, i.e., glass transition (or second transition) temperature,  $T_g$ , the free volume increases to be higher than 2.5 Vol.-%, permitting different kind of chain movements as well as moving in various directions [185, 223]. In addition, higher temperature also provides the polymer chain more energy and makes the chain movement even easier. Therefore, the elastic modulus decreases gradually due to this higher polymer chain mobility.

Glass transition temperature denotes a plastic material's onset of the transition of the reduced Young's modulus. The transition usually appears as a temperature range rather than just a deep-dropping step. This transition range is called the glass transition range. When the temperature passes the glass transition region, the elastic modulus enters another region called rubbery region. The plastic in this region has rubber-like response and its behavior can be predicted by viscous materials' model. The glass transition temperature usually defines one end of the materials' usage temperature, depending on what value the strength and stiffness is needed. The material can be used in the glassy region with a higher elastic modulus, or in the rubbery region with a lower elastic modulus. In any case, however, the operating range of the material should not fall within the glass transition region to avoid unpredictable material behaviors. Therefore, knowing the elastic modulus with a broad temperature spectrum and the temperature range of each region helps us select the right materials and also use it in the right operating temperature range. Furthermore, understanding the mechanism of the polymer elastic modulus transition can even help us tailor the materials' glass transition

temperature to fit our needs. This section would focus on the measurement of the glass transition temperature range of parylene-C and also several possible ways to modify it.

### **5.6.1 Identification of glass transition temperature**

#### ***5.6.1.1 Reported glass transition temperature of parylene-C***

Gorham did the first experiment to measure the glass transition temperature of parylene-C [172] in 1966 using secant modulus-temperature curve, and characterized parylene-C's glass transition temperature to be 80°C. Many researchers have attempted to study parylene-C's  $T_g$  after Gorham. A table listing some  $T_g$  measuring results is shown in Table 5-9. Although most the  $T_g$  values lie in the range of 13-150°C, the result demonstrate a sporadically spread numbers, indicating that the complexity of measuring parylene-C's glass transition temperature. As this second transition is attributed to the polymer movement as described before, it is postulated that the variation might be due to the parylene-C property difference (structure or crystallinity) of the samples obtained by different research groups, which might be influenced by different deposition conditions or post-deposition treatments. In this section, not only as-deposited parylene-C's  $T_g$  is characterized, but  $T_g$  of parylene-C annealed in different temperatures and environments is also studied to understand the  $T_g$  change with respect to the temperature, i.e., crystallinity.

As shown in Table 5-9, multiple approaches can be applied to measure parylene-C's glass transition temperature. From engineering point of view, measuring the relationship of the elastic modulus with respect to the temperature is most useful as it provides the information of not only elastic modulus at different temperature, but also the material thermodynamic properties including glass transition temperature. In this section,

the elastic modulus was measured by two methods: ramping-temperature-dependent modulus experiment and dynamic mechanical analysis (DMA).

Table 5-9: Some of the previous published parylene-C  $T_g$  characterizing results

Study	$T_g$ (°C)	Approach	Post script
Gorham, 1966 [172]	80	Secant modulus	
Gilch, 1966 [224]	70	NA	
Kubo, 1972 [199]	50–80	NA	
Alpaugh, 1974 [225]	50	DSC	
Iwamoto, 1975 [198]	65	DSC	As-deposited parylene-N, Heating rate: 10°C/min, Nitrogen atmosphere, Measured $T_g$ varies with respect to the polymerization temperature ( $T_g=63-78$ )
Beach, 1989 [101]	13	NA	$T_g$ is expected to have similar $T_g$ as parylene-N's.
Dabral, 1991[110]	150	Stress-temperature curve	Likely to be 50°C, according to the presented data.
Gratten, 1991 [187]	110	NA	
Senkevich, 1999 and 2000 [184, 226]	35–36, 44	DSC	Different testing rate corresponds to different $T_g$ results. Quoted by Kamezawa, Suzuki and Kasagi as 50°C [227].
Noh, 2004 [228, 229]	< 90	DSC	
Huang, 2005 [183]	42.5–62.5	Thermal coefficient of thickness expansion	$T_g$ is 10°C higher when thickness is < 50 nm.
Youn, 2007 [220]	90	NA	
Tewari, 2009 [230]	70	Current density peak	1- $\mu$ m-thick sample

### 5.6.1.2 Ramping-temperature-dependent modulus experiment

The concept of this ramping-temperature-dependent modulus experiment is shown in Figure 5-22. The test was done with samples under a temperature ramping

from  $-20^{\circ}\text{C}$  to  $150^{\circ}\text{C}$ . During the temperature ramping, a series of short and quick tensile tests were performed under  $0.3\text{N}$  as the applied static force. In Figure 5-22, every peak represents one uniaxial tensile test. The stress-strain curve of every uniaxial tensile test is obtained and the elastic modulus is calculated.

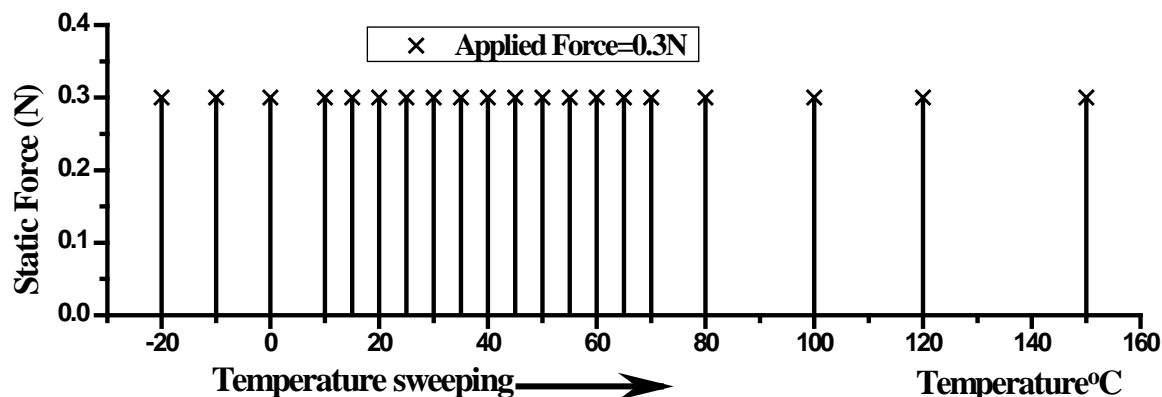


Figure 5-22: Concept of the ramping-temperature-dependent modulus experiment. Every peak represents one uniaxial tensile test.

Figure 5-23 shows four typical elastic modulus (Young's modulus) versus temperature curves, which are characterized by the ramping-temperature-dependent modulus experiments. Each curve in the Figure 5-23 can be identified into three regions: the glassy region, the transition region and the rubbery region. The measured elastic modulus and temperature range of each range of four differently-treated parylene-C are shown in Table 5-10. The first region (glassy region) shows the glassy state of the testing sample. The measured elastic modulus of parylene-C at this region varies mildly before the temperature reaches the onset of the next region. The range of the glass transition region was found between  $30\text{--}60^{\circ}\text{C}$  for as-deposited paryleneC and  $80\text{--}120^{\circ}\text{C}$  for parylene-C annealed at  $100^{\circ}\text{C}$ . When the temperature reaches the glass transition region,

the elastic modulus starts to drop quickly until the temperature reaches the onset of the third region, which is 60°C for as-deposited parylene-C and 120°C for parylene-C annealed at 100°C.

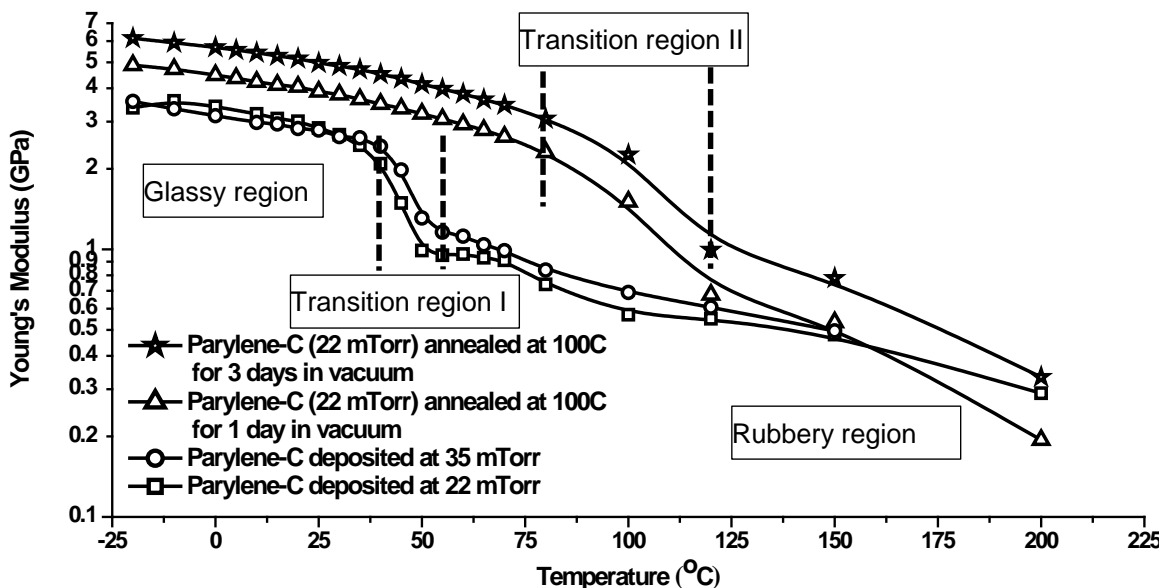


Figure 5-23: Elastic (Young's) modulus versus temperature curve. The transition region I represents the general glass transition region for as-deposited parylene-C, while transition region II represents the general glass transition region for parylene-C annealed at 100°C.

The four glass transition temperatures,  $T_g$ , which is normally defined as the maximum turndown point in the curve, i.e., maximum  $d^2E/dT^2$  [231], are found and shown all in Table 5-10. The obtained  $T_g$  of as-deposited parylene-C are both 50°C for samples deposited at 22 mTorr and 35 mTorr. The  $T_g$  of parylene-C annealed at 100°C is between 100–120°C, which will be identified more clearly in the next section. The elastic modulus of the parylene-C obtained in the rubbery region was approximately one

order smaller than in the glassy region, implying that parylene-C can be stretched much easier than in its glassy state.

Table 5-10: Measured elastic modulus and temperature range of glassy, transition, and rubbery regions

Parylene-C treatment	Glassy region range		Transition region range			Rubbery region range	
	GPa	(°C)	GPa	(°C)	Glass transition temperature, $T_g$ (°C)	GPa	(°C)
As-deposited (22 mT)	3.38–2.68	-20–30	2.68–0.96	30–60	50	0.96–0.29	60–200
As-deposited (35 mT)	3.57–2.64	-20–30	2.64–1.12	30–60	50	1.12–0.50	60–150
As-deposited annealed at 100°C for 1 day	4.88–2.31	-20–80	2.31–0.68	80–120	100	0.68–0.19	120–200
As-deposited annealed at 100°C for 3 days	6.15–3.08	-20–80	3.08–1.00	80–120	100	1.00–0.33	120–200

Although the ramping-temperature-dependent modulus experiment has shown its success characterizing  $T_g$  of the parylene-C samples, the uniaxial tensile test performed in this method is not continuous. If the temperature increment is too large, the  $T_g$  cannot be clearly resolved and only a rough  $T_g$  range can be identified. The  $T_g$  of parylene-C annealed at 100°C in Figure 5-23 demonstrates the problem. Another approach called dynamic mechanical analysis is commonly adopted to solve this problem and is introduced in the next section.

### 5.6.1.3 Dynamic mechanical analysis

Dynamic Mechanical Analysis (DMA) is a technique used to study material's viscoelastic/viscoplastic properties. As show in Figure 5-24 (a), the machine applied a continuous sinusoidal oscillatory stress, which is within material's linear elastic region, either by torsion, compression or tension to the specimen. The responded sinusoidal strain is recorded with respect to the time and the phase delay,  $\delta$ , between the applied stress and the responded strain can be found as well. For a perfectly elastic material,  $\delta$  equals to  $0^\circ$ ; for a viscous material,  $\delta$  equals to  $90^\circ$ . If  $\delta$  falls in between  $0^\circ$  and  $90^\circ$ , the material is called viscoelastic material [223]. If the amplitude of the measured strain,  $\varepsilon$ , is denoted as  $\varepsilon_0$ , the frequency of the applied stress is  $\omega$ , the measured strain can be represented as

$$\begin{aligned}\varepsilon &= \varepsilon_0 \sin(\omega t + \delta) = \varepsilon_0 \cos\delta \sin(\omega t) + \varepsilon_0 \sin\delta \cos(\omega t) \\ &= \varepsilon' \sin(\omega t) + \varepsilon'' \cos(\omega t),\end{aligned}\tag{5-4}$$

or

$$\varepsilon^* = \varepsilon' + i\varepsilon'',\tag{5-5}$$

where  $\varepsilon^*$  is called the complex strain,  $\varepsilon'$  is the strain which is in-phase with the applied stress and the  $\varepsilon''$  is the out-of-phase strain. If the amplitude of applied stress is  $\sigma_0$ , the modulus of the material can also be considered and represented as:

$$E = \left(\frac{\sigma_0}{\varepsilon_0}\right) \cos\delta + \left(\frac{\sigma_0}{\varepsilon_0}\right) \sin\delta = E' + iE'',\tag{5-6}$$

or

$$E^* = E' + iE'',\tag{5-7}$$

where  $E^*$  is called the complex modulus and the  $E'$  is called the storage modulus and the  $E''$  is called the loss modulus. The relationships of  $E^*$ ,  $E'$ , and  $E''$  can be shown in

Figure 5-24 (b). Physically,  $E''$  represents the energy dissipation of the materials during the oscillatory excitation.  $E'$  represents how elastic the material is and ideally it is equivalent to Young's modulus [223].  $\tan \delta$  is the parameter representing the damping properties of the materials.  $\tan \delta$  is an indicator of how efficiently the materials loses energy to molecular rearrangements and internal friction [223].

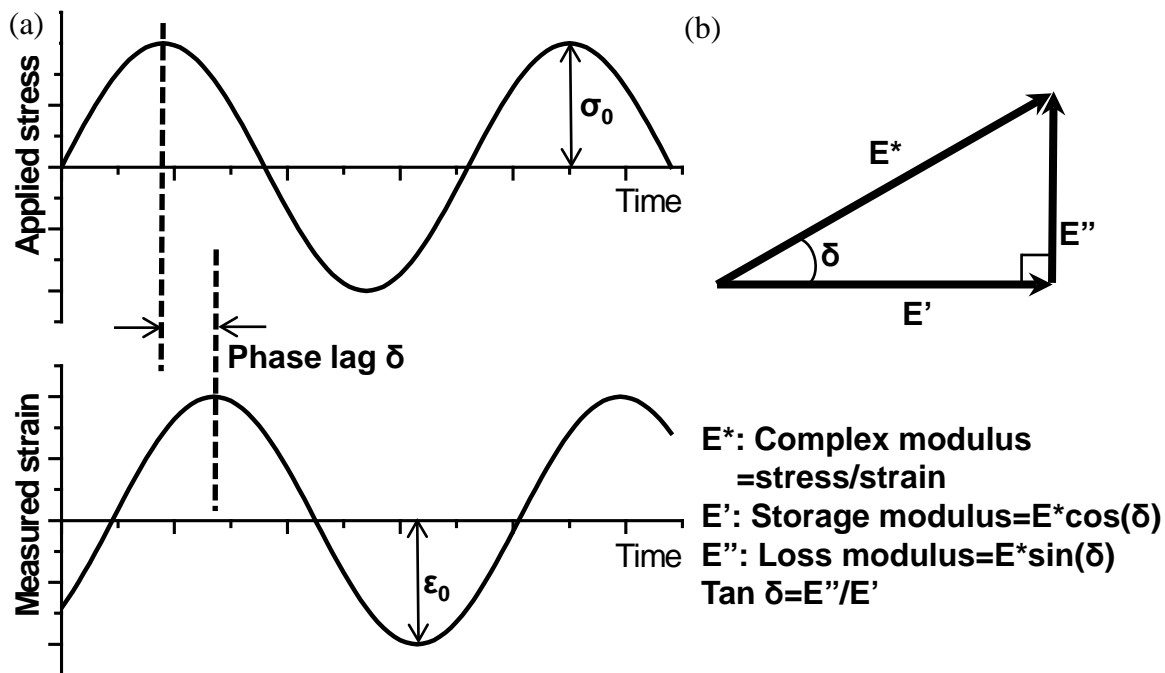


Figure 5-24: The concept of dynamic analytical analysis. (a) A sinusoidal oscillatory stress is applied and the material's sinusoidal strain response with a phase delay (viscoelastic materials) is measured. (b) The relationship of complex modulus ( $E^*$ ), the storage modulus ( $E'$ ), and the loss modulus ( $E''$ )

This sinusoidal oscillatory experiment can be performed under different temperatures and the corresponding mechanical parameters are then measured and calculated. A typical DMA result is shown in Figure 5-25. The solid line represents the

storage modulus of the specimen. For the rest of the two lines, one is the loss modulus and the other one is  $\tan \delta$ . It can be seen that the  $\tan \delta$  increases as the storage modulus decreases and the loss modulus increases. The  $\tan \delta$  reaches its maximum at the maximum ratio of the loss modulus to the storage modulus.

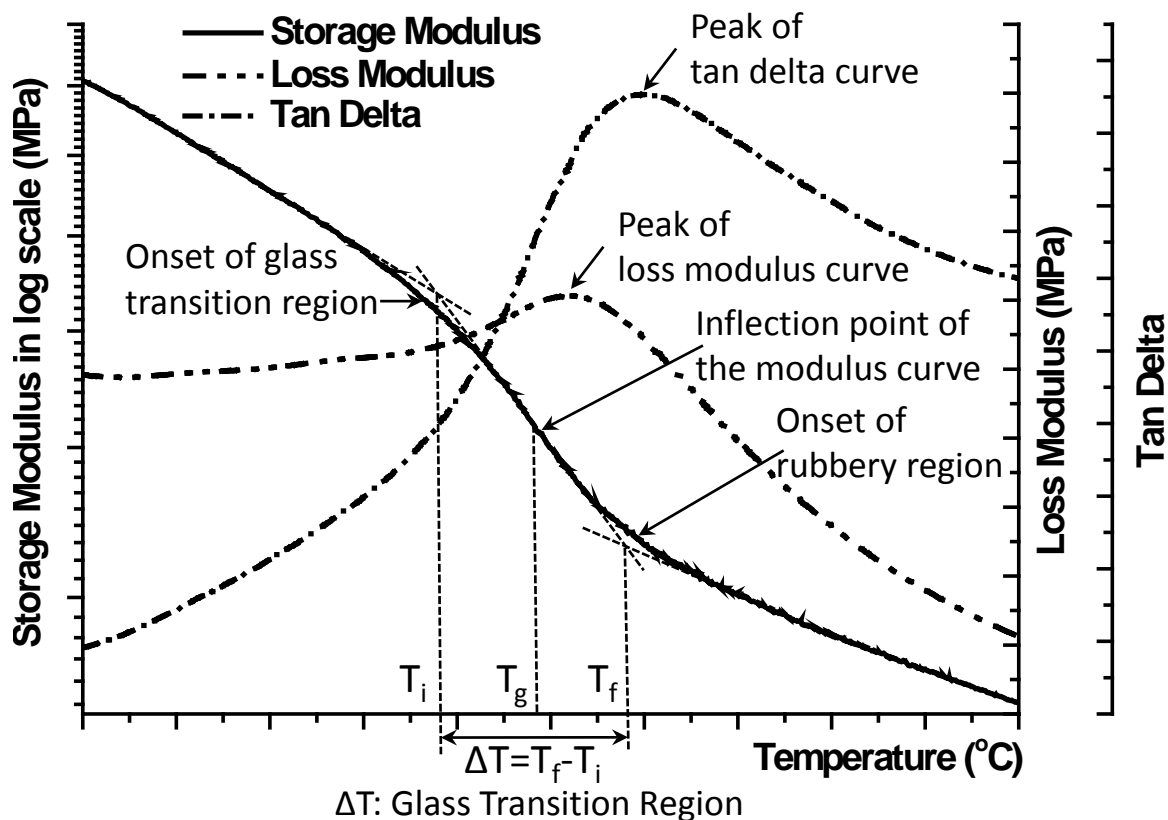


Figure 5-25: A typical DMA testing curve showing the results of storage modulus, loss modulus, and tan delta. Every curve has its corresponding definition to identify  $T_g$ .

Three different ways corresponding to the three curves in Figure 5-25 are commonly used to identify  $T_g$  of the testing samples from the DMA results [185]. For the storage modulus curve, the glass transition temperature,  $T_g$ , is defined at the inflection point of the glass transition region. The onset temperature of the glass transition region,

$T_i$ , is defined as the intersection of the two tangents of the storage modulus curve in the glassy region and the glass transition region. The onset temperature of the rubbery region, or the end of the glass transition region,  $T_f$ , is defined as the intersection of the two tangents of the storage modulus curve in the glass transition region and the rubbery region. The glass transition temperature of the loss modulus curve and the  $\tan \delta$  curve are both defined as the peak of the curves. As the storage modulus represents the Young's modulus, it is more meaningful to use the storage modulus curve to study the glass transition region, and therefore will be used in our whole glass transition temperature study.

To compare the accuracy and the capability of the two approaches discussed above, a comparison of two typical results of the two approaches is shown in Figure 5-26. The sample tested is the parylene-C annealed at 100°C for one day in vacuum oven. The  $T_g$  provided by DMA is 113.1°C and the other method measures the  $T_g$  to be in the range between 100°C and 110°C. The comparison shows that two methods both provide results which are very close to each other. The discrepancy found between two curves might be attributed to the testing frequency difference, which is worth more studying. From the analytical point of view, however, the DMA approach provides a much smoother, non-interrupted curve so that  $T_g$  is able to be defined more accurately. Therefore, DMA measurement is generally used in most glass transition temperature study in the thesis unless otherwise specified.

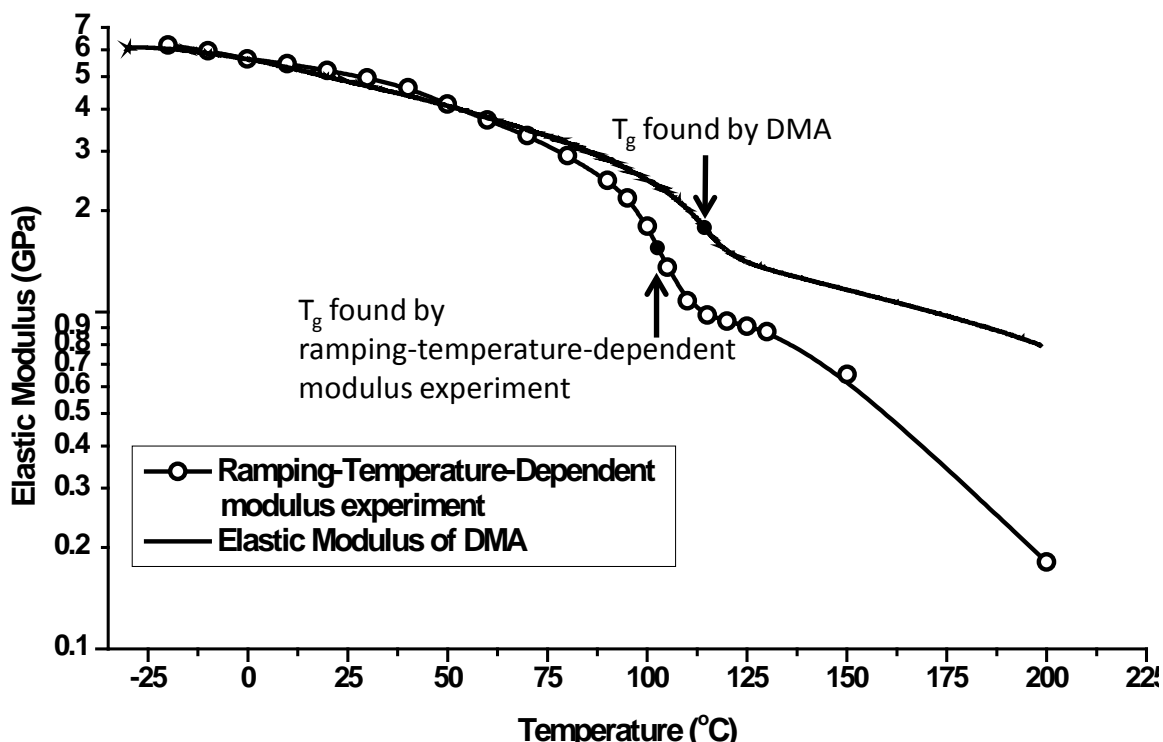


Figure 5-26: A comparison of the results of the ramping-temperature-dependent modulus experiment and the DMA test. Parylene-C sample was annealed at 100°C for one day in vacuum.  $T_g$  is found at the inflection point of each glass transition region.

### 5.6.2 Measuring results and discussion

Several selected measured storage modulus curves and their obtained corresponding  $T_g$  are shown in Figure 5-27, Figure 5-28, Figure 5-29, and Figure 5-30. The convection oven used in the  $T_g$  measurement experiment was always preheated to the target temperature before the parylene-C sample loading, and therefore samples always experienced step-function temperature profile during the annealing. In Figure 5-27, three samples were annealed at 100°C but for different annealing times with one curve representing the as-deposited parylene-C for comparison purposes. In Figure 5-28, four parylene-C samples were all annealed at 100°C, but for a different period of times shorter

than Figure 5-27, with one as-deposited parylene-C result for comparison. In Figure 5-29, two parylene-C samples were annealed at 200°C in vacuum for one and two days and one parylene-C annealed at 100°C for two days, with one as-deposited parylene-C result for comparison. In Figure 5-30, seven parylene-C samples were annealed at different temperatures as shown in the DMAQ800 chamber (no vacuum) for the first 30 minutes followed by the regular  $T_g$  measurement procedures. Several observations and conclusions can be found from those four figures:

1. It is clearly seen from Figure 5-27 to Figure 5-30 that the measured  $T_g$  increases as the annealing temperature increases. As shown in Figure 5-29, because all the parylene-C samples shown in the figure were all annealed in vacuum, the possibility of the oxidation effect could be eliminated. Therefore, the  $T_g$  increment is very likely attributed to the crystallinity increase after the parylene-C annealed at high temperature. Compared to the amorphous part of the polymer, the crystallite part is generally assumed to be much stronger and will remain intact under the applied force [185]. As it has been verified in Section 5.5 that the crystallinity increases when the annealing temperature increases, the deformable amorphous part of the annealed parylene-C reduces. Owing to the less amorphous part after higher temperature annealing, the molecular structure of parylene-C becomes more difficult to move, and hence the  $T_g$  is obtained to be higher after annealed. The result found agrees well with Senkevich's observation: "semicrystalline polymers exhibit an increase in their  $T_g$ , a larger  $T_g$  range and a decrease in  $\Delta C_p$ , making  $T_g$  determination more difficult as less amorphous material exists to contribute to the  $T_g$ " [184].

2. The measured T<sub>g</sub> increases as the annealing time increases. The effect can be found in Figure 5-27 to Figure 5-29. This phenomenon could be explained by the same reason of parylene-C crystallinity increment. As described in Section 5.5 that the longer annealing time increases the crystallinity of the parylene-C, and therefore it can thus increase the T<sub>g</sub> as well, as the amorphous part is the weaker part inside the polymer.
3. It is also found that the T<sub>g</sub> increases extremely fast at the early stage of the annealing when it experiences the elevated temperature. As shown in Figure 5-28, it can be seen that T<sub>g</sub> increases to 86.2°C after the first 30sec of annealing at 100°C and the T<sub>g</sub> increasing rate slows down afterward. According to the previous conclusion that parylene-C's T<sub>g</sub> increases due to its crystallization, the testing result is another strong evidence that parylene-C crystallizes fast when it experiences temperature higher than its T<sub>g</sub>, i.e., ~ 50°C found from Section 5.6.1.2. It further confirms that the time constant of the parylene-C crystallization is shorter than one minute, which agrees well with our findings in Section 5.5.2.
4. From Figure 5-27 to Figure 5-30, it is found that the obtained T<sub>g</sub> is usually close to, but a bit higher than, the annealing temperature. This can be explained that the free volume inside the annealed parylene-C has been reduced to or lower than 2.5% [185] during the annealing. As it requires making the free volume go over 2.5% to make the parylene-C reach glass transition again, the temperature needs to go at least as high as or even a bit higher than the prior annealing temperature and therefore the re-measured T<sub>g</sub> will be close to the prior annealing temperature.

5. The glass transition region of the storage modulus curve of parylene-C annealed at 200°C becomes very vague and hard to find a definite T<sub>g</sub>. According to the trend of other T<sub>g</sub> of the parylene-C annealed at lower temperature, this T<sub>g</sub> might be higher than 200°C and cannot be defined from Figure 5-29 because of the insufficient testing data. Both curves of parylene-C annealed at 200°C for either one or two days shown in Figure 5-29 look like almost linear, which implies parylene-C would behave similar to the perfectly elastic material at temperatures lower than 200°C after annealed at 200°C. This will be verified again by the creep tests in Section 5.8.1.
6. It can be found from Figure 5-30 that there is no significant difference between the T<sub>g</sub> measured at the temperature at 20°C and 40°C. As the T<sub>g</sub> of the as-deposited parylene-C can be revealed to be around 50°C from Figure 5-27, it is hypothesized that the crystallization does not happen at temperatures less or equal to 40°C. Therefore, when the parylene-C is annealed at 20 or 40°C, there is not enough energy to cause the parylene-C polymer chains to move and crystallize. It could be concluded that T<sub>g</sub> of parylene-C will not change as long as the prior annealing temperature is less than T<sub>g</sub>.
7. The measured elastic modulus, i.e., Young's modulus, increases when either the annealing temperature or time increases. As it is generally believed that the crystallite has a much stronger modulus than amorphous part, it could also imply that more parylene-C is crystallized at higher annealing temperatures or longer annealing times. This finding agrees well with what has been found in Section 5.5. In addition, the descending slopes of the storage modulus are all very similar

before and after the glass transition region. In the same region, either glassy or rubbery region, the descending slopes of the storage modulus curve of every sample are also similar to each other no matter what kind of treatment the sample has experienced prior to the DMA test.

8. It is observed that the glass transition range tends to broaden as either the annealing temperature or annealing time increases. It is also likely due to that fact that the amorphous part of the annealed parylene-C is reduced, and therefore it takes more energy, i.e., higher temperature, to bring parylene-C into the rubbery region.

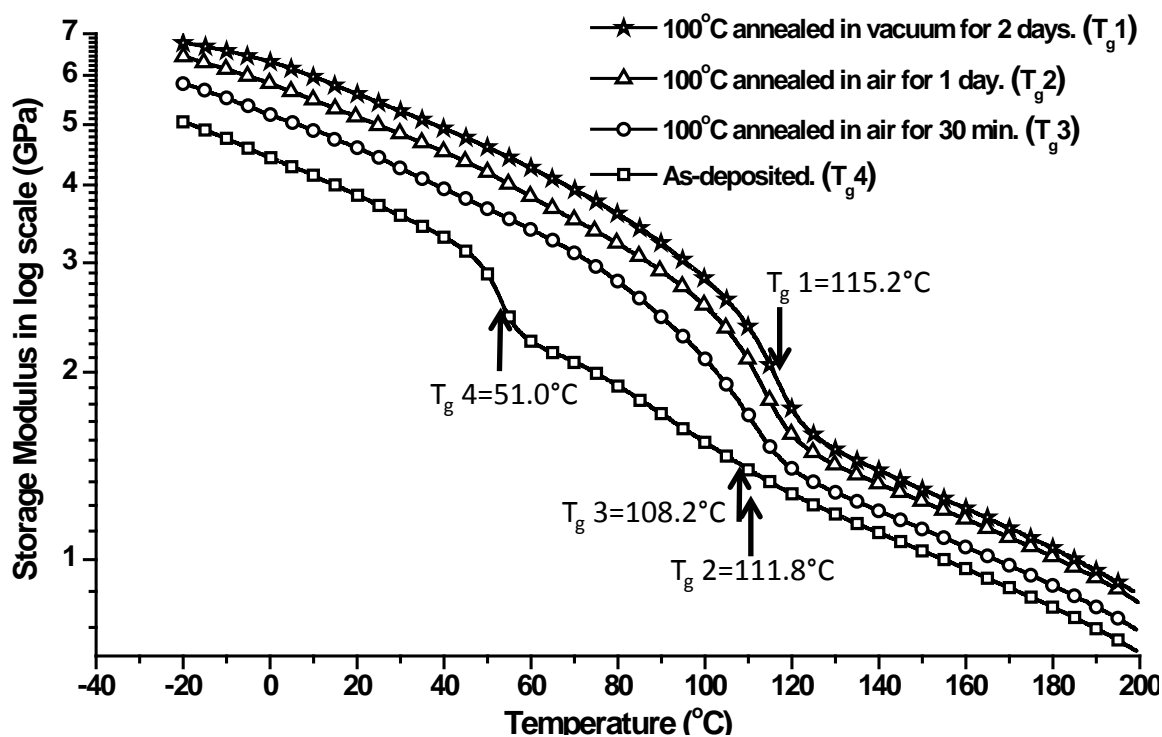


Figure 5-27: Measured  $T_g$  of four parylene-C annealed in different conditions: 3 samples at 100°C, with as-deposited parylene-C as a comparison

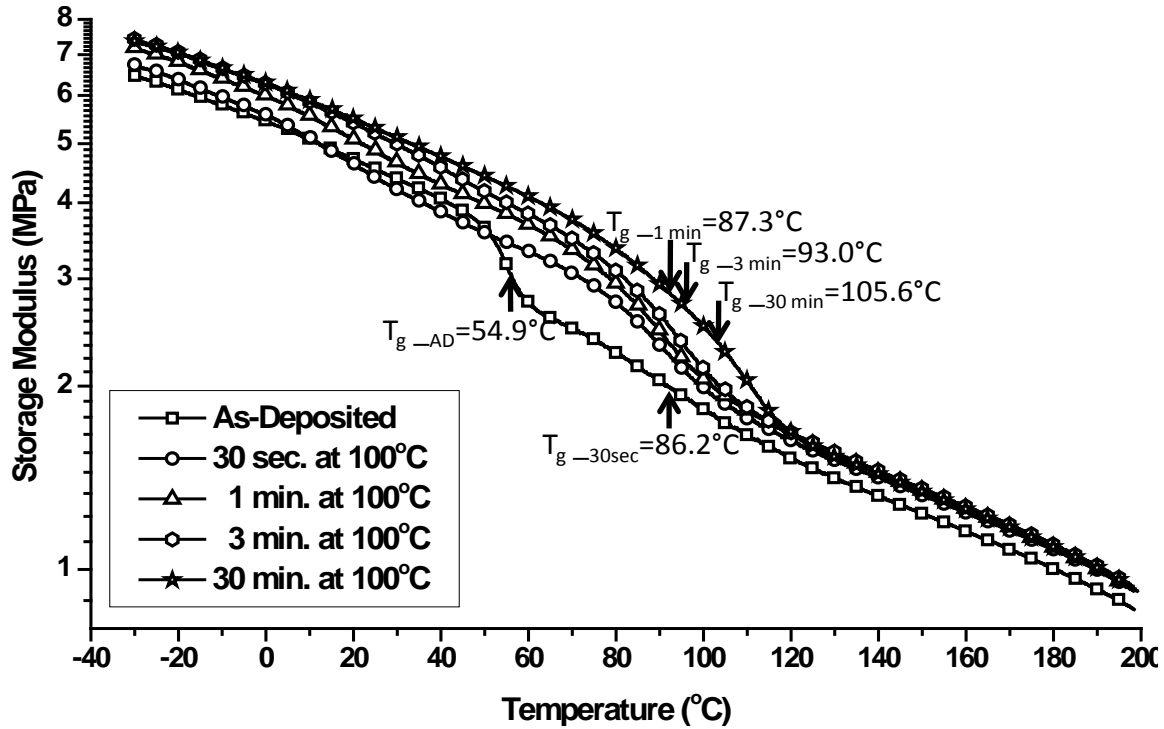


Figure 5-28: Measured  $T_g$  of parylene-C samples all annealed in  $100^\circ\text{C}$  but for different times: 30 sec, 1 min, 3 min, and 30 min

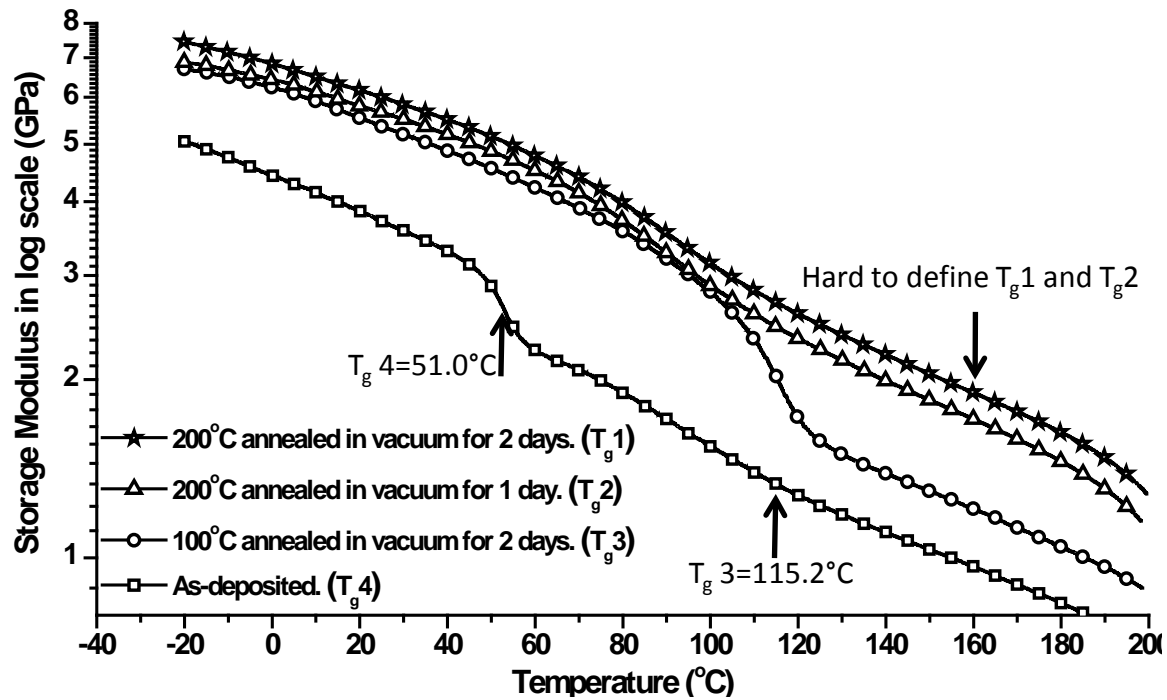


Figure 5-29: Measured  $T_g$  of four parylene-C samples annealed in different temperatures

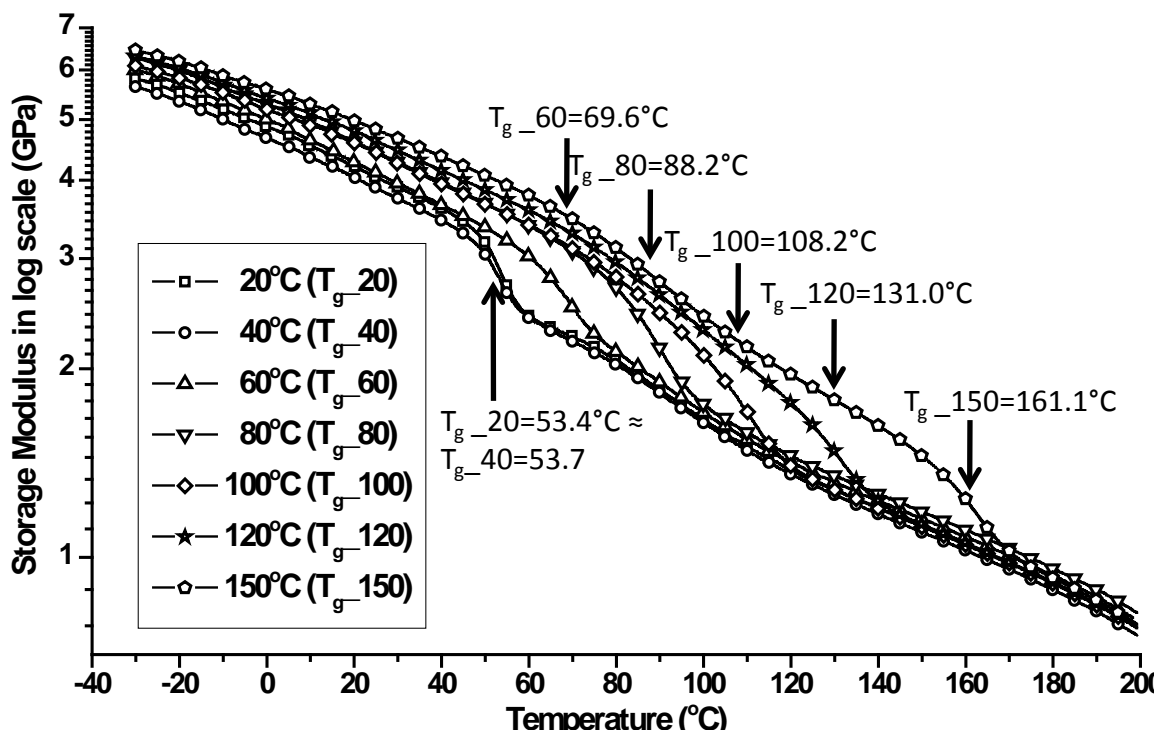


Figure 5-30: Measured  $T_g$  of seven parylene-C samples annealed in different temperatures. Samples were annealed in the DMA Q800 chamber for 30 min prior to the  $T_g$  test.

Table 5-11 systematically and quantitatively displays the measured  $T_g$  and the glass transition region of every testing sample shown in Figure 5-27 through Figure 5-30. In addition, the  $T_g$  obtained by the peak of loss modulus curve and the  $\tan \delta$  curve are also listed for comparison.

Table 5-11: Measured glass transition temperature *via* DMA approach

Parylene-C treatment	T <sub>g</sub> obtained by storage modulus (°C)				T <sub>g</sub> obtained by peak of loss modulus (°C)	T <sub>g</sub> obtained by peak of tan δ
	T <sub>i</sub>	T <sub>g</sub>	T <sub>f</sub>	ΔT		
<b>Sample treated in DMA chamber</b>	T <sub>i</sub>	T <sub>g</sub>	T <sub>f</sub>	ΔT	T <sub>L</sub>	
As-deposited	50.2	53.4	57.0	6.8	68.4	94.1
40°C in air for 30 min	50.8	53.7	55.5	4.7	67.2	91.6
60°C in air for 30 min	65.3	69.6	73.3	8	78.15	93.84
80°C in air for 30 min	83.6	88.2	94.9	11.3	95.3	101.14
100°C in air for 30 min	105.6	108.2	115.6	10	113.9	119.1
120°C in air for 30 min	124.9	131.0	138.0	13.1	136.8	143.6
150°C in air for 30 min	155.3	161.1	169.1	13.8	168.9	-
<b>Sample treated outside DMA chamber</b>	T <sub>i</sub>	T <sub>g</sub>	T <sub>f</sub>	ΔT	T <sub>L</sub>	
As-deposited at 35 mT	52.5	55.1	58.8	6.3	71.6	92
As-deposited	50.2	53.4	57.0	6.8	68.4	94.1
100°C in air for 30 sec	78.4	87.3	98.4	20	95.3	101.8
100°C in air for 1 min	81.8	86.2	100.6	18.8	93.7	103.9
100°C in air for 3 min	82.7	93.0	103.2	20.5	98.9	107.0
100°C in air for 30 min.	96.7	105.6	115.8	19.1	111.2	120.6
100°C in air for 1 hour	95.1	103.0	109.6	14.5	106.7	115.9
100°C in air for 2 hour	96.2	101.5	109.6	13.4	109.6	114.4
100°C in air for 3 hour	96.4	101.8	111.2	14.8	108.3	115.9
100°C in air for 6 hour	97.8	106.3	115.9	18.1	112.2	118.9
100°C in air for 16 hour	103.1	110.3	118.9	15.8	116.8	122.9
100°C in air for 1 day	104.4	111.8	119.7	15.3	117.4	123.3
100°C in air for 2 days	106.9	114.7	122.3	15.4	120.2	125.3
100°C in air for 3 days	111.4	116.9	122.2	10.8	122.1	128.0
100°C in vacuum for 1 day	100.5	113.1	121.5	21.0	118.4	124.7
100°C in vacuum for 2 days	103.7	115.2	122.4	18.7	120.2	125.3
200°C in vacuum for 1 day	Hard to find a T <sub>g</sub>					
200°C in vacuum for 2 days	Hard to find a T <sub>g</sub>					

Apart from the findings aforementioned, more things can be observed from Table 5-11:

1. The Tg of as-deposited parylene-C is found at 53.4°C. On the contrast to the ramping-temperature-dependent modulus experiment which provides a rough Tg and the glass transition range, DMA measurement provides much more accurate Tg of the parylene-C and also its range. Even though, Tg provided by both methods are very close, meaning that they are both reliable approaches.
2. It is shown in Table 5-11 that Tg of the parylene-C deposited at 35 mTorr (55.1°C) similar to 22 mTorr (53.4°C). Although it has been shown in Section 5.5.3 that the parylene-C is likely have lower crystallinity when the deposition pressure increases, the crystallinity difference does not seem to influence the Tg results of these two parylene-C samples. On the other hand, however, it also shows in Section 5.5.3 that the crystallite size of these two parylene-C deposited at different pressure are very similar, which might explain the Tg-similarity result obtained in this section. More future work is required to figure out the cause of this observation.
3. As discussed in Section 5.4, it is assumed that the mechanical properties of parylene-C annealed at 100°C have no significant difference between in the air or in the vacuum. The hypothesis applies in Table 5-11 as well. For instance, there is no distinguishable difference found between the Tg of the parylene-C annealed at 100°C for one day in air (111.8°C) or vacuum (113.1°C). Therefore, sample oxidation is likely not to be the dominant issue in terms of the Tg measurement.

4. Although  $T_g$  increases as the annealing time increases, it is found that  $T_g$  actually increases fast from  $53.4^\circ\text{C}$  to  $87.3^\circ\text{C}$  during the first 30 sec when annealed at  $100^\circ\text{C}$ , and reaches  $105.6^\circ\text{C}$  after 30 min of annealing. As the parylene-C's  $T_g$  change within only one minute agrees well with result of Section 5.5.1 that the time constant of the crystallization of parylene-C annealed at  $100^\circ\text{C}$  is less than 1 minute, it can be concluded that the  $T_g$  is mainly influenced by the fast progress of the crystallization of the parylene-C.
5. It is also phenomenally observed that the  $T_g$  obtained using the peak of the loss modulus curve and the  $\tan \delta$  curve is usually higher than storage modulus curve. In spite of the discrepancies between  $T_g$  obtained from storage modulus, loss modulus and  $\tan \delta$ , researchers accept it as the glass transition represents a range of the behavior and people have agreed to accept a single temperature as the indicator for certain standards [232]. Scientists working on different aspects may pick up different values from the same set of data. In our experiments, the order of the three  $T_g$  can be generally shown as:

$$\text{Storage modulus } T_g < \text{Loss modulus } T_g < \text{Tan } \delta T_g$$

6. Dabral et al. predicted the parylene-C  $T_g$  as  $150^\circ\text{C}$  according to the their obtained stress-temperature curve [110]. The  $T_g$  was determined by them at the time when the stress started to show no large variations. However, it is also noted that the  $T_g$  could be found as different via a different approach and therefore a different value is obtained according our new observation. It is first found from Dabral's curve that the as-deposited parylene-C shows  $-6 \text{ MPa}$  (i.e. compressive stress) after the deposition. The stress then decreases (i.e., becomes more compressive) as the

temperature increases until 50°C. The stress keeps increasing until it balances with the silicon substrate. From Dabral's reported curve of stress versus temperature, a turning point is found at 50°C. The most negative stress (i.e., the most compressive stress) is found at this turning point and then starts to increase as the temperature increases and then stabilizes after 100°C. The assumption of this phenomenon is that the parylene-C expands until 50°C due to thermal expansion of the sample, and starts to shrink after the temperature becomes higher than 50°C due to the crystallization. This result actually agrees well with what has been found in Section 5.3. Therefore, according to our discussion in Sections 5.3, 5.5 and also Dabral's stress-temperature curve, the parylene-C starts to crystallize at around 50°C, and therefore the  $T_g$  could be defined as 50°C.

### 5.6.3 Summary

Although the study of parylene-C  $T_g$  started as early as in 1966 by Gorham, the past results indicated that there still exists inconsistency of the reported glass transition temperatures of parylene C, which widely ranged from 13 to 150°C. It can be found from Table 5-9 that different measuring techniques can produce different  $T_g$  results. This is not surprising, though. Different researchers from research fields would adopt different approaches which is more relevant to their works. The different can be as much as 25 degree difference in data from a DSC to DMA data reported as peak of tan delta [232]. In two of our experiments, ramping-temperature-dependent modulus experiment and DMA analysis, the obtained  $T_g$  of as-deposited parylene-C show consistent results and all of them fall in the range of ~ 50–55°C. Our measured  $T_g$  agrees well with the numbers published by Alpaugh, Senkevich and Huang. Annealing temperature and time are

proved to be the main cause affecting the results of  $T_g$  and its range. High annealing temperature (higher than the  $T_g$  of as-deposited parylene-C) and long annealing time can make the parylene-C more crystallized and therefore increases its final  $T_g$ . Apart from the different measuring approaches, it could be concluded that unstandardized parylene-C sample preparation is likely one of the reasons causing the variation of the  $T_g$ 's literature value. On the other hand, the deposition pressure does not seem to influence the measured  $T_g$ , in our tests, which need more data points to verify this observation. Future work would also focus on the influence of the deposition temperature and also the deposition rate.

With its superb biocompatibility and its compatibility with the CMOS fabrication process, parylene-C is widely used as a biocompatible material in MEMS technology. Since many cleanroom processes introduce high temperature during the process, parylene-C is very likely to be annealed during the device fabrication. These heat-generating processes could cause the  $T_g$  to shift during the fabrication and the parylene-C will not behave the same as the as-deposited one after the clean room fabrication process. In other words, knowing the temperature history of the parylene-C fabrication is crucial and can be very helpful in predicting its glass transition temperature and also mechanical properties, therefore the device properties after the manufacturing. If the device's parylene-C mechanical property is the main concern during its operation, the temperature history needs to be recorded in order to control its final functional behaviors.

## **5.7 Uniaxial Tensile Test**

Uniaxial tensile test is one of the most fundamental and popular tests used to measure the mechanical properties of a material. Figure 5-31 shows a typical stress-

strain curve of an as-deposited parylene-C film obtained from our uniaxial tensile test at room temperature. The solid line shows the nominal stress-strain curve while the dashed line represents the modified true stress-strain one. From the regular engineering aspect, nominal curve is more conservative and therefore will be considered in this section unless otherwise specified. In most of the testing results, it is very common to see an artifact showing a toe region in the early stage of the testing curve as seen in the Figure 5-31. This is caused by a takeup of slack and needs to be corrected to obtain correct parameters following the ASTM standards D882-09 and D638-08 [233, 234]. In this section, five different parameters: elastic modulus (Young's modulus,  $E$ ), nominal tensile strength ( $\sigma_T$ ), yield strength ( $\sigma_Y$ ), percent elongation (%El) and percent elongation at yield ( $\epsilon_Y$ ) were considered and calculated according to the definition of ASTM standards. In terms of the identification of the yield point, there are different ways to find out the point depending on the curve feature of the material. Provided by ASTM standard D638-08, the yield point is defined as the first point on the stress-strain curve at which an increase in strain occurs without an increase in stress. By this definition, it is very likely the nominal tensile strength shares the same value of the yield strength due to parylene-C's stress-strain curve characteristics.

A film of 20 $\mu\text{m}$  thick parylene-C was first deposited on a clean glass plate and then the film was cut into 5.3- $\mu\text{m}$ -wide strips for testing. The gauge length was taken as 10 mm for uniaxial tensile test. The parylene-C strips were then treated at different temperatures to study the temperature effects. In addition, parylene-C film deposited at different pressure was also obtained to study the deposition pressure influence. As oxidation is recognized as a key control factor affecting final parylene-C's properties, it

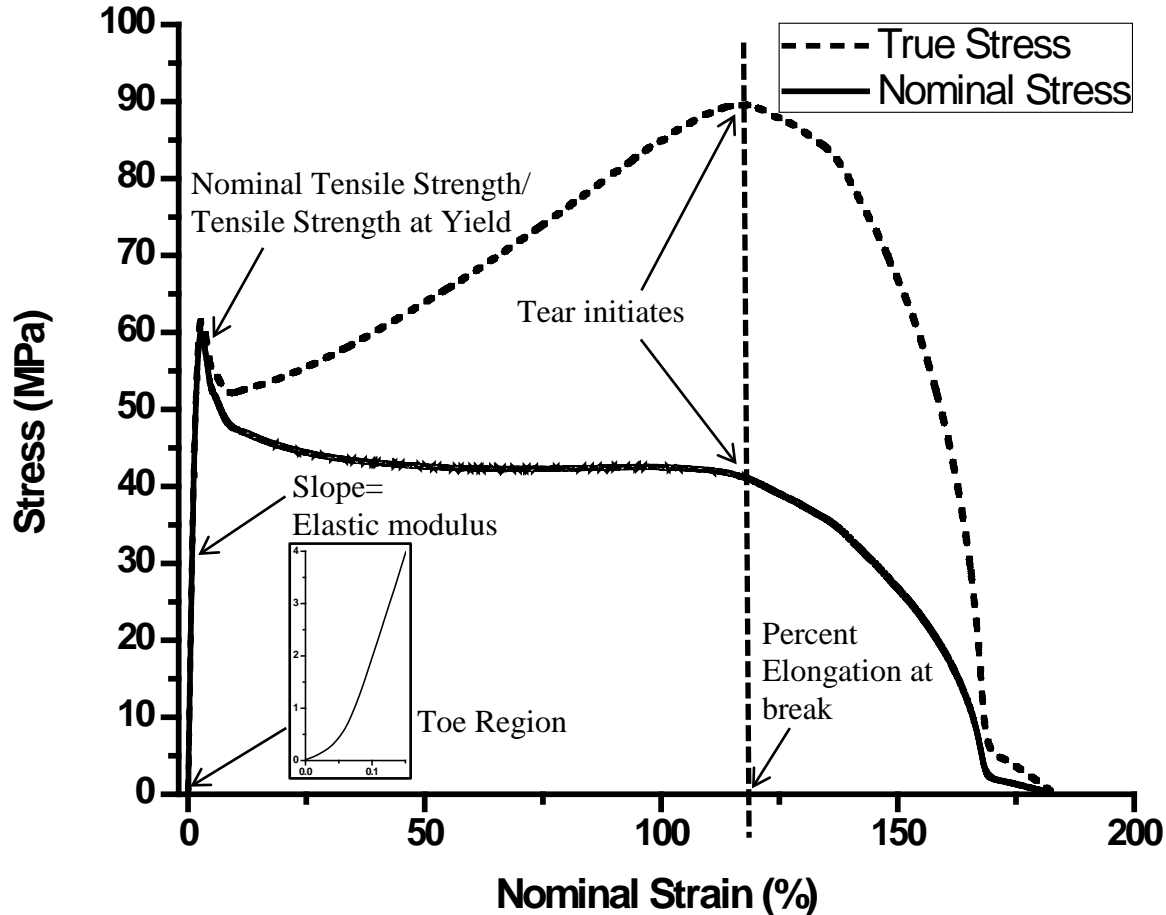


Figure 5-31: Typical as-deposited parylene-C film uniaxial tensile test results obtained by TA instrument DMA Q800 system. Toe region is compensated to give the final correct calculated parameters. All terminologies follow the definition of the ASTM standard D882-09 and D638-08 [233, 234].

was also explored in this section. The testing environmental temperature was 20°C unless otherwise specified. The strain loading rate was 1% / min. At least three samples treated in the same condition were tested to calculate the average number and standard deviation of the parameters. Table 5-12 shows the uniaxial tensile tests testing results of parylene-C film treated under different conditions. The literature numbers provided by SCS, and reported by Gorham [172], Spivack [235], Baker [195], and Beach [101, 102]

are also listed for comparison. The results of different post-deposition treatment and their different effects are discussed in the following sections.

### 5.7.1 As-deposited parylene-C film

The as-deposited parylene-C was deposited at 20°C and 22 mTorr. A typical uniaxial tensile curve of the as-deposited parylene-C is shown in Figure 5-31. Table 5-12 lists five different types of mechanical properties of the as-deposited parylene-C film obtained in our uniaxial tensile test. Due to a common toe region effect, elastic modulus can be calculated based on two different reference points. One is to take the tangent to a short section of the proportional region after toe region correction, denoted as  $E$ . The other is to take a slope from the measuring point with respect to 0 MPa in stress and 0 % in strain, denoted as  $E_0$ . The value shown in Table 5-12 is always higher than the literature values. Because the proportional region of parylene-C does not show a linear line but a gradually-changing curve, it is believed that the elastic modulus measured at different strain can be different and the value decreases with the increase of the strain.

Two values of tensile strength are provided here as well. One is the maximum nominal tensile stress,  $\sigma_T$ , according to ASTM standard D882-09, while the other one represents the modified maximum true stress,  $\sigma_T$ . For the tensile strength obtained from SCS, the value represents the maximum stress prior to plastic deformation. However, whether the value is calculated as nominal or true stress is not clearly stated from the parylene-C provider. Therefore both our measured numbers are listed to compare to the literature values.

Table 5-12: Measured mechanical properties of parylene-C film's uniaxial tensile test

<b>Parameter</b> <b>Parylene-C treatment</b>	<b>Elastic modulus</b>	<b>Elastic modulus from 0 MPa and 0%</b>	<b>Nominal tensile strength</b>	<b>Max true tensile stress</b>	<b>Yield strength</b>	<b>Percent elongation at yield</b>	<b>Percent elongation</b>
Symbol	E	E <sub>0</sub>	σ <sub>T</sub>	σ <sub>TT</sub>	σ <sub>Y</sub>	ε <sub>Y</sub>	%El
Unit	GPa	GPa	MPa	MPa	MPa	%	%
SCS	2.758		68.948*		55.158	2.9	Up to 200
Gorham [172]	3.172		73.08**		NA	NA	220
Spivack [235]*	2.354; 2.746 (1% strain)		61.302; 68.658		57.9; 54.9	4.2; 2.9	170; 200
Baker [195]	2.917		NA		56.904	NA	NA
Beach [101, 102]	3.2		70**		55	2.9	200
As-deposited (22 mTorr)	3.841	3.470	58.37	67.869	58.37	2.861	119.139
Standard deviation	0.315	0.285	5.718	7.290	5.718	0.472	17.611
As-deposited (35 mTorr)	2.999	2.452	49.189	50.45	49.189	2.506	66.325
Standard deviation	0.156	0.066	2.186	2.264	2.186	0.039	23.767
30 sec 100°C in air	4.339	3.650	77.506	80.938	77.506	4.260	43.969
Standard deviation	0.125	0.355	1.307	1.274	1.307	0.271	4.250
1 min 100°C in air	4.680	4.060	77.233	81.066	75.687	3.197	37.848
Standard deviation	0.094	0.197	6.660	6.016	9.188	0.873	11.224
3 min 100°C in air	4.467	3.757	81.087	84.733	81.087	4.164	43.383
Standard deviation	0.234	0.517	2.520	2.460	2.520	0.374	5.896
30 min 100°C in air	4.251	3.239	74.153	77.276	74.153	4.153	36.963
Standard deviation	0.057	0.052	4.273	4.147	4.273	0.598	6.037
1 day 100°C in air	4.547	4.070	83.921	86.834	83.921	3.367	8.526
Standard deviation	0.292	0.286	1.288	1.204	1.288	0.313	1.366
1 day 100°C in vacuum	4.312	4.058	72.700	75.166	72.700	2.200	6.897
Standard deviation	0.189	0.264	2.893	3.227	2.893	1.530	5.172
2 day 100°C in vacuum	5.298	4.835	92.185	95.135	92.185	3.157	6.313
Standard deviation	0.216	0.165	3.466	3.666	3.466	0.286	1.312
1 day 200°C in vacuum	4.961	4.472	81.659	84.636	81.659	3.399	6.515
Standard deviation	0.086	0.192	2.439	3.034	2.439	0.357	3.236
2 day 200°C in vacuum	6.058	5.629	102.933	106.591	102.933	3.449	4.512
Standard deviation	0.129	0.268	7.490	8.325	7.490	0.603	0.447

\*The first number corresponds to 0.12–28.0 μm thick while the second one is 25 μm thick.

\*\*It is not clearly specified what type of tensile strength— nominal or true tensile stress—is given in the SCS parylene-C data sheet and references [100–102].

The yield strength given by SCS is calculated with a 0.2% offset from the elastic strain. Because different elastic modulus could lead to different yield strength value, the tensile strength shown in Table 5-12 is calculated according to standard ASTM D882-09. The obtained value is higher than SCS's due to the offset, but the deviation is within 10%.

Percent of elongation is obtained as 119.14 %, which is much smaller than the literature value. It is believed that the testing specimen tore before the specimen really broke which is actually caused by a nicks or imperfect cutting edge. Cutting the parylene-C film specimen needs to be very careful to prevent nicks or tears at the edge. With the knowledge of the fracture mechanics, when the loading goes high, the nicks can induce stress concentration locally and suddenly propagate, becoming a crack causing the rupture earlier to happen and lead to anomalous results. Specimen with nicks at the edge will end up with a lower percent elongation at break. In practice, however, micro nicks are difficult to avoid and tears happen very often during the tests as shown in Figure 5-31. In addition, it is also found that the alignment of the specimen installed in the testing machine affects the percent of elongation. A proper installation of the specimen gets rid of unwanted bending stress and thus helpful in getting a more appropriate testing result.

### **5.7.2 Deposition pressure influence**

To study the deposition pressure influence of parylene-C mechanical properties, another parylene-C film deposited with pressure at 35 mTorr was also prepared with the same geometry and then tested under the same testing conditions. The testing data is also shown in Table 5-12. It is found that all mechanical properties of parylene-C film

deposited at 35 mTorr have smaller values compared with parylene-C film deposited at 22 mTorr. It is likely because the parylene-C deposited at higher pressure has a higher deposition rate and thus more polymerization centers form. It then results in more micro voids of the parylene-C film deposited at 35 mTorr than 22 mTorr, and thus the mechanical properties show smaller values. Such kind of parylene-C has more and shorter polymer chains and therefore cannot organize in order as they can at low deposition pressures [104]. As aforementioned in Sections 5.5 and 5.6, because amorphous parylene-C is weaker than crystalline parylene-C, it is reasonable that the mechanical properties of parylene-C deposited at 35 mTorr are more amorphous and therefore generally smaller than 22 mTorr.

Figure 5-32 shows the comparison of typical stress-strain curves of parylene-C film deposited at the pressures with both 35 mTorr and 22 mTorr. It is observed that the elongation of parylene-C film deposited at 35 mTorr is smaller than at 22 mTorr. It can also be seen that there is no strain hardening for parylene-C deposited at 35 mTorr. It is probably because the looser structure or the likely short polymer chain of the parylene-C film which cause the material easy to be broken, which means less ductility. Although the parylene-C film deposited at 22 mTorr shows better ductility, the sporadic spread data points, however, make it still hard to exactly conclude the influence of the deposition pressure to the percent elongation. The same phenomenon, i.e., widely spread percent of elongation data points, was also observed by Hassler [104]. One interesting observation in Hassler's result shows: in spite of the widely spread data values, Hassler's parylene-C film deposited at 20 mTorr has only 20% elongation at break in average, which is much less than the literature value of 200%, and also our testing value of 119.139%. In

addition, it also has been found that a lower strain rate will favor higher elongations and somewhat lower stress values [235]. Therefore, although Hassler prepared parylene-C samples with the same thickness as ours, it is shown that Hassler's strain rate was much faster than ours (about 1%/sec versus our 1%/min), and thus Hassler had much less percent of elongation results than ours.

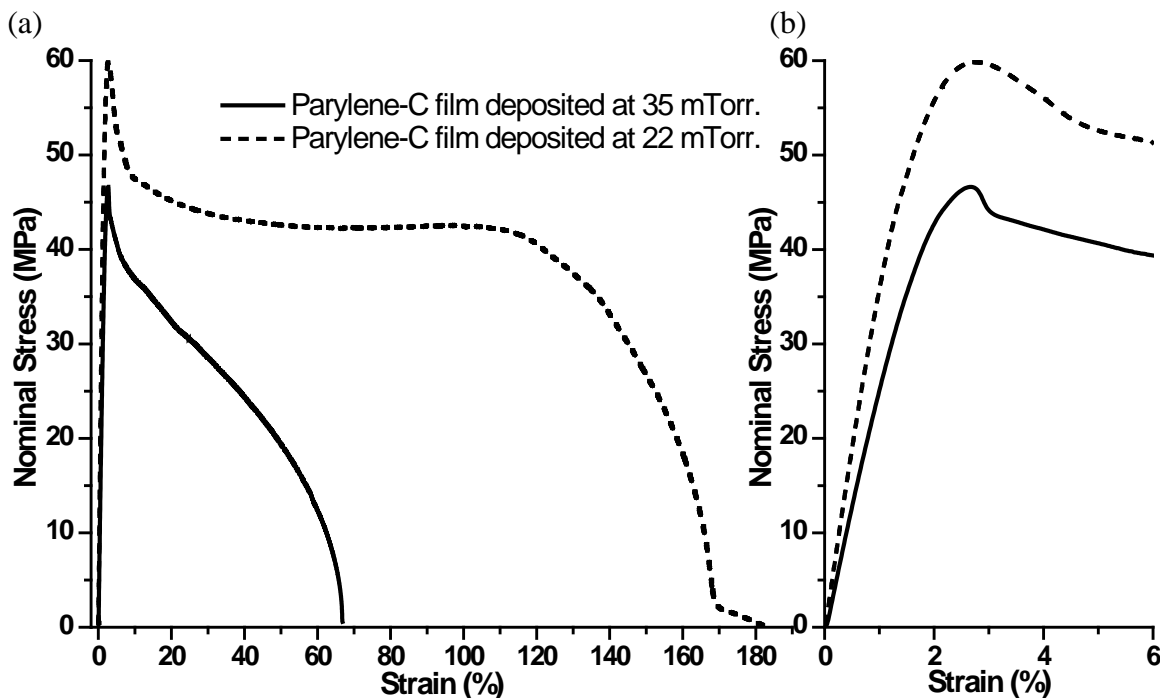


Figure 5-32: Comparison of parylene-C film deposited at different pressures. (a) Two stress-strain curves. (b) A closer view of elastic modulus and yield point

### 5.7.3 Oxidation effect

It has been discussed in Section 5.4 that parylene-C can be oxidized either by heat or ultraviolet (UV) light. To study the influence of the thermal oxidation effect on parylene-C's mechanical properties, two different parylene-C film samples are prepared: one is parylene-C film annealed at 100°C for 1 day in the convection oven, i.e., in the air, the other one is annealed at the same temperature for the same time but in vacuum. The

quantitative results are both shown in Table 5-12, and a closer view representing the strain less than 15% is shown in Figure 5-33.

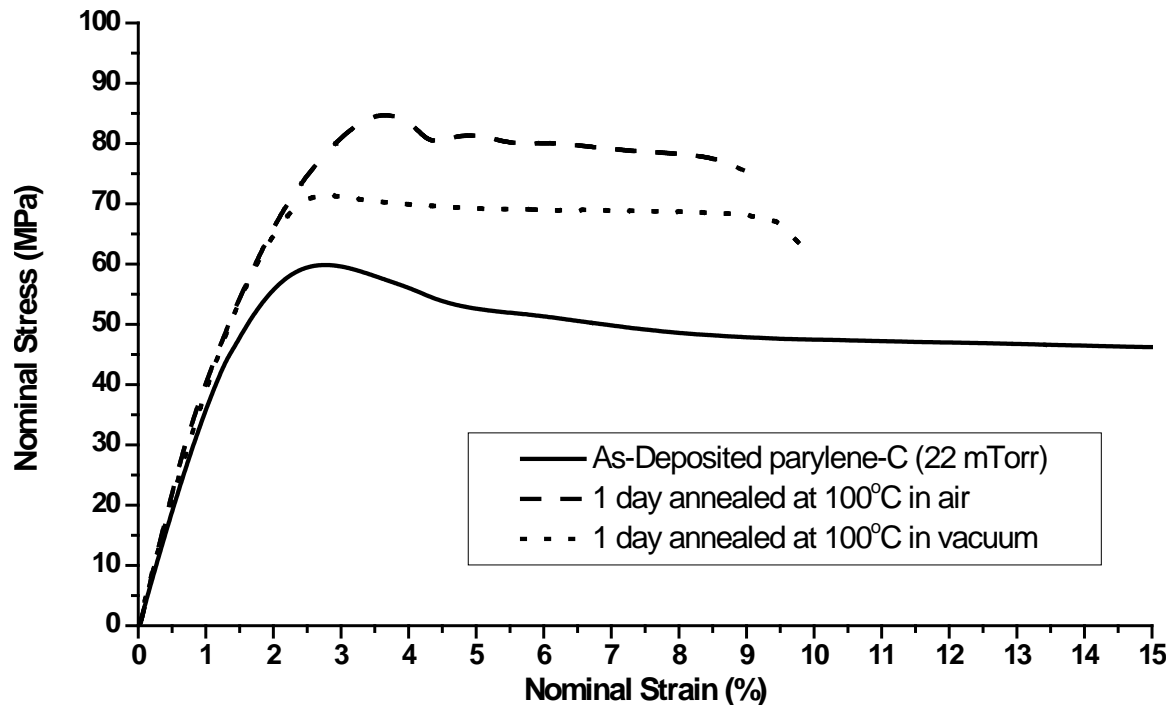


Figure 5-33: Comparison of uniaxial tensile test results of parylene-C film with three different treatments: as-deposited, 1 day annealed at 100°C in air, and 1 day annealed in vacuum

The Young's modulus of the sample annealed in the air is 4.547 GPa and 4.312 GPa in the vacuum, which are both higher than the as-deposited. This is attributed to the crystallization of the parylene-C film. Two Young's modulus do not show an significant difference as both average numbers fall in the other's standard deviation range. Two tensile strengths, or the yield strengths, are obtained as 83.9 MPa in the air and 72.7 MPa for in vacuum, which are both higher than the as-deposited parylene-C film. The tensile strength obtained for the samples annealed in the air seems to have consistantly higher values. It is likely implying that samples annealed in the vacuum system preserve the

parylene-C's mechanical properties. The tensile strength difference, however, is only within 13%. More tests need to be done to statistically isolate the two groups of results and confirm this hypothesis.

The percent of elongation of the two samples are both much lower than the as-deposited sample. Again, the difference between samples annealed in the air and in the vacuum still cannot be statistically distinguished. Lower percent of elongation infers that the parylene-C is more brittle. That is, the toughness decreases. This is attributed the crystallization that happens during the annealing at 100°C. Since two samples were both annealed at the same temperature for the same time, the crystallinity of the two samples should be similar and therefore it is reasonable that they had similar percent of elongations.

In summary, according to the uniaxial tensile test results of the two samples annealed at 100°C in the air and in vacuum, oxidation seems not to be mainly responsible for the mechanical properties change of parylene-C, which agrees well with the conclusion in Section 5.4. The main reason causing the mechanical properties to change should be the crystallization of the parylene-C, which happens quickly during the annealing.

### 5.7.4 Annealing temperature and time influence

The influence of the annealing temperature in terms of the mechanical properties of parylene-C will be discussed in the section. Five different parylene-C samples were annealed at five different conditions: 100°C for 30 min, one day and two days, and 200°C for one day and two days. To eliminate the possibility of the oxidation effect, all samples were annealed in vacuum with the exception of the sample annealed at 100°C for 30 min. The quantitative results are shown in Table 5-12 and graphical results of the full strain range are shown in Figure 5-34 with the result of as-deposited parylene-C for comparison. A closer view of the stress-strain curves within 5% strain is also shown in Figure 5-35.

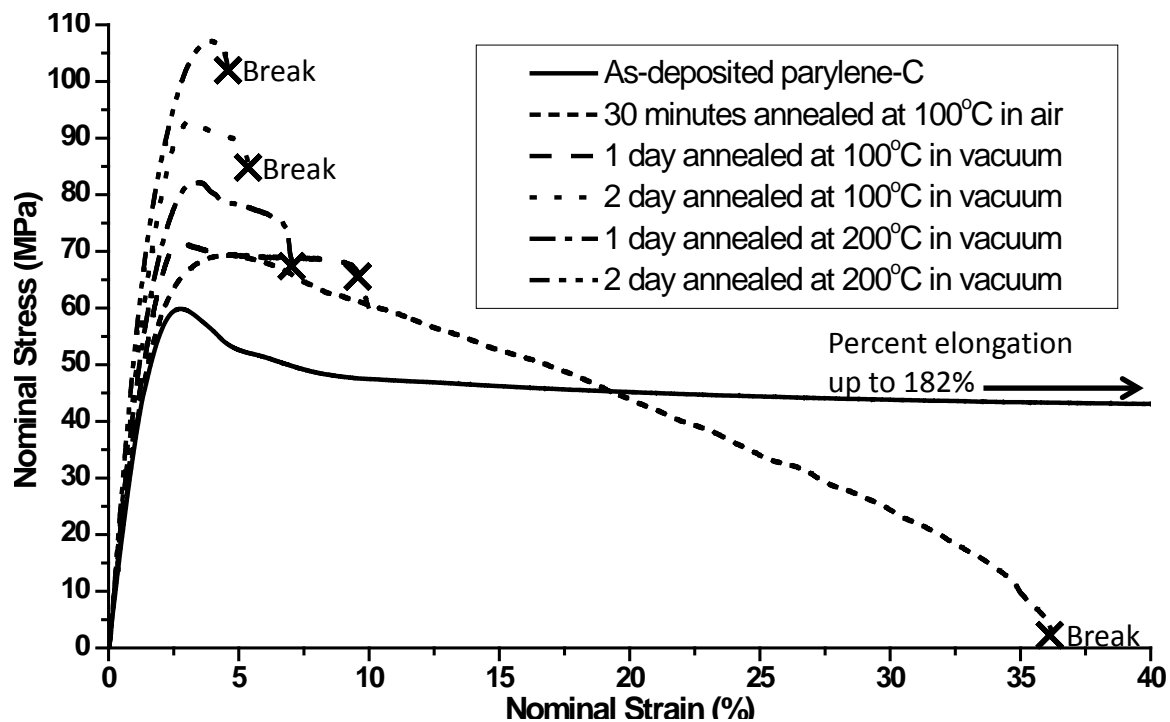


Figure 5-34: Comparison of uniaxial tensile test results of parylene-C film with six different treatments

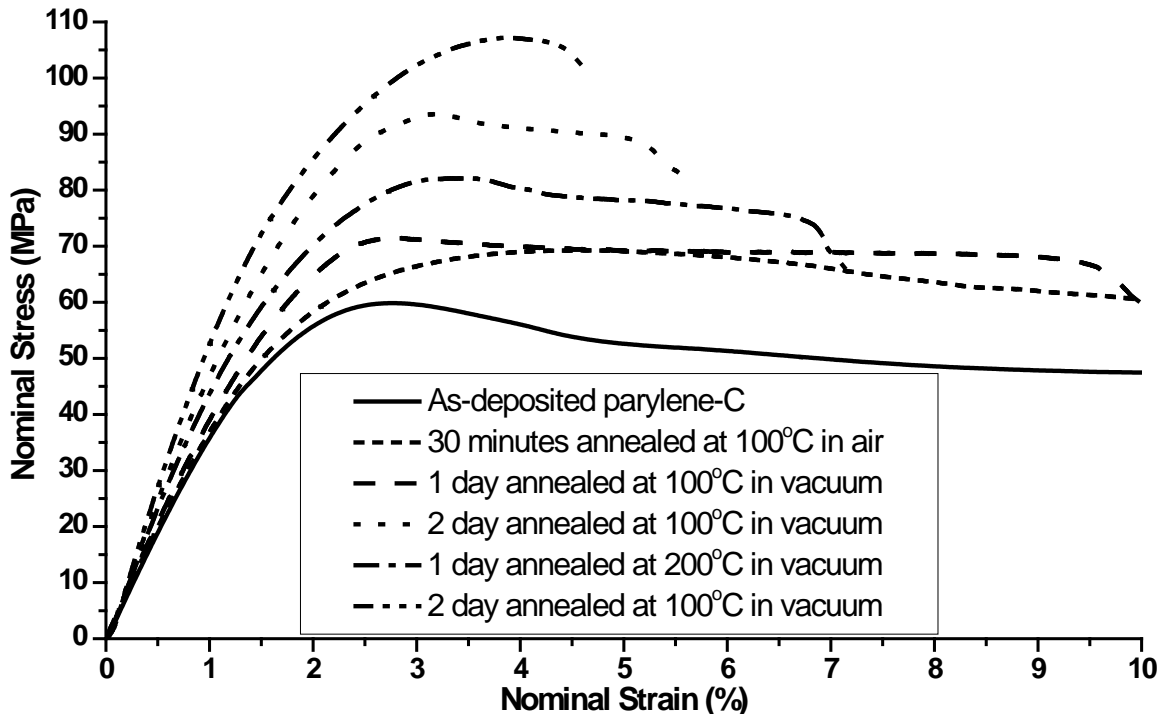


Figure 5-35: A closer view of Figure 5-34 (strain lower than 10%)

According to the testing results shown in Figure 5-35, the order of the Young's modulus of six parylene-C samples can be found as follows:

$$6.058 \text{ GPa (200}^\circ\text{C, 2 days)} > 5.298 \text{ GPa (100}^\circ\text{C, 2 days)} > 4.961 \text{ GPa (200}^\circ\text{C, 1 day)} > \\ 4.321 \text{ GPa (100}^\circ\text{C, 1 day)} > 4.251 \text{ GPa (100}^\circ\text{C, 30 min.)} > 3.841 \text{ GPa (as-deposited)}.$$

It is therefore observed that the Young's modulus increases as the temperature increases. Similar effects are also found on tensile strength and the percent of elongation. The order of the tensile strength is found as:

$$102.933 \text{ MPa (200}^\circ\text{C, 2 days)} > 92.185 \text{ MPa (100}^\circ\text{C, 2 days)} > 81.659 \text{ MPa (200}^\circ\text{C, 1 day)} \\ > 72.700 \text{ MPa (100}^\circ\text{C, 1 day)} > 74.153 \text{ MPa (100}^\circ\text{C, 30 min.)} > 58.370 \text{ MPa (as-deposited)}.$$

The order of the percent of elongation is found as:

$$4.512\% (200^{\circ}\text{C}, 2 \text{ days}) < 6.313\% (100^{\circ}\text{C}, 2 \text{ days}) < 6.515\% (200^{\circ}\text{C}, 1 \text{ day}) < \\ 6.897\% (100^{\circ}\text{C}, 1 \text{ day}) < 36.963\% (100^{\circ}\text{C}, 30 \text{ min.}) < 119.139\% (\text{as-deposited}).$$

Therefore, the parylene-C stiffness, tensile strength and the toughness (brittleness) can be tailored by annealing the material at the necessary temperature to achieve the desired properties. According to what has been found in Section 5.5, it is not surprising that parylene-C becomes stiffer, stronger and more brittle as either the annealing temperature or time increase. This is attributed to the occurrence of the parylene-C crystallization during the thermal annealing which reduces the amorphous part that is in charge of the polymer chain movement. During the sample preparation, it is found that parylene-C annealed at 200°C in air became too brittle to handle and mount on to the testing equipment after the first hour annealing. Therefore there are no data points obtained to represent the condition of annealing at 200°C in the air. This is in contrast to the results of parylene-C samples annealed at 200C in the vacuum, which can still be handled easily and still maintain most mechanical properties. It can be concluded that the oxidation is a strong effect that can deteriorate the parylene-C film at 200°C. This agrees well with the conclusion in Section 5.4.

The time constant of the parylene-C crystallization at 100°C has been found to be less than one minute in Section 5.5.2. It infers that the parylene-C's mechanical properties should have experienced a big change during the first few minutes due to the crystallization. To further confirm this, another three samples were also prepared and tested to verify the assumption. Those three samples were all annealed at 100°C but for different times: 30 sec, 1 min and 3 min, which are all much shorter than 30 min. The

results are also shown in Table 5-12. It can be seen that the elastic modulus increases from 3.841 GPa (as-deposited) to 4.339 GPa (30 sec annealing) within only 30 seconds. The value has already reached the number which normally can be found for 30 minutes annealing or longer. The elastic modulus does not seem to show any significant increment for the parylene-C samples annealed at the time longer than 30 sec until 2 days of annealing. Similarly, the tensile strength increases from 58.37 MPa (as-deposited) to 77.506 MPa (30 sec annealing) after only 30 seconds annealing and shows saturation (or grows slowly) afterward. Combining what we have found in Section 5.5.2, it is evident that the parylene-C does crystallize extremely fast with a time constant less than one minute (0.845 min) and therefore the mechanical properties change fast in the first few minutes. In addition, from the discussion in Section 5.6, it is also evident that the crystallization can actually affect the glass transition temperature, and therefore would hugely change parylene-C's viscoelastic/viscoplastic properties, as will be discussed later in Sections 5.8 and 5.9.

#### **5.7.5 Effect of testing environmental temperature**

Most of the uniaxial tensile tests discussed in the previous few sections were performed at room temperature. Because parylene-C is often used in implantable biomedical devices, the mechanical properties of parylene-C at different temperatures (especially the human body temperature) needs to be understood as well. In this section, seven uniaxial tensile tests of the as-deposited parylene-C were performed at seven different temperatures: 20°C, 40°C, 60°C, 80°C, 100°C, 120°C, and 150°C. The parylene-C sample were first heated up to the targeted temperature and then annealed for 30 minutes to crystallize and stabilize the mechanical properties. After that, rather than

cooling down to room temperature, the sample was pulled at the strain rate of 1%/min while the temperature was kept unchanged during the whole uniaxial tensile test.

Table 5-13: Measured mechanical properties obtained at different testing temperatures

<b>Parameter</b> <b>As-deposited</b> <b>parylene-C</b> <b>testing temperature</b>	<b>Elastic modulus</b>	<b>Elastic modulus from 0 MPa and 0%</b>	<b>Nominal tensile strength</b>	<b>Max true tensile stress</b>	<b>Yield strength</b>	<b>percent elongation at yield</b>	<b>Percent elongation</b>
Symbol	E	E <sub>0</sub>	$\sigma_T$	$\sigma_{TT}$	$\sigma_Y$	$\epsilon_Y$	%El
Unit	GPa	GPa	MPa	MPa	MPa	%	%
SCS	2.758		68.948*		55.158	2.9	Up to 200
Spivack [235]*	2.354;2.746 (1% strain)		61.302; 68.658		57.9; 54.9	4.2; 2.9	170; 200
Baker [195]	2.917		---		56.904	---	---
Beach [101, 102]	3.2		70**		55	2.9	200
20°C	3.654	2.641	56.275	100.163	56.275	2.955	>166.03
40°C	3.166	2.677	37.089	81.187	37.089	1.894	>165.68
60°C	2.400	2.400	23.987	77.047	23.987	2.223	161.98
80°C	2.270	2.270	21.699	65.511	21.699	3.513	>164.77
100°C	1.771	1.771	18.473	78.775	18.473	2.872	>165.49
120°C	1.575	1.575	16.897	72.557	16.897	3.717	>164.81
150°C	1.123	1.123	14.021	51.775	14.021	3.211	136.77

\*The first number corresponds to 0.12–28.0  $\mu\text{m}$  thick while the second one is 25  $\mu\text{m}$  thick.

\*\*It is not clearly specified what type of tensile strength—nominal or true tensile stress—is given in the SCS parylene-C data sheet and references [100–102].

The measured mechanical properties are listed in Table 5-13 and also graphically shown in Figure 5-36. A closer view of Figure 5-36 with strain less than 5% is also zoomed in and shown in Figure 5-37. The measured Young's modulus shown in Table 5-13 has very good agreement with the curve shown in Figure 5-27, which is measured by DMA method. The comparison is shown in Figure 5-38.

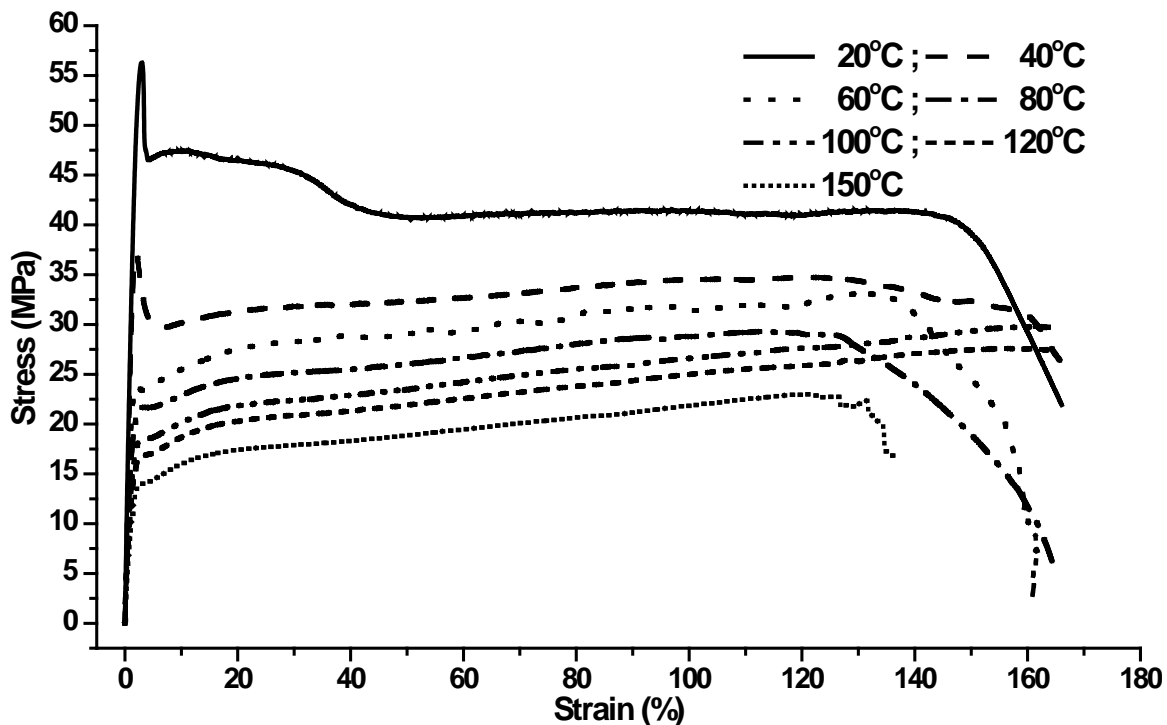


Figure 5-36: A series of uniaxial tensile tests of parylene-C performed at different environmental temperatures

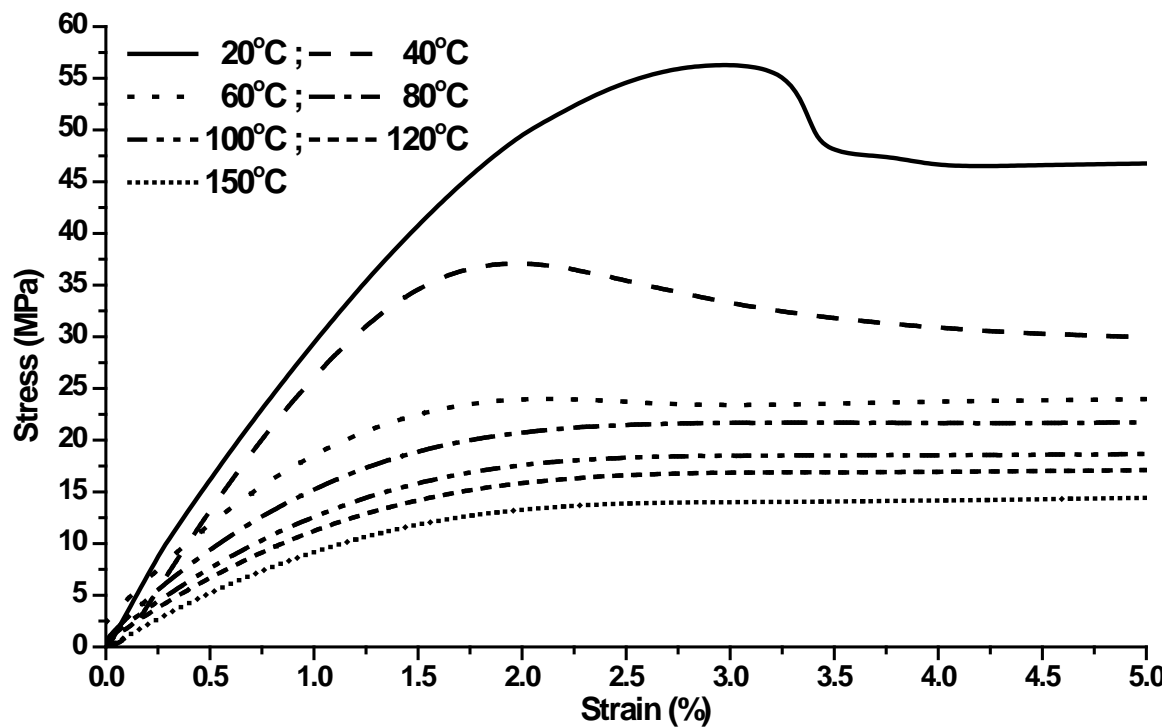


Figure 5-37: A closer view of Figure 5-36 (strain lower than 5%)

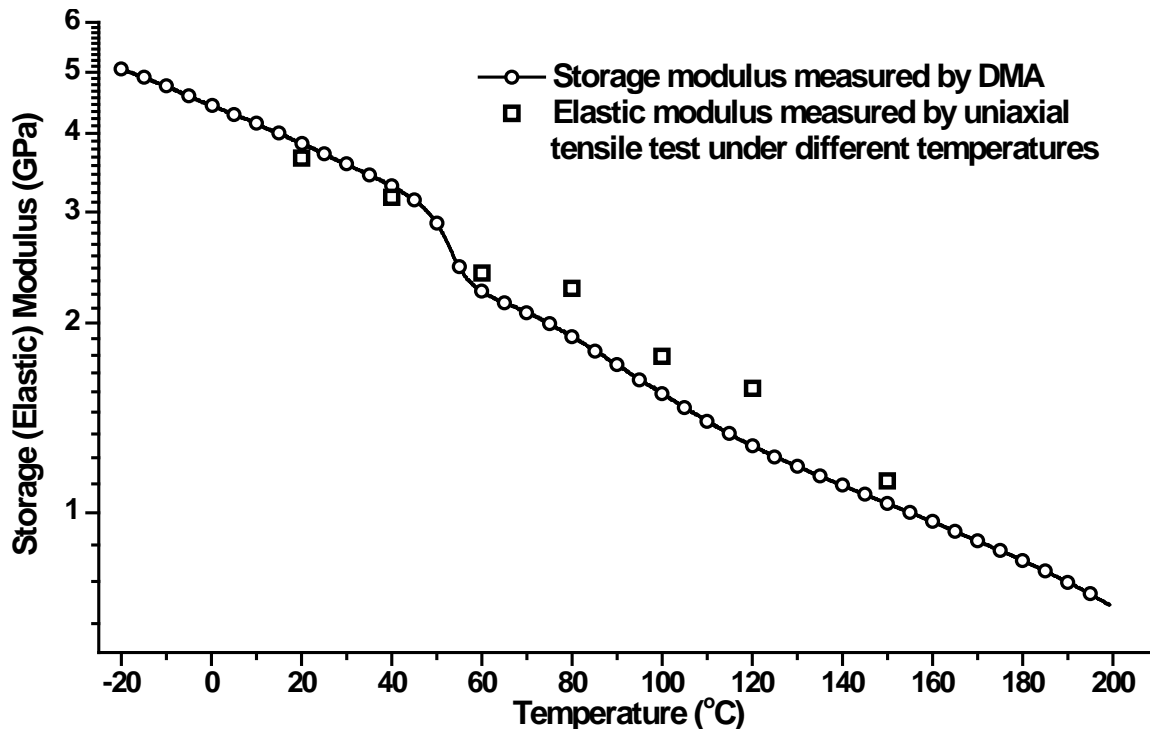


Figure 5-38: A comparison of elastic modulus measured by DMA (as-deposited curve in Figure 5-27 in 5.6) and obtained from Table 5-13

It is clearly found from Table 5-13 that the Young's modulus, tensile strength, and yield strength all decrease as the testing temperature increases. In addition, parylene-C tested at the elevated temperature normally shows elongation larger than 160%, except the one tested at 150°C. Many samples did not break when the machine reached its clamp displacement limit, meaning the parylene-C molecule can move easily without any interruption. Although the sample is crystallized, the results imply that the amorphous part of the material is softened at the elevated temperature. Therefore the parylene-C is weaker and more ductile when it is tested at the elevated temperatures.

One of the interesting results is found when the parylene-C was stretched at 150°C, which snapped earlier than most other lower temperatures. Although parylene-C might be expected even softer at 150°C than other temperatures, the phenomenon that

parylene-C snapped earlier at 150°C is likely due to sample at 150°C as described in the Section 5.4.

In terms of the yield strength determination, the numbers shown in Table 5-13 still follow the definition in ASTM standard D638-08. However, whether the sample can restore to its original length under a stress state lower than the yield strength shown in Table 5-13 is still questionable. A more accurate loading-unloading experiment, which will be introduced in Section 5.6, needs to be executed to figure out the yield point by definition: the point that material starts not to behave elastically.

### **5.7.6 Summary**

It is generally believed that parylene-C with higher crystallinity increases the Young's modulus and the tensile strength, and lowers the percent of elongation [101]. However, there is still lack of quantitative representation of the statements. In this section, the uniaxial tensile results quantitatively provide more information about the relationship between the crystallinity and the mechanical properties. Before every uniaxial tensile test, the crystallinity is tailored by systematically annealing the parylene-C samples at different temperatures and time. It is found that the first minute contributes to most of the change in mechanical. This implies that most sample crystallization has completed in this short period of annealing time. Higher crystallinity introduces larger Young's modulus, larger tensile strength, and less percent of elongation, which correspond to produce stiffer, stronger and more brittle (less tough) parylene-C. In addition, it is also found that the oxidation effect is not very obvious when parylene-C is annealed at 100°C. However, the early snapping of the parylene-C stretched at 150°C implies the oxidation plays an important role at this temperature.

As the annealing temperature influence the crystallinity of the parylene-C and thus the mechanical properties, Hsu suggested thermal anneal the device at a higher temperature than the device's designed operation temperature [201]. This would generate and maintain stable parylene-C crystallinity throughout the device operation period and thus the mechanical properties.

Thickness effect has never been discussed in the section. It has been pointed out by Spivack in 1972 that the uniaxial mechanical properties show very little variation with thickness [235]. Future work would focus on the time constants of the mechanical properties change. In addition, the degree of crystallinity may affect the electrical properties (dielectric loss) and the optical properties (birefringence) [201], which all needs more studies and attentions before the implantable devices are designed and fabricated.

## **5.8 Rheological Properties of Parylene-C Film**

It is well know that parylene-C is a thermoplastic material. Like many other thermoplastic materials such as polypropylene and polycarbonate, it shows viscoelastic/viscoplastic behaviors, i.e., characteristics with combined elastic and viscous properties especially beyond glass transition temperature,  $T_g$  [236, 237]. In addition, with its biocompatibility, parylene-C has been widely used for many biomedical implantable devices [238]. It is then important to study its viscoelasticity/viscoplasticity especially at human body temperature.

Unfortunately, although many properties, such as Young's modulus and tensile strength of parylene-C have been studied [100, 101, 172, 195, 235], there is still a lack of study of viscoelasticity/viscoplasticity of parylene-C. On the other hand, viscoelastic and

viscoplastic behaviors of a material depend upon many parameters such as temperatures, loading frequencies, and stress/strain rates. Among various viscoelastic tests, creep and stress relaxation are two of the most fundamental studies. Creep test, i.e., the tendency of a solid material to slowly move or deform under the influence of constant stress, is done as a tensile test that the applied stress is maintained constant while the strain is measured during the loading. On the other hand, stress relaxation, i.e., the tendency of a solid material to slowly release the built-in stress under the influence of a constant strain, is done as a tensile test that the applied strain is maintained constant while the stress is measured during the strain loading. Creep and stress relaxation tests characterize the time dependent behavior of a polymer [239].

In this section, a series of creep and stress relaxation tests are performed. Following previous sections, parylene-C samples annealed at different conditions are prepared for creep and stress-relaxation experiments.

As aforementioned, parylene-C annealed at different temperatures results in different crystallinity. Therefore, the creep and stress relaxation tests of parylene-C annealed at different temperature reveal the rheological response of the parylene-C at different crystallinity. However, to study the creep behavior of the as-deposited parylene-C, i.e., creep test without first 30 minutes thermal stabilization to avoid the crystallization as much as possible, the current DMA Q800 machine will not do the job due to its inherent limitations of the sample loading design and the temperature ramping rate. To overcome the problem, another creep experiment was also performed in the pre-heated convection oven with a transparent observing window.

## 5.8.1 Creep of parylene-C

### 5.8.1.1 Creep overview

A typical creep test curve measures the total strain (under a constant stress, Figure 5-39 (a)) versus time at a fixed temperature as shown in Figure 5-39 (b). As shown, the creep curve is traditionally divided into 3 different regions [240]. The primary creep, also called transient creep, represents the first instantaneous elastic strain and also the early stage of the creep behavior. In this stage, the main feature is that the strain rate of the polymer tends to decrease gradually from a very high initial rate. The secondary creep region, also called steady state region, shows a constant or little changing strain rate at a fixed temperature. The tertiary creep region shows an expedited or fast growing strain rate and ends at the material's rupture. In addition, the creep test is usually accompanied with a recovery test, i.e., strain recovery after the loading is removed, as shown in Figures 5-39 (c) and (d). For an ideal thermoset polymer, the total strain recovers to zero after a certain amount of time, whereas for a thermoplastic polymer, the strain never goes back to zero and a permanent deformation exists [239]. Creep is of great interest to us since parylene-C MEMS has to go through various fabrication processes with elevated temperatures and stresses, although mostly in the primary creep region. In addition, as the implantable parylene-C bioMEMS devices are being widely developed, creep behavior is more important to understand than ever. This section presents the study of the primary and secondary creep of parylene-C film. Burger's model is used to analyze the measured data points. Furthermore, the recovery behavior after the creep test is also performed and analyzed. For the viscoplastic behavior part will be discussed more in detail in Section 5.9.

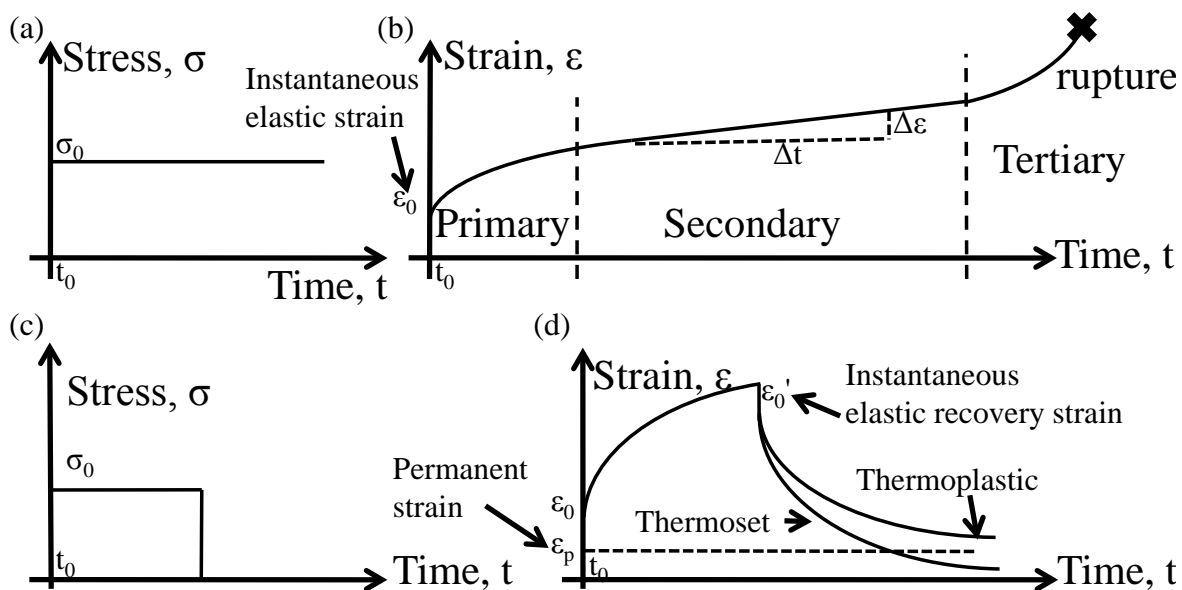


Figure 5-39: Creep behavior of polymers: (a) constant applied stress during creep test at a constant temperature; (b) total strain versus time; (c) removal of the stress at the beginning of the creep recovery test; (d) recovery strain curve

### 5.8.1.2 Introduction of the Burger's model

Many physical models have been developed and utilized to quantitatively analyze and represent the rheological behavior. The Maxwell model and the Kelvin model are two of the most fundamental ones. A single Maxwell model consists of one linear spring in series with a dashpot, while a single Kelvin model is composed of one spring in parallel with a dashpot, as shown as the inserts in Figure 5-40. Both Maxwell element and Kelvin element are often combined either in parallel or in series to model material's rheological behavior. Among all the possible combinations, one Maxwell element with multiple Kelvin elements in series is widely used for creep modeling due to its simple form of the differential equations and ease of solution [239]. In this section, it is found that 4-element Burger's model, i.e., a Kelvin element in series with a Maxwell element

(hence a single retardation time constant) is adequate to describe our data. Figure 5-40 shows the schematic diagram of the Burgers' model.

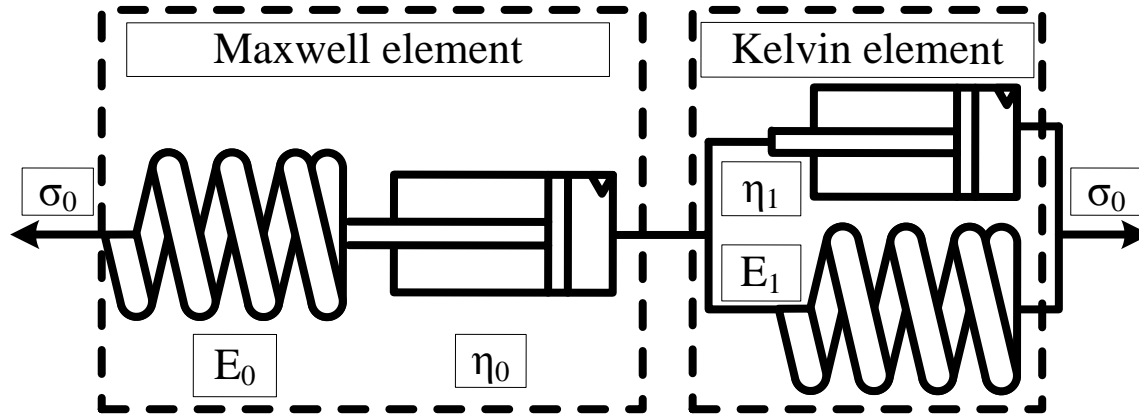


Figure 5-40: Schematic diagram of the Burger's model

#### 5.8.1.2.1 General Burger's model constitutive equation

As the Burger's model shown in Figure 5-40, the spring of the Maxwell element represents the instantaneous strain and the dashpot simulates the steady strain rate of the creep behavior in the long time. The equilibrium equation of the Burger's model is:

$$\sigma_0 = \sigma_M = \sigma_K, \quad (5-8)$$

where  $\sigma_M$  and  $\sigma_K$  are the stress applied to Maxwell and Kelvin element, respectively. The kinematic equation is:

$$\varepsilon = \varepsilon_s + \varepsilon_d + \varepsilon_K, \quad (5-9)$$

where  $\varepsilon_s$ ,  $\varepsilon_d$ , and  $\varepsilon_K$  are the strain of the spring, the dashpot and the Kelvin element, respectively.

The fundamental constitutive equation of one spring can be represented as:

$$\sigma_s = E_0 \varepsilon_s, \quad (5-10)$$

In addition, the fundamental constitutive equation of one dashpot can be represented as:

$$\sigma_d = \eta_0 \frac{d}{dt} \varepsilon_d, \quad (5-11)$$

where  $\eta_0$  is called the viscosity of the dashpot. Combining eqns. (5-8), (5-9), (5-10), and (5-11), the constitutive equations of the Burger's model can be represented as:

$$\sigma_0 + \left( \frac{\eta_0}{E_0} + \frac{\eta_0}{E_1} + \frac{\eta_1}{E_1} \right) \dot{\sigma}_0 + \frac{\eta_0 \eta_1}{E_0 E_1} \ddot{\sigma}_0 = \eta_0 \dot{\varepsilon} + \frac{\eta_0 \eta_1}{E_1} \ddot{\varepsilon}. \quad (5-12)$$

#### 5.8.1.2.2 Solution for creep behavior

The Burger's model can be fit to different rheological situation. To fit the creep results, given the initial condition as  $\sigma = \sigma_0 H(t)$ , where  $H(t)$  is the Heavyside function defined as:

$$H(t) = \begin{cases} 1, & \text{for } t \geq 0 \\ 0, & \text{for } t < 0 \end{cases} \quad (5-13)$$

the solution of the strain of the model can be derived as

$$\varepsilon(t) = \sigma_0 \left[ \frac{1}{E_0} + \frac{1}{E_1} \left( 1 - e^{-t/\tau_1} \right) + \frac{t}{\eta_0} \right]. \quad (5-14)$$

where  $\tau_1 = \eta_1/E_1$  is called the retardation time constant. The creep compliance is obtained as

$$D(t) = \frac{1}{E_0} + \frac{1}{E_1} \left( 1 - e^{-t/\tau_1} \right) + \frac{t}{\eta_0}. \quad (5-15)$$

#### 5.8.1.2.3 Solution for creep recovery behavior

To model the strain behavior of creep recovery after the applied stress is unloaded, the initial strain  $\varepsilon(t_0)$  is set to be  $\varepsilon(t_0) = \varepsilon(t_0)H(t_0 - t)$  in eqn. (5-12), where  $t_0$  is the starting point of the removal of the stress. The stress then can be derived as

$$\varepsilon(t) = P_1 + P_2 \exp\left(-\frac{(t - t_0)}{\tau_r}\right). \quad (5-16)$$

where the time constant  $\tau_r = \frac{E_1}{\eta_1}$ ,  $P_1$  and  $P_2$  are material dependents.

### ***5.8.1.3 Primary and secondary creep of parylene-C***

#### **5.8.1.3.1 Sample preparation and the experiments**

Parylene-C film was deposited using an SCS (Specialty Coating Systems) parylene deposition machine (i.e., PDS 2010 LABCOTER). The film was coated onto the surface a flat mask glass plate. The parylene-C film was then cut into uniform 5.3 mm wide strips. The length of each testing sample was  $15 \pm 0.05$  mm for the creep test. The tests were done by a dynamic mechanical analyzer, TA instruments DMA Q800. Similar to the previous Section 5.7, eight different parylene-C samples were treated differently by annealing in different conditions to study the oxidation effect, temperature effect, deposition pressure effect, and also annealing time effect. As it has been found in Section 5.6 that the glass transition temperature of the as-deposited parylene-C is about  $50^\circ\text{C}$ ,  $25^\circ\text{C}$  was chosen for tests of creep behavior below  $T_g$ ;  $40^\circ\text{C}$ , and  $60^\circ\text{C}$  were chosen to be around  $T_g$ , and  $80^\circ\text{C}$ ,  $100^\circ\text{C}$ ,  $120^\circ\text{C}$ , and  $150^\circ\text{C}$  were chosen to be above  $T_g$ .

Before the creep test started, the testing chamber was first heated up with the parylene-C sample mounted and then waited for 30 minutes to ensure that the whole system reaches thermal equilibrium with our targeted temperature, as graphically shown in Figure 5-41 (a). Then, a constant stress of 2.43MPa was applied onto the sample for 120 minutes, while the total strain is measured. To observe the recovery behavior of the sample, the stress was then removed and the total strain was continuously recorded for another 60 minutes.

### 5.8.1.3.2 Results and discussion

As a whole, the results of the creep test and the recovery of eight different pre-treated parylene-C are shown in Figure 5-41 (a) to Figure 5-48 (a). Each figure includes seven curves representing different testing temperatures. Besides, the Burger's model curve fitting results of the creep and recovery are also shown in Table 5-14 to Table 5-21. From these eight figures and tables, several observations and conclusions can be made:

1. It is noted from all figures that there is always little or no primary creep at the temperature lower than the glass transition temperature. For example, from the creep results of as-deposited parylene-C deposited at 35 mTorr shown in Figure 5-42 (a) (one extra curve was performed at 10°C), it can be found that 10° and 25°C, which are significantly below the glass transition temperature (55.1°C in Table 5-11) show no or very little creep. Figure 5-42 (a) further validated that the total strain obtained at 10° C is similar to that at 25° C because the Young's moduli at 10°C and 25 ° C are very close to each other. In addition, there is very little or no permanent strain found after the recovery, meaning that the parylene-C is in the elastic regime. The second example would focus on the creep results of the parylene-C annealed at 100°C for one day in vacuum as shown Figure 5-45 (a). Tg of this parylene-C sample is found as 113.1°C from Table 5-11. It is observed from Figure 5-45 (a) that there is also no or very little creep found at 25, 40, 60 and 80°C, which are all far below the Tg. Most of the strain remaining measured after the creep tests at these temperatures are also hard to identify. The third example would be aimed at the creep results of parylene-C annealed at 200°C for one day in vacuum as shown in Figure 5-47 (a). As also obtained from

Table 5-11,  $T_g$  of this parylene-C cannot be figured out by the experiments as described in Section 5.6. In one of our conclusions in 5.6.3, the measured  $T_g$  is found to be always a bit higher than the annealing temperature according to the observed experimental trend of  $T_g$ . Therefore the  $T_g$  would be expected as higher than  $200^\circ\text{C}$  in this parylene-C sample. Therefore, the creep results shown in Figure 5-47 (a) would not be surprising as all seven creep testing temperatures are far lower than  $200^\circ\text{C}$ . Consequently this parylene-C behaves like elastic material even at  $150^\circ\text{C}$  and thus very little creep is found in the experiment. In addition, also very little permanent strain is found after the recovery.

2. When the creep test started at  $t=t_0=30$  minutes, the applied stress suddenly loaded onto the sample and it is shown in eight figures that an instantaneous elastic deformation happens. According to the results, the higher temperature produced the larger instantaneous elastic strain under constant stress. This is explained by the smaller Young's modulus at higher temperature, which agrees well with what we found from our ramping-temperature-dependent modulus experiment and DMA tests shown in Section 5.6. These instantaneous strains at different temperatures were used to calculate the corresponding Young's moduli and the results are shown in the first column of the creep results in Table 5-14 to Table 5-21. It is found that Young's modulus determined at the starting point of the creep test in this section usually differs a bit than what we got from the ramping-temperature-dependent modulus experiment or DMA method. It is likely because of three possible reasons. The first reason would be the thickness variation which inherently comes from the parylene-C deposition. The second reason could be the

thermal history difference. In the DMA method in Section 5.6, the sample is always tested under the oscillatory force at the testing temperature. In this section, however, the Young's modulus is obtained after 30 minutes of annealing. As discussed in Section 5.5, parylene-C might have gone through a long period of crystallization and hence the mechanical properties could be different. The third reason might be the testing strain rate difference. Compared to 1Hz as the oscillation frequency in Section 5.6.1.3, the strain rate at the starting point of the creep test is high enough to cause the strain-rate effect in parylene-C [223]: higher strain rate would introduce higher Young's modulus. Combining these three effects, the measured Young's modulus could sometimes either higher or lower than in Section 5.6. Even though, the values are always very close to each other, and also, the descending trend with respect to the temperature still exists.

3. The Young's modulus at  $t=t_0+120=150$  min is found using the elastic recovery strain at the time when the applied stress is removed. The results are shown in the first column of the recovery in Table 5-14 to Table 5-21. It can be first seen that with temperatures around or higher than the glass transition temperature, the Young's modulus gets higher after it has being stretched at the constant temperature for 120 minutes. It is also obvious that at temperatures much higher than  $T_g$ , the increment can be even more serious. According to what has been demonstrated in the previous few sections, this effect is likely mainly attributed to the crystallization of the parylene-C. In addition, the similar effect can also be found at the temperature lower than  $T_g$ , although that as significant as at the temperature higher than  $T_g$ . It could be concluded that the pure stretching of the

parylene-C would also increase the Young's modulus either by inducing the crystallization or aligning the polymer chain under the tension force.

4. The primary creep is significant and increases with temperature. The further analysis of the creep needs the help of Burger's model. All creep and the recovery results were curve fitted to the Burger's model, and the results are shown in Table 5-14 to Table 5-21. According to the obtained correlation coefficient,  $R^2$ , the Burger's model explains well with our data whenever the testing temperature is higher than  $T_g$ . However, although Burger's model can also be forced to fit with the data lower than  $T_g$ , the physical model loses its physical sense because parylene-C showed little or no creep below  $T_g$ . This can be verified by the lower correlation coefficients ( $R^2 < 0.99$ ) of every creep experiment performed at the temperature lower than  $T_g$ . These data are shaded with grey background in the tables. As a result, except at the temperature lower than  $T_g$ , it is shown that the retardation time constant,  $\tau_1$ , decreases with the temperature. Because  $\tau_1$  are found to be approximately 6–10 minutes at temperatures higher than  $T_g$  no matter what type annealing history of the samples, it is evident that 120 minutes is long enough to make the creep go into secondary region, and the creep strain rates have already reached a steady state, which is shown in Figure 5-41 (a) to Figure 5-48 (a). The steady state slopes,  $\frac{\sigma_0}{\eta_0}$ , of the creep curves at the temperature higher than  $T_g$  increase slightly when creep temperature goes up. Both trends of  $\tau_1$  and  $\frac{\sigma_0}{\eta_0}$  show that parylene-C creeps more at higher temperature when the temperature is higher than  $T_g$ . The phenomenon demonstrates the viscoelastic/viscoplastic behavior of the parylene-C. On the other hand, the creep

performed at the temperature lower than  $T_g$ , shows little creep and proves that parylene-C is in the glassy region and thus behaves elastically. Young's modulus of the spring of the Kelvin's element, i.e.  $E_1$ , can be calculated from  $\frac{\sigma_0}{E_1}$  given  $\sigma_0=2.43\text{MPa}$ .  $E_1$  are also generally found to decrease as the testing temperature going up, which is similar to  $E_0$ .

5. By comparing the creep results of Figure 5-44 (a) (parylene-C pre-annealed at  $100^\circ\text{C}$  one day in the air) and Figure 5-45 (a) (parylene-C pre-annealed at  $100^\circ\text{C}$  one day in the vacuum), the results show that creep strain of the samples pre-annealed in vacuum has no distinguishable difference to in the air. It infers again that, even after one day of annealing at  $100^\circ\text{C}$  in the air, the oxidation has very little effect on parylene-C, which agrees well with the conclusion obtained in Section 5.4. Although the oxidation effect is very little for parylene-C annealed at  $100^\circ\text{C}$  in the air, it would be still worthwhile repeating the same creep tests with more parylene-C samples annealed at  $100^\circ\text{C}$  but for longer annealing time, such as more than 13 days as predicted in Section 5.4.3.
6. The crystallization effect can be investigated by the creep results as well. By comparing the Figure 5-43 (a) (parylene-C pre-annealed at  $100^\circ\text{C}$  30 min. in the air), Figure 5-45 (a) (parylene-C pre-annealed at  $100^\circ\text{C}$  one day in the vacuum), and Figure 5-46 (a) (parylene-C pre-annealed at  $100^\circ\text{C}$  two days in the vacuum), it is found that the creep curve of  $150^\circ\text{C}$  has a lower total strain after 2 days of annealing. In addition, the parylene-C pre-annealed at  $100^\circ\text{C}$  for 30 minutes has very little creep difference to two day annealing in terms of the creep temperatures lower than the  $T_g$ . This implies that the crystallization is mostly

done in the first 30 minutes annealing, which has been verified many times in the previous Sections 5.5.2, 5.6.1.3, and 5.7.4. In contrast to the results of 100°C, however, from Figure 5-47 (a) (parylene-C pre-annealed at 200°C one day in the vacuum) and Figure 5-48 (a) (parylene-C pre-annealed at 200°C two days in the vacuum), it can be found that Figure 5-48 (a) generally has a smaller total creep strain than Figure 5-47 (a). It can be explained as the stronger crystallization at 200°C than 100°C. The elastic behavior of the creep results of the parylene-C pre-annealed at 200°C implies that crystallinity is much higher than annealed at 100°C.

7. Burger's model also works for the recovery region and the curve fitting results are shown in Table 5-14 to Table 5-21. The retardation time constants are generally larger than those measured from the creep, meaning the recovering behavior progresses slower than the creep. As the time constants of the recovery found from Table 5-14 to Table 5-21 are generally about 10–15 minutes, it can be concluded that 60 minutes recovery time is long enough to decide whether the strain is recovered after the creep or not. As shown in Figure 5-41 (a) to Figure 5-46 (a), a clear permanent strain is generally observed at the testing temperature higher than each corresponding  $T_g$ . The permanent remaining strain under the stress of 2.43 MPa implies that parylene-C has gone into plastic region at the testing temperature. It can be seen that the permanent strain is higher when the testing temperature is higher. This would imply that the yield strength is lower as the testing temperature increases, and hence parylene-C deforms more at higher temperature under the same loading.

8. The permanent strain phenomenon after the creep test has been observed by many previous researchers. Many models have been proposed to analyze and predict this irreversible strain. One of the most commonly used models is combine the creep behavior before the recovery, and model the recovery behavior as well as predicting the irreversible strain by powers law. The system constitutive model can be represented as [241–251]:

$$\varepsilon_c = \varepsilon_0 + k\sigma_0 \sum_m C_m \left( 1 - \exp\left(-\frac{t}{a_\sigma \tau_m}\right) \right) + \varepsilon_{pl}(t, \sigma_0), \quad (5-17)$$

9. where  $\varepsilon_c$  is the total strain of the material,  $\varepsilon_0$  is the elastic strain,  $k$  is the stress invariant dependent material property,  $\sigma_0$  is the applied stress,  $C_m$  are constants,  $a_\sigma$  is the stress dependent time-scale factor, which is a function of stress, temperature and also humidity, and  $\varepsilon_{pl}$  is the viscoplastic strain. The term  $k\sigma_0 \sum_m C_m \left( 1 - \exp\left(1 - \frac{t}{a_\sigma \tau_m}\right) \right)$  in eqn. (5-17) actually represents the generalized Kelvin model, which consists of  $m$  series of multiple springs and dashpots in parallel. The viscoplastic strain  $\varepsilon_{pl}$  accumulated in the time period  $t_1$  can also be further modeled by powers law as [242]:

$$\varepsilon_{pl}(t_1, \sigma_0) = C_{pl} \sigma^{M^*m} t_1^m, \quad (5-18)$$

where  $C_{pl}$ ,  $M$ , and  $m$  must be determined experimentally. It is clearly that the term  $C_{pl} \sigma^{M^*m}$  would depend on the stress level, and also the testing temperatures.

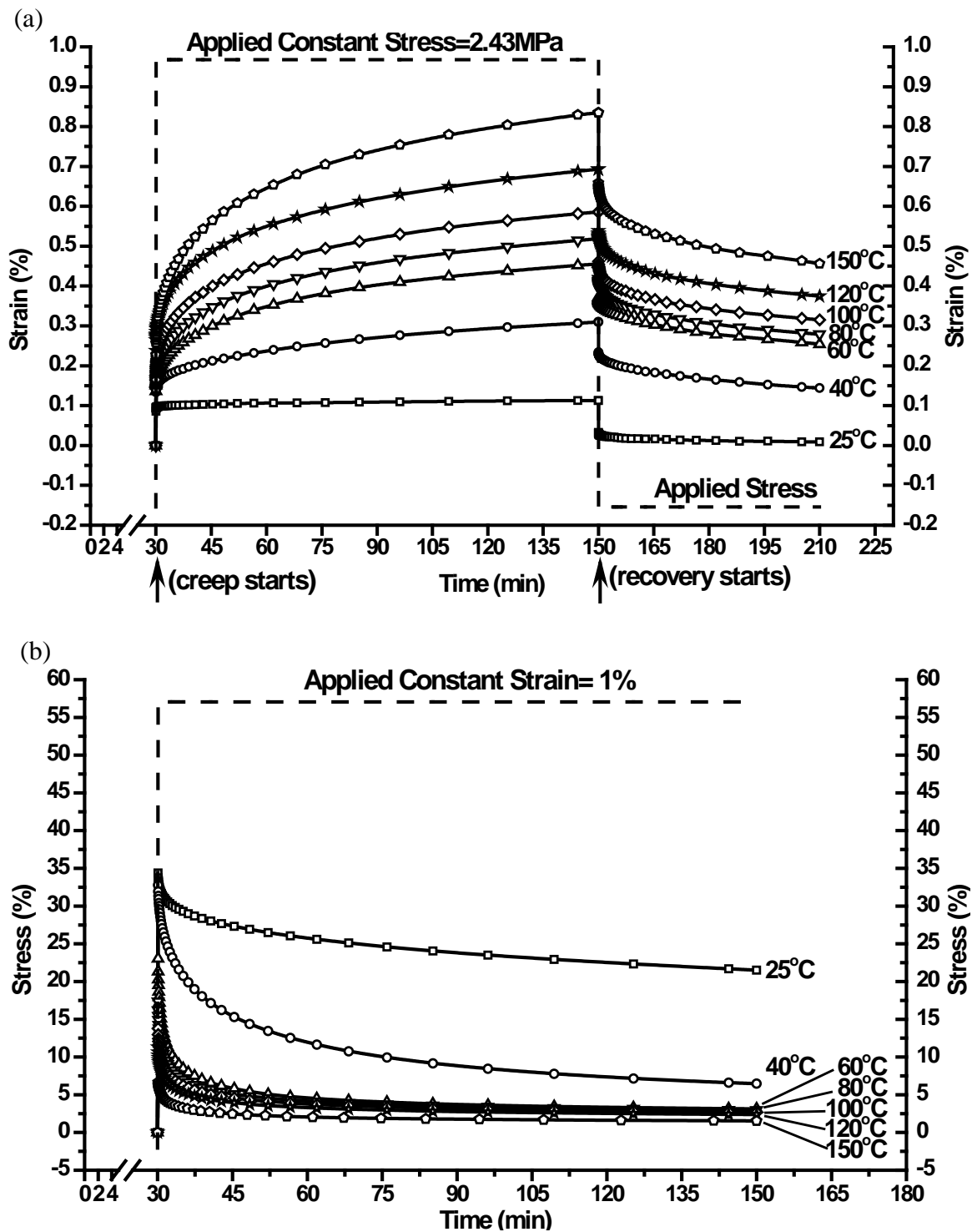


Figure 5-41 (a): Creep results of the as-deposited parylene-C deposited at 22 mTorr ( $T_g=53.4^\circ\text{C}$ ); (b): Stress relaxation results of the as-deposited parylene-C deposited at 22 mTorr ( $T_g=53.4^\circ\text{C}$ )

Table 5-14: Burger's model curve fitting results of the creep and stress relaxation behaviors of as-deposited parylene-C deposited at 22 mTorr ( $T_g=53.4^\circ\text{C}$ )

<b>Fitting Results of Parylene-C Creep Behavior</b>						
Temperature ( $^\circ\text{C}$ )	$E_0(t_0)$ (GPa)	$\sigma_0/E_0 + \sigma_0/E_1$	$\sigma_0/\eta_0$	$-\sigma_0/E_1$	$\tau_1$	$R^2$
150	0.947	0.586	0.00220	-0.296	7.342	0.992
120	0.918	0.504	0.00167	-0.214	7.334	0.992
100	1.296	0.414	0.00152	-0.203	7.269	0.992
80	1.564	0.362	0.00139	-0.184	7.386	0.992
60	1.615	0.323	0.00116	-0.157	9.472	0.994
40	1.678	0.219	0.00078	-0.068	10.248	0.995
25	2.613	0.103	0.00009	-0.007	4.924	0.976
<b>Fitting Results of Parylene-C Creep Recovery Behavior</b>						
Temperature ( $^\circ\text{C}$ )	$E_0(t_0+120)$ (GPa)	$P_1$	$P_2$	$\tau_r$	$R^2$	
150	1.325	0.473	0.158	12.708	0.966	
120	1.511	0.388	0.127	12.081	0.967	
100	1.861	0.327	0.112	12.041	0.966	
80	2.294	0.290	0.108	12.657	0.966	
60	2.796	0.261	0.097	16.108	0.975	
40	3.095	0.147	0.077	18.266	0.979	
25	2.967	0.011	0.016	8.462	0.947	
<b>Fitting Results of Parylene-C Stress Relaxation Behavior</b>						
Temperature ( $^\circ\text{C}$ )	$E_0(t_0)$ (GPa)	$A_1$	$\tau_{sr1}$	$A_2$	$\tau_{sr2}$	$R^2$
150	0.665	3.450	2.019	2.825	145.960	0.980
120	1.130	5.777	1.800	4.680	130.381	0.978
100	1.379	7.254	1.707	5.549	119.458	0.978
80	1.736	9.759	1.394	6.435	106.734	0.977
60	2.304	13.565	1.294	7.898	82.967	0.977
40	3.279	14.052	4.059	17.038	102.074	0.991
25	3.438	5.106	3.350	28.136	404.606	0.985

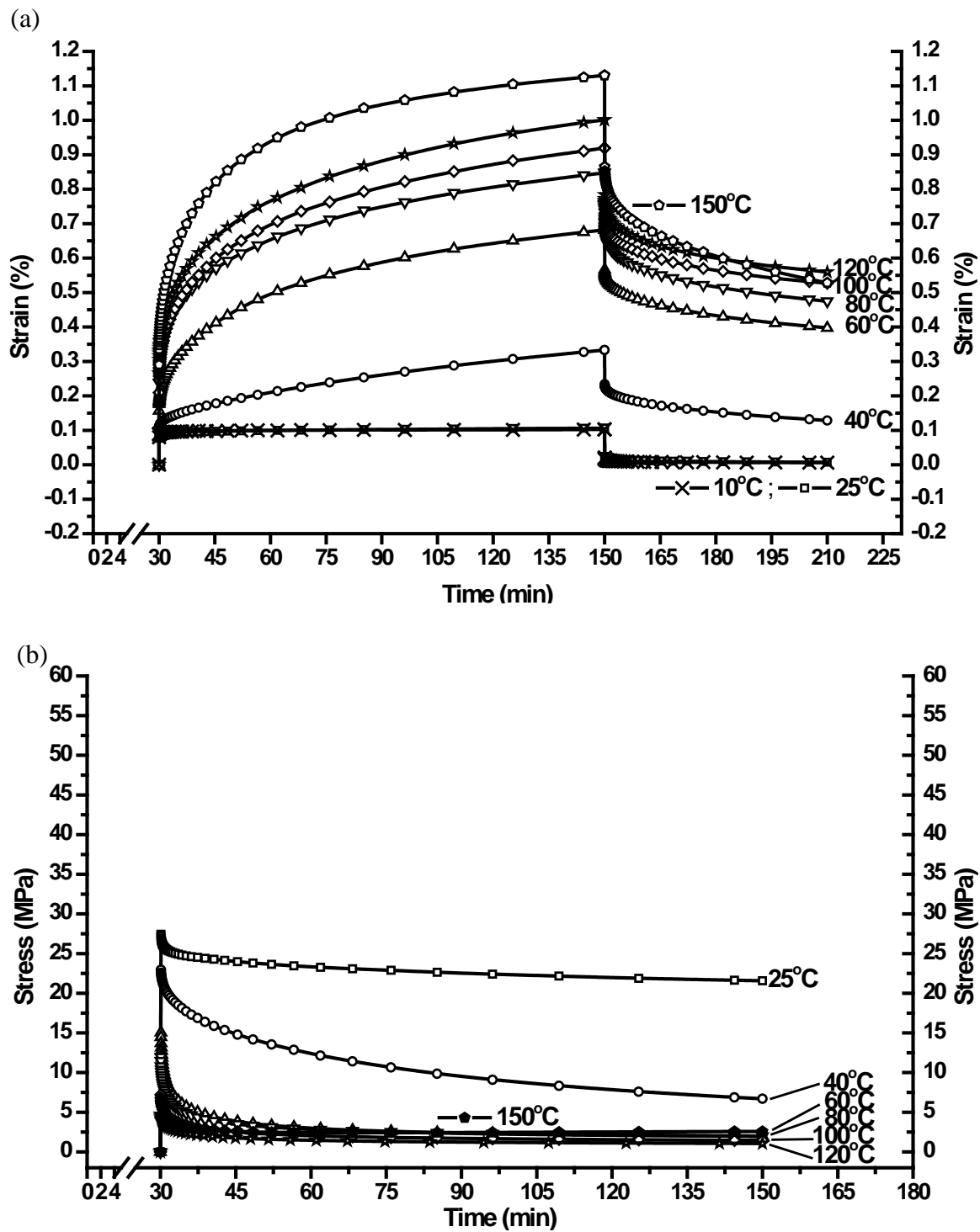
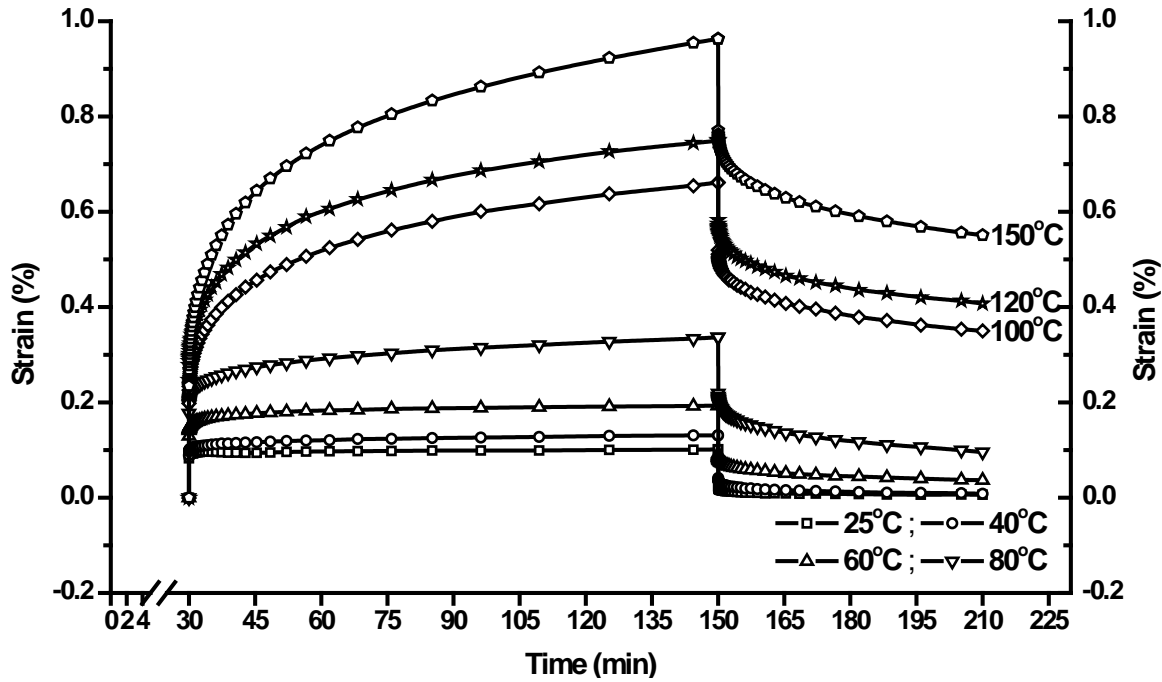


Figure 5-42 (a): Creep results of the as-deposited parylene-C deposited at 35 mTorr ( $T_g=55.1^\circ\text{C}$ ); (b): Stress relaxation results of the as-deposited parylene-C deposited at 35 mTorr ( $T_g=55.1^\circ\text{C}$ )

Table 5-15: Burger's model curve fitting results of the creep and stress relaxation behaviors of as-deposited parylene-C deposited at 35 mTorr ( $T_g=55.1^\circ\text{C}$ )

<b>Fitting Results of Parylene-C Creep Behavior</b>						
Temperature ( $^\circ\text{C}$ )	$E_0(t_0)$ (GPa)	$\sigma_0/E_0 + \sigma_0/E_1$	$\sigma_0/\eta_0$	$-\sigma_0/E_1$	$\tau_1$	$R^2$
150	0.725	0.878	0.00228	-0.492	7.393	0.992
120	0.795	0.696	0.00270	-0.349	7.964	0.993
100	0.984	0.626	0.00259	-0.338	7.518	0.992
80	0.896	0.591	0.00227	-0.284	7.445	0.992
60	1.380	0.459	0.00193	-0.259	10.816	0.995
40	2.224	0.176	0.00134	-0.059	10.902	0.997
25	2.864	0.096	0.00009	-0.009	4.459	0.983
<b>Fitting Results of Parylene-C Creep Recovery Behavior</b>						
Temperature ( $^\circ\text{C}$ )	$E_0(t_0+120)$ (GPa)	$P_1$	$P_2$	$\tau_r$	$R^2$	
150	0.876	0.548	0.274	15.733	0.971	
120	1.064	0.578	0.169	11.119	0.963	
100	1.289	0.545	0.160	10.939	0.960	
80	1.551	0.494	0.170	11.193	0.960	
60	2.011	0.409	0.136	13.842	0.971	
40	2.380	0.134	0.088	16.090	0.975	
25	2.896	0.009	0.011	4.936	0.935	
<b>Fitting Results of Parylene-C Stress Relaxation Behavior</b>						
Temperature ( $^\circ\text{C}$ )	$E_0(t_0)$ (GPa)	$A_1$	$\tau_{sr1}$	$A_2$	$\tau_{sr2}$	$R^2$
150	0.677	3.579	1.749	2.772	763.768	0.973
120	0.475	2.431	2.033	2.033	137.666	0.980
100	0.721	3.667	1.836	2.979	120.930	0.977
80	1.198	6.603	1.327	4.540	96.500	0.975
60	1.505	8.869	1.391	5.262	78.642	0.979
40	2.297	5.910	4.724	16.209	122.341	0.994
25	2.744	2.479	1.546	24.506	826.375	0.977

(a)



(b)

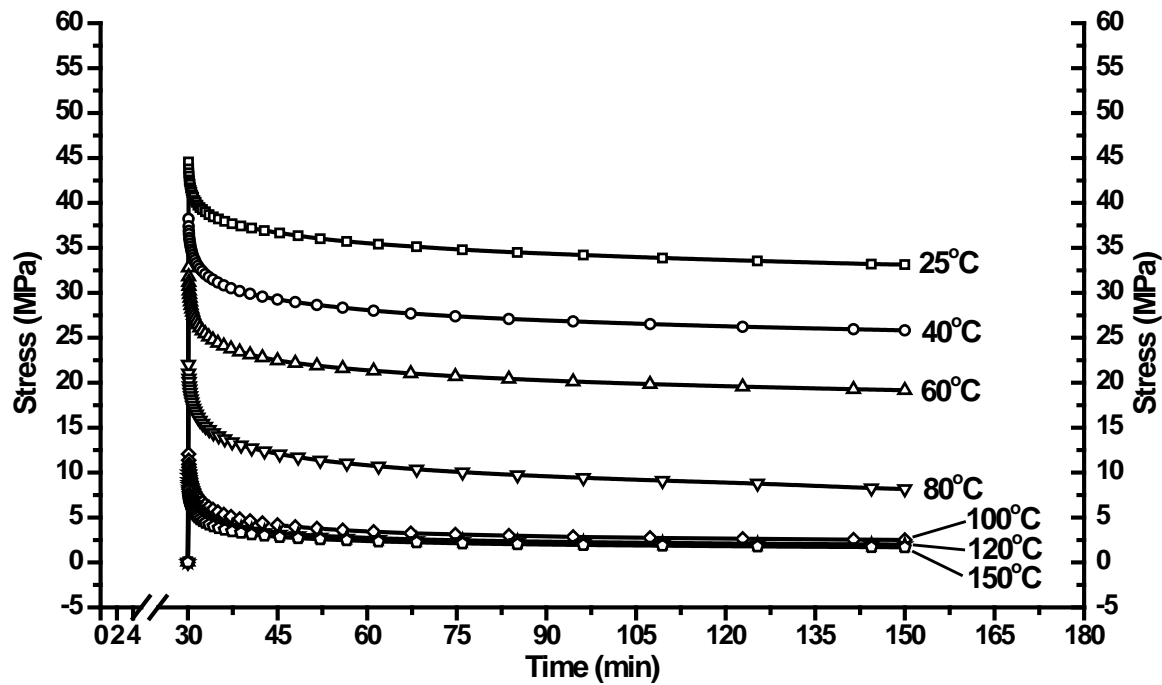
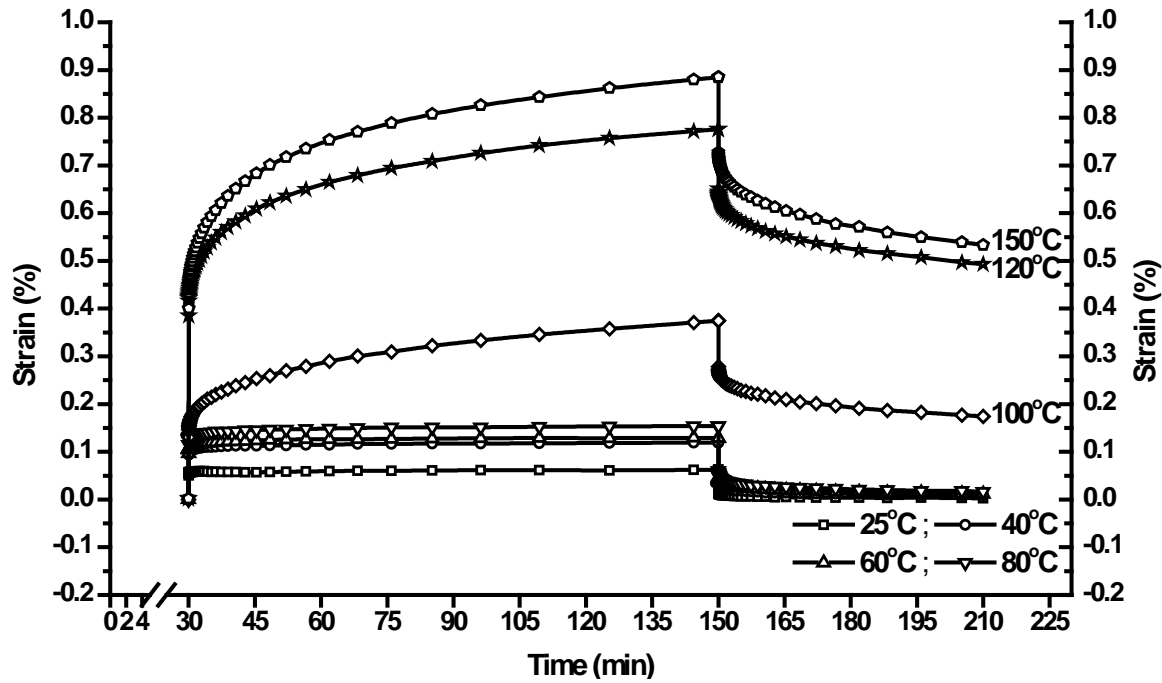


Figure 5-43 (a): Creep results of the parylene-C annealed at 100°C for 30 minutes in the convection oven ( $T_g=108.2^\circ\text{C}$ ); (b): Stress relaxation results of the parylene-C annealed at 100°C for 30 minutes in the convection oven ( $T_g=108.2^\circ\text{C}$ )

Table 5-16: Burger's model curve fitting results of the creep and stress relaxation behaviors of parylene-C annealed at 100°C for 30 minutes in the convection oven ( $T_g=108.2^\circ\text{C}$ )

<b>Fitting Results of Parylene-C Creep Behavior</b>						
Temperature ( $^\circ\text{C}$ )	$E_0(t_0)$ (GPa)	$\sigma_0/E_0 + \sigma_0/E_1$	$\sigma_0/\eta_0$	$-\sigma_0/E_1$	$\tau_1$	$R^2$
150	0.905	0.662	0.00266	-0.355	6.721	0.993
120	0.873	0.552	0.00175	-0.245	7.401	0.992
100	1.076	0.471	0.00168	-0.218	7.136	0.992
80	1.249	0.270	0.00059	-0.064	4.330	0.986
60	1.721	0.176	0.00016	-0.030	3.604	0.982
40	2.499	0.116	0.00014	-0.015	4.007	0.983
25	2.701	0.095	0.00005	-0.004	0.587	0.906
<b>Fitting Results of Parylene-C Creep Recovery Behavior</b>						
Temperature ( $^\circ\text{C}$ )	$E_0(t_0+120)$ (GPa)	$P_1$	$P_2$	$\tau_r$	$R^2$	
150	1.212	0.568	0.172	12.445	0.966	
120	1.381	0.422	0.133	11.599	0.966	
100	1.618	0.363	0.129	12.164	0.964	
80	1.953	0.107	0.090	10.837	0.956	
60	2.323	0.043	0.038	7.222	0.945	
40	2.642	0.012	0.021	5.470	0.933	
25	3.070	0.008	0.012	3.180	0.929	
<b>Fitting Results of Parylene-C Stress Relaxation Behavior</b>						
Temperature ( $^\circ\text{C}$ )	$E_0(t_0)$ (GPa)	$A_1$	$\tau_{sr1}$	$A_2$	$\tau_{sr2}$	$R^2$
150	0.827	4.217	1.888	3.540	127.971	0.980
120	0.998	5.204	1.768	4.136	125.010	0.979
100	1.206	6.180	1.712	5.011	126.250	0.977
80	2.202	7.515	1.905	13.185	212.748	0.978
60	3.281	7.989	1.775	23.459	494.229	0.974
40	3.824	6.942	2.259	29.976	683.368	0.975
25	4.456	6.067	1.905	37.400	843.503	0.975

(a)



(b)

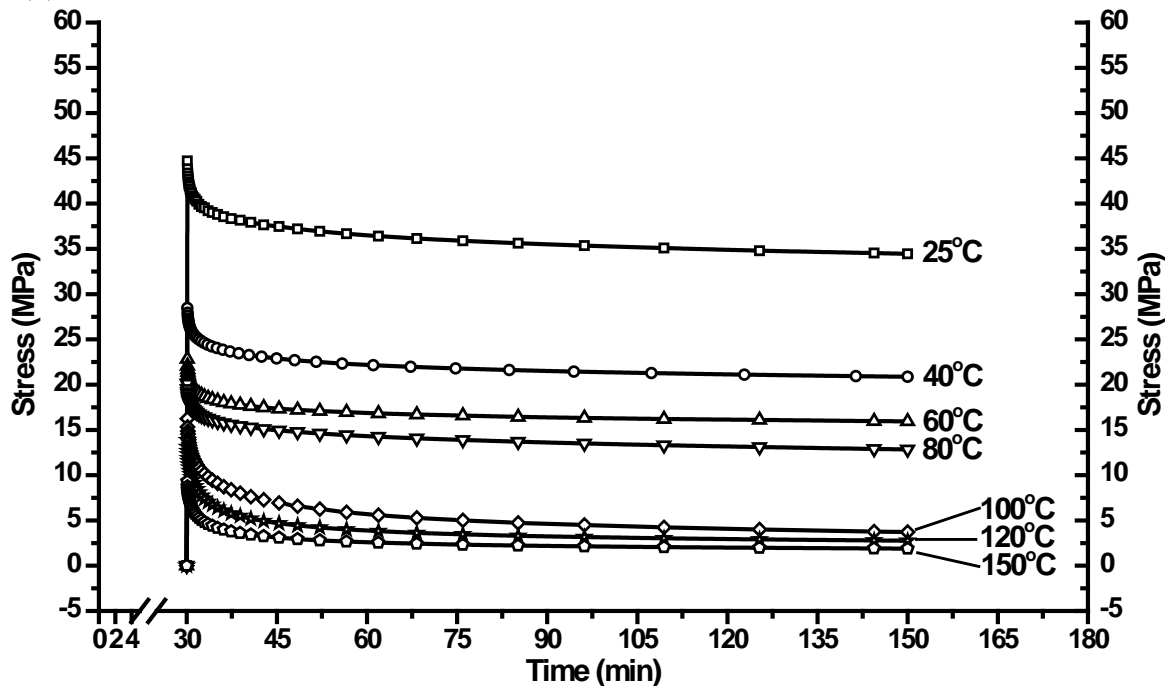


Figure 5-44 (a): Creep results of the parylene-C annealed at 100°C for 1 day in the convection oven ( $T_g=111.8^\circ\text{C}$ ); (b): Stress relaxation results of the parylene-C annealed at 100°C for 1 day in the convection oven ( $T_g=111.8^\circ\text{C}$ )

Table 5-17: Burger's model curve fitting results of the creep and stress relaxation behaviors of the parylene-C annealed at 100°C for 1 day in the convection oven ( $T_g=111.8^\circ\text{C}$ )

<b>Fitting Results of Parylene-C Creep Behavior</b>						
Temperature (°C)	$E_0(t_0)$ (GPa)	$\sigma_0/E_0 + \sigma_0/E_1$	$\sigma_0/\eta_0$	$-\sigma_0/E_1$	$\tau_1$	$R^2$
150	0.560	0.700	0.00164	-0.241	7.003	0.993
120	0.584	0.622	0.00137	-0.185	7.259	0.993
100	1.663	0.257	0.00103	-0.096	7.442	0.992
80	1.957	0.144	0.00009	-0.016	2.394	0.968
60	2.322	0.124	0.00005	-0.016	3.108	0.975
40	2.406	0.112	0.00006	-0.010	3.040	0.984
25	4.493	0.058	0.00004	-0.003	0.201	0.846
<b>Fitting Results of Parylene-C Creep Recovery Behavior</b>						
Temperature (°C)	$E_0(t_0+120)$ (GPa)	$P_1$	$P_2$	$\tau_r$	$R^2$	
150	1.487	0.548	0.154	13.031	0.969	
120	1.853	0.505	0.124	13.244	0.969	
100	2.395	0.183	0.078	11.773	0.961	
80	2.478	0.022	0.028	4.806	0.930	
60	2.885	0.016	0.023	5.188	0.940	
40	2.779	0.011	0.016	5.107	0.936	
25	4.980	0.004	0.008	4.058	0.939	
<b>Fitting Results of Parylene-C Stress Relaxation Behavior</b>						
Temperature (°C)	$E_0(t_0)$ (GPa)	$A_1$	$\tau_{sr1}$	$A_2$	$\tau_{sr2}$	$R^2$
150	0.932	4.925	1.647	3.740	126.344	0.978
120	1.386	7.334	1.813	5.617	123.350	0.980
100	1.624	6.969	2.435	7.985	123.436	0.981
80	2.010	3.870	1.701	15.492	543.957	0.973
60	2.283	4.186	1.372	17.838	868.723	0.964
40	2.847	4.386	2.175	23.300	907.844	0.973
25	4.472	5.457	1.786	38.130	1005.754	0.971

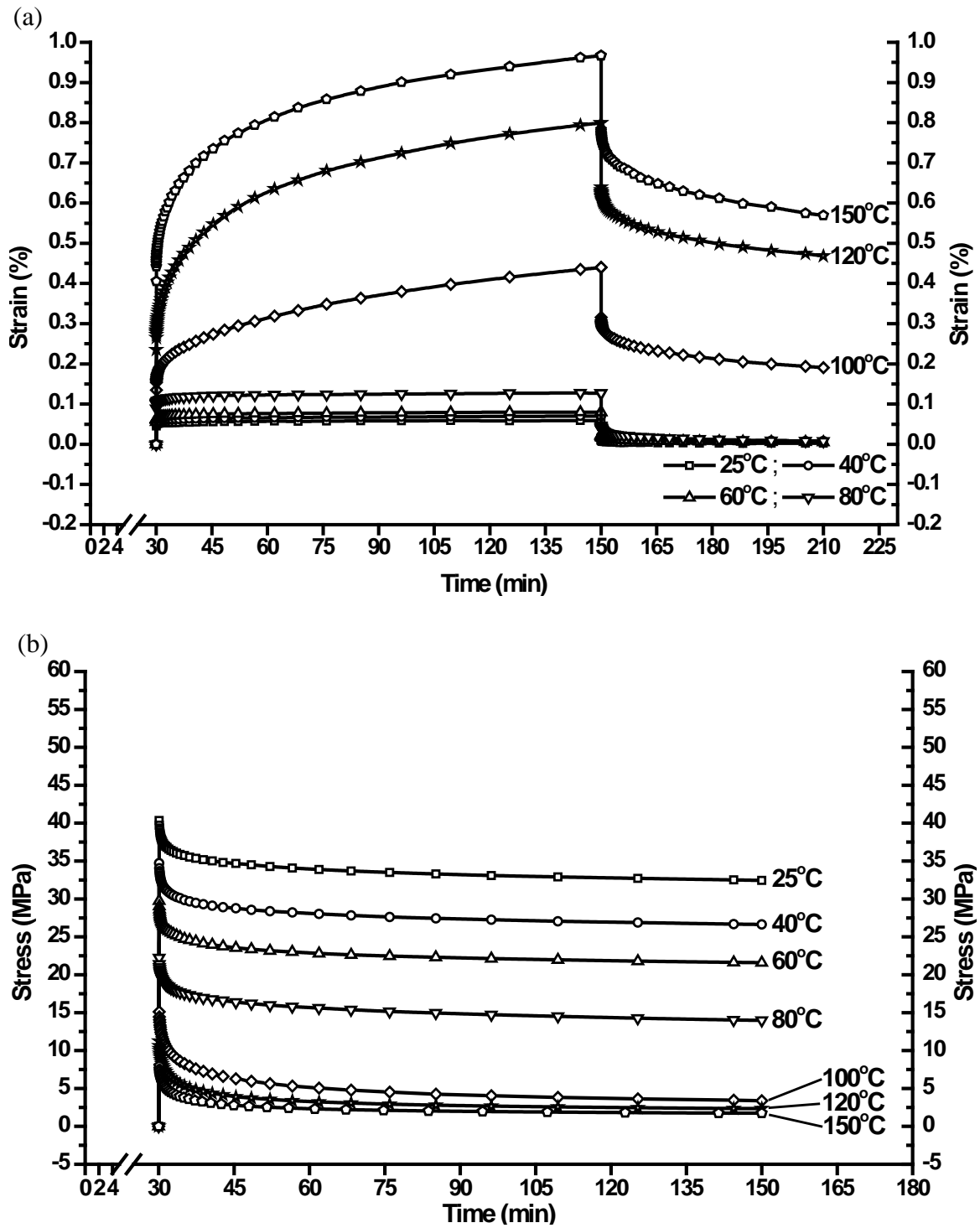


Figure 5-45 (a): Creep results of the parylene-C annealed at 100°C for 1 day in the vacuum oven ( $T_g=113.1^\circ\text{C}$ ); (b): Stress relaxation results of the parylene-C annealed at 100°C for 1 day in the vacuum oven ( $T_g=113.1^\circ\text{C}$ )

Table 5-18: Burger's model curve fitting results of the creep and stress relaxation behaviors of the parylene-C annealed at 100°C for 1 day in the vacuum oven ( $T_g=113.1^\circ\text{C}$ )

<b>Fitting Results of Parylene-C Creep Behavior</b>						
Temperature ( $^\circ\text{C}$ )	$E_0(t_0)$ (GPa)	$\sigma_0/E_0 + \sigma_0/E_1$	$\sigma_0/\eta_0$	$-\sigma_0/E_1$	$\tau_1$	$R^2$
150	0.549	0.754	0.00190	-0.280	6.804	0.992
120	0.917	0.575	0.00198	-0.279	7.907	0.993
100	1.581	0.275	0.00143	-0.105	7.876	0.993
80	2.460	0.119	0.00008	-0.017	1.983	0.974
60	3.976	0.075	0.00005	-0.011	3.026	0.979
40	4.452	0.064	0.00005	-0.008	3.305	0.983
25	4.868	0.056	0.00003	-0.004	6.095	0.946
<b>Fitting Results of Parylene-C Creep Recovery Behavior</b>						
Temperature ( $^\circ\text{C}$ )	$E_0(t_0+120)$ (GPa)	$P_1$	$P_2$	$\tau_r$	$R^2$	
150	1.285	0.587	0.168	12.718	0.964	
120	1.456	0.483	0.132	11.979	0.966	
100	1.856	0.202	0.093	10.985	0.960	
80	2.882	0.012	0.025	4.977	0.929	
60	4.176	0.007	0.012	4.447	0.931	
40	4.827	0.010	0.008	3.617	0.899	
25	4.915	0.003	0.006	3.066	0.925	
<b>Fitting Results of Parylene-C Stress Relaxation Behavior</b>						
Temperature ( $^\circ\text{C}$ )	$E_0(t_0)$ (GPa)	$A_1$	$\tau_{sr1}$	$A_2$	$\tau_{sr2}$	$R^2$
150	0.798	4.165	1.875	3.267	137.637	0.978
120	1.125	5.793	1.861	4.680	127.073	0.979
100	1.512	6.852	2.306	7.270	121.686	0.982
80	2.224	4.186	1.721	17.016	518.172	0.970
60	2.975	4.638	1.962	24.066	917.710	0.966
40	3.472	4.545	1.891	29.260	1077.451	0.972
25	4.035	4.340	1.678	35.202	1242.959	0.970

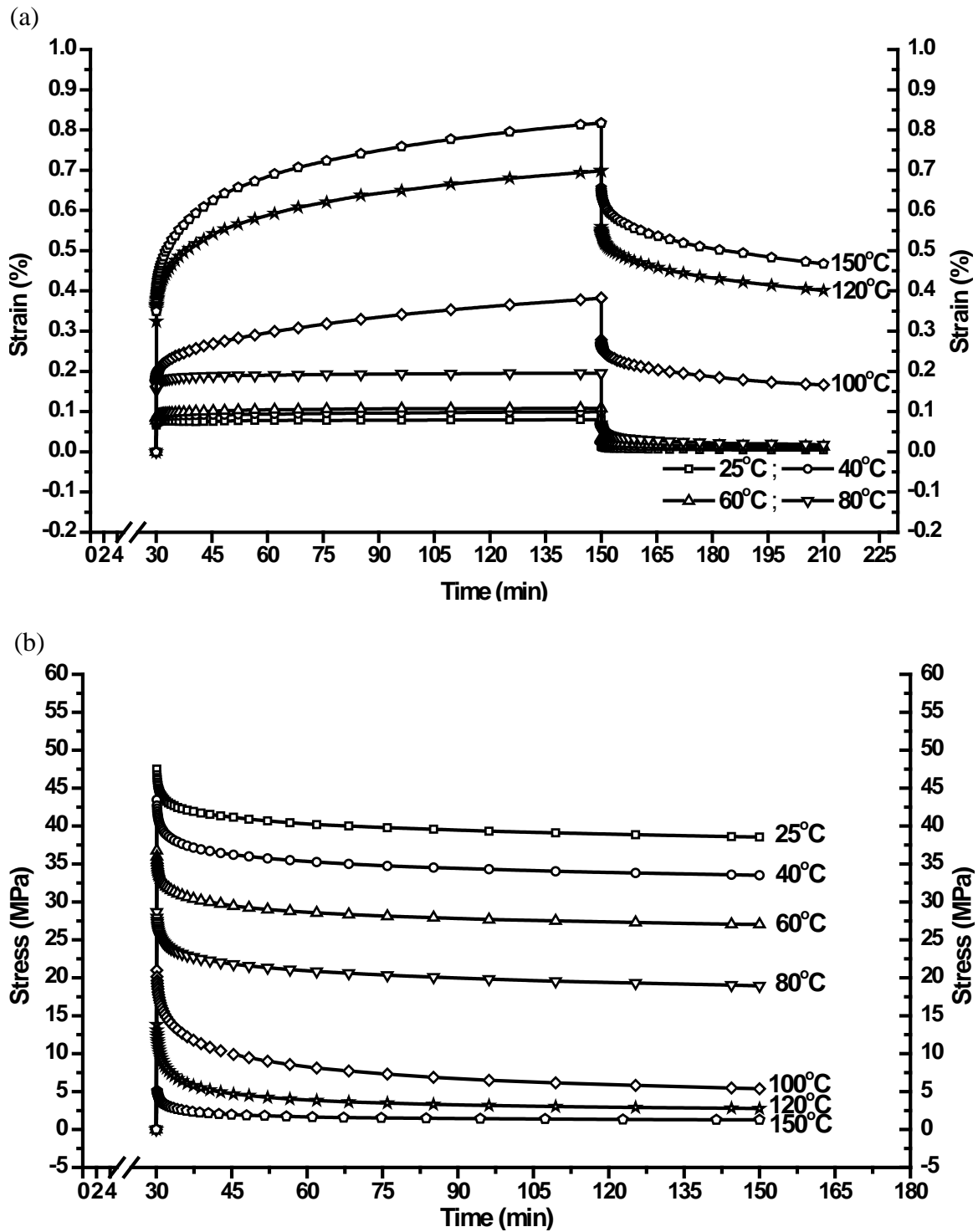


Figure 5-46 (a): Creep results of the parylene-C annealed at 100°C for 2 days in the vacuum oven ( $T_g=115.2^\circ\text{C}$ ); (b): Stress relaxation results of the parylene-C annealed at 100°C for 2 days in the vacuum oven ( $T_g=115.2^\circ\text{C}$ )

Table 5-19: Burger's model curve fitting results of the creep and stress relaxation behaviors of the parylene-C annealed at 100°C for 2 days in the vacuum oven ( $T_g=115.2^\circ\text{C}$ )

<b>Fitting Results of Parylene-C Creep Behavior</b>						
Temperature ( $^\circ\text{C}$ )	$E_0(t_0)$ (GPa)	$\sigma_0/E_0 + \sigma_0/E_1$	$\sigma_0/\eta_0$	$-\sigma_0/E_1$	$\tau_1$	$R^2$
150	0.638	0.637	0.00160	-0.229	6.647	0.992
120	0.686	0.549	0.00133	-0.175	6.535	0.992
100	1.352	0.267	0.00101	-0.074	6.695	0.992
80	1.465	0.187	0.00008	-0.017	2.058	0.967
60	2.876	0.102	0.00006	-0.014	3.760	0.976
40	2.978	0.091	0.00008	-0.008	2.624	0.984
25	3.407	0.076	0.00003	-0.005	0.241	0.900
<b>Fitting Results of Parylene-C Creep Recovery Behavior</b>						
Temperature ( $^\circ\text{C}$ )	$E_0(t_0+120)$ (GPa)	$P_1$	$P_2$	$\tau_r$	$R^2$	
150	1.455	0.482	0.149	12.553	0.967	
120	1.662	0.413	0.123	12.596	0.967	
100	2.216	0.175	0.084	11.763	0.961	
80	1.846	0.023	0.032	4.598	0.930	
60	3.249	0.016	0.014	3.669	0.929	
40	3.309	0.012	0.011	2.919	0.938	
25	3.821	0.006	0.008	2.744	0.921	
<b>Fitting Results of Parylene-C Stress Relaxation Behavior</b>						
Temperature ( $^\circ\text{C}$ )	$E_0(t_0)$ (GPa)	$A_1$	$\tau_{sr1}$	$A_2$	$\tau_{sr2}$	$R^2$
150	0.511	2.654	2.111	2.208	164.820	0.979
120	1.382	7.294	1.789	5.635	123.023	0.980
100	2.099	8.433	2.669	11.187	133.011	0.983
80	2.866	5.154	1.847	22.502	593.552	0.973
60	3.677	5.595	1.857	30.103	924.254	0.970
40	4.345	5.563	2.082	36.799	1085.072	0.973
25	4.751	4.874	1.668	41.734	1281.668	0.972

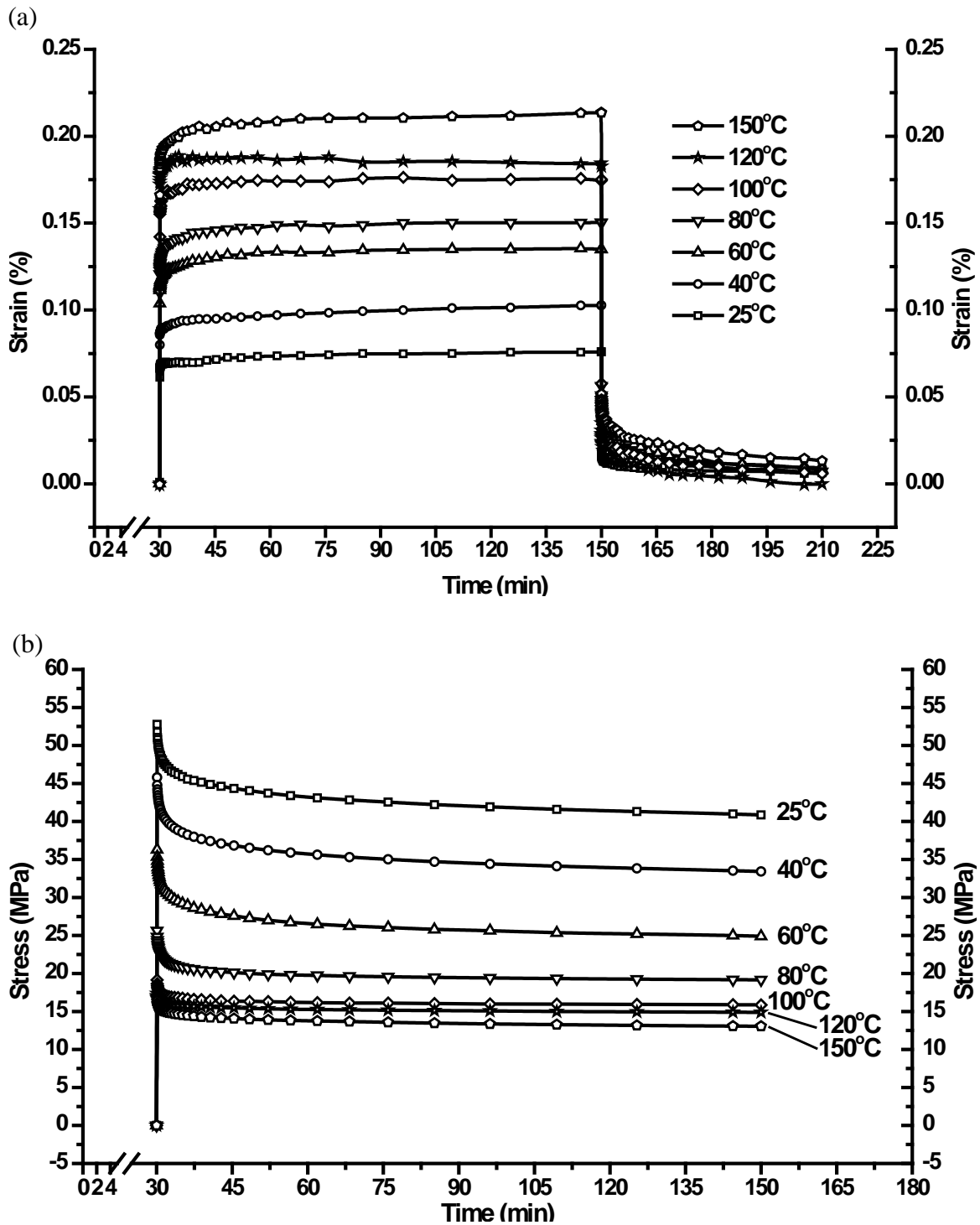


Figure 5-47 (a): Creep results of the parylene-C annealed at 200°C for 1 day in the vacuum oven ( $T_g > 200^\circ\text{C}$ ); (b): Stress relaxation results of the parylene-C annealed at 200°C for 1 day in the vacuum oven ( $T_g > 200^\circ\text{C}$ )

Table 5-20: Burger's model curve fitting results of the creep and stress relaxation behaviors of the parylene-C annealed at 200°C for 1 day in the vacuum oven ( $T_g > 200^\circ\text{C}$ )

<b>Fitting Results of Parylene-C Creep Behavior</b>						
Temperature (°C)	$E_0(t_0)$ (GPa)	$\sigma_0/E_0 + \sigma_0/E_1$	$\sigma_0/\eta_0$	$-\sigma_0/E_1$	$\tau_1$	$R^2$
150	1.338	0.205	0.00008	-0.019	2.963	0.974
120	1.410	0.187	-0.00003	-0.011	1.264	0.871
100	1.566	0.171	0.00004	-0.015	1.131	0.937
80	2.014	0.145	0.00006	-0.019	2.013	0.963
60	2.180	0.130	0.00005	-0.016	3.643	0.964
40	2.839	0.094	0.00007	-0.007	3.393	0.984
25	3.666	0.074	0.00002	-0.006	17.304	0.921
<b>Fitting Results of Parylene-C Creep Recovery Behavior</b>						
Temperature (°C)	$E_0(t_0+120)$ (GPa)	$P_1$	$P_2$	$\tau_r$	$R^2$	
150	1.474	0.018	0.025	6.511	0.938	
120	1.600	0.004	0.021	4.815	0.900	
100	1.971	0.012	0.031	1.891	0.908	
80	2.447	0.011	0.033	3.389	0.942	
60	2.812	0.012	0.030	6.498	0.947	
40	3.310	0.012	0.014	5.379	0.928	
25	4.094	0.007	0.008	4.357	0.944	
<b>Fitting Results of Parylene-C Stress Relaxation Behavior</b>						
Temperature (°C)	$E_0(t_0)$ (GPa)	$A_1$	$\tau_{sr1}$	$A_2$	$\tau_{sr2}$	$R^2$
150	1.639	1.692	2.060	14.278	1153.461	0.972
120	1.738	1.397	1.447	15.628	2066.978	0.958
100	1.914	2.179	0.819	16.644	1973.455	0.951
80	2.563	4.378	1.055	20.580	1316.844	0.960
60	3.630	6.736	1.884	28.259	782.956	0.969
40	4.579	6.826	1.975	37.590	865.992	0.972
25	5.277	6.295	1.792	45.117	1034.578	0.971

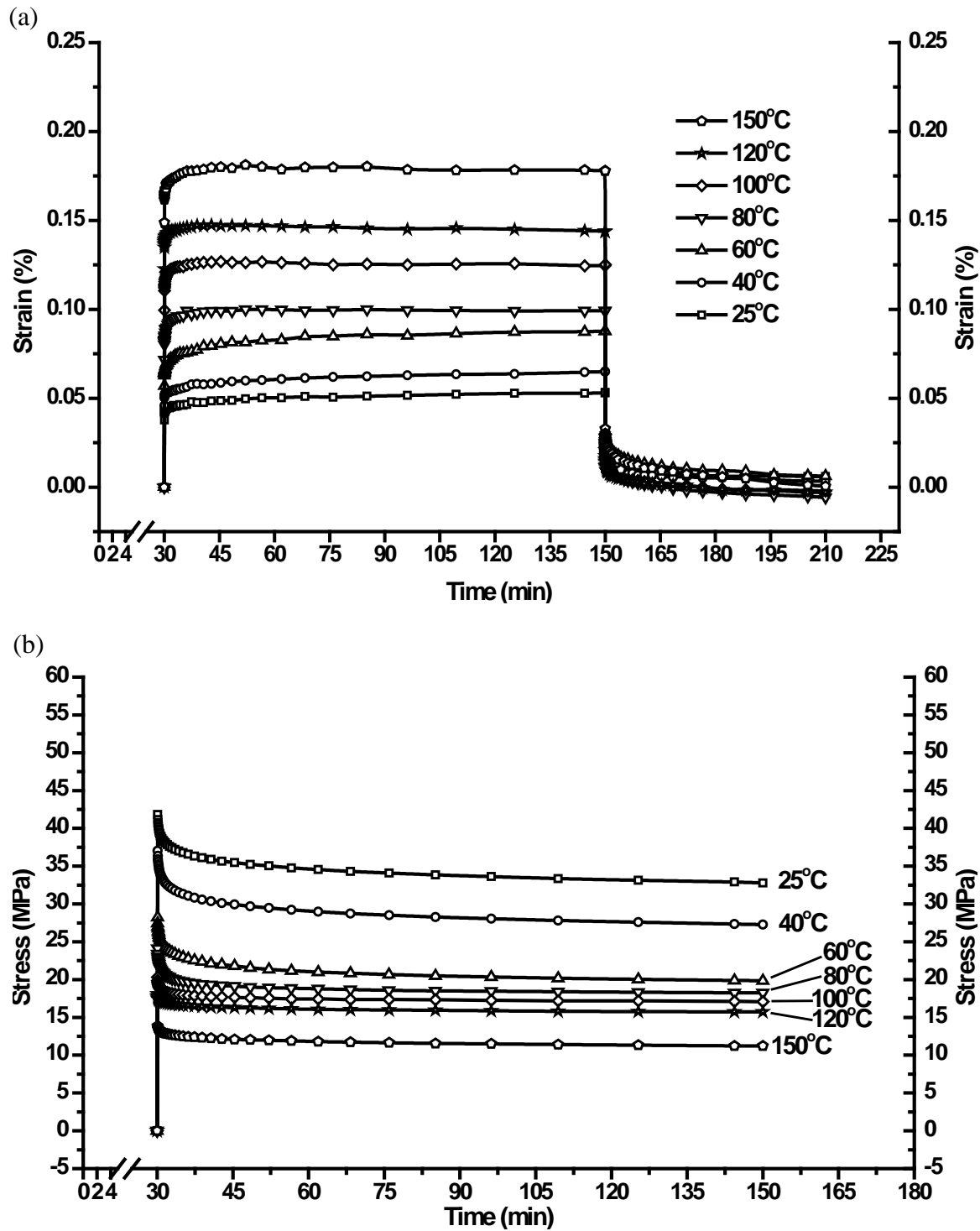


Figure 5-48 (a): Creep results of the parylene-C annealed at 200°C for 2 days in the vacuum oven ( $T_g > 200^\circ\text{C}$ ); (b): Stress relaxation results of the parylene-C annealed at 200°C for 2 days in the vacuum oven ( $T_g > 200^\circ\text{C}$ )

Table 5-21: Burger's model curve fitting results of the creep and stress relaxation behaviors of the parylene-C annealed at 200°C for 2 days in the vacuum oven ( $T_g > 200^\circ\text{C}$ )

<b>Fitting Results of Parylene-C Creep Behavior</b>						
Temperature ( $^\circ\text{C}$ )	$E_0(t_0)$ (GPa)	$\sigma_0/E_0 + \sigma_0/E_1$	$\sigma_0/\eta_0$	$-\sigma_0/E_1$	$\tau_1$	$R^2$
150	1.502	0.179	-0.00001	-0.015	2.114	0.961
120	1.803	0.147	-0.00002	-0.009	1.002	0.919
100	2.200	0.125	0.00000	-0.012	1.004	0.926
80	3.034	0.098	0.00001	-0.016	1.297	0.970
60	3.862	0.080	0.00007	-0.014	4.095	0.975
40	4.833	0.059	0.00005	-0.007	6.798	0.983
25	5.787	0.049	0.00004	-0.006	6.073	0.975
<b>Fitting Results of Parylene-C Creep Recovery Behavior</b>						
Temperature ( $^\circ\text{C}$ )	$E_0(t_0+120)$ (GPa)	$P_1$	$P_2$	$\tau_r$	$R^2$	
150	1.645	0.005	0.021	5.552	0.923	
120	1.925	0.000	0.013	3.700	0.891	
100	2.430	0.001	0.019	1.750	0.912	
80	3.261	-0.002	0.021	3.299	0.934	
60	4.187	0.009	0.017	5.497	0.946	
40	4.793	0.005	0.008	4.699	0.927	
25	5.930	0.007	0.004	2.800	0.926	
<b>Fitting Results of Parylene-C Stress Relaxation Behavior</b>						
Temperature ( $^\circ\text{C}$ )	$E_0(t_0)$ (GPa)	$A_1$	$\tau_{sr1}$	$A_2$	$\tau_{sr2}$	$R^2$
150	1.386	1.350	2.632	12.238	1194.563	0.978
120	1.813	1.323	1.594	16.456	2154.843	0.956
100	2.030	2.133	0.880	17.877	2167.343	0.958
80	2.411	3.972	1.109	19.528	1386.513	0.962
60	2.822	4.909	1.847	22.285	844.266	0.967
40	3.702	5.514	2.007	30.504	906.889	0.974
25	4.183	4.834	2.125	36.010	1104.291	0.973

#### 5.8.1.4 Summary

In this section, creep tests are performed with eight differently pre-annealed parylene-C samples. As it has been found in Section 5.6 that the as-deposited parylene-C starts to crystallize at the temperature higher than 50°C and thus the  $T_g$  changes, the parylene-C samples are annealed at different temperatures prior the creep tests to achieve different  $T_g$ . Creep tests at different temperatures correspond to the creep study of different crystallinity of the parylene-C. The testing temperatures are chosen to cover before and after the glass transition temperatures. The primary, secondary creep and recovery behavior are all investigated in this section. The results show that parylene-C has very little or no creep below  $T_g$ , but has increasing creep and creep rate above  $T_g$ . The Young's modulus at  $t=30$  min and  $t=150$  min of each samples are calculated, and it shows that the Young's modulus increases during the creep, implying that the crystallization takes place during the creep either due to thermal annealing or mechanical stretching.

As aforementioned, most of the parylene-C crystallization is done in the first minute once the annealing temperature reaches over the  $T_g$ . It turns out that the creep results shown in Figure 5-41 (a) cannot be fully regarded as the creep results of the "as-deposited" parylene-C. Because it takes the first 30 minutes to thermally stabilize the testing chamber, the parylene-C sample had been treated in the elevated temperature for 30 minutes in the testing chamber and crystallized during this thermal stabilization. Therefore, the strain level of the creep results at 100°C, 120°C, and 150°C show similar results in Figure 5-43 to Figure 5-46. As long as the temperature of the pre-annealing treatments of the parylene-C sample is less than its creep temperature, the parylene-C

sample also experiences further crystallization at the creep temperature during the 30 minutes stabilization. To overcome this problem, the best way to do is place the sample in a pre-heated and thermally stabilized chamber and starts the creep test right after the placement. The temperature profile of this experiment can be treated as a step function. As the crystallization time constant is found to be about 0.845 minute, some of the creep in this experiment happens before the first time constant of its crystallization. Unfortunately, DMA Q800 does not provide this kind of function due to its sample loading limitation. An alternate approach was proposed and performed to fulfill this idea, which will be discussed in Section 5.8.2.

A 4-element Burger's model is utilized in this section to curve fit our results and the model agrees well with our creep data according to the obtained correlation coefficients, with the exception of the results obtained at the temperature lower than  $T_g$ . The derived  $T_g$  is generally in between 7-10 minutes for the creep, meaning that 30 minutes, i.e. 3 time constants, is long enough for parylene-C to finish the primary creep behavior. As the permanent viscoplastic strain is found after the creep test at the temperature higher than  $T_g$ , it is believed that the yield point could be even less than 2.43 MPa at these temperature levels. The future work would focus on the study of this irreversible strain and also the yield strength of differently pre-annealed parylene-C at different temperatures. In addition, as only primary and secondary creep behavior have been studied here, it worth a study of the investigation of the tertiary region of the parylene-C creep, which leads to the rupture as shown in Figure 5-39 (b). This study can be achieved by either longer creep with 2.43 MPa, which might take a long time, or a higher creep loading stress to shorten the testing time.

## 5.8.2 As-deposited parylene-C creep study under a step temperature profile

### 5.8.2.1 Experimental setup

To solve the problem of the parylene-C's crystallization occurring during the first 30 minutes of the testing chamber's thermal stabilization prior to the creep test, a convection oven is pre-heated at the targeted temperature and thermally stabilized prior to the real creep tests. The testing setup is shown in Figure 5-49 (a)

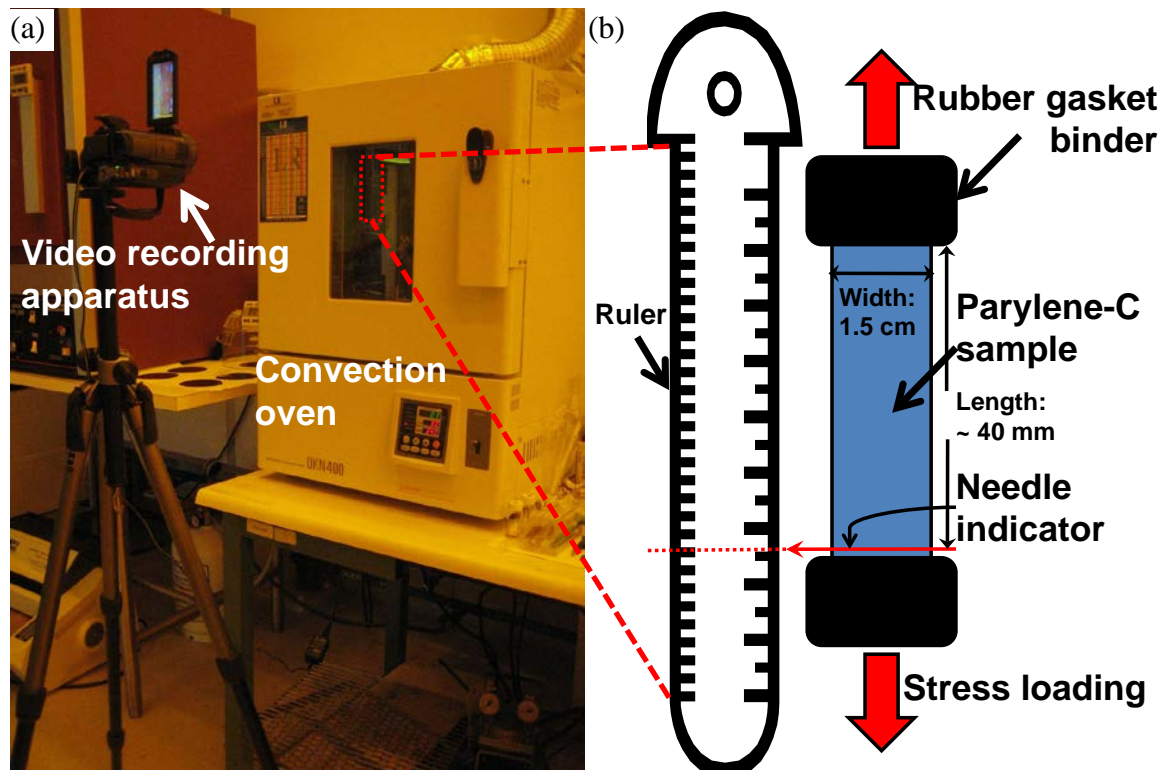


Figure 5-49: The testing setup of parylene-C creep with Heaviside temperature profile: (a) convection oven setup with a video recording apparatus, (b) parylene-C sample mounting configuration in the convection oven

Parylene-C film was deposited  $11.25\ \mu\text{m}$  thick and then cut into uniform 15-mm-wide strips, each with a length of more than 40 mm, facilitating later binding onto the

testing clamps. One third of the as-deposited samples were treated in a convection oven, and one third in a vacuum oven, all at 100°C for 30 minutes. A needle indicator was glued onto the bottom of the sample for convenient data reading, as can be seen in Figure 5-50. As shown in Figure 5-49 (b), the finished samples were clamped using two flat rubber gaskets to prevent the sample from sliding inside the clamp and ensure the uniform distribution of the tensile stress. A constant tensile stress of 2.43 MPa, which is the same as in Section 5.8.1, is applied to the samples by gravitational loading. The testing temperature was chosen as 80°C, 100°C, 120°C, and 150°C, which are all higher than the  $T_g$  of as-deposited parylene-C (~ 50°C).

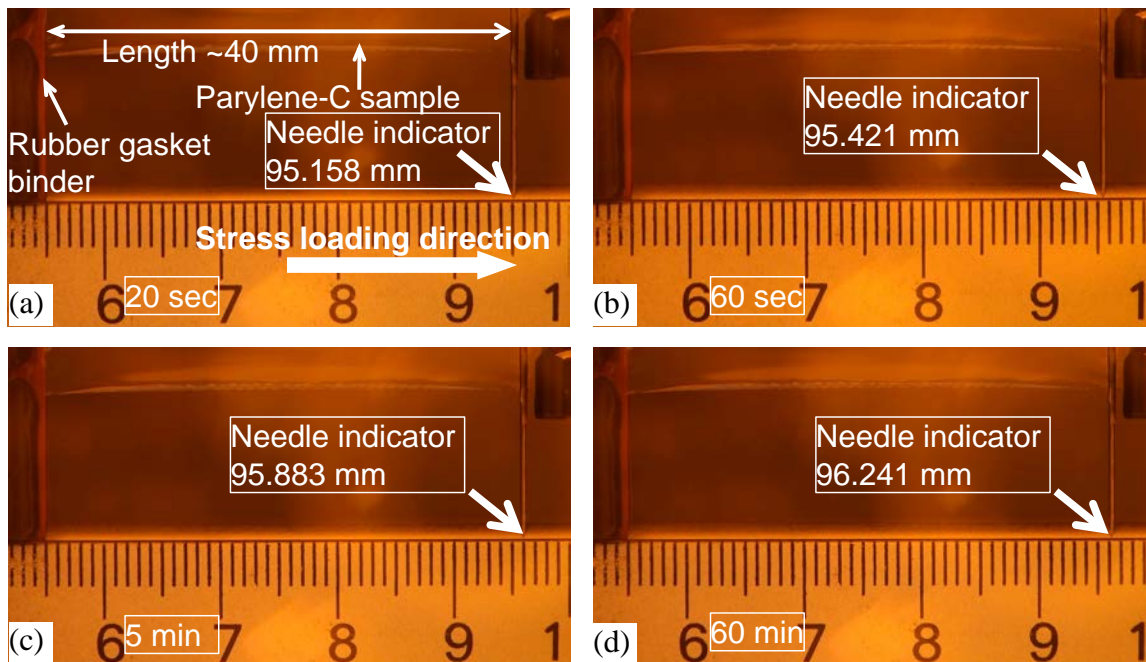


Figure 5-50: Typical capture photos of the parylene-C creep test (as-deposited parylene-C tested at 120°C) after (a) 20 sec, (b) 60 sec, (c) 5 minutes, and (d) 60 minutes. (Numbers shown on the measuring ruler represent centimeters.)

The convection oven was first pre-heated to the target temperature. Once the oven's temperature was stabilized, the parylene-C sample was placed in the oven and the door was closed immediately. As the Biot number is much less than one, the temperature distribution is assumed to be uniform within the samples [252]. The theoretical heat flux was also calculated and verified that the sample was in thermal equilibrium with the oven's inner ambient temperature in less than one second. Therefore, parylene-C film is assumed to fully experience the target temperature right after placement into the oven, and the samples can be mathematically assumed to experience a Heaviside temperature profile in this creep test.

The creep test was performed under the previous mentioned temperatures for longer than 60 minutes, while the location of the needle indicator was filmed by the video recording apparatus through the observing window of the convection oven, as shown in Figure 5-49 (a). A picture was first taken prior the sample placed in the oven so that the original length extension of the sample under the stress of 2.43 MPa can be first measured. Photos at several critical time intervals during the creep test were then captured from the video, enhanced by Photoshop and run through a Matlab program to determine the sample length as a function of time, as shown in Figure 5-50. Thermal expansion effect of the samples was also considered and eliminated during the data analysis.

### ***5.8.2.2 Experimental results and discussions***

The obtained creep curves of three different pre-annealed parylene-C samples are shown in Figure 5-51 to Figure 5-53. By comparing Figure 5-51 (the results of as-deposited parylene-C) and Figure 5-41 (a) (creep results of as-deposited parylene-C pre-

annealed for 30 minutes during the chamber thermal stabilization), it is found that the creep strain obtained under Heaviside temperature profile (Figure 5-51) is much higher than in Figure 5-41. Take the sample tested at 150°C for an example, the strain in Figure 5-51 is found to be 7% after 60 minutes of creep, while the strain in Figure 5-41 (a) is found to be only 0.7%. Because the creep temperature profile during the creep test in this section is a step function, the creep initiated right after the parylene-C sample was placed in the oven. Therefore, although the crystallization time constant is found less than one minute in Section 5.5.2, it still has lots of amorphous molecules when it starts to creep. As a result, the parylene-C tested in this section can extend much longer than in Section 5.8.1.

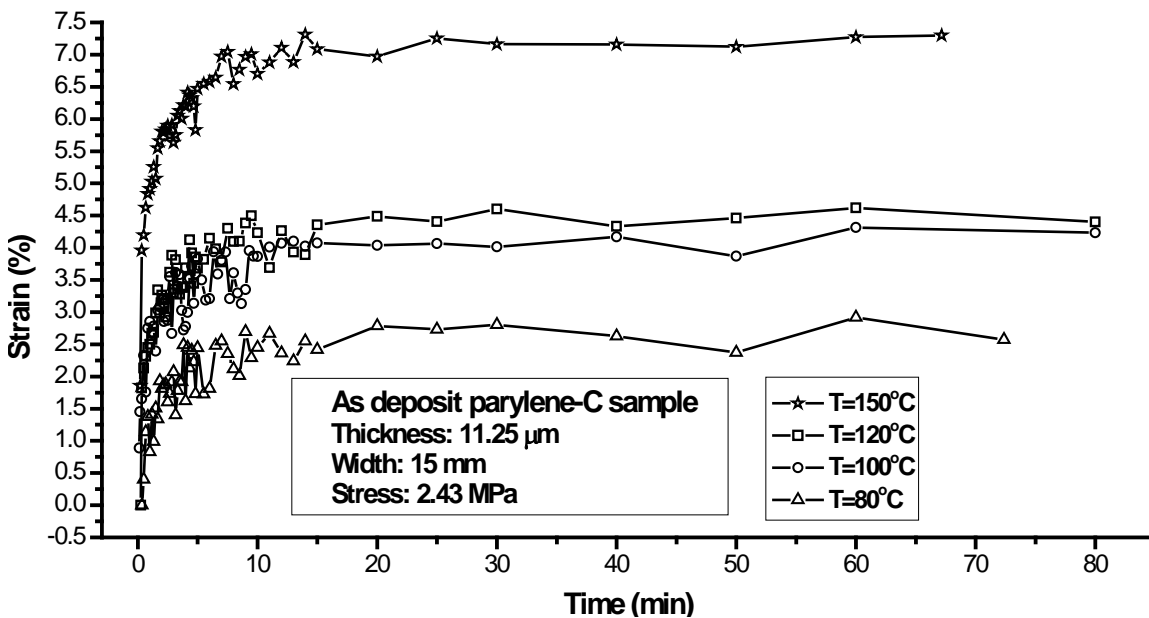


Figure 5-51: Creep results of as-deposited parylene-C performed at 80°C, 100°C, 120°C, and 150°C with a Heaviside temperature profile

It is also found that the creep saturates quickly in less than 10 minutes. However, unlike the curve shown in Figure 5-41 (a), which keeps expanding with a constant rate, the strain obtained in this section remains pretty flat afterward. The Burger's model is also used to curve fit the as-deposited data and the dominant time constants are extracted. The obtained time constants are shown in Table 5-22. It is found from Table 5-22 that the time constants also possess a descending trend as the temperature increases.

Table 5-22: Time constant of as-deposited parylene-C samples tested at different temperatures

<b>Time constants subjected to different testing temperatures</b>				
<b>Temperature (°C)</b>	<b>80</b>	<b>100</b>	<b>120</b>	<b>150</b>
<b>Time constant <math>\tau</math> (min)</b>	5.34	4.29	3.48	2.21

Figure 5-52 shows the creep results of parylene-C annealed at 100°C in the air for 30 minutes. Compare to the as-deposited parylene-C results in Figure 5-51, it can be seen that the samples pre-processed in the 100°C convection oven showed no significant signs of creep at temperatures of 80°C and 100°C, while it shows a creep similar to those found in as-deposit samples at the temperatures of 120°C and 150°C at a decreased rate and lesser overall displacement. This phenomenon is believed to be caused by the crystallization and the oxidation of the parylene-C that occurred when it was annealed in the 100°C convection oven. To understand the reliability of the creep test performed in this section, the creep curve representing pre-annealed parylene-C tested at 100°C shown in Figure 5-52 is compared to the curve representing as-deposited parylene-C thermally treated at 100°C for 30 minutes during the system thermal stabilization shown in Figure

5-41 (a). From Figure 5-41 (a), the sample tested at 100°C extends to about 0.5% after 60 minutes of creep, while the curve shown in Figure 5-52 has a strain ranging about 0.5% to 1%. Due to the low resolution of the method provided in this section, which is about 0.5%, these two strains do not show a significant difference and therefore the comparison verifies that the testing method performed in this section is a reliable approach.

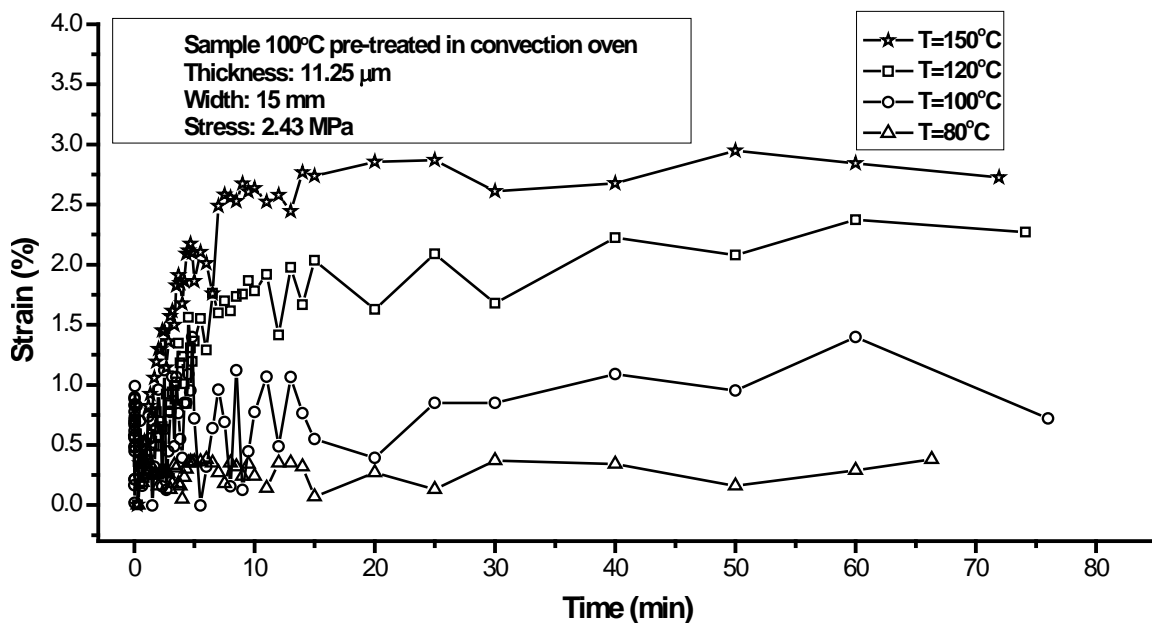


Figure 5-52: Creep results of parylene-C pre-annealed at 100°C in the air, performed at 80°C, 100°C, 120°C, and 150°C with a Heaviside temperature profile

As shown in Figure 5-53, the creep results of parylene-C samples pre-annealed in the 100°C vacuum oven show a similar behavior to the as-deposit samples at all four temperatures, but with a smaller creep strain. The lesser overall strain of the samples treated at 100°C in vacuum implies the intrinsic polymer transformation, which is mainly due to the crystallization.

The oxidation results can also be studied by comparing Figure 5-52 and Figure 5-53. It is found that the strain of the creep curves shown in Figure 5-53 is always higher than in Figure 5-52 at all four testing temperatures. As two samples are both pre-annealed at 100°C, in addition, the crystallization effect can be ignored at the time of instantaneous stain applied, it is evident that the oxidation does happen at 100°C and dominates the creep results in this study. It is believed that the oxygen atom embedded in the parylene-C sample deters the polymer movement during the creep tests. The results verify that annealing of parylene-C in vacuum keeps the sample oxygen-free and does preserve its properties.

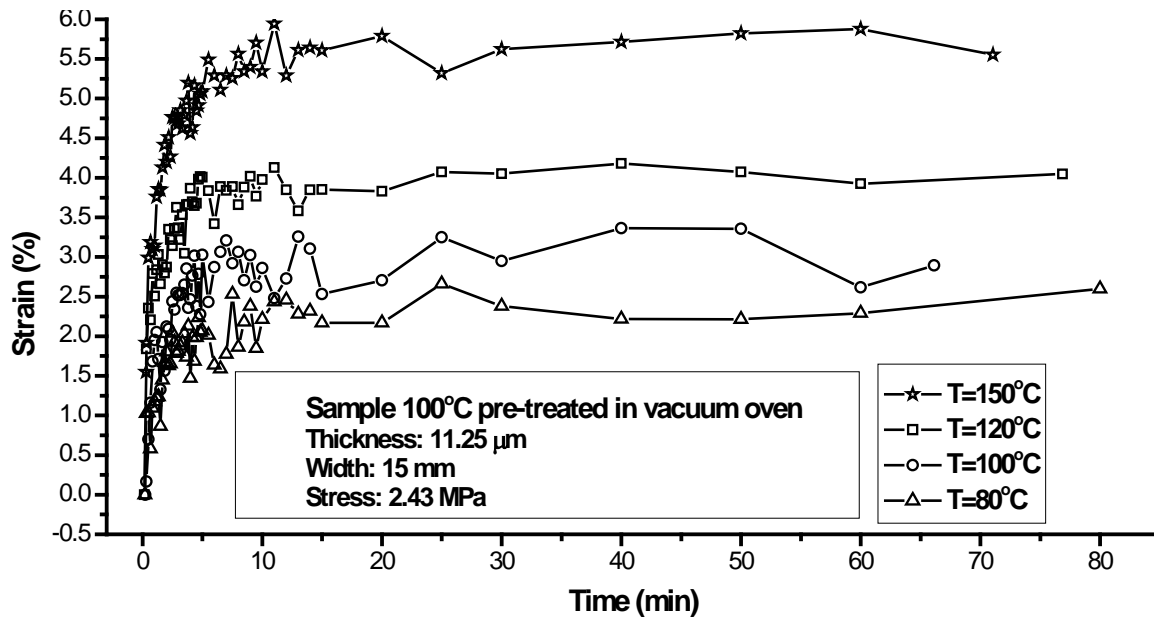


Figure 5-53: Creep results of parylene-C pre-annealed at 100°C in the vacuum, performed at 80°C, 100°C, 120°C, and 150°C with a Heaviside temperature profile

### 5.8.3 Stress relaxation of parylene-C

#### 5.8.3.1 Stress relaxation overview

Stress-relaxation is another experiment which is also commonly used to find the time-dependent mechanical behavior of the materials. The concept of the stress relaxation experiment is shown in Figure 5-54. As shown in Figure 5-54 (a), the stress relaxation test measures the stress evolution under a constant strain. The environmental temperature is generally constant. The corresponding output of the applied strain is shown in Figure 5-54 (b). The stress is first induced by the initial instantaneous strain at  $t=t_0$ . Both induced stress relaxes and the relaxing rate decrease gradually with respect to the time. A permanent stress could be found depends on the type of material tested. The induced stress of the thermoplastic polymer is generally relaxed to zero while a permanent stress is generally found with the thermoset polymer [239].

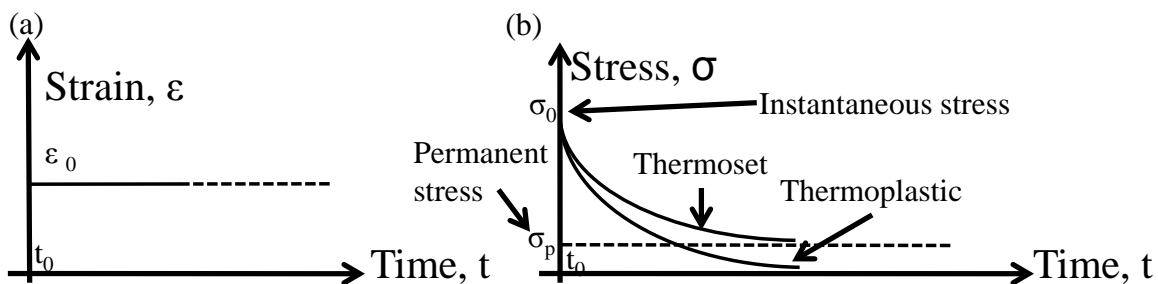


Figure 5-54: The stress relaxation test of polymers: (a) constant applied strain during the stress relaxation test at a constant temperature, (b) the corresponding stress output versus time

Similar to the creep tests of the parylene-C, stress relaxation tests are also of great importance as the implantable parylene-C MEMS devices would face the body

temperature, i.e., 37°C, during its operation, and the built-in stress might dominate the device's life. On the other hand, with the knowledge of the stress relaxation of parylene-C, the residual stress of parylene-C MEMS devices after the fabrication can be relaxed by treating in a proper post-annealing temperature and time.

### 5.8.3.2 Solution of the Burger's model for stress relaxation

With a proper initial condition, the constitutive equation of Burger's model expressed in eqn. (5-12) can be solved for stress relaxation. Rewrite eqn. (5-12) as:

$$\sigma_0 + p_1 \dot{\sigma} + p_2 \ddot{\sigma} = q_1 \dot{\varepsilon} + q_2 \ddot{\varepsilon}, \quad (5-19)$$

where

$$\begin{aligned} p_1 &= \frac{\eta_0}{E_0} + \frac{\eta_0}{E_1} + \frac{\eta_1}{E_1}, \\ p_2 &= \frac{\eta_0 \eta_1}{E_0 E_1}, \\ q_1 &= \eta_0, \\ q_2 &= \frac{\eta_0 \eta_1}{E_1}. \end{aligned} \quad (5-20)$$

To solve eqn. (5-19) for stress relaxation behavior, the initial strain conditions are expressed as  $\varepsilon(0) = \varepsilon_0 H(t)$ , where  $H(t)$  is the Heaviside function,  $\dot{\varepsilon}(0) = \varepsilon_0 \delta(t)$  and  $\ddot{\varepsilon}(0) = \varepsilon_0 \frac{\delta(t)}{dt}$ . Applied  $\varepsilon(0)$ ,  $\dot{\varepsilon}(0)$ ,  $\ddot{\varepsilon}(0)$  into eqn. (5-19), the solution of the obtained stress can be solved as [239, 253, 254]:

$$\sigma = \frac{\varepsilon_0}{\sqrt{p_1^2 - 4p_2}} [(q_1 - q_2 r_1) \exp^{-r_1 t} - (q_1 - q_2 r_2) \exp^{-r_2 t}], \quad (5-21)$$

or for simplicity:

$$\sigma = A_1 \exp^{-r_1 t} + A_2 \exp^{-r_2 t}, \quad (5-22)$$

In eqn. (5-21),  $r_1$  and  $r_2$  are expressed as:

$$r_1 = \frac{p_1 - \sqrt{p_1^2 - 4p_2}}{2p_2}, \text{ and } r_2 = \frac{p_1 + \sqrt{p_1^2 - 4p_2}}{2p_2}. \quad (5-23)$$

The values of four physical elements of the Burger's model can be calculated by the following expressions:

$$\begin{aligned} E_0 &= \frac{q_2}{q_1}, \\ \eta_0 &= q_0, \\ E_1 &= \frac{E_0 \eta_0^2}{p_1 E_0 \eta_0 - \eta_0^2 - q_2 E_0}, \\ \eta_1 &= \frac{q_2 E_1}{\eta_0}. \end{aligned} \quad (5-24)$$

In addition, the two time constants  $\tau_{sr1}$ , and  $\tau_{sr2}$  can be obtained by the reciprocal of  $r_1$  and  $r_2$  as:

$$\tau_{sr1} = \frac{1}{r_1}, \text{ and } \tau_{sr2} = \frac{1}{r_2}. \quad (5-25)$$

### 5.8.3.3 Stress relaxation experiment

#### 5.8.3.3.1 Sample preparation and the experiments

In this section, the stress relaxation was performed with eight parylene-C samples treated/annealed the same as in Section 5.8.1, as well as with the same geometry. Seven testing temperatures were also chosen the same as in Section 5.8.1 for comparison. During the stress relaxation experiment, an instantaneous strain of 1% was applied onto the sample and the corresponding stress relaxation was monitored for two hours. Similarly, the system was pre-heated to the target temperature for 30 minutes before the stress relaxation test.

### 5.8.3.3.2 Results and discussion

The results of the stress relaxation test of eight different pre-treated parylene-C samples are shown in Figure 5-41 (b) to Figure 5-48 (b) on pages 240 to 254. Similar to the figures of creep tests, each figure has seven curves corresponding to seven different testing temperatures. The Burger's curve fitting results are also shown in the stress relaxation parts in Table 5-14 to Table 5-21 on pages 241 to 255. From the results shown in those figures and tables, several findings can be made as follows:

1. It is found that the stress always demonstrates a descending trend at whatever temperature, and a permanent stress is always found as long as the 1% strain is applied to the samples. The permanent stress level depends on the testing temperature. The remaining permanent stress becomes much less when the testing temperature is higher than  $T_g$ . In this case, the higher the testing temperature, the lesser the permanent stress obtained. It implies the high mobility of the parylene-C polymer chain at higher temperature. The descending rate generally also increases as the testing temperature increases. However, when the testing temperature is lower than  $T_g$ , very little descending rate is observed and the permanent stress is relatively higher. It is evident that the glass transition temperature is a very important indicator that divides the results into two parts: very little stress is relaxed and also at a slower rate with temperature lower than  $T_g$ , while more stress is relaxed and at a faster relaxing rate at the temperature higher than  $T_g$ .
2. It is found from Burger's model expressed in eqn. (5-21) that the solution model has two time constants:  $\tau_{sr1}$  and  $\tau_{sr2}$ . The results of the first time constant,  $\tau_{sr1}$ ,

in Table 5-14 to Table 5-21 generally fall in the range of 1–5 minutes. However, the value of  $\tau_{sr1}$  spreads arbitrary and no obvious trend can be found. On the other hand, according to Table 5-14 to Table 5-21, the values of  $\tau_{sr2}$  are found ranging from about 100 up to 2150 minutes, which is much larger than the first time constant  $\tau_{sr1}$ . Another trend also can be found that  $\tau_{sr2}$  generally decreases as the testing temperature increases, with the exception of samples pre-annealed at 200°C (Table 5-20 and Table 5-21). Again, this infers that the parylene-C is softer at higher temperature and the polymer chain is easier to deform. The stress relaxation results of samples pre-annealed at 200°C all show very large  $\tau_{sr2}$ , implying very little stress relaxation. Therefore the parylene-C annealed at 200°C for either one or two days are very close to elastic material, which has also been predicted in Section 5.8.1. Because the annealing of parylene-C at 200°C was performed in the vacuum oven, it is believed that the oxidation effect can be ignored during the sample preparation, and thus this material property change (from viscoelastic to elastic) is attributed to the crystallization of the parylene-C. As the second time constant is usually longer than 120 minutes, the effect of the second time constant cannot be seen in the figures shown in this section. Further study needs to be done to verify the accuracy of model.

3. As aforementioned, it can be graphically found that the remaining permanent stress decreases as the testing temperature increases. In addition, more stress is relaxed when the testing temperature gets higher than  $T_g$ , which has been found usually close but a bit higher than the annealing temperature in Section 5.6. It infers that the parylene-C residual stress resulting from the clean room fabrication

can be relaxed by annealing the parylene-C at a temperature higher than the maximum processing temperature. It turns out that monitoring the temperature history of the parylene-C fabrication process is helpful in predicting and reducing its residual stress after the device is done. In our clean room, the temperature generated in most processes is generally controlled less than 200°C. Therefore, to relax the residual stress of the parylene-C-based device, it is suggested to anneal the device at 200°C in the vacuum oven. As aforementioned, the time first time constant  $\tau_{sr1}$  is generally in the range of 1–5 minutes, it can be concluded that the residual stress can be mostly relaxed in 15 minutes (3 time constants). Therefore, two-hours annealing would be long enough to relax most of the residual stress in the parylene-C device, according to what we have just found in this section.

4. It is also found that the remaining permanent stress is higher as the pre-annealing temperature gets higher. For example, at the testing temperature of 150°C, parylene-C pre-annealed at 200°C (shown in Figure 5-47 and Figure 5-48) has the highest stress remaining among all eight different parylene-C samples. This is likely due to the highest crystallinity coming from the high pre-annealing temperature. High crystallinity also results in slower stress relaxing rate. This means parylene-C annealed at 200°C behaves similar to an elastic material, which is also concluded in Section 5.8.1.
5. From Figure 5-41 (b) to Figure 5-48 (b), it can be seen that the stress is introduced immediately after the instantaneous 1% strain is applied. The level of the stress response depends on the Yong's modulus at the testing temperature. Similar to the Young's modulus calculation in Section 5.8.1, the Young's modulus can be

obtained by the measured stress divided by 1% of strain. The results of calculated Young's modulus are shown in the first column of the stress relaxation part in Table 5-14 to Table 5-21. As expected, the obtained Young's modulus decreases as the testing temperature increases. As expected, it is found that the Young's modulus obtained from stress relaxation experiments are close to the values obtained from creep experiments. The minor difference is likely attributable to thickness variation and clamping variations.

#### **5.8.3.4 Summary**

A series of stress relaxation experiments at seven different testing temperatures has been done with eight differently pre-treated parylene-C samples. The stress relaxation experiments performed at temperatures higher than  $T_g$  have faster stress relaxation rates and less residual stress after 120 minutes than experiments performed below  $T_g$ . The Burger's model solution for stress relaxation behavior is a solution with two-time-constants. The curve fitting results show that the first time constant is generally in the range of 1–5 minutes but no trend could be observed from the current data obtained in our tests. The second time constant is always found much larger than the first time constant, falling in the range of ~ 100–2150 minutes. In general the second time constant decreased with increasing testing temperature, except when parylene-C was pre-annealed at 200°C, which behaved elastically at the temperatures lower than 200°C. Because the second time constants are usually larger than 120 minutes, the effect of the second time constant cannot be clearly observed in our results in the Figure 5-41 (b) to Figure 5-48 (b). More stress relaxation experiments with longer testing time are needed to understand the second time constant behavior.

From the stress relaxation results, it is suggested that, in order to relax the residual stress of a parylene-C-based device, the device can be placed at the temperature which is higher than the highest temperature that the device had experienced during its fabrication. The time should be longer than three times the first time constant for complete relaxation. In our experience, annealing the device at 200°C in vacuum for two hours is preferable.

It is also found that the parylene-C pre-annealed at higher temperature has higher remaining permanent stress than at lower temperature after two hours of stress annealing experiment. This is due to the high crystallinity of the parylene-C generated during its pre-annealing process. Whether the remaining permanent stress is helpful depends on the devices' application. If the remaining permanent stress is not required in its final application, the device can be annealed at the elevated temperature. If the remained stress is necessary in the device, the parylene-C is suggested to be pre-annealed at a higher temperature than its final operational temperature to tailor the  $T_g$  to a higher value. By increasing  $T_g$ , it prevents the stress loss in the final application at the operational temperature and therefore the device's lifetime can become longer.

#### **5.8.4 Summary**

In this section, the creep and the stress relaxation behavior, which represent the time-dependent behavior of the parylene-C were investigated. This work provides useful information to help researchers design and make the parylene-C based devices. According to what has been found in this section, parylene-C is a very thermal-sensitive material and it takes a lot care to fabricate it carefully in the right temperature. In order to minimize or reduce the residual stress, the temperature needs to be carefully selected

during the device fabrication. The fabrication thermal history has to be monitored to prevent unpredicted device function behavior.

For example, it is recommended that the device should be pre-annealed at a temperature higher than its designed operation temperature to stabilize the parylene-C mechanical properties. In addition, by properly designing the fabrication temperatures and procedures, the required built-in stress of the device won't be relaxed during later clean room fabrication and its normal operations.

On the other hand, if it is necessary to eliminate residual stress or it is necessary to thermally deform and mold the parylene-C device, the temperature experienced during the device fabrication needs to be monitored. In such cases, a higher temperature than the temperature the device has experienced is required.

It is well known that high temperature could be introduced during the parylene-C fabrication or post fabrication. By understanding the relationship between the mechanical properties of parylene-C with respect to the temperature, people can design parylene-C devices to maintain functionality and extend lifetime.

## 5.9 Viscoplasticity of Parylene-C Film at Human Body Temperature

### 5.9.1 Overview of parylene-C viscoplasticity study

Due to its superior biocompatibility, parylene-C has been a prominent protective coating material for many biomedical devices since the 1950s [255]. In addition, there is a fast development of parylene-C bioMEMS technology with many potential applications, such as, spinal cord implant, glaucoma drainage device and cochlear implant [238, 255, 256]. However, there were reports on the aging degradation of parylene-C in animal body fluid. For an example, it was found that the as-deposited parylene-C showed long-term degradation in the monkey brain two years after the implantation [257]. Although there is suspicion that the plastic or viscoplastic behavior of parylene-C is part of the degradation mechanism, this has never been systematically studied. Therefore, there is concern that the lack of understanding of parylene-C's plastic behavior can lead to wrongful use of it, especially for long-term implant devices.

The creep behavior, i.e. total strain change with time under a constant loading stress, and the stress relaxation behavior, i.e., total stress change with time under a constant strain, of parylene-C film at different temperatures have been studied in Section 5.8.1. The testing results showed that as-deposited parylene-C film can have plastic deformation at 37°C as its glass transition temperature range is 35–60°C [258]. Therefore, this work is focused on the plastic, or more accurately, viscoplastic, behaviors of parylene-C film at 37°C due to its growing population in implantations. To understand the viscoplastic behaviors of parylene-C film, uniaxial tensile tests under various conditions are performed including tests under different strain rates, cyclic

loading/unloading tests, abrupt strain rate change tests, creep-recovery tests, and stress-relaxation tests [259, 260]

## **5.9.2 Sample preparation and viscoplastic experiments**

### ***5.9.2.1 Sample preparation and testing environment setup***

The testing parylene-C samples were prepared at the same deposition condition by the same coating system as described in previous few sections. The as-deposited film was then cut into strips with 5.3 mm in width and 10 mm in length. All tests were performed in the DMA Q800 by TA instruments at 37°C. Similarly, the testing chamber was first ramped to 37°C, and waited until the whole system reached thermal equilibrium before the tests started.

### ***5.9.2.2 Testing results***

All testing results from the machine are nominal stresses or strains. In this section, all nominal stresses and strains are readily converted to the true stresses and strains unless otherwise specified. (Strain rate tests) 5 different strain rates were chosen from  $8.33 \times 10^{-6} \text{ s}^{-1}$  to  $8.33 \times 10^{-2} \text{ s}^{-1}$  (i.e., the highest strain rate Q800 can apply), each of which has one order of magnitude jump, as shown in Figure 5-55. (Cyclic loading/unloading tests) The cyclic loading/unloading tests were done at the strain rate of  $8.33 \times 10^{-5} \text{ s}^{-1}$  (as shown in Figure 5-56). The first loading/unloading was done at 22.92 MPa and the second done at 32.92 MPa. (Abrupt strain rate change tests) The abrupt strain rate change test was done by changing strain rate from  $8.33 \times 10^{-5} \text{ S}^{-1}$  to  $8.33 \times 10^{-6} \text{ S}^{-1}$  during the uniaxial tensile tests. Two abrupt strain rate change tests were performed. One was done at the strain of 0.9% and the other at 1.1%, as shown in Figure 5-57.

(Creep tests) For creep tests, five stresses were applied: 2.5 MPa, 10 MPa, 20 MPa, 30 MPa, and 40 MPa. These stresses were applied for 120 minutes during the creep tests and then removed to observe the creep recovery for another 60 minutes. The creep results are shown in Figure 5-58 and fitted with Burger's model (discussed below).

(Stress relaxation tests) The stress relaxation tests were performed under 6 different strains: 0.25%, 0.5%, 0.75%, 1%, 1.5%, and 2%. These constant strains were applied onto the samples for 120 minutes to observe the stress relaxation behaviors of the parylene-C film. The stress relaxation results are shown in Figure 5-59, which are also fitted with Burger's model.

### **5.9.2.3 Discussion**

In this section, the Burger's model is still used to analyze all the results shown below due to its simplicity. Similar to Section 5.8, eqn. (5-14) is used for the creep strain analysis; eqn. (5-16) is used for the creep recovery analysis; and eqn. (5-22) is used for stress relaxation stress analysis.

Figure 5-55 shows the experimental results of uniaxial tensile tests under different strain rates and it clearly shows a rate-dependent behavior. The higher the strain rate, the larger the yield strength is. Note that, for the strain rates  $8.33 \times 10^{-2} \text{ s}^{-1}$ ,  $8.33 \times 10^{-3} \text{ s}^{-1}$  and  $8.33 \times 10^{-4} \text{ s}^{-1}$ , the end points of the three data curves are the sample fracture points. It is found that the parylene-C film tends to break more easily when the applied strain rate is higher. At strain rates higher than  $8.33 \times 10^{-4} \text{ s}^{-1}$ , the parylene-C film behaves like a brittle material. The Young's modulus is found to be about 3GPa for all five curves in the early linear region, which agrees well with the result found in Sections 5.6, 5.7, and 5.8.

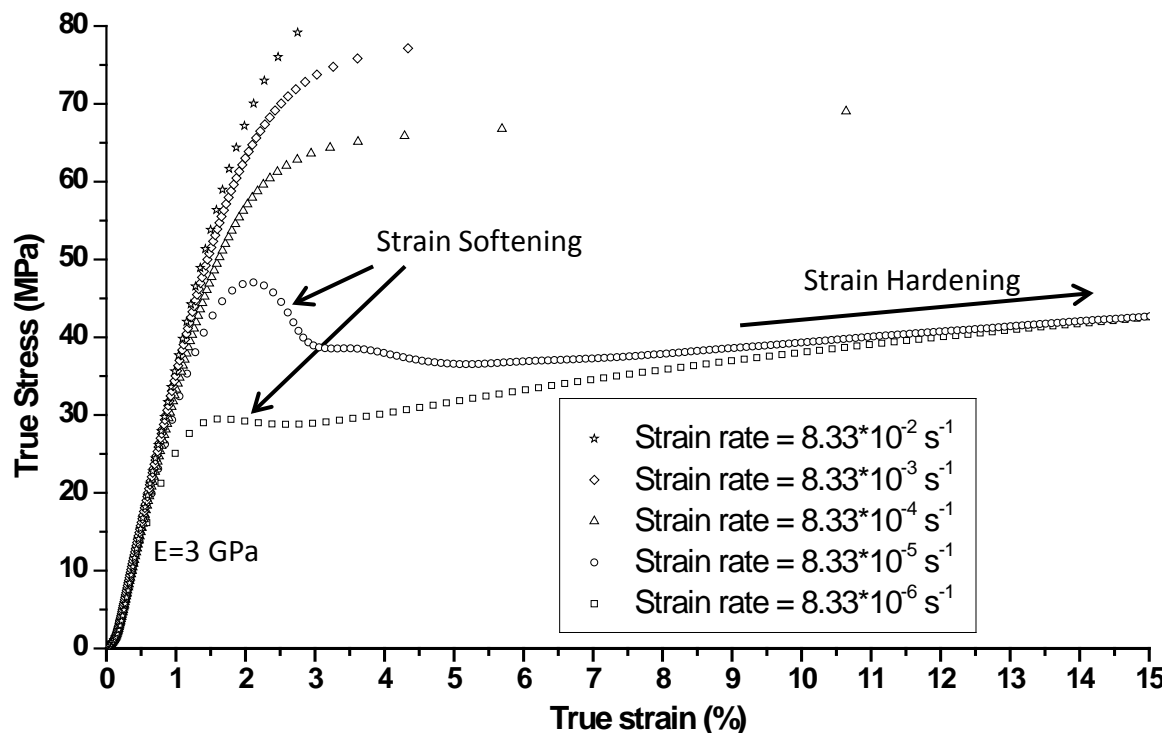


Figure 5-55: The results of constant strain-rate tests

Figure 5-56 shows the cyclic loading/unloading test results, where a permanent strain deformation of 0.09% of parylene-C remains after a stress of 22.92 MPa is loaded and then unloaded. When the stress is reloaded again, the stress-strain curve shows a hysteresis, which is another evidence of the creep recovery. However, after a while, the curves do approach the monotonic curve of the standard uniaxial tensile test without unloading.

Figure 5-57 is the results from the abrupt strain rate change experiments. It is found that when the strain rate abruptly decreases from  $8.33 \times 10^{-5} \text{ s}^{-1}$  to  $8.33 \times 10^{-6} \text{ s}^{-1}$ , the stress drops and gradually coincides with the lower strain rate curve. This means that, with a strain rate under  $8.33 \times 10^{-5} \text{ s}^{-1}$ , the Young's modulus is strain-rate dependent but not strain-rate-history dependent.

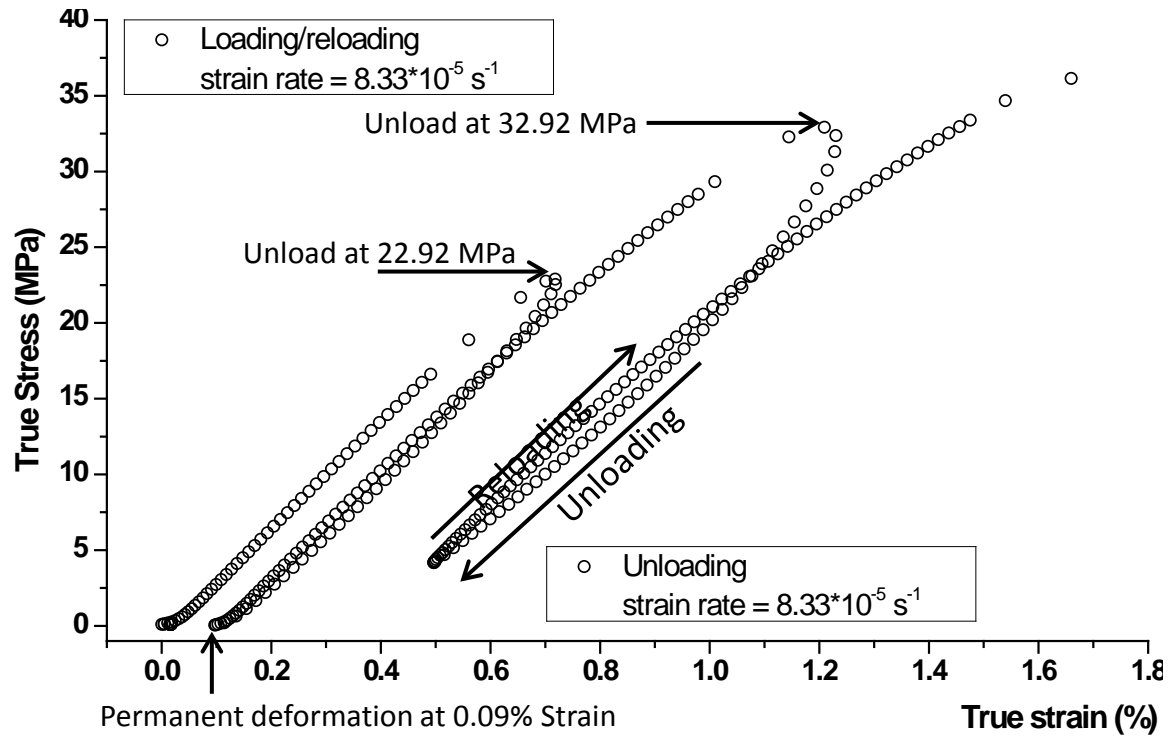


Figure 5-56: The results of cyclic loading/unloading tests

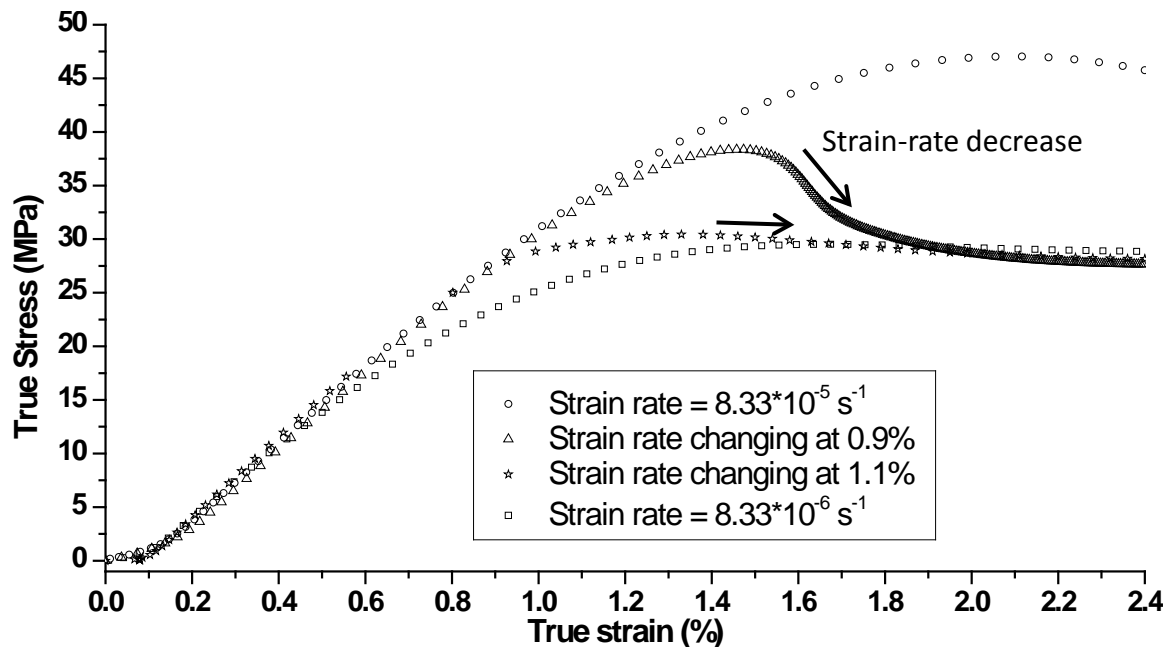


Figure 5-57: The results from the abrupt strain-rate change tests

Figure 5-58 shows the results of creep tests. Burger's model is used to fit the data curve for four different applied stresses (2.5 MPa, 10 MPa, 20 MPa, and 30 MPa). At applied stress lower than 30 MPa, the Burger's model fits well with the experimental results. The time constant is bigger for larger stress as shown in Table 5-23. At 40 MPa, the specimen simply breaks so no reliable creep data is recorded. The fitting parameters of the Burger's model for creep recovery are shown in Table 5-24. In comparison, the time constant for the creep recovery increases with decreasing loading stress, which is different from the creep case. When the applied stress is 2.5 MPa, it is found that the creep slope,  $\sigma_0/\eta_0$ , is very small so that the parylene-C film shows little or no creep behavior.

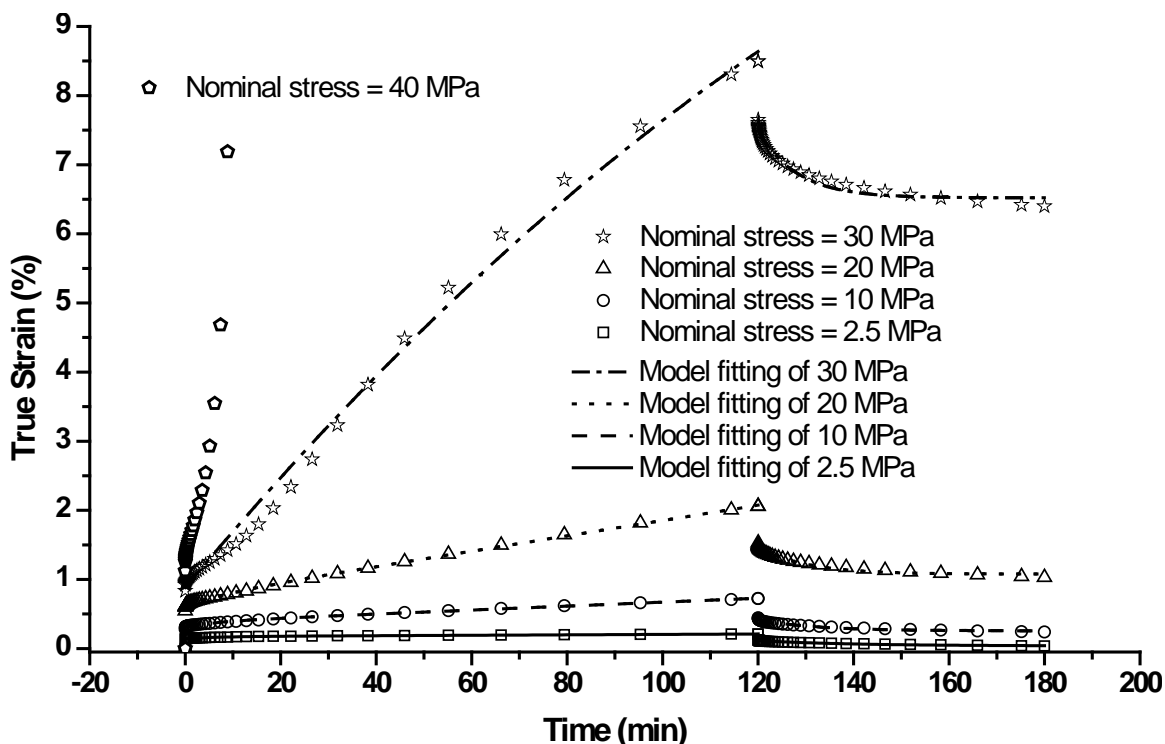


Figure 5-58: The results of creep tests of parylene-C film under different loading stresses:

Theoretical Burger's model shows good fitting for the applied stress less than 30 MPa.

Figure 5-59 shows the results and the modeling of the stress relaxation tests. Note that the stress relaxation solution of the Burger's model inherently give two time constants, hence Table 5-25 shows two time constants for each test. The first (and smaller) time constant is identified as the dominant time constant and it decreases as the applied strain increases. The second time constant is always at least an order of magnitude larger than the first time constant. Therefore, the second time constant will not be observed in our experiments due to a limited time span. Accordingly, the stress relaxation data is consistent with the creep data in the sense that parylene-C exhibits a significantly stronger plastic flow when the applied stress is higher than 35 MPa (corresponding to 1% strain). In addition, the stress is relaxed faster with higher stress loading.

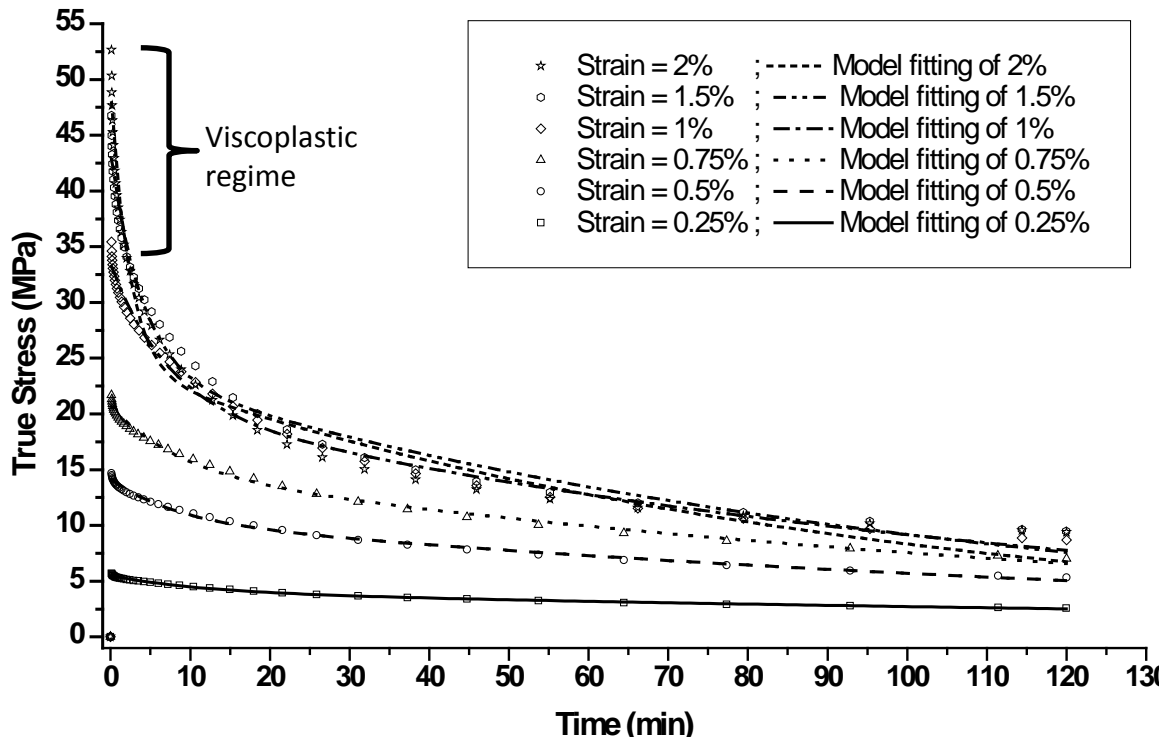


Figure 5-59: The results of stress relaxation tests. Stress relaxation is observed for all the chosen strains. Higher strain gives faster stress relaxation.

Table 5-23: Parameters of Burger's model for creep. At 40 MPa, the sample breaks and no creep could be recorded.

Applied Stress (MPa)	$\sigma_0/E_0 + \sigma_0/E_1$	$\sigma_0/\eta_0$	$\sigma_0/E_1$	$\tau_c$ (min)
2.5	0.00174	$3.096 \cdot 10^{-6}$	$-3.062 \cdot 10^{-4}$	7.522
10	0.00385	$2.861 \cdot 10^{-5}$	$-6.980 \cdot 10^{-4}$	7.512
20	0.00743	$1.109 \cdot 10^{-4}$	-0.0012	10.982
30	4.882	-0.00589	-14.873	2214.1
40	NA	NA	NA	NA

Table 5-24: Parameters of Burger's model for creep recovery

Applied Stress (MPa)	$P_1$	$P_2$	$\tau_r$
2.5	$3.766 \cdot 10^{-4}$	$7.707 \cdot 10^{-4}$	20.510
10	0.00256	0.00161	12.168
20	0.0108	0.00385	10.051
30	0.0652	0.00972	8.127
40	NA	NA	NA

Table 5-25: Parameters of Burger's model for stress relaxation

Applied Strain (%)	$P_3$	$\tau_{sr1}$ (min)	$P_4$	$\tau_{sr2}$ (min)
0.25	1.475	11.373	4.034	253.611
0.5	3.637	8.033	10.514	163.596
0.75	5.780	8.249	14.971	146.124
1	12.446	7.107	20.989	120.705
1.5	19.500	3.987	23.851	104.838
2	24.778	2.366	24.177	93.888

In summary, it is found that the time constants of creep, creep recovery and stress relaxation are functions of applied stress (or strain), as well as temperature found in [257]. Besides, above a small strain around 0.1% ( $\sim 2.5$  MPa), the parylene-C is clearly plastic and rate-dependent, hence viscoplastic.

### 5.9.3 Summary

Five different uniaxial tensile tests under different testing conditions were performed to study the viscoplastic behaviors of as-deposited 20- $\mu\text{m}$ -thick parylene-C films. The results show that, above about 0.1% of strain ( $\sim 2.5$  MPa) parylene-C is a strain (or stress) and strain-rate-dependent material. Burger's model is adequate to describe its creep and stress relaxation behaviors. Future work would focus on a more delicate viscoplastic model, e.g., Bodner-Partom model, to analyze parylene-C viscoplastic behavior [259–266].

## 5.10 Summary and Conclusion

Several mechanical properties and polymer properties of parylene-C are investigated in this chapter. The simplest densification experiment is first demonstrated. It shows that as-deposited parylene-C first extends at temperature lower than  $\sim 50^\circ\text{C}$  and starts to shrink at higher temperature, implying that the parylene-C starts to crystallize at  $\sim 50^\circ\text{C}$ . This assumption was verified by repeating the testing on the same sample with the same temperature profile. It is found that the parylene-C length does not shrink until the previous testing temperature, implying the thorough crystallization during the previous thermal annealing. The thermal coefficient of as-deposited parylene-C is found as  $35.5 \text{ ppm}/^\circ\text{C}$ , which agrees very well with the available literature value.

Oxidation of parylene-C is investigated qualitatively by XPS and FTIR. The results show that the oxidation of parylene-C is very little at 100°C while it becomes serious at 200°C. This agrees with the prediction by Nowlin's neutron activation oxygen analysis. In contrast to the XPS's scanning only the surface of the materials, the FTIR results can prove that the oxidation of parylene-C actually happens through the specimen thickness. After annealed in air at 200°C, FTIR result also show that the oxidized parylene-C is composed of CO double bond and CO single bond, and the observed broad OH spectrum also indicates the likely decomposition and hydrolysis of parylene-C at high temperature.

Crystallization of parylene-C is studied by using x-ray diffraction technology. Crystallinity, d-spacing, and crystallite size are all investigated according to the XRD data. The crystallinity of as-deposited is reported in the literature as 60% to which all XRD results are calibrated accordingly. It is shown that the parylene-C crystallinity and crystallite size increase rapidly when the specimens experience the high testing temperature. The crystallite size gets bigger with the progression of the annealing time and also as the annealing temperature increases. The time constant is found as 0.845 minutes according to the pre-annealed parylene-C crystallite size data. It also shows that the crystallization does not happen until temperature reaches ~ 50°C, which is strong evidence of showing parylene-C's glass transition temperature at 50°C. The d-spacing of (020) plane of parylene-C remains constant at around 6.31 Å during the isothermal XRD scanning at 100°C.

The glass transition temperature is investigated by using DMA scanning. Different pre-treated parylene-C specimens are prepared to study the oxidation effect,

influences of annealing temperature and of the annealing time. The glass transition temperature of as-deposited parylene-C is obtained as 53.4°C with glass transition range as 50.2–57°C. It is found that the glass transition temperature keeps up with the pre-annealing temperature higher than 60°C, while no  $T_g$  shift is found after pre-annealed at 40°C for 30 minutes. On the other hand, the glass transition range gets broader as the pre-annealing temperature increases.  $T_g$  is always obtained as the temperature close to and a bit higher than the pre-annealing temperature. No  $T_g$  difference is found regardless whether the specimen is pre-annealed in air or in vacuum oven at 100°C. Therefore, it can be concluded that the  $T_g$  is not seriously influenced by oxidation, or the oxidation effect is not the dominant effect at 100°C.  $T_g$  slightly increases with the longer pre-annealing time at the same annealing temperature. According to the  $T_g$  results, it is found that the  $T_g$  is very sensitive to the pre-annealing temperature. Combined with the crystallization study of the parylene-C, the  $T_g$  results can lead to the conclusion that the crystallization would be the main factor that causes the shift of the glass transition temperature. It is found that the glass transition temperatures previously reported by different groups vary widely from room temperature to 150°C. It is likely due to the non-standardized preparation of parylene-C samples which might have experienced different thermal processes prior to the glass transition temperature testing, causing difference in levels of crystallinity among the specimens.

The uniaxial tensile tests are performed on differently pre-annealed parylene-C samples in this chapter to investigate the influence of the crystallinity on the uniaxial tensile test results. It is found that parylene-C with higher crystallinity results in larger Young's modulus, tensile strength and less percent of elongation, which correspond to

stiffer, stronger and more brittle results. In addition, uniaxial tensile tests are also performed at different temperatures higher than 20°C. It shows that the Young's modulus decreases as the testing temperature increases, indicating the softening of the material and also proves parylene-C as the thermoplastic material.

Viscoelastic and viscoplastic properties of parylene-C have never been studied before and very rare papers about them are published. In this chapter, the viscoelastic and viscoplastic properties of parylene-C are first ever explored. It shows that the creep and stress relaxation results highly depend on the pre-annealing temperature. It is attributed to the  $T_g$  shift after the pre-annealing which renders the crystallinity change at the temperature for the pre-annealing processes. The creep results of parylene-C demonstrate a permanent strain remaining after the test, indicating that the parylene-C is a viscoplastic material. The conclusion can also be derived from the remaining permanent stress obtained after the stress-relaxation test. The remaining permanent strain or stress indicating that the yielding point of the parylene-C has changed at the elevated temperature, and cannot be found just by the regular point where the strain increases with no stress increase. Therefore, the loading/unloading experiment is performed at 37°C to understand this phenomenon. With the widely used parylene-C in the development of the biomedical devices, the viscoelastic and viscoplastic properties of parylene-C at 37°C need to be understood in more detail to avoid the unwanted device behavior happening in the human body after the devices implanted.

In summary, all experimental results presented in this chapter suggest that parylene-C film is a highly temperature-dependent polymer. With all the knowledge obtained in this chapter, people can tailor parylene-C's properties in order to satisfy their

needs for different applications. Because the CVD as-deposited parylene-C is deposited at the metastable state, it tends to crystallize immediately at the temperature higher than  $T_g$  and then transforms itself to a more stable state. In order to have devices with more stable parylene-C mechanical properties, it is suggested to pre-anneal the parylene-C at the temperature higher than the device's designed operation temperature prior to the usage of the devices to prevent the occurrence of the crystallization during its real operation.

---

# CHAPTER 6

---

## GENERAL CONCLUSION

In this thesis, a dual-valved GDD to fulfill the “band-pass” flow regulation has been developed and *in vitro/ex vivo* tested. Our GDD has been verified capable of draining out eye fluid when IOP is higher than 20 mmHg, and stopping the drainage when IOP is lower than 20 mmHg to prevent hypotony. A new IOP sensor is proposed with a new implantation location so that the quality factor can be retained and also the concern of water filling the capacitor chamber is solved. To accurately design the desired cracking pressure and also predict the life-time of a NC check-valve, parylene-C’s mechanical, thermal and polymer properties are investigated. The results show that parylene-C is a highly temperature-sensitive material, and therefore it can be tailored by thermal annealing to obtain the desired properties.

In chapter 2, a paradigm of NC check-valve is proposed with several slanted tethers to transmit the necessary downward force and therefore the NC check-valve is capable of supplying the desired cracking pressure. The desired residual tensile stress can be achieved by stretching the tethers based on several mechanisms such as: pop-up/self-stiction mechanisms; or by thermal annealing the tethers at the elevated temperature, and then quenching them down to room temperature to introduce the high thermal tensile stress. Therefore, three different approaches are developed to create the slanted tethers: generating and adopting sloped sacrificial photoresist, using pop-up

mechanism, and using the self-stiction bonding which inevitably happens after the drying process. The cracking pressure of the NC check-valve can be controlled by several parameters such as the number of the slanted tethers, the sloping angle of the slanted tethers, the geometry of the slanted tethers (the width and the thickness), and also the residual stress of the slanted tethers which can be manipulated by the annealing temperatures. The testing results show that the residual thermal tensile stress is the most controllable method among all, and can introduce the highest cracking pressure.

In chapter 3, a new dual-valved glaucoma drainage device with “band-pass” flow profile regulation capability is proposed by integrating four crucial components: one self-stiction bonding NC check-valve developed in chapter 2, one NO valve, one parylene-C fixation anchor, and one all parylene-C protective hollow tube. Our GDD is designed with the form factor that can be put in a #19-gauge needle to fulfill the minimally invasive implantation surgical procedure and the implantation can be done in a 15 minute surgery. The #19-gauge needle creates a wound less than 2 mm in diameter, and therefore it will seal by itself after the surgery and the suture is never needed. Two types of GDD integration approaches are proposed to facilitate the capability of optimizing the check-valves’ position. The GDD is placed in the translimbal area with one end staying in the anterior chamber and the other end staying subconjunctivally. The cracking pressure of the NC check-valve of the GDD is designed as 10–20 mmHg. Therefore, the dual-valved GDD is capable of draining away the excessive aqueous when the IOP is in the range of 20–50 mmHg. The NC check-valve also protects the eye from postoperative hypotony as it closes when IOP is lower than 10 mmHg. In addition, the GDD also has a benefit of closing at the sudden unexpected high IOP to prevent hypotony.

In chapter 4, two methods are proposed to improve the performance of the IOP sensor, whose quality factor was reported to degrade during the *ex/in vivo* implantation due to the high loss tangent of the aqueous humor. The first approach is to mount an implantation tube on the accessing hole on the back side of the sensing part. The new IOP sensor is implanted at the pars plana with the implantation tube penetrating through the choroid, while the sensing part is still left outside the eyeball but covered under the conjunctiva. The sensing coil, therefore, can skip the influence of the aqueous humor by this new approach which is also used by Ahmed Glaucoma valve [70]. The *in vitro* characterization experiment demonstrates its feasibility and the capability of preventing the sensing coil from immersing in the aqueous humor. The other approach is to cover the sensing part with thicker low loss tangent materials such as parylene-C to isolate the sensing coil and the surrounding lossy solution. The benchtop tests prove the concept of using low loss tangent materials to preserve the quality factor of the IOP sensor while submerging in the saline solution. Among all the tested low loss materials, the experiments using parylene-C film as the passivation layer shows that the quality factor can be recovered by covering the sensing coil with extra 20  $\mu\text{m}$  parylene-C film, which results in an IOP sensor with 27- $\mu\text{m}$ -thick parylene-C film above the coil metal. The 27- $\mu\text{m}$ -thick parylene-C film can be easily deposited and patterned with the regular surface micromachining techniques. Therefore thickening the IOP sensing coil by depositing thicker parylene-C film during the clean room fabrication is a practical and feasible concept to enhance the electromagnetic coupling between the sensing coil and the external reader to enable the telemetric IOP sensing.

Several important parylene-C properties related to the development of GDD and IOP sensor are measured and demonstrated in chapter 5. Those properties include: polymer properties such as densification, glass transition temperature measurement, and crystallization; thermal properties such as oxidation; and mechanical properties such as Young's modulus, tensile strength, yield point, percentage of elongation, creep, stress relaxation, and viscoplasticity properties, etc. As parylene-C has been widely used in bioMEMS development, those properties mentioned above become very important in developing the bioMEMS devices, especially the implantable ones. Wrongful using of the parylene-C can lead to cracking of the device, short lifetime, or even unpredictable malfunctions.

As for densification, parylene-C starts to shrink when the surrounding temperature gets higher than  $\sim 50^{\circ}\text{C}$ , implying the occurrence of the crystallization and also the  $T_g$  of  $\sim 50^{\circ}\text{C}$ .

When annealed at  $100^{\circ}\text{C}$ , oxidation of parylene-C is not observable by FTIR, implying that very little oxidation happens during the annealing at  $100^{\circ}\text{C}$ . Therefore, soft baking of parylene-C film in the convection oven during the lithography process should not seriously deteriorate the parylene-C within couple of hours. For high temperature annealing, vacuum system is suggested to preserve the parylene-C properties.

The XRD scanning results show that the parylene-C crystallizes rapidly once the temperature goes beyond  $T_g$ . The crystallinity and the crystallite size increase as the annealing temperature increase and the annealing time gets longer. The time constant of parylene-C crystallization at  $100^{\circ}\text{C}$  is found as 0.845 min.

The glass transition temperature highly depends on the pre-annealing temperature of the tested parylene-C samples.  $T_g$  of as-deposited parylene-C is found in between 50.2-57°C, while  $T_g$  of pre-annealed parylene-C samples changes depending on the pre-annealing temperatures. It is assumed that the crystallization during the parylene-C annealing could be the major effect causing the  $T_g$  shifting.

As different annealing condition corresponds to different crystallinity of parylene-C films, uniaxial tensile test are performed onto differently pre-annealed parylene-C samples to study the relationship between the crystallinity and its mechanical properties change. It shows that parylene-C with higher crystallinity behaves stiffer, stronger and more brittle than as-deposited parylene-C film.

The creep and stress relaxation behavior are significantly influenced by the glass transition temperature. For the creep and stress relaxation tested at the temperature lower than  $T_g$ , the parylene-C behaves similar to elastic material. On the other hand, parylene-C behaves like viscoelastic material when tested at a temperature higher than  $T_g$ . Therefore, in order to have more stable mechanical properties at its operating temperature, the parylene-C properties can (and have to) be tailored to a proper  $T_g$  by pre-annealing the parylene-C at the appropriate temperature. In addition, the stress relaxation results of parylene-C provide very important information for people to predict the lifetime of the slanted tether parylene-C NC check-valves.

The preliminary viscoplastic results of parylene-C tested at 37°C concludes that parylene-C is a viscoplastic material when operated in human body temperature. That is, the parylene-C's mechanical properties might not be the same as the as-deposited parylene-C that people have studied and reported in the past. Therefore, more detail

researches need to be done to understand parylene-C's properties at 37°C so that a more reliable and safer parylene-C-based implant can be developed and implanted in the human bodies.

## BIBLIOGRAPHY

- [1] I. S. Solomon. (2012, Jan. 13). *Aqueous Humor Dynamics* [Online]. Available: <http://www.nyee.edu/pdf/solomonaqhumor.pdf>
- [2] C. R. Neagu, "A Medical Microactuator based on an Electrochemical Principle," Ph.D. dissertation, MESA Research Institute, Univ. of Twente, Enschede, The Netherlands, 1998.
- [3] M. Yanoff, J. S. Duker, and J. J. Augsburger, *Ophthalmology*, 2nd ed. St. Louis, MO: Mosby, 2004.
- [4] H. A. Quigley, "Number of people with glaucoma worldwide," *British Journal of Ophthalmology*, vol. 80, no. 5, pp. 389–393, May 1996.
- [5] National Glaucoma Research. (2012, Jan. 15). [Online]. Available: <http://www.ahaf.org/glaucoma/about/>
- [6] Glaucoma Research Foundation. (2012, Jan. 12). [Online]. Available: <http://www.glaucoma.org/>
- [7] eHow. (2012, Jan. 13). *What Are the Treatments for Refractory Glaucoma?* [Online]. Available: [http://www.ehow.com/facts\\_5632872\\_treatments-refractory-glaucoma\\_.html](http://www.ehow.com/facts_5632872_treatments-refractory-glaucoma_.html)
- [8] Wikipedia. (2012, Jan. 13). *Timolol* [Online]. Available: <http://en.wikipedia.org/wiki/Timolol>
- [9] Wikipedia. (2012, Jan. 13). *Travoprost* [Online]. Available: <http://en.wikipedia.org/wiki/Travoprost>

- [10] Wikipedia. (2012, Jan. 13). *Latanoprost* [Online]. Available: <http://en.wikipedia.org/wiki/Latanoprost>
- [11] Drugs.com. (2012, Jan. 13). *Pilocarpine* [Online]. Available: <http://www.drugs.com/pro/pilocarpine.html>
- [12] K. S. Lim, B. D. S. Allan, A. W. Lloyd, A. Muir, and P. T. Khaw, "Glaucoma drainage devices; past, present, and future," *British Journal of Ophthalmology*, vol. 82, no. 9, pp. 1083–1089, Sep 1998.
- [13] Eyewiki. (2012, Jan. 13). *Trabeculectomy* [Online]. Available: <http://eyewiki.aao.org/Trabeculectomy>
- [14] Wikipedia. (2012, Jan. 13). *Glaucoma valve* [Online]. Available: [http://en.wikipedia.org/wiki/Glaucoma\\_valve](http://en.wikipedia.org/wiki/Glaucoma_valve)
- [15] B. Bae, N. Kim, H. Kee, S. Kim, Y. Lee, and K. Park, "Design and analysis of an electromagnetically driven valve for a glaucoma implant," in *Proc. of the IEEE International Conference on Robotics and Automation*, Seoul, Korea, 2001, pp. 145–150.
- [16] B. Bae, N. Kim, H. Kee, S. H. Kim, Y. Lee, S. Lee, and K. Park, "Feasibility test of an electromagnetically driven valve actuator for glaucoma treatment," *Journal of Microelectromechanical Systems*, vol. 11, no. 4, pp. 344–354, Aug 2002.
- [17] B. Bae, K. Park, and M. A. Shannon, "MEMS Application of Actuators and Sensors for Glaucoma Treatment," in *MEMS/NEMS Handbook*, C. T. Leondes, Ed., New York, NY: Springer US, 2006, pp. 1386–1428.
- [18] B. H. Bae, H. S. Kee, S. H. Kim, Y. Lee, T. S. Sim, Y. W. Kim, and K. H. Park, "In vitro experiment of the pressure regulating valve for a glaucoma implant,"

*Journal of Micromechanics and Microengineering*, vol. 13, no. 5, pp. 613–619, Sep 2003.

- [19] C. H. Hong, A. Arosemena, D. Zurakowski, and R. S. Ayyala, "Glaucoma drainage devices: A systematic literature review and current controversies," *Survey of Ophthalmology*, vol. 50, no. 1, pp. 48–60, Jan–Feb 2005.
- [20] R. S. Ayyala, J. L. Duarte, and N. Sahiner, "Glaucoma drainage devices: state of the art," *Expert Review of Medical Devices*, vol. 3, no. 4, pp. 509–521, Jul 2006.
- [21] A. Zorab, "The reduction of tension in chronic glaucoma," *Ophthalmoscope*, vol. 10, pp. 258–261, 1912.
- [22] J. Stefansson, "An operation for glaucoma," *Am J Ophthalmol*, vol. 8, pp. 681–693, 1925.
- [23] M. U. Troncoso, "Use of Tantalum Implants for Inducing a Permanent Hypotony in Rabbits' Eyes," *American Journal of Ophthalmology*, vol. 32, no. 4, pp. 499–508, 1949.
- [24] R. H. Bock, "Subconjunctival Drainage of the Anterior Chamber by a Glass Seton," *American Journal of Ophthalmology*, vol. 33, no. 6, pp. 929–933, 1950.
- [25] W. E. Muldoon, P. H. Ripple, and H. C. Wilder, "Platinum Implant in Glaucoma Surgery," *AMA Archives of Ophthalmology*, vol. 45, no. 6, pp. 666–672, 1951.
- [26] E. Epstein, "Fibrosing Response to Aqueous. Its Relation to Glaucoma," *Br J Ophthalmol.*, vol. 43, pp. 641–647, 1959.
- [27] A. C. B. Molteno, "New Implant for Drainage in Glaucoma—Animal Trial," *British Journal of Ophthalmology*, vol. 53, no. 3, pp. 161–168, 1969.

- [28] A. C. B. Molteno, "New Implant for Drainage in Glaucoma—Clinical Trial," *British Journal of Ophthalmology*, vol. 53, no. 9, pp. 606–615, 1969.
- [29] A. C. B. Molteno, J. L. Straughan, and E. Ancker, "Long Tube Implants in Management of Glaucoma," *South African Medical Journal*, vol. 50, no. 27, pp. 1062–1066, 1976.
- [30] T. Krupin, S. M. Podos, B. Becker, and J. B. Newkirk, "Valve Implants in Filtering Surgery," *American Journal of Ophthalmology*, vol. 81, no. 2, pp. 232–235, 1976.
- [31] R. S. Ayyala, D. Zurakowski, J. A. Smith, R. Monshizadeh, P. A. Netland, D. W. Richards, and W. E. Layden, "A clinical study of the Ahmed glaucoma valve implant in advanced glaucoma," *Ophthalmology*, vol. 105, no. 10, pp. 1968–1976, Oct 1998.
- [32] A. L. Coleman, R. Hill, M. R. Wilson, N. Choplin, R. Kotasneumann, M. Tam, J. Bacharach, and W. C. Panek, "Initial Clinical Experience with the Ahmed Glaucoma Valve Implant," *American Journal of Ophthalmology*, vol. 120, no. 1, pp. 23–31, Jul 1995.
- [33] M. C. Huang, P. A. Netland, A. L. Coleman, S. W. Siegner, M. R. Moster, and R. A. Hill, "Intermediate-term clinical experience with the Ahmed Glaucoma Valve implant," *American Journal of Ophthalmology*, vol. 127, no. 1, pp. 27–33, Jan 1999.
- [34] F. Topouzis, A. L. Coleman, N. Choplin, M. M. Bethlem, R. Hill, F. Yu, W. C. Panek, and M. R. Wilson, "Follow-up of the original cohort with the Ahmed

- glaucoma valve implant," *American Journal of Ophthalmology*, vol. 128, no. 2, pp. 198–204, Aug 1999.
- [35] M. T. Britt, L. D. LaBree, M. A. Lloyd, D. S. Minckler, D. K. Heuer, G. Baerveldt, and R. Varma, "Randomized clinical trial of the 350-mm(2) versus the 500-mm(2) Baerveldt implant: Longer term results—Is bigger better?," *Ophthalmology*, vol. 106, no. 12, pp. 2312–2318, Dec 1999.
- [36] D. K. Heuer, M. A. Lloyd, D. A. Abrams, G. Baerveldt, D. S. Minckler, M. B. Lee, and J. F. Martone, "Which Is Better? One or two? A Randomized Clinical Trial of Single-Plate Versus Double-Plate Molteno Implantation for Glaucomas in Aphakia and Pseudophakia," *Ophthalmology*, vol. 99, no. 10, pp. 1512–1519, Oct 1992.
- [37] D. S. Minckler, A. Shamma, M. Wilcox, and T. E. Ogden, "Experimental studies of aqueous filtration using the Molteno implant," *Trans Am Ophthalmol Soc.*, vol. 85, pp. 368–392, 1987.
- [38] A. C. B. Molteno, "The optimal design of drainage implants for glaucoma," *Trans Ophthalmol Soc NZ*, vol. 33, pp. 39–41, 1981.
- [39] M. F. Smith, M. B. Sherwood, and S. P. Mcgorray, "Comparison of the Double-Plate Molteno Drainage Implant with the Schocket Procedure," *Archives of Ophthalmology*, vol. 110, no. 9, pp. 1246–1250, Sep 1992.
- [40] M. A. Lloyd, G. Baerveldt, P. S. Fellenbaum, P. A. Sidoti, D. S. Minckler, J. F. Martone, L. Labree, and D. K. Heuer, "Intermediate-Term Results of a Randomized Clinical-Trial of the 350 Versus the 500-Mm(2) Baerveldt Implant," *Ophthalmology*, vol. 101, no. 8, pp. 1456–1463, Aug 1994.

- [41] S. W. Siegner, P. A. Netland, R. C. Urban, A. S. Williams, D. W. Richards, M. A. Latina, and J. D. Brandt, "Clinical Experience with the Baerveldt Glaucoma Drainage Implant," *Ophthalmology*, vol. 102, no. 9, pp. 1298–1307, Sep 1995.
- [42] S. L. Smith, R. J. Starita, R. L. Fellman, and J. R. Lynn, "Early Clinical-Experience with the Baerveldt 350-Mm(2) Glaucoma Implant and Associated Extraocular-Muscle Imbalance," *Ophthalmology*, vol. 100, no. 6, pp. 914–918, Jun 1993.
- [43] M. Rollett and M. Moreau, "Le drainage au crin de la chambre anterieure contre l'hypertonie et la douleur," *Rev Gen Ophthalmol*, vol. 26, pp. 289–292, 1907.
- [44] H. Row, "Operation to control glaucoma—Preliminary report," *Archives of Ophthalmology*, vol. 12, no. 3, pp. 325–329, Sep 1934.
- [45] M. U. Troncoso, "Cyclodialysis with insertion of a metal implant in the treatment of glaucoma—A preliminary report," *Archives of Ophthalmology*, vol. 23, no. 2, pp. 270–297, Feb 1940.
- [46] G. G. Gibson, "Transscleral Lacrimal Canaliculus Transplants," *Trans Am Ophthalmol Soc*, vol. 40, pp. 499–515, 1942.
- [47] M. W. Bick, "Use of Tantalum for Ocular Drainage," *Archives of Ophthalmology*, vol. 42, no. 4, pp. 373–388, 1949.
- [48] W. Losche, "Vorschlage zur Verbesserung der Zyklodialyse," *Klin Monatsbl Augenheilkd*, vol. 121, pp. 715–716, 1952.
- [49] G. B. Bietti, "The present state of the use of plastics in eye surgery," *Acta Ophthalmol*, vol. 33, pp. 337–370, 1955.
- [50] V. La Rocca, *Int Cong Ophthalmol (Brussels)*, 1958.

- [51] R. A. Ellis, "Reduction of Intraocular Pressure Using Plastics in Surgery," *American Journal of Ophthalmology*, vol. 50, no. 5, pp. 733–743, 1960.
- [52] N. T. Mascati, "A new surgical approach for the control of a class of glaucomas," *Int Surg*, vol. 47, pp. 10–15, 1967.
- [53] P. F. Lee and W. T. Wong, "Aqueous-Venous Shunt for Glaucoma - Report on 15 Cases," *Annals of Ophthalmology*, vol. 6, no. 10, pp. 1083–1088, 1974.
- [54] F. M. Honrubia, M. P. Grijalbo, M. L. Gomez, and A. Lopez, "Surgical-Treatment of Neovascular Glaucoma," *Transactions of the Ophthalmological Societies of the United Kingdom*, vol. 99, pp. 89–91, 1979.
- [55] S. S. Schocket, V. Lakhanpal, and R. D. Richards, "Anterior-Chamber Tube Shunt to an Encircling Band in the Treatment of Neovascular Glaucoma," *Ophthalmology*, vol. 89, no. 10, pp. 1188–1194, 1982.
- [56] T. C. White, "A new implantable ocular pressure relief device. A preliminary report," *Glaucoma*, vol. 7, pp. 289–294, 1985.
- [57] N. H. Joseph, M. B. Sherwood, G. Trantas, R. A. Hitchings, and L. Lattimer, "A One-Piece Drainage System for Glaucoma Surgery," *Transactions of the Ophthalmological Societies of the United Kingdom*, vol. 105, pp. 657–664, 1986.
- [58] P. S. Fellenbaum, A. R. Almeida, D. S. Minckler, P. A. Sidoti, G. Baerveldt, and D. K. Heuer, "Krupin Disk Implantation for Complicated Glaucomas," *Ophthalmology*, vol. 101, no. 7, pp. 1178–1182, Jul 1994.
- [59] M. A. Lloyd, G. Baerveldt, D. K. Heuer, J. F. Martone, D. S. Minckler, J. L. Zhao, and Q. H. Nguyen, "The Baerveldt Glaucoma Implant—Long-Term

- Histologic Studies in Rabbits and Clinical Experience in Humans," *Investigative Ophthalmology & Visual Science*, vol. 32, no. 4, pp. 746–746, Mar 15 1991.
- [60] D. D. Kim and J. E. Memmen, "Spontaneous disengagement of the Optimed implant," *Archives of Ophthalmology*, vol. 114, no. 11, pp. 1420–1421, Nov 1996.
- [61] S. G. Smith and J. C. Galanis, "One-Year Results of the Intrasclear Glaucoma Implant," *Journal of Cataract and Refractive Surgery*, vol. 21, no. 4, pp. 453–456, Jul 1995.
- [62] A. D. Pandya, C. Rich, D. E. Eifrig, J. Hanker, and R. L. Peiffer, "Experimental evaluation of a hydroxylapatite reservoir tube shunt in rabbits," *Ophthalmic Surgery and Lasers*, vol. 27, no. 4, pp. 308–314, Apr 1996.
- [63] Y. Glovinsky and M. Belkin, "Evaluation of the "G-plant" glaucoma shunt in rabbit eyes," *Investigative Ophthalmology & Visual Science*, vol. 38, no. 4, pp. 38–53, Mar 15 1997.
- [64] P. Helies, M. Savoldelli, J. M. Legeais, J. M. Parel, and G. J. Renard, "Artificial meshwork (MESH). Clinical and histological study in the rabbit with a six months follow up.," *Investigative Ophthalmology & Visual Science*, vol. 38, no. 4, p. 1246, Mar 15 1997.
- [65] F. M. White, *Fluid mechanics*, 3rd ed. New York: McGraw-Hill, 1994.
- [66] J. A. Beswick and C. McCulloch, "Effect of Hyaluronidase on the Viscosity of the Aqueous Humour," *Br J Ophthalmol.*, vol. 40, pp. 545–548, 1956.
- [67] M. Johnson, C. R. Ethier, R. D. Kamm, W. M. Grant, D. L. Epstein, and D. Gaasterland, "The Flow of Aqueous-Humor through Microporous Filters,"

- Investigative Ophthalmology & Visual Science*, vol. 27, no. 1, pp. 92–97, Jan 1986.
- [68] R. S. Ayyala, D. Zurakowski, R. Monshizadeh, C. H. Hong, D. Richards, W. E. Layden, B. T. Hutchinson, and A. R. Bellows, "Comparison of double-plate Molteno and Ahmed glaucoma valve in patients with advanced uncontrolled glaucoma," *Ophthalmic Surgery and Lasers*, vol. 33, no. 2, pp. 94–101, Mar–Apr 2002.
- [69] D. C. Broadway, M. Iester, M. Schulzer, and G. R. Douglas, "Survival analysis for success of Molteno tube implants," *British Journal of Ophthalmology*, vol. 85, no. 6, pp. 689–695, Jun 2001.
- [70] *Ahmed Glaucoma Valve* [Online]. Available: <http://www.ahmedvalve.com/>
- [71] Abbott Medical Optics. (2012, Jan. 13). *Baerveldt Glaucoma Implant Package Insert* [Online]. Available: [http://www.amo-inc.com/pdf/Baerveldt\\_packageinsert.pdf](http://www.amo-inc.com/pdf/Baerveldt_packageinsert.pdf)
- [72] IOP Ophthalmics, Inc. (2012, Jan. 14). [Online]. Available: <http://www.iopinc.com/store/molteno/>
- [73] L. Cantor, J. Burgoyne, S. Sanders, V. Bhavnani, J. Hoop, and E. Brizendine, "The effect of mitomycin C on molteno implant surgery: A 1-year randomized, masked, prospective study," *Journal of Glaucoma*, vol. 7, no. 4, pp. 240–246, Aug 1998.
- [74] P. A. Sidoti, A. Y. Mosny, D. C. Ritterband, and J. A. Seedor, "Pars plana tube insertion of glaucoma drainage implants and penetrating keratoplasty in patients

- with coexisting glaucoma and corneal disease," *Ophthalmology*, vol. 108, no. 6, pp. 1050–1058, Jun 2001.
- [75] Q. H. Nguyen, D. L. Budenz, and R. K. Parrish, "Complications of Baerveldt glaucoma drainage implants," *Archives of Ophthalmology*, vol. 116, no. 5, pp. 571–575, May 1998.
- [76] S. Shoji, "Fluids for sensor systems," *Microsystem Technology in Chemistry and Life Science*, vol. 194, pp. 163–188, 1998.
- [77] A. van den Berg and T. S. J. Lammerink, "Micro total analysis systems: Microfluidic aspects, integration concept and applications," *Microsystem Technology in Chemistry and Life Science*, vol. 194, pp. 21–49, 1998.
- [78] D. Cline, H. W. Hofstetter, and J. R. Griffin, *Dictionary of visual science*, 4th ed. Boston: Butterworth-Heinemann, 1997.
- [79] H. Cao, "Pressure Sensors," in *Minimally Invasive Medical Technology*: Taylor & Francis, 2001, pp. 33–45.
- [80] N. Ducrey, J. Geinoz, and R. Faggioni, "Non-Contact Applanation Tonometry," *Ophthalmologica*, vol. 170, no. 5, pp. 446–449, 1975.
- [81] C. R. Ethier, M. Johnson, and J. Ruberti, "Ocular biomechanics and biotransport," *Annual Review of Biomedical Engineering*, vol. 6, pp. 249–273, 2004.
- [82] I. G. Pallikaris, G. D. Kymionis, H. S. Ginis, G. A. Kounis, and M. K. Tsilimbaris, "Ocular rigidity in living human eyes," *Investigative Ophthalmology & Visual Science*, vol. 46, no. 2, pp. 409–414, Feb 2005.
- [83] P. A. Tonnu, T. Ho, T. Newson, A. El Sheikh, K. Sharma, E. White, C. Bunce, and D. Garway-Heath, "The influence of central corneal thickness and age on

- intraocular pressure measured by pneumotonometry, noncontact tonometry, the Tono-Pen XL, and Goldmann applanation tonometry," *British Journal of Ophthalmology*, vol. 89, no. 7, pp. 851–854, Jul 2005.
- [84] S. Asrani, R. Zeimer, J. Wilensky, D. Gieser, S. Vitale, and K. Lindenmuth, "Large diurnal fluctuations in intraocular pressure are an independent risk factor in patients with glaucoma," *Journal of Glaucoma*, vol. 9, no. 2, pp. 134–142, Apr 2000.
- [85] E. Hughes, P. Spry, and J. Diamond, "24-hour monitoring of intraocular pressure in glaucoma management: A retrospective review," *Journal of Glaucoma*, vol. 12, no. 3, pp. 232–236, Jun 2003.
- [86] R. Puers, G. Vandevoorde, and D. De Bruyker, "Electrodeposited copper inductors for intraocular pressure telemetry," *Journal of Micromechanics and Microengineering*, vol. 10, no. 2, pp. 124–129, Jun 2000.
- [87] K. C. Katuri, S. Asrani, and M. K. Ramasubramanian, "Intraocular pressure monitoring sensors," *IEEE Sensors Journal*, vol. 8, no. ro1–2, pp. 12–19, Jan–Feb 2008.
- [88] J. W. McLaren, R. F. Brubaker, and J. S. FitzSimon, "Continuous measurement of intraocular pressure in rabbits by telemetry," *Investigative Ophthalmology & Visual Science*, vol. 37, no. 6, pp. 966–975, May 1996.
- [89] W. Mokwa and U. Schnakenberg, "Micro-transponder systems for medical applications," *IEEE Transactions on Instrumentation and Measurement*, vol. 50, no. 6, pp. 1551–1555, Dec 2001.

- [90] Sajeeda and T. J. Kaiser, "Passive telemetric readout system," *IEEE Sensors Journal*, vol. 6, no. 5, pp. 1340–1345, Oct 2006.
- [91] C. C. Collins, "Miniature Passive Pressure Transensor for Implanting in Eye," *IEEE Transactions on Biomedical Engineering*, vol. BME-14, no. 2, pp. 74–83, 1967.
- [92] O. Akar, T. Akin, and K. Najafi, "A wireless batch sealed absolute capacitive pressure sensor," *Sensors and Actuators A: Physical*, vol. 95, no. 1, pp. 29–38, Dec 15 2001.
- [93] A. Baldi, W. Choi, and B. Ziaie, "A self-resonant frequency-modulated micromachined passive pressure transensor," *IEEE Sensors Journal*, vol. 3, no. 6, pp. 728–733, Dec 2003.
- [94] A. DeHennis and K. D. Wise, "A double-sided single-chip wireless pressure sensor," in *Proc. of the 15th IEEE International Conference on Micro Electro Mechanical Systems*, Las Vegas, NV, 2002, pp. 252–255.
- [95] M. A. Fonseca, M. G. Allen, J. Kroh, and J. White, "Flexible wireless passive pressure sensors for biomedical applications," in *Technical Digest of the 12th IEEE Solid-State Sensors, Actuators, and Microsystems Workshop*, Hilton Head Island, SC, 2006, pp. 37–42.
- [96] L. Rosengren, P. Rangsten, Y. Backlund, B. Hok, B. Svedbergh, and G. Selen, "A System for Passive Implantable Pressure Sensors," *Sensors and Actuators A: Physical*, vol. 43, no. 1–3, pp. 55–58, May 1994.

- [97] P.-J. Chen, "Implantable Wireless Intraocular Pressure Sensors," Ph.D. dissertation, Electrical Engineering, California Institute of Technology, Pasadena, CA, 2008.
- [98] P.-J. Chen, S. Saati, R. Varma, M. S. Humayun, and Y. C. Tai, "Wireless Intraocular Pressure Sensing Using Microfabricated Minimally Invasive Flexible-Coiled LC Sensor Implant," *Journal of Microelectromechanical Systems*, vol. 19, no. 4, pp. 721–734, Aug. 2010.
- [99] Parylene Engineering. (2012, Jan. 13). *Why Parylene* [Online]. Available: [http://www.paryleneengineering.com/why\\_use\\_parylene.html](http://www.paryleneengineering.com/why_use_parylene.html)
- [100] Specialty Coating Systems. (2012, Jan. 13). *SCS Parylene Properties* [Online]. Available: <http://www.scscoatings.com/index.aspx>
- [101] W. F. Beach, "Parylene Coatings," in *Electronic materials handbook: Packaging* Materials Park, OH: ASM International, 1989, pp. 789–801.
- [102] W. F. Beach, "Xylylene Polymers," in *Encyclopedia of Polymer Science and Technology*: John Wiley & Sons, Inc., 2002.
- [103] C. Y. Shih, T. A. Harder, and Y. C. Tai, "Yield strength of thin-film parylene-C," *Microsystem Technologies—Micro- and Nanosystems Information Storage and Processing Systems* vol. 10, no. 5, pp. 407–411, Aug 2004.
- [104] C. Hassler, R. P. von Metzen, P. Ruther, and T. Stieglitz, "Characterization of parylene C as an encapsulation material for implanted neural prostheses," *Journal of Biomedical Materials Research Part B—Applied Biomaterials*, vol. 93B, no. 1, pp. 266–274, Apr 2010.

- [105] M. Koch, A. Evans, and A. Brunnschweiler, *Microfluidic technology and applications*. Philadelphia, PA: Research Studies Press, 2000.
- [106] X. Q. Wang, Q. Lin, and Y. C. Tai, "A Parylene micro check valve," in *Proc. of the 12th IEEE International Conference on Micro Electro Mechanical Systems*, Orlando, FL, 1999, pp. 177–182.
- [107] X.-Q. Wang and Y.-C. Tai, "A normally closed in-channel micro check valve," in *Proc. of the IEEE 13th International Conference on Micro Electro Mechanical Systems (MEMS)*, Miyazaki, Japan, 2000, pp. 68–73.
- [108] J. Xie, X. Yang, X. Q. Wang, and Y. C. Tai, "Surface micromachined leakage proof parylene check valve," in *Technical Digest of the 14th IEEE International Conference on Micro Electro Mechanical Systems*, Interlaken, Switzerland, 2001, pp. 539–542.
- [109] R. A. Habing, "Flow and Plate Motion in Compressor Valves," Ph.D. dissertation, Univ. of Twente, Enschede, The Netherlands, 2005.
- [110] S. Dabral, J. Vanetten, X. Zhang, C. Apblett, G. R. Yang, P. Ficalora, and J. F. McDonald, "Stress in Thermally Annealed Parylene Films," *Journal of Electronic Materials*, vol. 21, no. 10, pp. 989–994, Oct 1992.
- [111] M. LeCompte, X. Gao, and D. W. Prather, "Photoresist characterization and linearization procedure for the gray-scale fabrication of diffractive optical elements," *Applied Optics*, vol. 40, no. 32, pp. 5921–5927, Nov 10 2001.
- [112] L. A. Mosher, C. M. Waits, B. Morgan, and R. Ghodssi, "A new paradigm for high resolution 3D lithography," in *Proc. of the 21st IEEE International*

- Conference on Micro Electro Mechanical Systems*, Tucson, Arizona, 2008, pp. 395–398.
- [113] Y. Oppliger, P. Sixt, J. M. Stauffer, J. M. Mayor, P. Regnault, and G. Voirin, "One-Step 3d Shaping Using a Gray-Tone Mask for Optical and Microelectronic Applications," *Microelectronic Engineering*, vol. 23, no. 1–4, pp. 449–454, Jan 1994.
- [114] J. Q. Su, J. L. Du, J. Yao, F. H. Gao, Y. K. Guo, and Z. Cui, "A new method to design half-tone mask for the fabrication of continuous micro relief structure," *Proc. SPIE 3680*, pp. 879–886, 1999.
- [115] T. J. Suleski and D. C. O'Shea, "Gray-Scale Masks for Diffractive-Optics Fabrication .1. Commercial Slide Imagers," *Applied Optics*, vol. 34, no. 32, pp. 7507–7517, Nov 10 1995.
- [116] B. Wagner, H. J. Quenzer, W. Henke, W. Hoppe, and W. Pilz, "Microfabrication of Complex Surface Topographies Using Grey-Tone Lithography," *Sensors and Actuators A: Physical*, vol. 46, no. 1–3, pp. 89–94, Jan–Feb 1995.
- [117] C. M. Waits, A. Modafe, and R. Ghodssi, "Investigation of gray-scale technology for large area 3D silicon MEMS structures," *Journal of Micromechanics and Microengineering*, vol. 13, no. 2, pp. 170–177, Mar 2003.
- [118] H. A. Zhang, S. Wang, and Y. Xu, "Study and applications of a parylene self-sealing structure," *MEMS 2006: 19th IEEE International Conference on Micro Electro Mechanical Systems, Technical Digest*, pp. 282–285, 2006.

- [119] C. H. Mastrangelo and C. H. Hsu, "Mechanical stability and adhesion of microstructures under capillary forces. I. Basic theory," *Journal of Microelectromechanical Systems*, vol. 2, no. 1, pp. 33–43, 1993.
- [120] C. H. Mastrangelo and C. H. Hsu, "Mechanical stability and adhesion of microstructures under capillary forces. II. Experiments," *Journal of Microelectromechanical Systems*, vol. 2, no. 1, pp. 44–55, 1993.
- [121] N. Tas, T. Sonnenberg, H. Jansen, R. Legtenberg, and M. Elwenspoek, "Stiction in surface micromachining," *Journal of Micromechanics and Microengineering*, vol. 6, no. 4, pp. 385–397, Dec 1996.
- [122] T. J. Yao, X. Yang, and Y. C. Tai, "BrF<sub>3</sub> dry release technology for large freestanding Parylene MEMS," in *Technical Digest of the 11th International Conference on Solid-State Sensors and Actuators (Transducers '01, Eurosensors XV)*, Munich, Germany, 2001, pp. 652–655.
- [123] T. J. Yao, X. Yang, and Y. C. Tai, "BrF<sub>3</sub> dry release technology for large freestanding parylene microstructures and electrostatic actuators," *Sensors and Actuators A: Physical*, vol. 97–98, pp. 771–775, Apr 1 2002.
- [124] A. Witvrouw, H. A. C. Tilmans, and I. De Wolf, "Materials issues in the processing, the operation and the reliability of MEMS," *Microelectronic Engineering*, vol. 76, no. 1–4, pp. 245–257, Oct 2004.
- [125] J. Han, B. Flachsbart, R. I. Masel, and M. A. Shannon, "Micro-fabricated membrane gas valves with a non-stiction coating deposited by C(4)F(8)/Ar plasma," *Journal of Micromechanics and Microengineering*, vol. 18, no. 9, Sep 2008.

- [126] R. Maboudian, W. R. Ashurst, and C. Carraro, "Self-assembled monolayers as anti-stiction coatings for MEMS: characteristics and recent developments," *Sensors and Actuators A: Physical*, vol. 82, no. 1–3, pp. 219–223, May 15 2000.
- [127] M. Mehregany, M. G. Allen, and S. D. Senturia, "The Use of Micromachined Structures for The Measurement of Mechanical Properties and Adhesion of Thin Films," in *Technical Digest of the 3rd IEEE Solid State Sensors Workshop*, Hilton Head Island, SC, 1986, pp. 58–61.
- [128] B. J. Briscoe and S. S. Panesar, "The Application of the Blister Test to an Elastomeric Adhesive," *Proc. of the Royal Society of London Series A: Mathematical Physical and Engineering Sciences*, vol. 433, no. 1887, pp. 23–43, Apr 8 1991.
- [129] Y. Z. Chu and C. J. Durning, "Application of the Blister Test to the Study of Polymer Polymer Adhesion," *Journal of Applied Polymer Science*, vol. 45, no. 7, pp. 1151–1164, Jul 5 1992.
- [130] A. N. Gent and L. H. Lewandowski, "Blow-Off Pressures for Adhering Layers," *Journal of Applied Polymer Science*, vol. 33, no. 5, pp. 1567–1577, Apr 1987.
- [131] J. A. Hinkley, "A Blister Test for Adhesion of Polymer-Films to SiO<sub>2</sub>," *Journal of Adhesion*, vol. 16, no. 2, pp. 115–125, 1983.
- [132] H. S. Jeong, Y. Z. Chu, C. J. Durning, and R. C. White, "Adhesion Study of Polyimide to Si Surfaces," *Surface and Interface Analysis*, vol. 18, no. 4, pp. 289–292, Apr 1992.
- [133] K. Kendall, "Thin-Film Peeling—Elastic Term," *Journal of Physics D: Applied Physics*, vol. 8, no. 13, pp. 1449–1452, 1975.

- [134] K. T. Wan and Y. W. Mai, "Fracture-Mechanics of a New Blister Test with Stable Crack-Growth," *Acta Metallurgica Et Materialia*, vol. 43, no. 11, pp. 4109–4115, Nov 1995.
- [135] K. T. Wan and Y. W. Mai, "Modified blister tests for evaluation of thin flexible membrane adhesion on rigid substrate," *Materials Science Research International*, vol. 1, no. 2, pp. 78–81, Jun 1995.
- [136] C. Wang, "Measurements of interfacial strength from the blister test," *Journal of Applied Polymer Science*, vol. 73, no. 10, pp. 1899–1912, Sep 6 1999.
- [137] M. G. Allen and S. D. Senturia, "Analysis of Critical Debonding Pressures of Stressed Thin-Films in the Blister Test," *Journal of Adhesion*, vol. 25, no. 4, pp. 303–315, 1988.
- [138] T. A. Harder, T. J. Yao, Q. He, C. Y. Shih, and Y. C. Tai, "Residual stress in thin-film parylene-C," in *Proc. of the 15th IEEE International Conference on Micro Electro Mechanical Systems*, Las Vegas, NV, 2002, pp. 435–438.
- [139] P.-J. Chen, D. C. Rodger, E. M. Meng, M. S. Humayun, and Y. C. Tai, "Surface-micromachined parylene dual valves for on-chip unpowered microflow regulation," *Journal of Microelectromechanical Systems*, vol. 16, no. 2, pp. 223–231, Apr. 2007.
- [140] P.-J. Chen, D. C. Rodger, M. S. Humayun, and Y. C. Tai, "Floating-Disk Parylene Microvalves for Self-Pressure-Regulating Flow Controls," *Journal of Microelectromechanical Systems*, vol. 17, no. 6, pp. 1352–1361, Dec. 2008.
- [141] P.-J. Chen, D. C. Rodger, S. Saati, J. C. Altamirano, C.-H. Lin, R. Agrawal, R. Varma, M. Humayun, and Y. C. Tai, "Implementation of Microfabricated

- Sutureless Flexible Parylene Tissue Anchors on Minimally Invasive Biomedical Implants," in *Proc. of the 11th International Conference on Miniaturized Systems for Chemistry and Life Sciences*, Paris, France, 2007, pp. 518–520.
- [142] K. Dietz, *Dry Film Photoresist Processing Technology* Port Erin, British Isles: Electrochemical Publications Ltd, 2001.
- [143] P. R. Kanikella, "Process Development and Applications of A Dry Film Photoresist," M.S. thesis, Department of Materials Science and Engineering, Univ. of Missouri-Rolla, Rolla, MI, 2007.
- [144] E. Koukharenko, M. Kraft, G. J. Ensell, and N. Hollinshead, "A comparative study of different thick photoresists for MEMS applications," *Journal of Materials Science—Materials in Electronics*, vol. 16, no. 11–12, pp. 741–747, Nov 2005.
- [145] E. Kukhareuka, M. M. Farooqui, L. Grigore, M. Kraft, and N. Hollinshead, "Electroplating moulds using dry film thick negative photoresist," *Journal of Micromechanics and Microengineering*, vol. 13, no. 4, pp. S67–S74, Jul 2003.
- [146] X. C. Shan, Y. F. Jin, H. J. Lu, and C. K. Wong, "Process development of negative tone dry film photoresist for MEMS applications," in *Proc. of the 7th International Conference on Solid-State and Integrated Circuits Technology*, Beijing, China, 2004, pp. 575–578.
- [147] M. O. Heuschkel, L. Guerin, B. Buisson, D. Bertrand, and P. Renaud, "Buried microchannels in photopolymer for delivering of solutions to neurons in a network," *Sensors and Actuators B: Chemical*, vol. 48, no. 1–3, pp. 356–361, May 30 1998.

- [148] K. Stephan, P. Pittet, L. Renaud, P. Kleimann, P. Morin, N. Ouaini, and R. Ferrigno, "Fast prototyping using a dry film photoresist: microfabrication of soft-lithography masters for microfluidic structures," *Journal of Micromechanics and Microengineering*, vol. 17, no. 10, pp. N69–N74, Oct 2007.
- [149] Y. C. Tsai, H. P. Jen, K. W. Lin, and Y. Z. Hsieh, "Fabrication of microfluidic devices using dry film photoresist for microchip capillary electrophoresis," *Journal of Chromatography A*, vol. 1111, no. 2, pp. 267–271, Apr 14 2006.
- [150] P. Vulto, N. Glade, L. Altomare, J. Bablet, L. Del Tin, G. Medoro, I. Chartier, N. Manaresi, M. Tartagni, and R. Guerrieri, "Microfluidic channel fabrication in dry film resist for production and prototyping of hybrid chips," *Lab on a Chip*, vol. 5, no. 2, pp. 158–162, 2005.
- [151] P. Vulto, N. Glade, L. Altomare, J. Bablet, G. Medoro, A. Leonardi, A. Romani, I. Chartier, N. Manaresi, M. Tartagni, and R. Guerrieri, "Dry film resist for fast fluidic prototyping," in *Proc. of the 8th International Conference on Miniatureized Systems for Chemistry and Life Sciences*, Malmö, Sweden, 2005, pp. 43–45.
- [152] T. N. Pornsin-Sirirak, S. W. Lee, H. Nassef, J. Grasmeyer, Y. C. Tai, C. M. Ho, and M. Keennon, "MEMS wing technology for a battery-powered ornithopter," in *Proc. of the IEEE 13th International Conference on Micro Electro Mechanical Systems (MEMS)*, Miyazaki, Japan, 2000, pp. 799–804.
- [153] T. N. Pornsin-sirirak, Y. C. Tai, H. Nassef, and C. M. Ho, "Titanium-alloy MEMS wing technology for a micro aerial vehicle application," *Sensors and Actuators A: Physical*, vol. 89, no. 1–2, pp. 95–103, Mar 20 2001.

- [154] P. Jorge and M. Toepper, "An Assessment of Thick Dry Photoresist for Wafer Bumping," pp. 1–6.
- [155] Lea-Test Ltd. (2012, Jan. 13). *Glaucoma* [Online]. Available: <http://www.lea-test.fi/en/eyes/glaucoma.html>
- [156] R. Sampaolesi, N. Calixto, D. Carvalho, CA, and R. Reça, "Diurnal Variation of Intraocular Pressure in Healthy Suspected and Glaucomatous Eyes," *Bibliotheca Ophthalmologica*, no. 74, pp. 1–23, 1968.
- [157] M. L. Dietsche, J. T. Wilensky, D. K. Gieser, M. T. Mori, and R. Zeimer, "The Individual Nature of Diurnal-Variations in Intraocular-Pressure," *Investigative Ophthalmology & Visual Science*, vol. 32, no. 4, pp. 809–809, Mar. 15 1991.
- [158] J. T. Wilensky, "Diurnal variations in intraocular pressure," *Trans Am Ophthalmol Soc*, vol. 89, pp. 757–90, 1991.
- [159] A. M. Leung, W. H. Ko, T. M. Spear, and J. A. Bettice, "Intracranial-Pressure Telemetry System Using Semicustom Integrated-Circuits," *IEEE Transactions on Biomedical Engineering*, vol. 33, no. 4, pp. 386–395, Apr. 1986.
- [160] M. Leonardi, P. Leuenberger, D. Bertrand, A. Bertsch, and P. Renaud, "First steps toward noninvasive intraocular pressure monitoring with a sensing contact lens," *Investigative Ophthalmology & Visual Science*, vol. 45, no. 9, pp. 3113–3117, Sep. 2004.
- [161] E. Y. Chow, A. L. Chlebowski, and P. P. Irazoqui, "A Miniature-Implantable RF-Wireless Active Glaucoma Intraocular Pressure Monitor," *IEEE Transactions on Biomedical Circuits and Systems*, vol. 4, no. 6, pp. 340–349, Dec. 2010.

- [162] M. A. Fonseca, J. M. English, M. von Arx, and M. G. Allen, "Wireless micromachined ceramic pressure sensor for high-temperature applications," *Journal of Microelectromechanical Systems*, vol. 11, no. 4, pp. 337–343, Aug 2002.
- [163] Y. Backlund, L. Rosengren, B. Hok, and B. Svedbergh, "Passive Silicon Transensor Intended for Biomedical, Remote Pressure Monitoring," *Sensors and Actuators A: Physical*, vol. 21, no. 1–3, pp. 58–61, Feb 1990.
- [164] L. Rosengren, Y. Backlund, T. Sjostrom, B. Hok, and B. Svedbergh, "A system for wireless intra-ocular pressure measurements using a silicon micromachined sensor," *Journal of Micromechanics and Microengineering*, vol. 2, no. 3, p. 202, 1992.
- [165] J. Shih, J. Xie, and Y. C. Tai, "Surface micromachined and integrated capacitive sensors for microfluidic applications," in *Proc. of the the 12th IEEE International Conference on Solid-State Sensors, Actuators and Microsystems (Transducers'03)*, Boston, MA, 2003, pp. 388–391.
- [166] T. H. Lee, *The design of CMOS radio-frequency integrated circuits*, 2nd ed. Cambridge, UK ; New York: Cambridge University Press, 2004.
- [167] S. Timoshenko and S. Woinowsky-Krieger, *Theory of plates and shells*, 2d ed. New York, NY: McGraw-Hill, 1959.
- [168] D. K. Cheng, *Field and wave electromagnetics*. Reading, MA: Addison-Wesley, 1989.
- [169] J. M. Kim, D. H. Oh, J. H. Park, J. W. Cho, Y. W. Kwon, C. Y. Cheon, and Y. K. Kim, "Permittivity measurements up to 30 GHz using micromachined probe,"

*Journal of Micromechanics and Microengineering*, vol. 15, no. 3, pp. 543–550, Mar 2005.

- [170] A. Nyshadham, C. L. Sibbald, and S. S. Stuchly, "Permittivity Measurements Using Open-Ended Sensors and Reference Liquid Calibration—an Uncertainty Analysis," *IEEE Transactions on Microwave Theory and Techniques*, vol. 40, no. 2, pp. 305–314, Feb 1992.
- [171] Microwaves101.com. (2012, Jan. 13). *Miscellaneous dielectric constants* [Online]. Available: <http://www.microwaves101.com/encyclopedia/Miscdielectrics.cfm>
- [172] W. F. Gorham, "A New General Synthetic Method for Preparation of Linear Poly-P-Xylylenes," *Journal of Polymer Science Part A—1: Polymer Chemistry*, vol. 4, no. 12PA, pp. 3027–3039, 1966.
- [173] M. Gazicki, G. Surendran, W. James, and H. Yasuda, "Polymerization of Para-Xylylene Derivatives (Parylene Polymerization) .2. Heat-Effects during Deposition of Parylene-C at Different Temperatures," *Journal of Polymer Science Part A: Polymer Chemistry*, vol. 23, no. 8, pp. 2255–2277, 1985.
- [174] G. Surendran, M. Gazicki, W. J. James, and H. Yasuda, "Polymerization of Para-Xylylene Derivatives .5. Effects of the Sublimation Rate of Di-P-Xylylene on the Crystallinity of Parylene-C Deposited at Different Temperatures," *Journal of Polymer Science Part A: Polymer Chemistry*, vol. 25, no. 8, pp. 2089–2106, Aug 1987.

- [175] M. Gazicki-Lipman, "Vapor Deposition Polymerization of para-Xylylene Derivatives—Mechanism and Applications," *Journal of the Vacuum Society of Japan*, vol. 50, no. 10, pp. 601–608, 2007.
- [176] L. A. Errede, R. S. Gregorian, and J. M. Hoyt, "The Chemistry of Xylylenes .6. The Polymerization of Para-Xylylene," *Journal of the American Chemical Society*, vol. 82, no. 19, pp. 5218–5223, 1960.
- [177] W. F. Beach, "Model for Vapor-Deposition Polymerization of Para-Xylylene," *Macromolecules*, vol. 11, no. 1, pp. 72–76, 1978.
- [178] J. B. Fortin and T. M. Lu, "A model for the chemical vapor deposition of poly(para-xylylene) (parylene) thin films," *Chemistry of Materials*, vol. 14, no. 5, pp. 1945–1949, May 2002.
- [179] J. F. Gaynor, "A heterogeneous model for the chemical vapor polymerization of poly-p-xylylenes," in *Proceedings of the Second International Symposium on Low and High Dielectric Constant Materials—Materials Science, Processing, and Reliability Issues*, Montreal, Quebec, Canada, 1997, pp. 176–185.
- [180] S. Rogojevic, J. A. Moore, and W. N. Gill, "Modeling vapor deposition of low-K polymers: Parylene and polynaphthalene," *Journal of Vacuum Science & Technology A: Vacuum Surfaces and Films*, vol. 17, no. 1, pp. 266–274, Jan–Feb 1999.
- [181] G. R. Yang, S. Ganguli, J. Karcz, W. N. Gill, and T. M. Lu, "High deposition rate parylene films," *Journal of Crystal Growth*, vol. 183, no. 3, pp. 385–390, Jan 1998.

- [182] P. K. Wu, G. R. Yang, J. F. McDonald, and T. M. Lu, "Surface-Reaction and Stability of Parylene-N and Parylene-F Thin-Films at Elevated-Temperatures," *Journal of Electronic Materials*, vol. 24, no. 1, pp. 53–58, Jan 1995.
- [183] H. L. Huang, Y. G. Xu, and H. Y. Low, "Effects of film thickness on moisture sorption, glass transition temperature and morphology of poly(chloro-p-xylylene) film," *Polymer*, vol. 46, no. 16, pp. 5949–5955, Jul 25 2005.
- [184] J. J. Senkevich and S. B. Desu, "Morphology of poly(chloro-p-xylylene) CVD thin films," *Polymer*, vol. 40, no. 21, pp. 5751–5759, Oct 1999.
- [185] G. W. Ehrenstein and R. P. Theriault, *Polymeric materials: structure, properties, applications*. Munich; Cincinnati, OH: Hanser ; Hanser Gardner Publications, 2001.
- [186] W. D. Niegisch, "Molecular Orientation in Poly-P-Xylylene Films," *Journal of Applied Physics*, vol. 38, no. 11, pp. 4110–4117, 1967.
- [187] D. W. Grattan and M. Bilz, "The Thermal Aging of Parylene and the Effect of Antioxidant," *Studies in Conservation*, vol. 36, no. 1, pp. 44–52, 1991.
- [188] D. J. Monk, H. S. Toh, and J. Wertz, "Oxidative degradation of parylene C (poly(monochloro-para-xylylene)) thin films on bulk micromachined piezoresistive silicon pressure sensors," *Sensors and Materials*, vol. 9, no. 5, pp. 307–319, 1997.
- [189] T. E. Nowlin, D. Foss smith Jr., and G. S. Cieloszyk, "Thermal Oxidative Stability of Poly-P-Xylylenes," *Journal of Polymer Science Part A: Polymer Chemistry*, vol. 18, no. 7, pp. 2103–2119, 1980.

- [190] M. Bera, A. Rivaton, C. Gandon, and J. L. Gardette, "Photooxidation of poly(para-xylylene)," *European Polymer Journal*, vol. 36, no. 9, pp. 1753–1764, Sep 2000.
- [191] M. Kochi, K. Oguro, and I. Mita, "Photoluminescence of Solid Aromatic Polymers .1. Poly(P-Xylylene)," *European Polymer Journal*, vol. 24, no. 10, pp. 917–921, 1988.
- [192] B. Lu, S. Y. Zheng, B. Q. Quach, and Y. C. Tai, "A study of the autofluorescence of parylene materials for  $\mu$ TAS applications," *Lab on a Chip*, vol. 10, no. 14, pp. 1826–1834, 2010.
- [193] K. G. Pruden and S. P. Beaudoin, "Model for the photooxidation of parylenes," *Journal of Polymer Science Part A: Polymer Chemistry*, vol. 42, no. 11, pp. 2666–2677, Jun 1 2004.
- [194] K. G. Pruden, K. Sinclair, and S. Beaudoin, "Characterization of parylene-N and parylene-C photooxidation," *Journal of Polymer Science Part A: Polymer Chemistry*, vol. 41, no. 10, pp. 1486–1496, May 15 2003.
- [195] T. E. Baker, S. L. Bagdasarian, G. L. Fix, and J. S. Judge, "Characterization of Vapor-Deposited Paraxylylene Coatings," *Journal of the Electrochemical Society*, vol. 124, no. 6, pp. 897–900, 1977.
- [196] ALS Infrared Beamlines. (2012, Jan. 13). *Characteristic IR Band Positions* [Online]. Available: <http://infrared.als.lbl.gov/content/web-links/60-ir-band-positions>
- [197] Y. Long, R. A. Shanks, and Z. H. Stachurski, "Kinetics of Polymer Crystallization," *Progress in Polymer Science*, vol. 20, no. 4, pp. 651–701, 1995.

- [198] R. Iwamoto, R. C. Bopp, and B. Wunderlich, "Crystallization during Polymerization of Poly-P-Xylylene .3. Crystal-Structure and Molecular-Orientation as a Function of Temperature," *Journal of Polymer Science Part B: Polymer Physics*, vol. 13, no. 10, pp. 1925–1938, 1975.
- [199] S. Kubo and B. Wunderlich, "Crystallization during Polymerization of Poly-P-Xylylene," *Journal of Polymer Science Part B: Polymer Physics*, vol. 10, no. 10, pp. 1949–1966, 1972.
- [200] L. You, G. R. Yang, D. B. Knorr, J. F. McDonald, and T. M. Lu, "Texture of Vapor-Deposited Parylene Thin-Films," *Applied Physics Letters*, vol. 64, no. 21, pp. 2812–2814, May 23 1994.
- [201] J. M. Hsu, L. Rieth, S. Kammer, M. Orthner, and F. Solzbacher, "Effect of thermal and deposition processes on surface morphology, crystallinity, and adhesion of Parylene-C," *Sensors and Materials*, vol. 20, no. 2, pp. 87–102, 2008.
- [202] L. Mandelkern, *Crystallization of polymers*, 2nd ed. Cambridge, UK ; New York: Cambridge University Press, 2002.
- [203] G. Treiber, K. Boehlke, A. Weitz, and B. Wunderlich, "Crystallization during Polymerization of Poly-Para-Xylylene .2. Polymerization at Low-Temperature," *Journal of Polymer Science Part B: Polymer Physics*, vol. 11, no. 6, pp. 1111–1116, 1973.
- [204] B. Wunderlich, "Crystallization during Polymerization," *Angewandte Chemie—International Edition*, vol. 7, no. 12, pp. 912–919, 1968.
- [205] C. J. Brown, "Lin-Poly-Para-Xylylene .2. The Crystal Structure of Di-P-Xylylene," *Journal of the Chemical Society*, pp. 3265–3270, 1953.

- [206] C. J. Brown and A. C. Farthing, "Lin-Poly-Para-Xylylene .3. Preparation by the Wurtz Reaction, and Investigation of Structure," *Journal of the Chemical Society*, pp. 3270–3278, 1953.
- [207] W. D. Niegisch, "Crystallography of Poly-P-Xylylene," *Journal of Applied Physics*, vol. 37, no. 11, pp. 4041–4046, 1966.
- [208] R. Iwamoto and B. Wunderlich, "Crystal-Structure of Poly-P-Xylylene .1. Alpha Form," *Journal of Polymer Science Part B: Polymer Physics*, vol. 11, no. 12, pp. 2403–2411, 1973.
- [209] N. S. Murthy and H. G. Kim, "Molecular Packing in Alkylated and Chlorinated Poly-P-Xylylenes," *Polymer*, vol. 25, no. 8, pp. 1093–1096, 1984.
- [210] G. Surendran, M. Gazicki, W. J. James, and H. Yasuda, "Polymerization of Para-Xylylene Derivatives (Parylene Polymerization) .4. Effects of the Sublimation Rate of Di-Para-Xylylene on the Morphology and Crystallinity of Parylene-N Deposited at Different Temperatures," *Journal of Polymer Science Part a-Polymer Chemistry*, vol. 25, no. 6, pp. 1481–1503, Jun 1987.
- [211] J. E. Field, "An x-ray study of the proportion of crystalline and amorphous components in stretched rubber," *Journal of Applied Physics*, vol. 12, no. 1, pp. 23–34, Jan 1941.
- [212] J. M. Goppel, "On the Degree of Crystallinity in Natural Rubber .2. The Orientation of the Rubber Crystallites in Stretched Samples," *Applied Scientific Research Section A: Mechanics, Heat, Chemical Engineering, Mathematical Methods*, vol. 1, no. 1, pp. 18–26, 1947.

- [213] J. M. Goppel, "On the Degree of Crystallinity in Natural Rubber .1. An Improved Method to Determine the Degree of Crystallization in Rubber," *Applied Scientific Research Section A: Mechanics, Heat, Chemical Engineering, Mathematical Methods*, vol. 1, no. 1, pp. 3–17, 1947.
- [214] S. Krimm and A. V. Tobolsky, "Quantitative X-Ray Studies of Order in Amorphous and Crystalline Polymers—Scattering from Various Polymers and a Study of the Glass Transition in Polystyrene and Polymethyl Methacrylate," *Textile Research Journal*, vol. 21, no. 11, pp. 805–822, 1951.
- [215] P. H. Hermans and A. Weidinger, "Quantitative X-Ray Investigations on the Crystallinity of Cellulose Fibers—a Background Analysis," *Journal of Applied Physics*, vol. 19, no. 5, pp. 491–506, 1948.
- [216] P. H. Hermans and A. Weidinger, "X-Ray Studies on the Crystallinity of Cellulose," *Journal of Polymer Science*, vol. 4, no. 2, pp. 135–144, 1949.
- [217] P. H. Hermans and A. Weidinger, "Crystallinity of Precipitated Cellulose," *Journal of Polymer Science*, vol. 5, no. 5, pp. 565–568, 1950.
- [218] L. E. Alexander, *X-ray diffraction methods in polymer science*. New York, NY: Wiley-Interscience, 1969.
- [219] W. D. Niegisch, "Morphology of Poly-P-Xylylene," *Journal of Polymer Science Part B: Polymer Letters*, vol. 4, no. 8, pp. 531–536, 1966.
- [220] S. W. Youn, H. Goto, S. Oyama, M. Takahashi, and R. Maeda, "Control of parameters influencing the thermal imprint of parylene/silicon," *Japanese Journal of Applied Physics Part 1: Regular Papers, Brief Communications & Review Papers*, vol. 46, no. 9B, pp. 6363–6369, Sep 2007.

- [221] J. B. Fortin and T. M. Lu, *Chemical vapor deposition polymerization: the growth and properties of parylene thin films*. Boston: Kluwer Academic Publishers, 2004.
- [222] R. G. Shaw, Y. L. Yeh, and J. W. Lewis, "Polymers of Improved Performance Capabilities and Processes Therefor," U.S. Patent 3 503 903, Mar. 31, 1970.
- [223] K. P. Menard, *Dynamic mechanical analysis: a practical introduction*. Boca Raton, FL: CRC Press, 2008.
- [224] H. G. Gilch and W. L. Wheelwright, "Polymerization of Alpha-Halogenated P-Xylenes with Base," *Journal of Polymer Science Part A—1: Polymer Chemistry*, vol. 4, no. 6, pp. 1337–1349, 1966.
- [225] W. A. Alpaugh and D. R. Morrow, "The thermal properties of monochloro-para-xylylene," *Thermochimica Acta*, vol. 9, no. 2, pp. 171–204, 1974.
- [226] J. J. Senkevich, "Thickness effects in ultrathin film chemical vapor deposition polymers," *Journal of Vacuum Science & Technology A: Vacuum Surfaces and Films*, vol. 18, no. 5, pp. 2586–2590, Sep–Oct 2000.
- [227] C. Kamezawa, Y. Suzuki, and N. Kasagi, "Mechanical Response Evaluation of High-Thermally-Stable-Grade Parylene Spring," in *Proc. of the IEEE 22nd International Conference on Micro Electro Mechanical Systems (MEMS)*, Sorrento, Italy, 2009, pp. 615–618.
- [228] H. S. Noh, Y. Huang, and P. J. Hesketh, "Parylene micromolding, a rapid and low-cost fabrication method for parylene microchannel," *Sensors and Actuators B: Chemical*, vol. 102, no. 1, pp. 78–85, Sep 1 2004.

- [229] H. S. Noh, K. S. Moon, A. Cannon, P. J. Hesketh, and C. P. Wong, "Wafer bonding using microwave heating of parylene intermediate layers," *Journal of Micromechanics and Microengineering*, vol. 14, no. 4, pp. 625–631, Apr 2004.
- [230] P. Tewari, R. Rajagopalan, E. Furman, and M. T. Lanagan, "Control of interfaces on electrical properties of SiO<sub>2</sub>-Parylene-C laminar composite dielectrics," *Journal of Colloid and Interface Science*, vol. 332, no. 1, pp. 65–73, Apr 1 2009.
- [231] M. Chanda and S. K. Roy, *Plastics technology handbook*, 4th ed. Boca Raton, FL: CRC Press/Taylor & Francis Group, 2007.
- [232] PerkinElmer. (2012, Jan. 13). *Introduction to Dynamic Mechanical Analysis (DMA): A Beginner's Guide* [Online]. Available: [http://www.perkinelmer.com/CMSResources/Images/44-74546GDE\\_IntroductionToDMA.pdf](http://www.perkinelmer.com/CMSResources/Images/44-74546GDE_IntroductionToDMA.pdf)
- [233] *Standard Test Method for Tensile Properties of Thin Plastic Sheeting*, ASTM Standard D882, 2009.
- [234] *Standard Test Method for Tensile Properties of Plastics*, ASTM Standard D638, 2008.
- [235] M. A. Spivack, "Mechanical Properties of Very Thin Polymer Films," *Review of Scientific Instruments*, vol. 43, no. 7, pp. 985–990, 1972.
- [236] J. M. Hutchins and N. G. McCrum, "Effect of Thermal Fluctuation on Creep of Polyethylene," *Nature-Physical Science*, vol. 236, no. 69, pp. 115–117, 1972.
- [237] A. W. Thornton, "Creep of Polyethylene above Room Temperature," *Journal of Applied Physics*, vol. 41, no. 11, pp. 4347–4350, 1970.

- [238] J. C. H. Lin, C. Po-Jui, B. Yu, M. Humayun, and T. Yu-Chong, "Minimally Invasive Parylene Dual-Valved Flow Drainage Shunt for Glaucoma Implant," in *Proc. of the 22nd IEEE International Conference on Micro Electro Mechanical Systems (MEMS)*, Sorrento, Italy, 2009, pp. 196–199.
- [239] H. F. Brinson, *Polymer engineering science and viscoelasticity: an introduction*. New York: Springer, 2007.
- [240] A. Plaseied and A. Fatemi, "Tensile Creep and Deformation Modeling of Vinyl Ester Polymer and Its Nanocomposite," *Journal of Reinforced Plastics and Composites*, vol. 28, no. 14, pp. 1775–1788, Jul 2009.
- [241] A. Pasricha, M. E. Turtle, and A. F. Emery, "Time-dependent response of IM7/5260 composites subjected to cyclic thermo-mechanical loading," *Composites Science and Technology*, vol. 56, no. 1, pp. 55–62, 1996.
- [242] E. Marklund, J. Varna, and L. Wallstrom, "Nonlinear viscoelasticity and viscoplasticity of flax/polypropylene composites," *Journal of Engineering Materials and Technology—Transactions of the ASME*, vol. 128, no. 4, pp. 527–536, Oct 2006.
- [243] L. O. Nordin and J. Varna, "Nonlinear viscoplastic and nonlinear viscoelastic material model for paper fiber composites in compression," *Composites Part A: Applied Science and Manufacturing*, vol. 37, no. 2, pp. 344–355, 2006.
- [244] M. E. Tuttle, A. Pasricha, and A. F. Emery, "The Nonlinear Viscoelastic-Viscoplastic Behavior of Im7/5260 Composites Subjected to Cyclic Loading," *Journal of Composite Materials*, vol. 29, no. 15, pp. 2025–2046, 1995.

- [245] L. J. Zapas and J. M. Crissman, "Creep and Recovery Behavior of Ultrahigh Molecular-Weight Polyethylene in the Region of Small Uniaxial Deformations," *Polymer*, vol. 25, no. 1, pp. 57–62, 1984.
- [246] E. Chailleux and P. Davies, "Modelling the non-linear viscoelastic and viscoplastic behaviour of aramid fibre yarns," *Mechanics of Time-Dependent Materials*, vol. 7, no. 3–4, pp. 291–303, 2003.
- [247] Y. C. Lou and R. A. Schapery, "Viscoelastic Characterization of a Nonlinear Fiber-Reinforced Plastic," *Journal of Composite Materials*, vol. 5, pp. 208–234, 1971.
- [248] M. Megnis and J. Varna, "Nonlinear viscoelastic, viscoplastic characterization of unidirectional GF/EP composite," *Mechanics of Time-Dependent Materials*, vol. 7, no. 3-4, pp. 269–290, 2003.
- [249] M. Megnis and J. Varna, "Micromechanics based modeling of nonlinear viscoplastic response of unidirectional composite," *Composites Science and Technology*, vol. 63, no. 1, pp. 19–31, 2003.
- [250] L. O. Nordin and J. Varna, "Nonlinear viscoelastic behavior of paper fiber composites," *Composites Science and Technology*, vol. 65, no. 10, pp. 1609–1625, Aug 2005.
- [251] R. Miranda Guedes, A. Torres Marques, and A. Cardon, "Analytical and Experimental Evaluation of Nonlinear Viscoelastic-Viscoplastic Composite Laminates under Creep, Creep-Recovery, Relaxation and Ramp Loading," *Mechanics of Time-Dependent Materials*, vol. 2, no. 2, pp. 113–128, 1998.

- [252] F. P. Incropera and D. P. DeWitt, *Fundamentals of heat and mass transfer*, 4th ed. New York: Wiley, 1996.
- [253] P. K. Chandra and P. J. d. A. Sobral, "Calculation of viscoelastic properties of edible films: application of three models," *Ciência e Tecnologia de Alimentos*, vol. 20, pp. 250–256, 2000.
- [254] D. D. Joye, "Stress-Relaxation in 3-Element and 4-Element Mechanical Models of Viscoelastic Materials," *Journal of Applied Polymer Science*, vol. 47, no. 2, pp. 345–350, Jan 10 1993.
- [255] M. S. Nandra, I. A. Lavrov, V. R. Edgerton, and Y. C. Tai, "A Parylene-Based Microelectrode Array Implant for Spinal Cord Stimulation in Rats," in *Proc. of the IEEE 24th International Conference on Micro Electro Mechanical Systems (MEMS)*, Cancun, MEXICO, 2011, pp. 1007–1010.
- [256] K. D. Wise, P. T. Bhatti, J. B. Wang, and C. R. Friedrich, "High-density cochlear implants with position sensing and control," *Hearing Research*, vol. 242, no. 1–2, pp. 22–30, Aug 2008.
- [257] E. M. Schmidt, J. S. McIntosh, and M. J. Bak, "Long-Term Implants of Parylene-C Coated Microelectrodes," *Medical & Biological Engineering & Computing*, vol. 26, no. 1, pp. 96–101, Jan 1988.
- [258] J. C. H. Lin, D. Peigang, G. Lam, L. Bo, L. Yi-Kuen, and T. Yu-Chong, "Creep of parylene-C film," in *Proc. of the 16th International Solid-State Sensors, Actuators and Microsystems Conference (Transducers'11)*, Beijing, China, 2011, pp. 2698–2701.

- [259] C. T. Zhang and I. D. Moore, "Nonlinear mechanical response of high density polyethylene .1. Experimental investigation and model evaluation," *Polymer Engineering and Science*, vol. 37, no. 2, pp. 404–413, Feb 1997.
- [260] C. T. Zhang and I. D. Moore, "Nonlinear mechanical response of high density polyethylene .2. Uniaxial constitutive modeling," *Polymer Engineering and Science*, vol. 37, no. 2, pp. 414–420, Feb 1997.
- [261] S. R. Bodner and Y. Partom, "Large Deformation Elastic-Viscoplastic Analysis of a Thick-Walled Spherical Shell," *Journal of Applied Mechanics*, vol. 39, no. 3, pp. 751–757, 1972.
- [262] S. R. Bodner and Y. Partom, "Constitutive Equations for Elastic-Viscoplastic Strain-Hardening Materials," *Journal of Applied Mechanics—Transactions of the ASME*, vol. 42, no. 2, pp. 385–389, 1975.
- [263] K. S. Chan, S. R. Bodner, and U. S. Lindholm, "Phenomenological Modeling of Hardening and Thermal Recovery in Metals," *Journal of Engineering Materials and Technology—Transactions of the ASME*, vol. 110, no. 1, pp. 1–8, Jan 1988.
- [264] M. Pyrz and F. Zairi, "Identification of viscoplastic parameters of phenomenological constitutive equations for polymers by deterministic and evolutionary approach," *Modelling and Simulation in Materials Science and Engineering*, vol. 15, no. 2, pp. 85–103, Mar 2007.
- [265] F. Zairi, M. Nait-Abdelaziz, K. Woznica, and J. M. Gloaguen, "Elasto-viscoplastic constitutive equations for the description of glassy polymers behavior at constant strain rate," *Journal of Engineering Materials and Technology—Transactions of the ASME*, vol. 129, no. 1, pp. 29–35, Jan 2007.

- [266] F. Zairi, K. Woznica, and M. Nait-Abdelaziz, "Phenomenological nonlinear modelling of glassy polymers," *Comptes Rendus Mecanique*, vol. 333, no. 4, pp. 359–364, Apr 2005.